A Thesis for the Degree of Doctor of Philosophy

Computational simulation of near-field plume-surface interaction and regolith erosion along with particle dispersal during the lunar landing

By

Amin Rahimi

Department of Mechanical and Aerospace Engineering

Graduate School

Gyeongsang National University

August, 2019

Computational simulation of near-field plume-surface interaction and regolith erosion along with particle dispersal during the lunar landing

A Dissertation Submitted to the Faculty of the Graduate School of the Gyeongsang National University

By

Amin Rahimi

In partial fulfillment of the requirements for the degree of

Ph.D. in Engineering

August, 2019

Prof. Rho Shin Myong, Dissertation Supervisor

Approved by committees of the Graduate School of Gyeongsang National University in partial fulfillment of the requirements for the degree of Doctor of Philosophy

Dissertation Committee:

Prof. Dr. Jae Hyun Park
Chairman

Prof. Dr. Hyung Bum Kim

Dr. Omid Ejtehadi

Prof. Dr. Rakesh Kumar

Prof. Dr. Rho Shin Myong
Supervisor

Date: 2019.07

Department of Mechanical and Aerospace Engineering
Graduate School
Gyeongsang National University

Acknowledgment

Throughout doing of Ph.D., I have received a great deal of support and assistance. Firstly, I would like to express my special appreciation to my supervisor, Professor Rho Shin Myong, whose expertise was invaluable in guiding to accomplish this work. I took advantage of his advice, at many stages of this research project, particularly when exploring new ideas. Moreover, I have been inspired and confident not only in my research but also my life due to his positive outlook and confidence.

I would like to acknowledge the committee members of my thesis: Professor Hyung Bum Kim from department of Mechanical engineering and Professor Jae Hyun Park from Aerospace engineering of Gyeongsang National University, South Korea, Professor Rakesh Kumar from Indian Institute of Technology Kanpur, India, and Dr. Omid Ejtehadi from Korea Institute of Science and Technology Information for their fruitful assessments that facilitated my effort to finalized this dissertation.

I wish to thank the Korean government for providing financial support including the Brain Korean 21 plus (BK 21+) program as well as National Research Foundation (NRF) of South Korea (2017R1A2B2007634) in terms of grants and scholarships.

My special thanks go to my fellow lab mates in Aerospace Computational Modeling Laboratory, particularly Korean friends who helped me to overcome the living barrier in a foreign country. It would have been impossible doing administrative works without their assistance. My sincere gratitude goes to my best friend and brother Dr. Omid Ejtehadi, by which I cannot forget his help during tough moments.

I would take this opportunity to thank my wife Atieh, with whom I shared the joy and bitterness of research and living abroad throughout all the stages of my Ph.D. and life. I also owe a huge debt of gratitude to my parents, my brother and his wife, and my mother in law

who kept in touch while I was miles and miles far from home. It is not easy to put in words how thankful I am for all their supports from long distance.

At the end, I especially appreciate the Iranian community in Jinju city, who were the source of energy in times when academic life was not smooth.

Dedication

To my beloved wife, Atieh

To my parents

To my brother and sister Hesam and Shohreh

To my sweetheart Sora

To my mother in law

(Thanks for your never-ending care and support)

Table of Contents

List of figures

List of tables

Nomenclatures

Greek

α	volume fraction, section 2.3.1
β	particulate loading, section 2.3.4
γ	the ratio of the specific heats
γ_s	dissipation of kinetic energy due to inelastic particle collisions
Δ	excess normal stress
ζ, η, ξ	reference coordinates
θ	azimuthal angel
$\boldsymbol{\Theta}$	boundary contribution vector in matrix form
$\boldsymbol{\Theta'}$	source terms contribution vector in matrix form
κ	thermal conductivity
λ	molecular mean free path
$\boldsymbol{\Lambda}$	dissipative term
μ	viscosity
$\bar{v}$	average molecular velocity
ρ	bulk density
σ_c	calortropy production
τ_c	mean collision time
τ_v	momentum response time of the particle
τ_T	thermal response time of the particle
φ	basis function
$\boldsymbol{\Psi}$	high order flux term
$\hat{\Psi}$	local calortropy density
Ω_e	standard element
Ω_h	local element
$\boldsymbol{\Pi}$	viscous stress tensor

Latin

$\mathbf{A}$	vector of auxiliary variables
a	speed of sound

b	impact parameter of two-body collision
C	concentration
c	thermal velocity vector
$\bar{c}$	mean thermal velocity
C_D	Drag coefficient
c_m	specific heat of the particle material
C_m	The coefficient of Magnus force
c_p	specific heat at constant pressure
c_v	specific heat at constant volume
d	particle diameter
D	drag force
e	total energy
Ec	Eckert number, ($Ec=u^2/C_pT$), Table 7
F	external force
f	singlet probability distribution function
f^0	equilibrium probability distribution function
f^c	canonical probability distribution function
$\mathbf{F}_{\text{inv}}$	inviscid flux vector
$\mathbf{F}_{\text{visc}}$	viscous flux vector
Fr	Froude number, ($Fr=u/(gL)^{0.5}$), Table 7
H_{rot}	rotational Hamiltonian of the molecule
I	moment of inertia
J	Jacobian matrix
j	the magnitude of angular momentum
k_B	Boltzmann constant
Kn	Knudsen number, (Kn= λ /L), section 7.3
l	particle spacing
L	Reference length
M	Mach number, ($M=u/a$), Table 7
m	molecular mass
$\dot{m}$	mass flux
n	number density
N	number of molecules
N_δ	non-equilibrium quantifier, (N_δ=Kn$M(2\gamma/\pi)^{0.5}$), section 7.3
n_d	normalization factor

Nu	Nusselt number, ($Nu=hL/\kappa$), Table 7
p	pressure
P	Pressure tensor
Pe	Peclet number, (Pe=Lu/κ), Table 7
Pr	Prandtl number, ($Pr=\mu C_p/\kappa$), Table 7
Q	Heat flux vector
Q	heat transfer between phases
R	gas constant
r	The cartesian coordinate of the physical space
Re	Reynolds number, (Re=$\rho uL/\mu$), Table 7
s	specific entropy
St	Stokes number, ($St=\tau_v/\tau_c$), Table 7
T	temperature
t	time
u	stream velocity vector
V	volume
v	molecular velocity vector
z	mass loading
Z	kinematic term

Abbreviation

BCF	bearing capacity failure
BGK	Bhatnagar, Gross and Krook
BR1	the first method of Bassi and Rebay
BR2	the second method of Bassi and Rebay
BTE	Boltzmann transport equation
CFD	computational fluid dynamics
CFL	Courant-Friedrich-Levy
CPR	correction procedure reconstruction
DCD	dust contact discontinuity
DDF	diffusion-driven flow
DDPM	dense discrete phase model
DEM	discrete element method

DG	discontinuous Galerkin
DGE	diffused gas eruption
DMR	double Mach reflection
DPM	discrete particle model
DSMC	direct simulation Monte carlo
FDM	finite difference method
FDS	flux difference splitting
FEM	finite element method
FR	flux reconstruction
FVM	finite volume method
FVS	flux vector splitting
HEM	homogenous equilibrium model
KTGF	kinetic theory of granular flows
LBM	lattice Boltzmann method
LCP	lifting collocation penalty
LDG	local discontinuous Galerkin
LLF	local Lax-Friedrichs
MD	molecular dynamics
NCCR	non-linear coupled constitutive relationships
NSF	Navier-Stokes-Fourier
PIC	particle-in-cell
SD	spectral difference
SET	standard Enskog theory
SMR	single Mach reflection
SV	spectral volume
UGKS	unified gas-kinetic scheme
VE	viscous erosion
VOF	volume of fluid
CVD	chemical vapor deposition
OLED	organic light emitting diode

Abstract

Computational simulation of near-filed plume-surface interaction and regolith erosion along with particle dispersal during the lunar landing

Amin Rahimi

Department of Mechanical and Aerospace Engineering

Graduate School, Gyeongsang National University

Supervised by Prof. Rho Shin Myong

In the last few decades, human never attempted landing on the other planet after the first touchdown on the lunar surface on the Apollo 11 mission. Fifty years since then, exploring the Moon has resumed. Similar to other developed nations, South Korea has aspirations for such exciting missions. Therefore, they are planning to design a lunar lander module with all necessary components as well as considering all the steps of reaching to the Lunar surface. To achieve this goal, running simulation and conducting experiments are highly crucial. The current work is part of the project above, focusing on the descending phase of the lunar landing aspect of the mission.

As the lunar lander approaches its landing site, the rocket plume impinging on the lunar surface can cause significant dust dispersal. This study investigates the near-field rocket plume-lunar surface interaction and subsequent regolith erosion and particle dispersal. These subjects are challenging because of the complicated flow physics associated with the inherently multi-physics multi-scale problem, which is further complicated by the special lunar conditions characterized by micro-gravity, near-vacuum, extreme dryness, and the unique properties of the regolith. To understand the effect of surface erosion on the flow

characteristics, in conjunction with the finite volume method of plume impingement of a rocket nozzle, the Roberts erosion model was employed for obtaining the influx mass flow rate of dust particles based on excess shear stress. The particulate phase was then handled in a Lagrangian framework using the discrete phase model. A parametric study on erosion rate was also conducted to examine the effect of particle density, particle diameter, Mach number, and hover altitude.

Additionally, the maximum speed and inclined angle of the particles from the surface were computed for various particle diameters and hover altitudes. The resulting information about the pressure and heat flux distribution on lunar module components can be used for engineering design. Finally, high-fidelity simulations of particles eroded from the surface indicated that several scenarios may occur depending on particle diameters, grain-inclined angles from the surface, and hover altitudes.

To have better insight on the physics of dusty-gas flows and to understand the gas and solid particle interactions, one and two-dimensional dusty gas benchmark problems were tested. The Eulerian-Eulerian approach was applied by solving the conservation laws along with source terms by utilizing Discontinuous Galerkin (DG) method; where the numerically problematic treatment of the source terms was circumvented by inherent features of DG method which eliminates the need of any conventional procedures. Furthermore, the DG method gives the opportunity of applying high-order numerical methods in our simulations. All the numerical results were verified and/or validated with previous works to ensure the fidelity of present studies.

It is worth mentioning that such capability (solving near-vacuum/vacuum state problems) can be applied to practical applications, including semiconductor fabrication. An example would be the Chemical Vapor Deposition (CVD) process in producing large Organic Light Emitting Diode (OLED) displays, which will be discussed briefly in the current study.

Abstract in Korean

Computational simulation of near-filed plume-surface interaction and regolith erosion along with particle dispersal during the lunar landing

아민 라히미

경상대학교 공과대학

기계항공공학부

항공우주공학 전공

지도교수: 명 노 신

지난 수십 년간, 인류는 아폴로 11 임무를 통한 첫 번째 달 착륙 이후로 다른 행성으로의 착륙을 시도하지 않았다. 아폴로 11 미션으로부터 50 년 이후, 달 탐험이 재개되었다. 다른 선진국들과 마찬가지로, 대한민국도 그러한 흥미로운 임무에 대한 포부를 갖고 있기 때문에, 달 표면에 도달하는 절차 및 그러한 절차에 필요한 모든 구성 요소를 갖춘 달 착륙선 모듈을 설계할 계획을 갖고 있다. 이러한 계획을 달성하기 위해, 전산해석 및 실제 실험을 수행하는 것은 매우 중요하다. 현행 연구는 달 착륙의 하강 절차에 초점을 맞춘 프로젝트의 일부이다.

달 착륙선이 착륙 지점에 도달하면, 달 표면에 부딪히는 로켓 플룸은 상당한 먼지 입자의 분산을 유발할 수 있다. 이 연구는 로켓 플룸과 달 표면의 근거리 상호작용과 그 이후의 표토 침식 및 입자 분산에 대해 연구한다. 이러한 주제는 본질적으로 다물리 및 다차원적 문제와 관련된 복잡한 유체역학적 문제로 인해 더욱 어려워지며, 이는 달의 미소 중력, 진공, 극도의 건조함 및 표토의 고유 속성들에 의해 특징지어지는 특수한 착륙 조건에 의해 더욱 복잡해진다. 표면 침식이 유동 특성에 미치는 영향을 이해하기 위해, 로켓 노즐의 플룸 충돌의 유한 체적법과 연계하여, 먼지 입자의 유입 질유량을 얻기 위해 잉여전단응력에 근거한 Roberts 침식 모델을 사용하였다. 그런 다음, 입자상(Particulate phase)은 이산 유동 모델(Discrete phase model)을 사용한 라그랑지안 체계(Lagrangian framework) 내에서 처리하였다. 입자 밀도, 입자 직경, 마하 수, 호버링 고도의 영향을 조사하기 위해 침식률에 대한 파라메트릭 연구 또한 수행하였다.

추가적으로, 다양한 입자 직경과 호버링 고도에서 표면 입자의 최대 속도와 상승각을 계산하였다. 달 착륙 모듈의 구성 요소들에 가해지는 압력과 열 전도 분포에 대한 정보는 공학적 설계에 사용할 수 있다. 마지막으로, 표면으로부터 침식된 입자에 대한 높은 신뢰도 시뮬레이션은 입자의 직경, 표면에서의 입자 경사각 및 호버링 고도에 따라 여러 시나리오가 발생할 수 있음을 나타냈다.

Dust-기체 다상 유동(Dusty gas flow)의 물리적 현상에 대해 더 나은 직관을 갖고 고체-입자 간 상호작용을 이해하기 위해, 1 차원과 2 차원 Dust-기체 다상 유동에 대한 벤치마크 문제를 시험하였다. Eulerian-Eulerian 접근법은 불연속 갤러킨(Discontinuous Galerkin, DG) 기법을 활용하여 용출항(Source term)및 보존 법칙(Conservation law)을 해석함으로써 적용되었다. 여기서, 수치적으로 문제가 되는 용출항(Source term)에 대한 처리는 불연속 갤러킨 방법의 내재된 특성(관습적인 절차의 요구를 제거함)에 의해 해결되었다. 또한, 불연속 갤러킨 기법을 이용하면 시뮬레이션에 대해 고차 수치기법을 적용할 수 있다. 모든 수치적 결과는 현재 연구의 신뢰성을 보장하기 위해 선행 연구 결과에 대해 검증되었다.

진공 상태의 문제를 해결하는 이러한 방법들은 반도체 제조 산업 등의 응용 분야에 적용될 수 있다. 한 가지 예시로는, 현재 연구에서 간략히 설명될 대형 유기 발광 다이오드(Organic light emitting diode, OLED) 디스플레이 제조 공정에 사용되는 화학기상증착법(Chemical vapor deposition, CVD)이다.

Chapter 1. Introduction

1.1 Motivation and objectives of the current work

Fifty years after Apollo 11's the first Moon landing [1], lunar exploration has recently been resumed. While early lunar explorations were largely propelled by national prestige, the driving force now is the pursuit of opportunities to expand the economic sphere of the Earth to the Moon. Such opportunities include, for example, the discovery of water ice in the craters of the south pole of the Moon [2].

Reaching the Moon involves several stages, including launching from the earth, Earth-Moon transfer, circumlunar orbit, and the final powered descent phase [3]. During the powered descent phase of landing on the Moon, as well as the ascent from the lunar surface after exploration, a complex dusty gas problem may occur, caused by the rapid expansion of rocket plume gas through the nozzle and its subsequent interaction with the lunar surface. The report of the appearance of a granular medium near to the lunar surface was covered by the early Moon exploration programs including Surveyors I and III.

When the lander approaches the lunar surface in the final step of the landing procedure, it is possible that the plume flow gets deflected toward the lander and effects the components loaded on the module. This deflected flow may exert disturbing torque as well as heat flux on sensitive parts of the lander. Further, once the rocket motor plume interacts with the lunar surface, some eroded particles from the regolith may get entrained into the flow field. These particles can not only alter the flow features but can also damage module elements of the explorer or previously settled vehicles and equipment at adjacent sites.

Moreover, as observed in the Apollo programs (11, 12, 14-17), the particles can block vision and cause the malfunctioning of tracking sensors. To minimize the effects of dust,

the later Apollo 14 program adopted a pinpoint landing procedure, rather than the initial Apollo 11's landing procedure, which allowed the lander to move horizontally a considerable distance at low altitude while under the dust influence. Also, in NASA's 2012 Mars Science Laboratory mission with the Curiosity lander, a two-step soft landing was adopted. This involved, first, hovering at an altitude high enough to avoid dust effects, and second, lowering the rover down to the Mars surface on bridles and an umbilical cord (called the Sky Crane maneuver). Furthermore, since many planetary investigations by major space agencies such as ESA, JAXA, NASA, ISRO, and CNSA were conducted, the plume-dust interaction issue became an essential and significant study. Variety of such mission is as follows: the Indian Space Research Organization (ISRO) plan for the first lunar landing in 2018, the Chang'E-4 lunar lander of China National Space Administration (CNSA) by the end of 2018, and NASA's InSight (Interior Exploration using Seismic Investigations, Geodesy and Heat Transport) Mars lander in November of 2018.

In addition to the above issues, the entrained particles may jeopardize long-term exploration that relies on solar panels, which can be degraded by thermal effects and dust contamination. Electrically charged of dust particle was also reported by those who walked on the Moon. By all the observations, as Gaier [4] expressed, the influence of dust grains on the lunar surface can be assorted into nine categories: vision obscuration, false instrument readings, dust coating, and contamination, loss of traction, clogging of mechanisms, abrasion, thermal control problems, seal failures, and inhalation and irritation. Hence, having a comprehensive vision regarding the physics of gas-particle interaction is vitally important, particularly at the last stage of power descend of planetary missions. For these reasons, the Apollo astronaut John Young has claimed, "*Dust is the number one concern in returning to the Moon!*"[5].

A schematic of an impinging rocket motor plume and the subsequent dusty gas flow formed by the ejection of solid particles from the regolith is illustrated in Fig. 1. The multi-scale nature of the physical phenomena in this problem leads to the coexistence of various flow regimes; the plume expansion, shock and stagnation regions, local erosion, granular flow, dusty jet flow, and rarefied flow, which make the computational simulation extremely challenging [6].

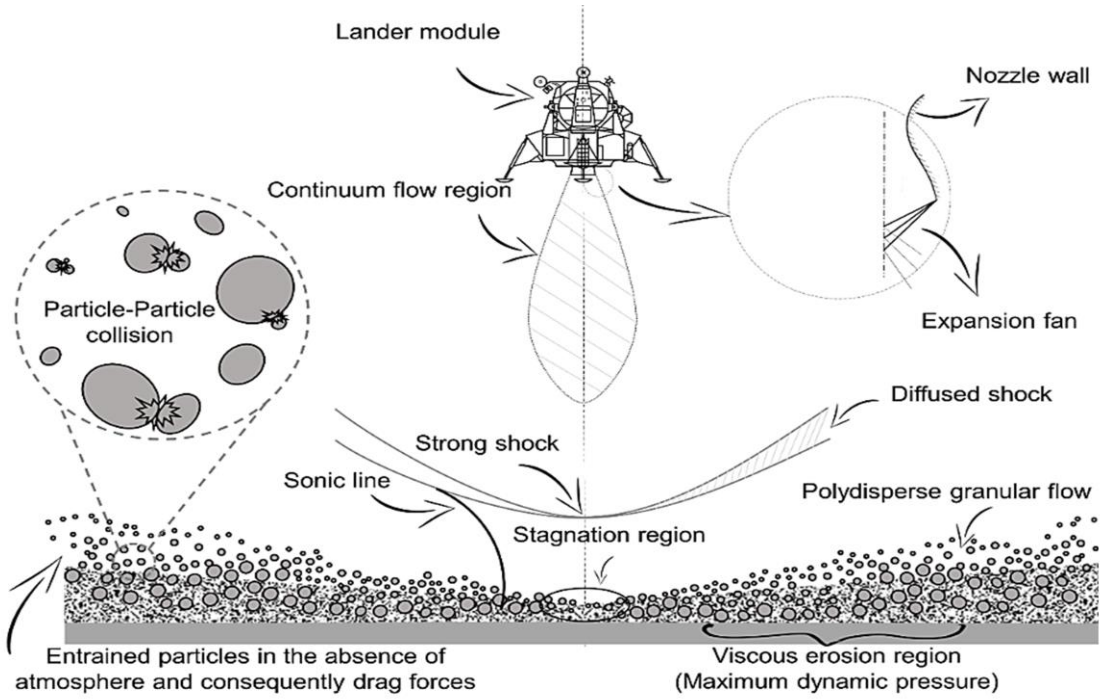

Fig. 1 Schematic of an impinging rocket motor plume and the subsequent dusty gas flow formed by the ejection of solid particles from the regolith during the lunar landing adapted from [7]

It is worthwhile mentioning that designing experiments, which resemble the lunar circumstances on the earth if not impossible is an overwhelming task. Indeed, this sort of restrictions makes computational fluid dynamics (CFD) an efficient tool for predicting this type of flow regimes. The conventional methods for solving highly non-equilibrium regimes including direct simulation Monte Carlo (DSMC) method or hybrid approaches (CFD-DSMC) provide accurate numerical simulation results, particularly for the flow in presence of dust grains, since DSMC method is based on the Lagrangian framework, and

it can handle particles with minor alteration in the general form of algorithm. Despite that, the multiscale nature of the power descending phase problem with the coexistence of various regime's states including equilibrium, near equilibrium, slightly deviated from equilibrium, considerably deviated from equilibrium, and free molecular makes the use of DSMC method an inefficient approach for simulating the entire transient flow. Also, in the case of solving the near surface domain in which the flow would be continuum pair with the occurrence of eroded particles from the lunar surface, the application of hybrid method may not be appropriate. In the present study, we investigated the near-field rocket plume-lunar surface interaction and subsequent regolith erosion and particle dispersal in detail. As the first task for this endeavor, the physical conservation laws with the classical constitutive relations of Navier-Stokes-Fourier (NSF) were solved, based on an FVM discretization. It is well-known that the NSF equations will fail to predict the flow in a highly rarefied condition. Therefore, applying the NSF model to problems in the near vacuum condition of the Moon may be questionable.

However, when the focus is the near-field interaction of the plume and surface in a low altitude hover on the order of a few meters, most flow regimes turn out to be in either continuum or near-continuum. Further, for a five-nozzle configuration, the situation becomes even closer to the continuum condition. The use of the NSF model in the present problem will be justified by a comprehensive analysis of the degree of local thermal non-equilibrium in the dynamic flow field based on the non-equilibrium entropy production associated with the energy dissipation arising from molecular collisions. Therefore, the present methodology can be regarded as an efficient simulation tool for engineering design purposes, compared to the previous computationally expensive DSMC method. Nonetheless, the second-order Boltzmann-based constitutive relations developed by the

authors [8-12] beyond the present first-order NSF constitutive relations may be necessary for a more accurate and far-field description of this challenging problem.

Another vital piece in the present work is the regolith erosion and particle dispersal, both of which demand challenging modeling work. Few studies on modeling the regolith erosion and the effect of entrained particles on the gaseous phase have been reported in the past. Mathematical modeling and simulation of erosion phenomena from plume impingement on the surface for the Apollo mission was pioneered by Roberts [13, 14]. Based on the density distribution at the nozzle exit and the gas properties on the surface derived by normal shock relations, he calculated pressure distribution on the surface in terms of hover altitude, nozzle Mach number, the ratio of specific heats and pressure of the chamber. In another important work by Lane and Metzger [15], the trajectory of grains was predicted by utilizing the DSMC solution as input for simple equations of the particle trajectory model (PTM). Also, they modified the drag and lift equations to include the rarefaction and compressibility effects [16]. In another study, Li *et al*. [17] considered two-way coupling model of gas-particle flow with two different methods of treating particles to obtain a better insight of the impact of entrained grains on the module and surrounding area.

To treat particle dispersal in gas, there are two distinctive approaches; Lagrangian and Eulerian [18]. In the present study, we employ a Lagrangian framework in which one- and two-way coupling of the discrete phase model (DPM) [19] with the NSF equations is easily described. In this model, particles are injected into the domain to simulate the eroded lunar surface particles. The coupling between the dust and gas can be either one or two-way, depending on the level of interaction of the phases. To determine the rate of particle influx, the Roberts model based on excess shear stress in [20] is applied at the lunar surface boundary. Also, a sensitivity analysis on the effect of the variation of

parameters on erosion influx in the Roberts model was conducted. Finally, the maximum speed and inclined angle of the particles from the surface were computed for various particle diameters and hover altitudes, which may provide valuable information for the analysis of landing procedures.

In parallel to the above-mentioned numerical simulations, to have better insight regarding the physics in dusty-gas flows and knowing more about the effect of gas and solid particle interaction, one- and two-dimensional two-fluid model benchmark problems were adopted. The Eulerian-Eulerian approach was applied by solving the conservation laws along with source terms by utilizing Discontinuous Galerkin (DG) method; where the numerically problematic treatment of the source terms was circumvented by inherent features of DG method by which eliminates the need of any conventional procedures. Furthermore, the DG method gives the opportunity of applying the high-order solution in our numerical simulations. All the numerical results were verified and validated for zero-order Euler and first-order Navier-Stokes-Fourier equations in single phase and multiphase problems with previous works to make sure the fidelity of present studies.

As the fidelity of the aforementioned numerical results was approved, one can extend the numerical method by considering some modifications such as applying slip or temperature jump boundary condition pair with conservation laws and first-order constitutive relations to solve more complicated problems under the condition of equilibrium, near equilibrium, and slightly deviated from the equilibrium state. To consider the effect of highly non-equilibrium regimes, one can implement the conservation laws along with second-order constitutive relations as [7] has done. An example can be an estimation of accumulation of organic material in chemical vapor

deposition (CVD) systems to fabricate micro- to large panel displays (LCD or OLED) subject to vacuum or near vacuum circumstances.

1.2 Background and review of previous studies

As the main concern of this study is focusing on near-filed plume surface interaction as well as the dispersal of eroded particles, before digging into the main problem a literature review of the previous studies related the problem is needed. To this end, the survey is divided into three parts. Firstly, some critical works on the subject of nozzle plume and plume interaction will be studied. Secondly, the surface erosion physics and model will be discussed in the various highlighted works, and at the end, relevant papers will be investigated by considering the effect of rarefaction on multiphase flow.

1.2.1 Literature survey on 'plume and plume impingement simulation.'

The complexity of plume associated with surface interaction, resulting in the occurrence of various wave patterns such as expansion fan, different shock waves as well as strong shear layer, and also the existence of stagnation region which leads to a challenging issue called jet impingement. Since the jet impingement problem can be investigated from different aspects, in the present study, we will restrict to works relevant to the topic of this dissertation.

In the case of non-zero ambient pressure (near vacuum) which significantly differs from extremely vacuum condition, when the gas flow emanates from the nozzle exit expands freely into the flow filed. The gas at high pressure tends to adjust itself with the environment state to equalize the pressures. As a result, a jet boundary called the free boundary, associated with Kelvin-Helmholtz instability appears. All the waves, including the shocks and expansions, must reflect from the jet boundary in such a way to preserve the pressure downstream of the jet exit. In contrast to the solid boundary where the waves

are reflected as they collide, the free boundary returns a compression wave as expansion impinges and reflects an expansion when compression wave encounters the free boundary. The compression waves accumulate and form a barrel shock. A normal shock front is observed just after the interaction of hot jet gas with high velocity to the surrounding quiescent and extends towards the axis in a Mach-disk configuration. Several experiments [21-26] have provided valuable knowledge in plume-surface interaction; where, surface pressure was measured with respect to change in pressure ratio, flat plate inclination angle, and nozzle-plate distance. Nakai [25] has proved that the distance from the nozzle lip to the point where the jet shock first collides on the plate, plays an essential role in defining flow pattern.

Analytical solution for the highly rarefied jet, in the collision-less limit, has been suggested by Khasawneh *et al.* [27] in the case of jet impingement on a flat surface. The results have been verified by DSMC solutions. In the other works, Cai [28] generalized the relations provided by Khasawneh for the case of inclined plates. Later, he [29] investigated the effects of rarefaction on jet impingement loads for a variety of regimes from continuum to collision-less flows, purposed analytical relations, and verified the results with DSMC solutions.

Due to the restrictions of an experiment in producing rarefied conditions, and the associated high-priced equipment, researchers tend to use numerical tools. In many of the studies which deal with highly non-equilibrium regimes, and the main focus was toward the rarefaction effects, DSMC method [30-33] were utilized. Tosh *et al.* [6] applied a hybrid continuum-rarefied method to simulate the impingement of hypersonic rocket exhaust gas on the surface at the lunar environmental conditions. The final results (with the first-order accuracy in space) have been validated with available experiments. In the last few decades, various studies have investigated not only the rocket nozzle plume [34,

35], but also the effect of exhaust gas on the field of operation [36-39], the lander module components in space missions [40], and the surface of the landing site.

He *et al*. [41] illustrated the aerodynamic effects of cushion engines on the explorer's bottom, the landfall legs, and antenna in Chinese "Tanyue" project. They conducted a numerical study based on the DSMC method and analyzed the engine plume and its impacts on the lander components. It showed the existence of compression waves near the landfall legs, as well as high-pressure regions on the bottom caused by the presence of the landfall legs. In another work, Yim *et al*. [42] carried out an analysis for European service modules (ESM) on the plume effects of various engines, such as the reaction control system (RCS), auxiliary engines, and orbital maneuvering system engine (OMS-E). They evaluated the heat flux generated by the plume on sensitive surfaces, and particularly on the solar panels, during a thermal analysis of the ESM engine. Sharma *et al*. [43] investigated the effect of multiple engine plumes and thermal load on India's second lunar exploration mission, Chandrayaan-2, using a Navier-Stokes solver coupled with the radiative transport equation. Zheng *et al*. [44, 45] and Wei *et al*. [44, 45] investigated the dynamics of soft-landing under different scenarios to guide the future design of manned lander or larger modules in lunar landing missions.

1.2.2 Literature survey on '*surface erosion modeling.*'

The surface erosion occurs once the kinetic energy of the exhaust gas emanated from jet exit transfers to the surface stresses, and as a result, regolith particle being dislodged from the rest position and entrained into flow-filed. As demonstrated in [46], the erosion can be influenced by nozzle characteristics including the thrust level, the hover altitude and the degree of expansion of the jet, as well as regolith cohesion strength and particle size. As noted earlier, the surface erosion modeling for simulating erosion rate induced by plume-surface interaction for Apollo mission mathematically was suggested by

Roberts [47, 48] for the first time. The model is based upon the first principle assumption that the mentioned phenomenon occurs only when the gas-phase shear stress exceeds the critical shear strength of the soil. The model above has a deficiency on rigorous anticipation of erosion rate below a critical hover altitude. Moreover, it doesn't cover the fundamentally variable lunar condition and merely deals with shear process. Later on, Metzger *et al.* [20, 49] improved Roberts' theory by scrutinizing the assumptions. The previously unrecognized diffusion-driven mechanism accommodated the new model. It is worth discussing that more fundamental elaboration is required in order to provide advanced models whereby it can take into account the complex phenomenological processes of surface erosion. Nevertheless, based on the objectives of simulation, the current models are capable of demonstrating large-scale phenomena to an acceptable level. For instance, the Roberts model was expanded upon by Morris et al. [50-52] vastly, and it was revealed that regardless of various reality-inconsistent assumptions, the theory is an adequate tool depending upon the purpose of simulation.

1.2.3 Literature survey on 'rarefied multiphase flow.'

The number of numerical studies considering the existence of solid particles in the plume flow field and their interaction on each other is considerably scarce. The extension of the suggested DSMC approach by Gallis *et al.* [53] was carried out by Burt and Boyd [54] where the attention was given to solve the transportation of spherical particles in a rarefied gas flow according to apply two-way coupling. In other work, to circumvent the deficiency of the DSMC method in a continuum regime, Gimelshein *et al.* [32], by means of a hybrid model, simulated the small aluminized propellent thruster interacting with plume flow and expanding into the rarefied atmosphere by employing CFD-DSMC algorithm. A numerical approach based on the discrete element method (DEM) was developed by Liu *et al.* [55] in order to consider a single dust particle injection. The

injected particles are scattered in the flow field solution domain established by DSMC and gas kinetic BGK method. However, the inherent feature of the DEM, which is deterministic makes this approach expensive from the computational cost standpoint. He *et al.* [56] employed the DSMC method to the problem of the last stage of lunar landing called as power descend phase. He included all the possible interactions of dust grains and gas molecules. Morris *et al.* [50, 57] took advantage of NASA's continuum flow solver [58] called as DPLR and loosely coupled with DSMC method to investigate the effect of the interaction of exhaust gas and lunar surface in two- and three-dimensional space. The continuum solver calculated the nozzle core flow and the non-equilibrium regime as well as eroded particle handled by DSMC solver [51, 52]. The significant effects of granular particles on the flow structures including shocks, wakes, and surface properties in high speed flows was investigated by Chinnappan *et al.* [59].

1.2.4 Literature survey on 'fabrication of Organic Light Emitting Diode (OLED)

Emission of light from OLEDs by applying electricity makes them suitable for digital displays. However, the manufacturing cost of OLEDs is very high. The high rate of waste of expensive organic materials is one of the most important reasons for the high manufacturing cost of OLEDs. To deal with this problem, Tung et al. [60] developed a novel thin-film deposition system which uses a planar source, loadable with any solvent-mixed organic compounds. In order to prove the possibility of utilizing this system to a large area and various organic materials, they presented an experimental investigation along with DSMC simulation. They claimed that this system provides low-cost manufacturing for OLEDs by improving the material utilization rate and scaling up for deposition of large area-size substrate.

Farber et al. [61] simulated the production of organic light-emitting diodes. In this process, they deposited the layers of organic molecules from the gas phase on a substrate. The deposition takes place in a high-vacuum chamber. Simulation of this process is challenging because different parts of this system have different length scales from the order of 1 meter in the whole system to order of millimeter in nozzles of outgoing pipes. Furthermore, the OLED layer thickness is in the order of nanometers and pressure throughout the system differs from 10^{-1} to 10^{-5} Pa. Since in this system, the pressure decreases, and the Knudsen number increases sharply, only a coupled Navier-Stokes/DSMC simulation is possible. They used ANSYS Fluent for the whole domain, while DSMCFOAM solver was applied in high Knudsen number regions.

In optoelectronic devices such as thin film transistors (TFTs), organic photovoltaics (OPVs) and OLEDs, thin metal films have been used as cathodes and anodes. Different techniques are used to deposit metals such as Physical Vapor Deposition (PVD), Vacuum Thermal Evaporation (VTE). The latter is a high vacuum method which is commonly used for OLEDs, OPVs and TFTs.

High vacuum methods have some disadvantages such as inefficient material utilization and high expense for large substances. However, by utilizing high vacuum, long mean free paths will be achieved, which makes it possible for metal atoms to reach the substrate without any collision. Consequently, providing uniform films is possible. Since methods like VTE using directional line-of-sight trajectory, the formation of conformal films on non-uniform substrates is not possible. As a result, deposition techniques based on non-line-of-sight such as chemical vapor deposition (CVD) and atomic layer deposition (ALD) attract the researcher's attention. Navarro et al. [62] used a new technique to fabricate thin metal films based on vapor phase deposition (VPD), which is a non-line-of-sight method.

1.3 Outline

This dissertation is comprised of three main parts starting with the section includes the first four chapters explain the theory, the next three belonging to second part and discuss the numerical results obtained in physics study of dusty gas flow during the descending phase of the lunar landing , and the last section contains a recent work associated with the OLED fabrication.

In Chapter 2, the fundamentals of multiphase are briefly introduced. Chapter 3 discusses the governing equations of the mathematical model of gas-particle multiphase flow pair with erosion mechanism and modeling. The discontinuous Galerkin method, finite volume method along with Discrete phase model as the numerical approaches for solving the Eulerian-Eulerian and Eulerian-Lagrangian mathematical models, are outlined in Chapter 4.

Chapters 5, 6, and 7 are devoted to providing the results obtained in inviscid flow conditions (conservation law along with zeroth-order constitutive relation), viscous flow conditions (conservation law along with first-order constitutive relation) and near-field plume-surface interaction. The newly onset research regarding OLED deposition in near vacuum regime is included in chapter 8. Finally, in Chapter 9, conclusions are drawn, and the possible directions for future works are briefly pointed out.

Chapter 2. Physics of Multiphase Flows

Multiphase flow is simply any fluid flow system:

- ✓ Consisting of two or more different phases co-existing in the mixture, and
- ✓ Having the same level of phase separation at a scale well above the molecular level.

It should be noted that in multiphase flow, a phase can be clearly expressed as a distinct category of material that has a specific inertial response and interaction with the flow in which it is immersed.

Multiphase flows are vastly observed in different geophysical flow conditions and technological applications. Biological flows like blood as well as most of the liquids we deal with on a daily basis such as milk and paints are examples of liquid bases containing suspensions. Preparation of coffee in a percolator needs steam and hot water to pass through coffee beans and is another example of multiphase flows which we may encounter daily. In this chapter, various types of multiphase flow are introduced. Since the main focus of the current study is on gas-solid flows after the introductory summary of the primary principles, then we resume our discussion by taking advantage of what is mentioned in this chapter.

2.1 Various classification of multiphase flows

Four general groups of multiphase flow have been identified based on the combination of the phases which are as liquid-liquid or gas-liquid, gas-solid, liquid-solid, and simultaneous existence of three phases. In this section, we will explain each of the aforementioned multi-phases pairings with some examples.

2.1.1 Characteristics of liquid-liquid and gas-liquid flow

Liquid-liquid two-phase flow is composed of two immiscible liquids and is employed in various engineering applications, particularly in the petroleum industries, where transportation of oil and water mixture is the primary concern. From engineering design purposes, it is crucial to predict the characteristics of oil-water flow, including flow pattern, water holdup, and pressure gradient rigorously. On the other extreme, despite the liquid-liquid importance, it has not been investigated to the same level as gas-liquid flows. The most complex two-phase flow is gas-liquid, thanks to coexistence of interface deformation and compressibility features of carrier phase. There is an infinite number of configurations that could be formed by the gas-liquid interfacial distribution. However, these configurations can be categorized into commonly called flow patterns. Various flow patterns have been observed either in vertical flow including bubble, churn, and slug flow or in horizontal flows, which particular example is stratified flow.

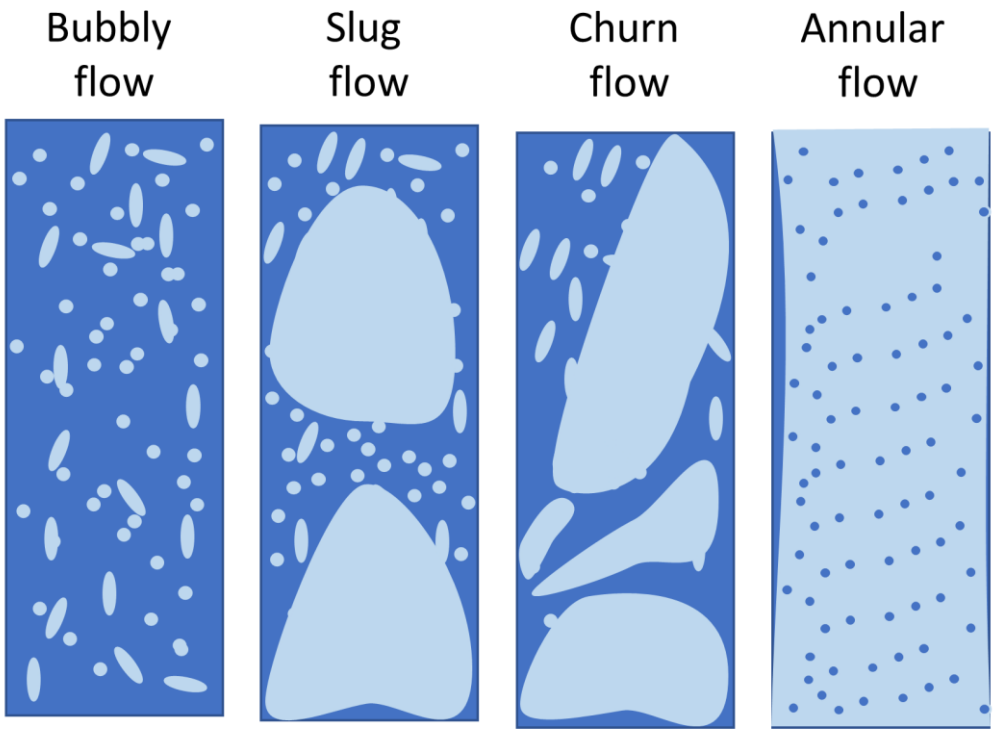

Fig. 2 Flow patterns for vertical pipe flow of air and water.

2.1.2 Characteristics of gas-solid flows

The gas-solid flows are involved in many applications. From technological processes to geophysical phenomena. The flow consists of the gaseous phase with suspended particle grains. The summary of the most well-known applications of such flow is illustrated below:

Table 1 Presence of dusty-gas flows in various applications

Technological processes	Solid rocket boosters
	Flight in the presence of particles
	Fluidized beds
	Dust collectors
	Coal mine explosions
Geophysical phenomena	Volcanoes
	Avalanches
	Star formation
	Cosmic Explosions
	Dust (Sand) storms
	Quick-sands

The gas-solid is assumed to be a granular flow when wall-particle or particle-particle collisions are more dominant compared to the interstitial forces. In the case of stationary particles, the governing physics identified on the particle surface is prevailed by viscous force. Thus the flow turns to the porous medium.

2.1.3 Characteristics of liquid-solid flows

It is called to flow with liquid continuum fluid companied by dispersed solid particles where the solid particles are transported in liquid. The fluid influences the solid grains by exerting drag and pressure forces. The slurry flow, which falls into this category, contains a thin sloppy fluid mixture occupied by fine particles in liquid for a vast range of industrial purposes as well as sediment transportation. Some natural instances illustrated in soil erosion due to rain and storm, waterjet cutting in industrial processes, and sediment transport in rivers and sea.

2.1.4 Characteristics of multiple phases (three-phase) flow

This flow is also included in some engineering problems. As the name implies, these types of flow are identified by the simultaneous presence of three phases. Mostly they can be distinguished as a combination of two of the above categories. Examples include bubbles in a slurry flow and simultaneous presence of droplets and particles in gaseous flows.

2.2 Overview of gas particulate flows

As noted earlier, the presence of solid grains in the gaseous phase, which identified as the gas-solid flow has occupied the significant portion of industrial applications among all the various categories of the multiphase flows. A class of multi-phase flows, composed of compressible gases carrying a substantial amount of small particles like dust or droplets, has emerged as an exciting topic in recent years. The interest is largely driven by the increasing need to understand technological processes (e.g., explosions in coal mines [63], the separation of particulate matter from fluids [64], and the interaction of rocket plumes and lunar dust [65]) and natural geophysical phenomena (e.g., volcanic eruptions [66], cosmic explosions [67], and star formation [68]), as summarized in Fig. 3.

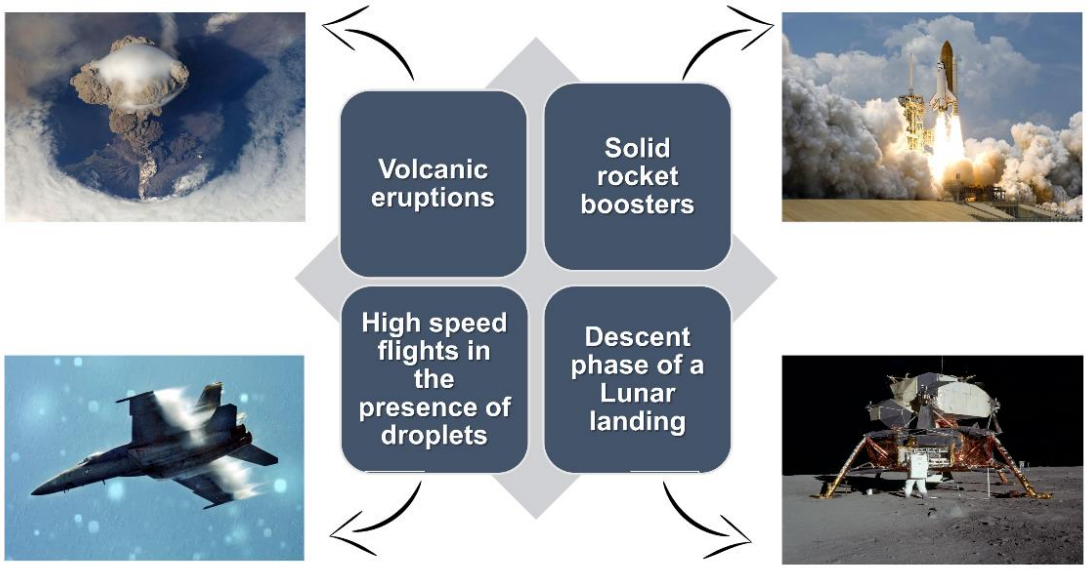

Fig. 3 Various applications of dusty gas flows adapted from [18]

The dynamics of dusty gas flows are known to be significantly different from those of pure gas flows. This difference is mainly caused by the mass, momentum, and heat exchange that occurs between the two phases. In dusty gas flows with shock waves, such as coal mine explosions or the interaction of the lunar lander's rocket plume with the dusty surface of the moon during the descent phase, there is a transition region where the velocity of the shock wave continuously changes due to the inertia and the heat capacity of the particles. Moreover, the mass exchange effects as a result of phase change or chemical reactions are essential in many applications [69]. Such complexities have motivated various theoretical [70, 71] and experimental [72, 73] studies. However, most of these studies have mainly focused on the one-dimensional shock tube problem in order to obtain a comprehensive physical understanding of the dusty gas flows, and consequently, the development of proper mathematical models.

From a theoretical standpoint, there are two common approaches for predicting the dispersed flows: the trajectory (discrete or Lagrangian) and two-fluid (Eulerian-Eulerian) models [74]. In the trajectory model, the dispersed phase is described in the Lagrangian framework, while in the two-fluid model, the dispersed phase is treated as a continuum.

In the present study, the two-fluid model is preferred over the trajectory model, since it is not only applicable to a wide spectrum of particulate loading in multi-phase regimes but also incur a less computational cost, compared to the Lagrangian counterpart. The model is, however, not efficient when the distribution of particle size is the main interest since a separate set of equations should be solved for each diameter size.

While most of the theoretical research has been limited to the one-dimensional numerical problem [75-79], many recent studies have focused on developing multi-dimensional numerical tools with the capability of handling unstructured grids. Saito [80], [81] developed a two-dimensional numerical tool to solve the two systems of conservation laws using the finite volume method. Igra *et al.* [82] investigated shock wave reflection from a wedge in a dusty gas flow by using an accurate second-order scheme in a finite difference framework based on the generalized Riemann problem and dimensional splitting. Moreover, they conducted an extensive parametric study on particle size and mass loading in two different time steps. In another attempt, Igra *et al.* [83] extensively studied shock wave reflection from a wedge placed in various suspensions by using a finite volume method of a two-fluid model.

On the other hand, Volkov *et al.* [84] solved the viscous two-phase gas-particle flow over a blunt body using a Eulerian-Lagrangian approach and investigated the effects of inter-particle collisions and two-way coupling. Pelanti and LeVeque [85] developed the fractional step method in the finite volume framework and applied the method to the one-dimensional shock tube and two-dimensional volcanic eruption problems. Gurris *et al.* [86] solved the two-fluid model of dusty gas flows with a high-resolution finite element method along with a TVD type limiter, and Douglas-Rachford splitting method to handle the source terms. Recently, Carcano *et al.* [87] solved the problem of jet decomposition in both two and three dimensions using a second-order accurate semi-implicit finite

volume method. In another work, Carcano *et al.* [88] extensively investigated the grain-size distribution on the dynamics of under-expanded volcanic jets. Vié *et al.* [89] analyzed the capability of the Eulerian moment method for solving two-way coupled particle-laden turbulent flow systems.

2.3 Principle parameters of gas-particle flows

Prior to deal with the model selection, some substantial parameters need to be defined in order to choose proper mathematical approaches. The volume fraction of the dispersed phase (α_s) and the mass loading (β) are used to define the extreme of phases' interaction. Therefore, one can neglect the impact of solid phase on the carrier phase by applying a small magnitude of α_s and β as a result the one-way coupling is satisfactory. In cases where the masses of both phases are comparable, to take both phases into account, the two-way coupling is necessary. For larger α_s, to consider more governing physics including the particle-particle interactions (collision), agglomeration, and break-up may not be ignored, requiring a four-way coupling. The next factor which plays a significant role in defining the solid grains flow pattern in the flow field and enumerates how the phases can equilibrate is the Stokes number, calculated as the ratio of the aerodynamic response time of the particle (τ_s) to some characteristic time of the carrier phase (t_{ref}). The readers are referred to [90] regarding more details and comprehensive explanation of multiphase parameters.

2.3.1 Definition of the volume fraction and densities

In our considered multiphase gas-solid system, the solid phase is defined as small separate grains in such a fashion that the volume of each particle is small compared to the

overall volume of the solid material. The volume fraction of solid (dispersed) phase is then defined as,

$$\alpha_s = \lim_{V \to V_0} \frac{V_s}{V}. \tag{1}$$

Here V_s and V are the volumes occupied by the solid and the total volume, respectively. The limiting volume, V_0 is the volume in which flow properties do not vary significantly from point to point. Equivalently, the volume fraction of the gas (continuous) phase can be defined as:

$$\alpha_g = \lim_{V \to V_0} \frac{V_g}{V}, \tag{2}$$

where V_g is the volume of the gas phase in the total volume,, which is referred to as the void fraction in some literature. The sum of the volume fractions must be unity (the axiom of continuity).

$$\alpha_s + \alpha_g = 1. \tag{3}$$

Accordingly, the bulk densities (apparent density) of the dispersed and continuous phase, which are related to the material density can be given by:

$$\bar{\rho}_s = \alpha_s \rho_s. \tag{4}$$

$$\bar{\rho}_g = \alpha_g \rho_g \tag{5}$$

2.3.2 Definition of the particle spacing

Another parameter which plays a vital role in characterizing the mechanics of a dispersed phase flow is the particle (or droplet) spacing and is defined as the average distance between the dispersed phase elements. This parameter can be used to determine if a particle can be treated as an isolated system or not. The relation between particle spacing and volume fraction is as follows

$$\frac{l}{d}=\left(\frac{\pi}{6\alpha_s}\right)^{\frac{1}{3}}. \tag{6}$$

Here d is the particle diameter. For $l >> d$, the particles can be treated as isolated and when $l \sim 1$ the interaction between particles cannot be neglected.

2.3.3 Definition of the momentum and temperature response times

The momentum (velocity) and thermal response times (τ_V and τ_T) are essential parameters in establishing dimensionless parameters to characterize the flow. The velocity responds time refers to a time that the particle or droplet takes action on the velocity alteration. The term called temperature response time is defined by the responsiveness of suspended grains or droplets to the thermal changes in the carrier fluid. These parameters are defined in [91] as

$$\tau_{\mathrm{V}}=\frac{\rho_s d^2}{18\mu_g} \tag{7}$$

$$\tau_{\mathrm{T}}=\frac{\rho_s c_m d^2}{12\kappa_g} \tag{8}$$

where ρ_s and c_m are solid phase bulk density and specific heat of the particle material. μ_g and κ_g represent gas viscosity and thermal conductivity, respectively.

2.3.4 Definition of the concentration and loading

The ratio of the mass of the dispersed phase to that of the continuous phase in the multiphase mixture is defined as dispersed phase mass concentration or as the mass particle ratio. It should be noted that in some literature, the volume fraction of the dispersed phase is considered as concentration.

$$C=\frac{\bar{\rho}_s}{\bar{\rho}_g}=\frac{\alpha_s\rho_s}{\alpha_g\rho_g}. \tag{9}$$

Another critical parameter to the definition of the particulate flows is loading, which can be defined as the ratio of particulate mass flux to that of the continuous phase. The terms loading, mass loading, and particulate loading have also been used to denote the concentration.

$$\beta = \frac{\dot{m}_s}{\dot{m}_g}. \tag{10}$$

2.3.5 Definition of the Stokes number

A crucial parameter in fluid-particle flows to characterize the response rate of the particles to changes in fluid motion or, to evaluate the kinetic equilibrium of the particles with the carrier gas, is the Stokes number, defined as

$$St = \frac{\tau_V}{t_{ref}}. \tag{11}$$

$St \ll 1$ implies that the response time of the particles is much less than the characteristic time of the flow. In this case, the particles have enough time to equilibrate with the career phase leading to nearly equal velocities. These types of flows can be safely simulated with a one-way coupled model. On the other extreme, when $St \gg 1$, the response time of the particles is much more than that of the career phase. Consequently, particle velocity is little affected by the fluid velocity change. A two-way coupling algorithm should thus take into account the back-influence of the particle phase on the career fluid.

With the same methodology, a thermal Stokes number can be defined as the ratio of the thermal response time to the characteristic time of the flow to provide an understanding about the response rate of the particles towards temporal changes in the flow.

Chapter 3. Governing mathematical model of multiphase gas-particles flows

3.1 Survey on various mathematical models for multiphase flows

To describe mathematically the dusty-gas flow and all other multiphase classes based on assumptions made in the dispersed phase, one can categorize the models into two distinct families. The first group would be Eulerian where the particles are considered as a continuous phase identical to carrier fluid, and the second category is the Lagrangian approach in which the grains are analyzed as a discrete phase. In the latter framework (alternatively known as *trajectory*, *non-continuum* or *Eulerian-Lagrangian* model), the motion equation of Newton is governed to each particle which is traced in the entire domain. On the other hand, in the Eulerian approach (also referred to as *continuum* or *Eulerian-Eulerian* model), a system of partial differential equations are applied to the continuum solver in which the particles are assumed as a united phase. There would be another family to categorize multiphase modeling where basically it is covered by the Eulerian framework. This group is called a *mixture* model, where the phases are considered as an equivalent single phase with the characteristics of a continuous fluid and can be included in sub-division of the Eulerian framework. The properties of the mixture phase are derived from the averaged features of the phases.

. A third category (or a sub-category of *Eulerian models*) can be devoted to *mixture* models, where both phases are defined by solving the continuum-based equation of a

single fluid with modified properties. Throughout the present study, the carrier fluid (gas phase) being modeled by applying the Eulerian framework. However, it should be noted that employing a Lagrangian approach to solve continuum fluids could be an efficient strategy in specific cases.

The Eulerian family, in comparison with the Lagrangian counterpart, is more diverse in terms of sets of sub-categories to be applied. While two-fluid and mixture models are capable candidates for the solution of dispersed flows, volume of fluid (VOF) method, homogeneous equilibrium model (HEM) and two-fluid VOF method have shown desirable features in resolving separated flows or in conditions where the tracking and locating the fluid-fluid interface is of importance. The most popular models of the Lagrangian family include discrete particle model (DPM) and discrete element method (DEM). While DPM can produce fast computations compared to DEM, it is known to be appropriate only for modeling dilute particle flow (with particle volume fractions of less than 0.12). On the other hand, DEM can provide accurate solutions for a broader range of flow regimes based on particle concentration. The high computational demands in the methods above motivated the development of models such as the dense discrete phase model (DDPM) and multiphase particle-in-cell (MP-PIC) method in which the particle-particle and particle-wall collisions are presented by a force function rather than being explicitly tracked. This categorization is summarized in Table 2.

Table 2 Most well-known mathematical models for the simulation of particulate flows

<table>
<tr><td rowspan="6">Gas-particle flows numerical models</td><td colspan="6">Eulerian</td></tr>
<tr><td colspan="3">Two-fluid models</td><td colspan="3">Mixture models</td></tr>
<tr><td colspan="2">Dispersed</td><td>Separated</td><td colspan="2">Homogeneous</td><td>Mixture</td></tr>
<tr><td>Euler-Euler</td><td>Euler-Granular</td><td>Multi-fluid VOF</td><td>VOF</td><td>HEM</td><td>Slip mixture model</td></tr>
<tr><td colspan="6">Lagrangian</td></tr>
<tr><td>DPM</td><td>DDPM</td><td>MP-PIC</td><td colspan="2">CFD-DSMC</td><td>CFD-DEM</td></tr>
</table>

3.2 Selection of appropriate model

The determination of an appropriate approach is based upon the investigated characteristics of the flow under study and the feasibility of the model to resolve the features of interest. In fact, due to the relative merits and limitations of every computational model or scheme, one should conclude specifying a suitable method for a specific application. From a more general standpoint, it is believed that the Eulerian-Eulerian approaches are computationally more economic than that of the Eulerian-Lagrangian (or Lagrangian-Lagrangian) methods, though the latter predicts rigorous numerical solutions. The preference of computationally low-cost model may provide an opportunity to investigate more details of the whole transient phase of the flow. While it may require relatively more considerable computational effort to the same applied to the Lagrangian models. A comparison between the two general categories of models of simulating multiphase flows, which summarizes the merits and drawbacks of each model is provided in Table 3.

Table 3 Comparison of Eulerian and Lagrangian

	Advantages	Deficiencies
Eulerian	✓ Easy incorporation of particle diffusion effects ✓ Simple extendibility to multidimensional flows ✓ Wide range of validity	✓ Numerical instabilities ✓ Numerical diffusion ✓ Large storage requirements for multiple particle sizes ✓ Additional modeling for inter-particle interaction
Lagrangian	✓ Embodying the "natural" solution schemes for each phase ✓ No numerical diffusion of the particulate phase ✓ No excessive storage requirements for multiple particle size	✓ Need for empirical diffusion velocity or more expensive Monte Carlo methods ✓ Not easy to couple with Eulerian phase ✓ Computationally expensive in high particulate loadings

It can be deduced from the tabulated pros and cons of the two approaches that the proper model of resolving the flows should be applied according to the strength of each model and based on the specific requirement of the simulation.

The volume fraction of the solid phase flow can be considered as one factor of the model selection to define various regimes of flow. Fig. 4 is illustrating the classification as mentioned earlier [90].

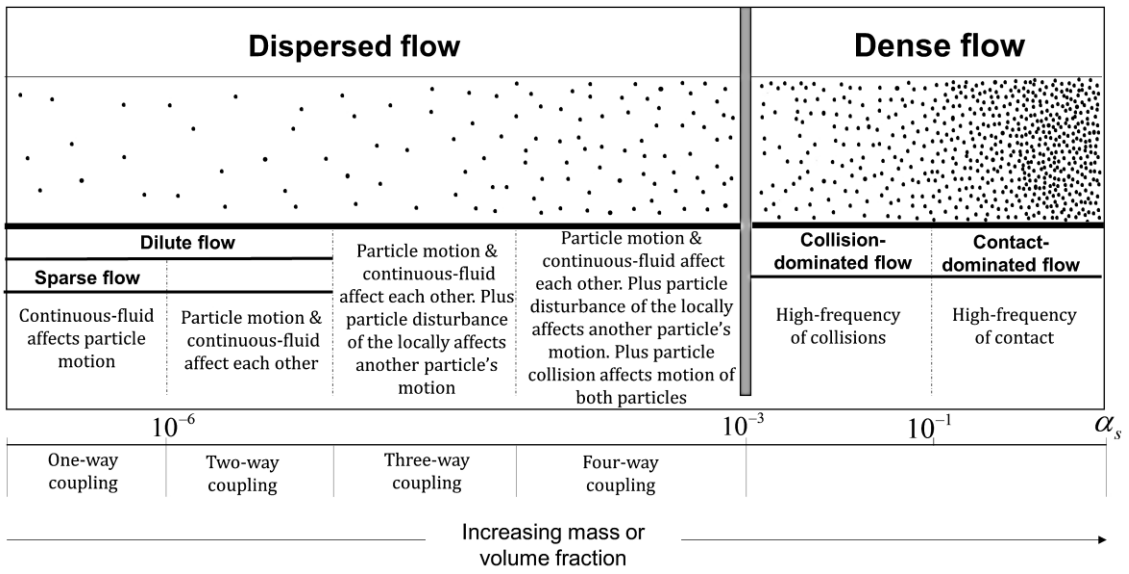

Fig. 4 Classification of particulate flows and the coupling effects based on solid volume fraction

The particulate flows (including dusty gas flows) can be categorized into dispersed and dense. For volume fractions higher than 10^{-3}, the regime is categorized as dense, where high-frequency particle-particle collisions and contacts influence the flow structure. The volume fraction of 10^{-1} marks the boundary of collision dominated, and contact dominated flows. The other extreme, i.e., volume fractions of less than 10^{-3} corresponds to the dispersed flow regime. When the volume fraction is less than 10^{-6} (or 10^{-4} in some literature), the flow is called sparse, and only a one-way coupled modeling can provide satisfactory solutions [91]. In Table 4, the suitable mathematical model based on the loading level is illustrated.

Table 4 Selection of the most efficient model based on the type of multiphase problem, adapted from [7]

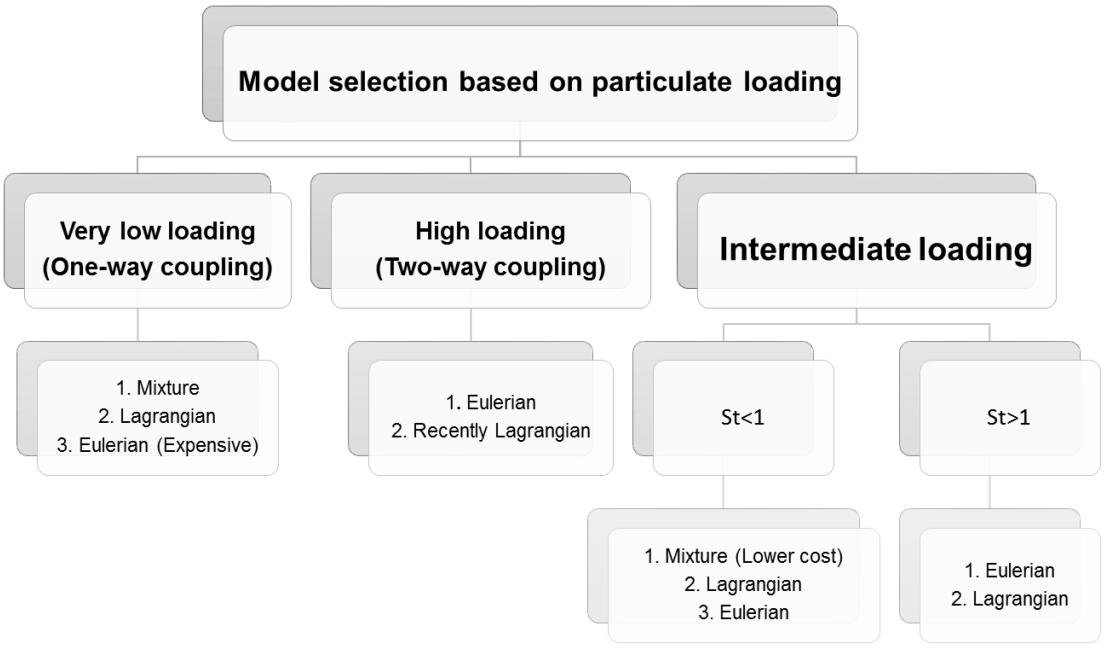

In the problem of Lunar landing, which has been the central motif of this dissertation, a wide range of particulate loadings may exist. Moreover, the Eulerian models can provide acceptable results in a wide range of applications— especially when the volume fraction of the two phases is comparable or when the interaction of the phases signifies

the hydrodynamics of the flow as shown in Table 4. Also, it should be mentioned that we have also applied Lagrangian for very low loading and low volume fraction since the model can be computationally economic in this range as it is depicted in Table 4. In Fig. 5, categorization of flow regimes based on the volume fraction of particles, number density, and particle diameter is provided. Moreover, the regime of interest (marked by a dashed circle) is determined based on the approximate values of the parameters above in a typical Lunar landing obtained from previously published results for Apollo descent engine. Thus, the two-fluid Eulerian model has been employed to the number of dusty-gas benchmark problems as well as the Eulerian-Lagrangian one- and two-way coupled approach has been considered as a suitable/efficient tool to be applied in the Lunar landing problem.

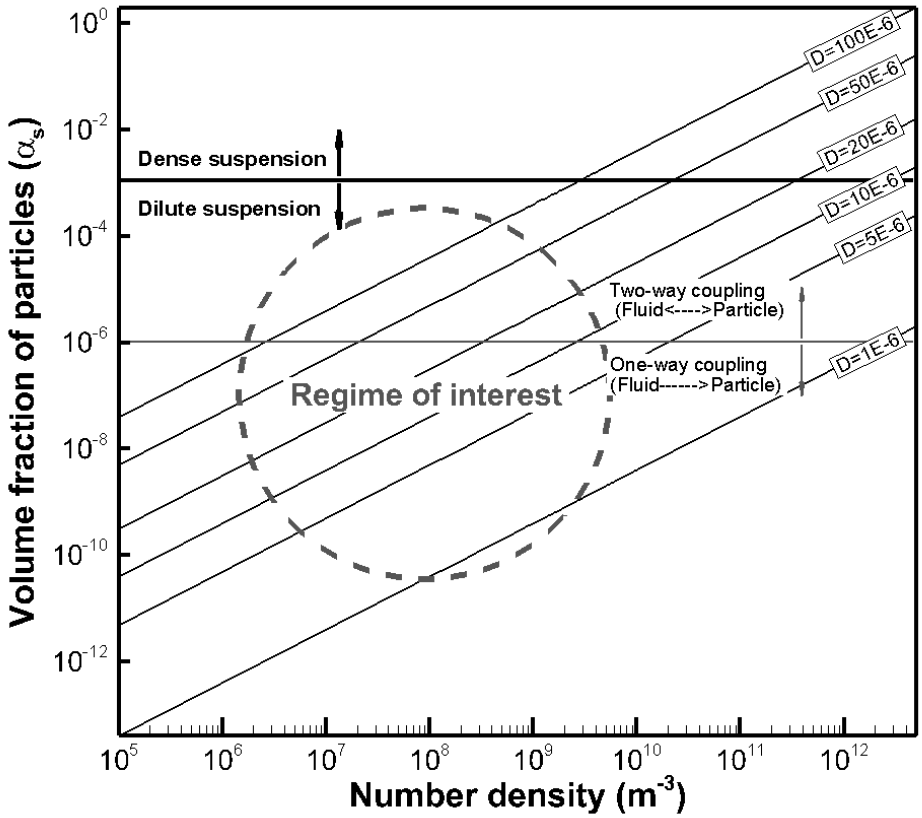

Fig. 5 The range of encountered regimes in the Lunar landing problem overlaid on the classification of the particulate flows based on number density and particles volume fraction

It is worth to note that both dusty gas flows and gas-droplet flows are a sub-division of gas-particle flows. They are distinguished by the fact that mass transfer does not occur in the former but occurs in the latter. Thus, the above discussions are extendable to gas-droplet flows as well.

The rest of this chapter is devoted to the introduction of the generic form of the two-fluid model, which is the focus of current work. Furthermore, variants of the models for different types of problems are discussed, and constitutive relations of non-conserved variables, which are the primary source of the deviation of models are introduced.

3.3 General two-fluid model balanced laws

The two-fluid model is formulated by considering two separate sets of conservation equations which govern the balance of mass, momentum, and energy for each phase of the two-phase system. The interaction of the two phases is then taken into account via source terms, i.e., by momentum and heat transfer exchange between the gas and particles. Other interfacial effects, including lift and gravity, can be neglected since they are small compared to drag and heat transfer. In cases where the interface tracking is of interest, solving an additional face tracking model is necessary. However, in most of the dispersed solid-gas multiphase flows, the evolution and growth of interface if not unimportant, it is of secondary importance. In this section, the conventional assumptions made for computation of dusty gas flows are introduced. Then the general form of the conservation laws is provided, and the constitutive equations necessary to close the equations are introduced in the subsequent subsections. Finally, we provide the dimensionless form of these equations and briefly explain the significance and role of the non-dimensional parameters that appear in the mathematical model.

3.3.1 Adopted hypotheticals of a two-fluid dusty gas model

Several assumptions, conventional in the pioneering and previous literature are introduced in order to simplify the computations. These assumptions might be further refined for specific purpose applications in order to resolve the governing physical phenomena which are significant in that specific problem. These general assumptions in the majority of the works which considered dusty gas flows are as follows

- the gas phase is considered as compressible which follows the perfect-gas law;
- the solid phase is considered as incompressible;
- the particles have a constant density (constant microscopic density);
- the thermal and Brownian motion of particles are neglected;
- the number density of the particles should be large enough not to violate the continuum assumption;
- particles are assumed to be uniform sized spheres with a constant diameter;
- the inter-particle collisions are neglected (and thus no pressure term in the solid phase conservation law);
- specific heat of the particle's material is constant, and the temperature is uniform within each particle;
- the particles are considered as inert;
- the gravitational and buoyant forces are negligible;
- the volume occupied by the solid phase is negligible compared to that of gas;
- The gas is considered as inviscid. Therefore, viscous and heat-conduction effects are solely considered between the gas and particles;
- the turbulence effects of gas and particles are neglected
- the effect of particles' wake is neglected.

While some of the assumptions introduced above are consequent of fundamental characteristics of the model which cannot be ignored, there is room for modifying some

of the other assumptions which have been used in the previous literature in order to provide solutions closer to reality specific to the problem under investigation. For example, the effect of gravity (which finds importance in problems such as volcanic eruptions) can be quickly taken into account by additional source terms without disturbing any fundamental assumptions [87, 92, 93]. The models for inter-particle collisions has been also proposed [94-96]. The viscous effects in the gas phase can also be considered. Kinetic theory approaches have also been considered for continuum modeling of the dispersed phase [97].

3.3.2 Conservation laws of partial differential equations

In this section, a simplified but general two-fluid model of dusty gas flows will be explained briefly. In what follows, the carrier phase (gas) and the dispersed phase (solid dust) are indicated by the subscripts *g* and *s*.

Under the conditions above, the conservation law can be written as follows:

For the gas phase,

$$\partial_t \mathbf{U}_g + \nabla \cdot \mathbf{F}_g = \mathbf{S}, \tag{12}$$

$$\mathbf{U}_g = \begin{bmatrix} \alpha_g \rho_g \\ \alpha_g \rho_g \mathbf{u}_g \\ \alpha_g \rho_g E_g \end{bmatrix}, \quad \mathbf{F}_g = \begin{bmatrix} \alpha_g \rho_g \mathbf{u}_g \\ \alpha_g \rho_g \mathbf{u}_g \mathbf{u}_g + p\mathbf{I} + \mathbf{\Pi}_g \\ (\alpha_g \rho_g E_g + p)\mathbf{u}_g + \mathbf{\Pi}_g . \mathbf{u}_g + \mathbf{Q}_g \end{bmatrix},$$
$$\mathbf{S} = \begin{bmatrix} 0 \\ D_{g,s}(\mathbf{u}_s - \mathbf{u}_g) \\ D_{g,s}(\mathbf{u}_s - \mathbf{u}_g)\mathbf{u}_s + Q_{g,s}(T_s - T_g) \end{bmatrix}, \tag{13}$$

moreover, for the solid phase,

$$\partial_t \mathbf{U}_s + \nabla \cdot \mathbf{F}_s = -\mathbf{S}, \tag{14}$$

$$\mathbf{U}_s = \begin{bmatrix} \alpha_s \rho_s \\ \alpha_s \rho_s \mathbf{u}_s \\ \alpha_s \rho_s E_s \end{bmatrix}, \quad \mathbf{F}_s = \begin{bmatrix} \alpha_s \rho_s \mathbf{u}_s \\ \alpha_s \rho_s \mathbf{u}_s \mathbf{u}_s + \mathbf{\Pi}_s \\ (\alpha_s \rho_s E_s)\mathbf{u}_s + \mathbf{\Pi}_s . \mathbf{u}_s + \mathbf{Q}_s \end{bmatrix}, \tag{15}$$

Here the **U**, **F**, and **S** are the vectors of conservative variables, fluxes, and source terms, respectively. The variables *t*, α, *ρ*, **u**, *E*, *p*, *T*, **Π**, and **Q** represent time, volume fraction, density, velocity vector, total energy, pressure, temperature, stress tensor, and heat flux vector. Further, *D* and *Q* show interphase drag and heat flux, respectively. The dust density ρ_s is assumed to be constant.

3.3.3 Axisymmetric conservation law equations in three-dimensional space form

The above system of equations was written in a general form and can be easily re-written for one to three-dimensional flows. However, a particular case is the three-dimensional flows with axial symmetry. A two-dimensional formulation in the two space variables (*x*, *r*) can be achieved by rewriting the equations in cylindrical coordinates (*x*, *r*, *θ*). Axisymmetric flow equations for the inviscid gas phase are provided in here as they are the governing equation in most of the cases of this thesis. Extension of this system of equation for viscous flows and as well as for the dust phase is trivial.

$$\frac{\partial}{\partial t}(\mathbf{U}_g) + \frac{\partial}{\partial x}\mathbf{F}_g(\mathbf{U}_g) + \frac{\partial}{\partial r}\mathbf{G}_g(\mathbf{U}_g) = \mathbf{S}_1 + \mathbf{S}_2 \tag{16}$$

$$\mathbf{U}_g = \begin{bmatrix} \alpha_g \rho_g \\ \alpha_g \rho_g u_g \\ \alpha_g \rho_g v_g \\ \alpha_g \rho_g E_g \end{bmatrix}, \quad \mathbf{F}_g = \begin{bmatrix} \alpha_g \rho_g u_g \\ \alpha_g \rho_g u_g^2 + p \\ \alpha_g \rho_g u_g v_g \\ (\alpha_g \rho_g E_g + p) u_g \end{bmatrix}, \quad \mathbf{G}_g = \begin{bmatrix} \alpha_g \rho_g v_g \\ \alpha_g \rho_g u_g v_g \\ \alpha_g \rho_g v_g^2 + p \\ (\alpha_g \rho_g E_g + p) v_g \end{bmatrix}$$

$$\mathbf{S}_1 = \begin{bmatrix} 0 \\ D_{g,s}(u_s - u_g) \\ D_{g,s}(v_s - v_g) \\ D_{g,s}\left((u_s - u_g)u_s + (v_s - v_g)v_s\right) + Q_g(T_s - T_g) \end{bmatrix}, \tag{17}$$

$$\mathbf{S}_2 = \frac{1}{r}\begin{bmatrix} \alpha_g \rho_g v_g \\ \alpha_g \rho_g u_g v_g \\ \alpha_g \rho_g v_g^2 \\ (\alpha_g \rho_g E_g + p) v_g \end{bmatrix}.$$

In the above relation, x and r are the axial and radial directions; u and v are the corresponding velocities. **F** and **G** are the inviscid flux in axial and radial directions. $\mathbf{S}_1$ and $\mathbf{S}_2$ are source terms responsible for phase interactions and axisymmetric geometry.

3.4 Constitutive relations for a two-fluid dusty gas model

To close the conservation law equations mentioned in the previous sections series of constitutive relations are necessitated. These closure relations are introduced in this section. Employment of different constitutive relations for the non-conserved variables results in variants of the generic model, which will also be discussed in the following sections.

3.4.1 Closure of volume fraction

This closure is an indication that the phases are treated as interpenetrating continua, defined as

$$0 \le \alpha_g \le 1, \quad 0 \le \alpha_s \le 1,$$
$$\alpha_g + \alpha_s = 1. \tag{18}$$

3.4.2 Equation of state and total energy for an ideal gas

The equation of state expresses the gas pressure in terms of other gas properties:

$$p = \rho_g R T_g , \tag{19}$$

where R is the gas constant.

The solid phase does not require the equation of state since it is treated as incompressible. The total specific energy of the gas and particulate phases are defined as

$$E_g = c_v T_g + \frac{1}{2}\left|\mathbf{u}_g\right|^2 , \tag{20}$$

$$E_s = c_m T_p + \frac{1}{2}\left|\mathbf{u}_s\right|^2 , \tag{21}$$

where c_v and c_m are the specific heat capacity of the gas at constant volume and the specific heat of the particle material.

3.4.3 Drag forces on spherical particles

As stated by Miura and Glass [75], the drag force that solid particles exert on the gas phase can be expressed as,

$$D_{g,s} = \frac{3}{4} C_D \frac{\alpha_s \rho_g}{d}\left|\mathbf{u}_g - \mathbf{u}_s\right|, \tag{22}$$

in which d is the particle diameter and C_D is the drag coefficient computed as a function of the Reynolds number based on the particle diameter and relative velocity of the particle to the gas (i.e. $\mathrm{Re}_d = \rho_g d\left|\mathbf{u}_g - \mathbf{u}_s\right| / \mu_g$). Based on experimental studies of Morsi and Alexander [98], drag coefficient on a particle can be defined as a function of Reynolds number as follows

$$C_D = a_0 + \frac{a_1}{\mathrm{Re}_p} + \frac{a_2}{\mathrm{Re}_p^2} . \tag{23}$$

where a_0, a_1 and a_2 are empirical coefficients which differ for different Reynolds numbers.

The other expression for C_D, which is widely used is provided by Durst *et al.* [99]

$$C_D = \frac{24}{\mathrm{Re}_p}(1+0.15\,\mathrm{Re}_p^{0.687}). \tag{24}$$

A better estimate is the following well-established semi-empirical correlation [92],

$$C_D = \begin{cases} \dfrac{24}{\mathrm{Re}_d}\left(1+0.15\,\mathrm{Re}_d^{\,0.687}\right), & \text{if} \quad \mathrm{Re}_d < 1000 \\ 0.44, & \text{if} \quad \mathrm{Re}_d > 1000 \end{cases} \tag{25}$$

Other drag coefficient models are also evaluated in the literature [100] including the early models by Newton, Stokes and Oseen defined as

$$\begin{array}{lll} \text{Newton} & C_D = 0.44 & 1000 \le \mathrm{Re}_d \le 2 \sim 4.10^5 \\ \text{Stokes} & C_D = \dfrac{24}{\mathrm{Re}_d} & \mathrm{Re}_d \le 1 \\ \text{Oseen} & C_D = \dfrac{24}{\mathrm{Re}_d}\left(1+\dfrac{3}{16}\mathrm{Re}\right) & \mathrm{Re}_d \le 1 \end{array} \tag{26}$$

Researchers were kept improving the calculation of drag coefficient to obtain a wide range of validity, a number of those estimations are introduced, such as:

$$\begin{array}{lll} \text{Klychko [101]} & C_D = \dfrac{24}{\mathrm{Re}_d}\left(1+\dfrac{(\mathrm{Re})^{2/3}}{6}\right) & \mathrm{Re}_d \le 1000 \\ \text{Gilbert [102]} & C_D = 0.48 + 28(\mathrm{Re})^{-0.85} & \mathrm{Re}_d \le 2 \sim 4.10^5 \end{array}$$

Clift [103]

$$C_D = \begin{cases} \dfrac{24}{\mathrm{Re}_d}\left(1+0.15\,\mathrm{Re}_d^{\,0.687}\right), & \text{if} \quad 0 < \mathrm{Re}_d < 800 \\ \dfrac{24}{\mathrm{Re}_d}\left(1+0.15\,\mathrm{Re}_d^{\,0.687}\right) + \dfrac{0.42}{1+42500(\mathrm{Re})^{-1.16}}, & \text{if} \quad 800 < \mathrm{Re}_d > 3.10^5 \end{cases} \tag{27}$$

To consider the gas compressibility, different models of modified drag coefficient based on Mach number, have also been proposed by Henderson [104].

$$C_D=\begin{cases}\dfrac{24}{\mathrm{Re}_d+S\left\{4.33+\dfrac{3.65-1.53\Theta/T}{1+0.353\Theta/T}\exp\left(-0.247\dfrac{\mathrm{Re}}{S}\right)\right\}}\\ +\exp(-0.5\dfrac{M}{\sqrt{\mathrm{Re}}})\left\{\dfrac{4.5+0.38\left(0.3\,\mathrm{Re}+0.48\sqrt{\mathrm{Re}}\right)}{1+0.03\,\mathrm{Re}+0.48\sqrt{\mathrm{Re}}}0.1M^2+0.2M^8\right\}\\ +0.6S\left\{1-\exp\left(-\dfrac{M}{\mathrm{Re}}\right)\right\}, & \text{if } M<1.0\\ C_D\big|_{M=1.0}+\dfrac{4}{3}(M-1.0)\left(C_D\big|_{M=1.75}-C_D\big|_{M=1.0}\right) & \text{if } 1.0<M<1.75\\ \dfrac{0.9+\dfrac{0.34}{M^2}+1.86\sqrt{\dfrac{M}{\mathrm{Re}}}\left(2+\dfrac{2}{S^2}+\dfrac{1.058}{S}\sqrt{\Theta/T}-\dfrac{1}{S^4}\right)}{1+1.86\sqrt{M/\mathrm{Re}}}, & \text{if } M\geq 1.75\end{cases} \tag{28}$$

where,

$$S=M\sqrt{\frac{\gamma}{2}}. \tag{29}$$

The effect of Knudsen number is also taken into account in determining the drag coefficients which can be found in the literature [105],

$C_D=A\left(24/\mathrm{Re}\right)(1+0.25\,\mathrm{Re}^{0.687})$ where $A=1/\left[1+\mathrm{Kn}\left(3.83+1.28\exp(-1/\mathrm{Kn})\right)\right]$.

Selection of suitable and efficient drag models applied in the dusty gas flows are available in the literature such as [81]. Calculation of the drag in the studies above indicated almost similar results except for low Reynolds number (Re<1) where Stokes and Oseen hypothesis is valid. However, negligible variation in results may lead to the choice of a model with less complexity. As it is stated in [106], the use of incompressible drag coefficient for Mach number in the early stages of the supersonic regime could be sufficient. Therefore, even though most of the flow problems under investigation in this work are compressible flow simple piecewise functions such as the one provided in (25)

is used. The main purpose of this selection is to keep consistency with previous studies [80, 85, 86] as well as taking into account the computational efficiency. It is worth mentioning that more investigation on the calculation of the drag coefficient is needed after obtaining an intermediate solution.

The heat transfer, which is proportional to temperature difference, can be expressed as a function of the Nusselt number [107],

$$Q_{g,s} = \frac{6\mathrm{Nu}\kappa_{\mathrm{g}}}{d^2}\alpha_s(T_g - T_s), \tag{30}$$

$$\mathrm{Nu} = 2 + 0.65\,\mathrm{Re}_d^{\frac{1}{2}}\,\mathrm{Pr}^{\frac{1}{3}},\ \mathrm{Pr} = \frac{c_p\mu_g}{\kappa_g}. \tag{31}$$

Here μ_g and κ_g represent the viscosity and thermal conductivity of the gas, respectively. More sophisticated relations for Nu number are expressed in [108-110].

3.4.4 Calculation of non-conserved variable of the carrier phase

The first step in describing the modeling of the majority of the particulate flow is the foundation of a rigorous hydrodynamic explanation for particulate phase[111]. However, in the Lunar landing problem, this is not the case, i.e., the establishment of the accurate model is as important as or even more critical than the modeling of the dust phase. The zeroth and first-order approximation of high order terms in constitutive relations would recover the Euler and Navier-Stokes classical relationships. However, by a second order approximation (equipped with the concept of balanced closure) a non-linear coupled constitutive relationship (NCCR) can be achieved, where proposed by [12]. When the viscous effects become significant, the validity of classical relationships are questionable, and the application of second-order Boltzmann-based relationships are necessary. These relations are introduced in this section, for the sake of comparison, particularly the second-order relations are also included. However, the numerical simulations of the

present study covers only up to the first-order constitutive relations due to the fact that under specific adopted circumstances as well as the governing physics of the near-filed plume-surface interaction problem in the lunar landing case, the closure relations are free of using second-order approximation.

The constitutive relations from zero-order to second order based on the balanced closure of Myong [112] are provided in Table 5.

Table 5 Summary of zeroth to second order Boltzmann-based constitutive relationships, adapted from [7]

Zeroth-order Boltzmann based (Euler-type) constitutive models
$\mathbf{\Pi}_g = 0,$ $\mathbf{\Delta}_g = 0,$ $\mathbf{Q}_g = 0.$
First-order Boltzmann based (NF type) constitutive models
$\mathbf{\Pi}_g = -2\mu_g \left[\nabla \mathbf{u}_g\right]^{(2)},$ $\mathbf{\Delta}_g = -\mu_b \nabla . \mathbf{u}_g,$ $\mathbf{Q}_g = -\kappa_g \nabla T_g.$
Second-order Boltzmann based (NCCR type) constitutive models
$\left(2p_g + \Delta_g\right)[\nabla \mathbf{u}_g]^{(2)} + 2[\mathbf{\Pi}_g \cdot \nabla \mathbf{u}_g]^{(2)} = -\frac{p_g}{\mu_g}\mathbf{\Pi}_{g\,2nd}\left(\kappa_1\right),$ $2\gamma_g'\left(\mathbf{\Pi}_g + \mathbf{\Delta}_g \mathbf{I}\right) : \nabla \mathbf{u}_g + \frac{2}{3}\gamma_g' p_g \nabla . \mathbf{u}_g = -\frac{2}{3}\gamma_g' \frac{p_g}{\mu_b}\mathbf{\Delta} q_{g\,2nd}\left(\kappa_1\right),$ $\left(p_g + \mathbf{\Delta}_g\right) C_p \nabla T_g + \mathbf{\Pi}_g . C_p \nabla T_g + \mathbf{Q}_g . \nabla \mathbf{u}_g = -\frac{p_g C_p}{\kappa_g}\mathbf{Q}_g q_{2nd}\left(\kappa_1\right).$

The bulk viscosity, shear viscosity, and second coefficient viscosity are related according to the following relation,

$$\mu_b = \lambda + \tfrac{2}{3}\mu. \tag{32}$$

Here, a distinction should be made regarding Navier-Fourier (NF) and Navier-Stokes-Fourier (NSF) terms. In the latter, the Stokes hypothesis ($\mu_b = 0$) implies $\lambda = -\tfrac{2}{3}\mu$.

3.4.5 Calculation of non-conserved variables of the solid phase

The most portion of previous woks in application of dusty gas flows have presented the numerical results for Euler-type relations ($\mathbf{\Pi}_s$=0 and $\mathbf{Q}_s$=0) [69, 71, 75, 76, 83, 85, 106, 113-117] by two-fluid model and it was revealed that their approach is capable of explaining the hydrodynamic behavior of solid phase sufficiently. The pressureless assumption in the solid grain phase equations in dilute regimes appears when the pressure and the shear stresses tend to zero as the collision term is proportional to the square of particle phase volume fraction. Nevertheless, the above-mentioned presumption results in a flaw in the two-fluid model thanks to occurrence of delta-shocks and advent of intense particle segregation. Moreover, when the role of particle-particle collisions in the description of the solid phase is not negligible, the closures models for the solid stress tensor would play a significant role in the modeling. The closure models are the main elements that make the two-fluid models to be distinguished from each other considerably [111]. As Castellanos *et al.* [118] expressed, four different granular regimes can be defined as illustrated in Fig. 6. These are plastic, inertial, fluidized, and entrained regimes which are characterized by the tightly packed granular bed, inter-particle collisions, interstitial effects, and large mean free paths, respectively. The latter, also known as rapid granular flow, is of interest when the simulation of erosion and

consequent entrainment of the eroded particles into flow field due to impingement of descent engine plume of a Lunar Lander.

Before every simulation steps, the characteristics of every existing regime should be identified to have a wise selection of mathematical modeling. In power descend phase of the lunar landing problem as it is depicted in Fig. 7 three different regions near to nozzle proximity could be defined in order to estimate the Stokes number and particulate loading. Region 1, just beneath the nozzle, is the onset of erosion. Here the gas flow after undertaking the strong stand-off shock wave would stagnate because of a confrontation with the surface. In this area, the gas static pressure is maximized, and the gas velocity is tending to zero. In the second region, the fictitious passage formed by the stand-off shock and the surface is resembling converging-diverging nozzle whereby the gas accelerating to reach supersonic velocities. The maximum erosion happens in this area due to the high dynamic pressure. In region 3, both the particles and gas molecules expand further into Moon semi-vacuum atmosphere and undergo free traveling with high velocities. The data range of the simulation results by previous studies indicates that the granular flows in the limits of suspensions and early fluidized bed may emerge depending on the erosion rate.

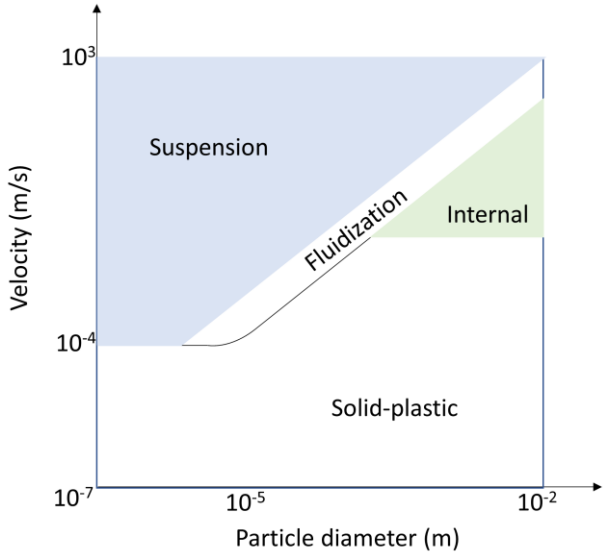

Fig. 6 A typical phase diagram determining the transition between granular flow regimes as a function of particle diameter, adapted from [118]

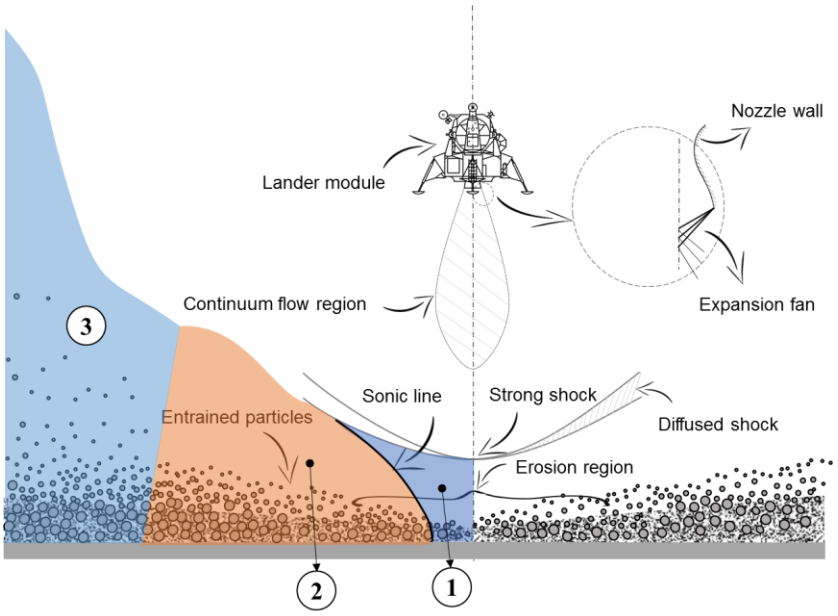

Fig. 7 Graphical categorization of different regions with various specifications. Regions 1-3 are quantified in Table 6, adapted from [7]

Properties of the various regions from Fig. 7 have been summarized in Table 6.

Table 6 Range of important parameters in different regions of Fig. 7

	Region 1	Region 2	Region 3
$\mathbf{u}_g$	Very low	High	High
$\mathbf{u}_s$	0	Low	High
ρ_g	$O\,(10^{-3})$	$O\,(10^{-4})$	$\geq O\,(10^{-4})$
ρ_s	Constant	Constant	Constant
α_s	Very low	High	Intermediate
α_g	≈1	Low	Intermediate
β	≈0	Intermediate	High
St	$\ll 1$	< 1	≈ 1

As shear stresses are depended on viscosity, the first step to investigate the available models to define solid shear stresses is to classify the solid viscosity, where three approaches have been illustrated. Several early experimental researches [119-121] have conducted an investigation into the dependency of solid phase pressure on particle volume fraction in which the experiments were carried out by using constant viscosity. These models are known as *constant viscosity models* (CVM). The second introduced model belongs to particle turbulent viscosity. Nonetheless, this model is confined to dilute dusty gas flows since particle-particle interactions are negligible. Also, kinetic theory-based relations have been proposed that leads to a class of closure models for kinetic-collisional stresses[97, 122-125]. These approaches are known as the *kinetic theory of granular flows* (KTGF). The significant feature of this model is referred to providing a connection between microscopic and macroscopic descriptions of the granular flow. These models have been mostly employed in fluidized beds and moving beds, nonetheless, they can be applied (with a reasonable level of approximation) in different applications when the particle-particle collisions (through binary and frictional contacts) modeling is crucial. It should be noticed that the particle granular and molecular gas flows are two different worlds where one can find significant differences. The main discrepancies come form 1. elastic collisions in gases versus elastic-plastic deformation and surface friction in particles and, 2. conservation of kinetic energy in an isothermal system for gases versus inexistence of an equilibrium state in granular systems without external energy sources [111]. The considerable improvement compared to the DEM solution was observed by Schneiderbauer *et al.* [125] by applying the model to their method. Two-fluid models based on KTGF has indicated the appropriate capability in providing the particle pressure, viscosity, and other transport coefficients; besides, less *ad hoc* adjustments are needed, compared to the previously discussed models. Despite all

features, the models undergo some restrictions [124] which are under development. An alternative approach for the models above is the application of higher-order constitutive relations, which can be derived with a similar approach applied for the gas phase, detailed in [7]. Even though the KTGF provides promising results for particle volume fractions less than 40%, once it increases more than 40% and the multiple particle-particle fractional contacts come into the picture. As a result, the physics description of the dense granular flow would fail in the context of kinetic theory.

The formulations of KTGF are comprehensively being addressed in [7] but to become more familiar with those relations, a brief introduction is provided here. The KTGF allocates the time evolution of the granular temperature as follows,

$$\frac{3}{2}\left[\frac{\partial}{\partial t}\left(\alpha_s\rho_s T_s\right)+\nabla.\left(\alpha_s\rho_s T_s\mathbf{u}_s\right)\right]=-\left(p_s\mathbf{I}+\mathbf{\Pi}_s\right):\nabla\mathbf{u}_s-\nabla.\mathbf{Q}_s-3\beta\mathbf{T}_s-\gamma_s\,, \tag{33}$$

where β and γ_s are the momentum exchange coefficient and the dissipation of kinetic energy due to inelastic particle collisions, respectively. Moreover, pressure tensor (indicates the transport of momentum by thermal velocity):

$$\mathbf{P}_s=\left\langle m\mathbf{c}\mathbf{c}f\left(t,\mathbf{r},\mathbf{v}\right)\right\rangle=\int_{-\infty}^{\infty}\int_{-\infty}^{\infty}\int_{-\infty}^{\infty}m\mathbf{c}\mathbf{c}f_s(t,\mathbf{r},\mathbf{v})d\mathbf{v}\,, \tag{34}$$

$$\mathbf{Q}_s=\left\langle\frac{1}{2}mc^2\mathbf{c}f_s(t,\mathbf{r},\mathbf{v})\right\rangle=\int_{-\infty}^{\infty}\int_{-\infty}^{\infty}\int_{-\infty}^{\infty}\frac{1}{2}mc^2\mathbf{c}f_s(t,\mathbf{r},\mathbf{v})d\mathbf{v}\,. \tag{35}$$

where **r** is the Cartesian coordinates of the physical space and **v** the molecular velocity which can be stated in terms of the stream (macroscopic) velocity **u** and thermal (peculiar) velocity **c.** The symbol $\langle\ldots\rangle$ represents integration over velocity space **v**.

In KTGF, to achieve explicit expressions for the above variables, the distribution function is expanded about the equilibrium distribution function to second order (via the Chapman-Enskog expansion) to yield the following expansion

$$\mathbf{P}_s = p_s\mathbf{I} + \mathbf{\Pi}_s, \tag{36}$$

$$\mathbf{Q}_s = -\kappa_s \nabla T_s. \tag{37}$$

Thus,

$$\mathbf{\Pi}_s = -\mu_s\left[\left(\nabla\mathbf{u}_s\right) + \left(\nabla\mathbf{u}_s\right)^T\right] - \left(\lambda_s - \frac{2}{3}\mu_s\right)\left[\left(\nabla.\mathbf{u}_s\right)\mathbf{I}\right]. \tag{38}$$

The undefined variables in the above relations, viz., κ_s, λ_s, μ_s, and p_s, can be determined if the collision integral of the Boltzmann equation for the solid particles are identified. Hence, after introducing a joint probability function $f_s^{(2)}$ in terms of solid distribution function f_s and pair distribution function g (which itself is dependant upon the distance $r_{12} = \left|\mathbf{r}_2 - \mathbf{r}_1\right|$ and the solid fraction), the collision integral of the solid phase can be estimated bringing about explicit expressions for pressure, shear viscosity, and thermal conductivity:

$$\mu_s = \frac{5}{96}\pi\rho_s d\sqrt{\frac{T_s}{\pi}} \tag{39}$$

$$\kappa_s = \frac{75}{384}\pi\rho_s d\sqrt{\frac{T_s}{\pi}} \tag{40}$$

$$p_s = \alpha_s\rho_s T_s \tag{41}$$

The above expressions are derived for sufficiently low particle density ($g = 1$) and can be applied to the limit of dilute flow.

3.5 Governing equations of the two-fluid dusty gas model in dimensionless form

The following dimensionless variables and parameters are used to derive the non-dimensional governing system of equations. Here the dimensionless parameters are superscripted by *, and the subscript *ref* denotes the reference values,

$$\begin{aligned}
&\mathbf{x}^* = \frac{\mathbf{x}}{L}, \quad t^* = \frac{t}{t_{ref}}, \quad \mathbf{u}^* = \frac{\mathbf{u}}{u_{ref}}, \quad T^* = \frac{T}{T_{ref}}, \quad \rho^* = \frac{\rho}{\rho_{ref}}, \quad p^* = \frac{p}{p_{ref}}, \\
&E^* = \frac{E}{E_{ref}}, \quad Q^* = \frac{Q}{Q_{ref}}, \quad \mu^* = \frac{\mu}{\mu_{ref}}, \quad \kappa^* = \frac{\kappa}{\kappa_{ref}}, \\
&c_p{}^* = \frac{c_p}{c_{p_{ref}}}, \quad c_v{}^* = \frac{c_v}{c_{v_{ref}}}.
\end{aligned} \tag{42}$$

In the above relations, $\mathbf{x}$ and c_p are the spatial coordinates and the specific heat capacity at constant pressure, respectively. We then define the references and non-dimensional parameters as follows:

$$\begin{aligned}
&t_{ref} = \frac{L}{u_{ref}}, \quad \tau_s = \frac{\rho_s d_s^2}{18\mu_{ref}} \quad E_{ref} = u_{ref}^2, \quad Q_{ref} = \frac{\kappa_{ref}\Delta T_{ref}}{L}, \\
&M = \frac{u_{ref}}{a_{ref}}, \quad \mathrm{Re} = \frac{\rho_{ref} u_{ref} L}{\mu_{ref}}, \quad \mathrm{Pr} = \frac{\mu_{ref} C_{p_{ref}}}{\kappa_{ref}}, \quad \mathrm{Pe} = \mathrm{Re}\,\mathrm{Pr}, \\
&\gamma = \frac{C_{p_{ref}}}{C_{v_{ref}}}, \quad \frac{1}{N_\delta \,\mathrm{Re}} = \frac{p_{ref}}{\rho_{ref} u_{ref}^2}, \\
&N_\delta = \frac{\mu_{ref} u_{ref}}{p_{ref} L}, \quad \frac{1}{\mathrm{Re}\,\mathrm{Pr}\,\mathrm{Ec}} = \frac{1}{\mathrm{Pe}} \frac{C_{p_{ref}} T_{ref}}{u_{ref}^2}, \\
&St = \frac{\rho_{ref} u_{ref}}{D_{g,s} L}, \quad Nu = \frac{Q_s L^2}{k_{ref}}, \quad Ec = \frac{u_{ref}^2}{C_{p_{ref}} T_{ref}}.
\end{aligned} \tag{43}$$

After applying these to equations (12) and (15), the following non-dimensional system of equations can be derived:

$$\partial_t \mathbf{U}_g + \nabla \cdot \mathbf{F}_g = \mathbf{S},$$

$$\mathbf{U}_g = \begin{bmatrix} \alpha_g \rho_g \\ \alpha_g \rho_g \mathbf{u}_g \\ \alpha_g \rho_g E_g \end{bmatrix},$$

$$\mathbf{F}_g = \begin{bmatrix} \alpha_g \rho_g \mathbf{u}_g \\ \alpha_g \rho_g \mathbf{u}_g \mathbf{u}_g + \dfrac{1}{N_\delta \,\mathrm{Re}}\, p\mathbf{I} + \dfrac{1}{\mathrm{Re}} \mathbf{\Pi}_g \\ (\alpha_g \rho_g E_g + \dfrac{1}{N_\delta \,\mathrm{Re}}\, p)\mathbf{u}_g + \dfrac{1}{\mathrm{Re}} \mathbf{\Pi}_g . \mathbf{u}_g + \dfrac{1}{Ec\,\mathrm{Pr}\,\mathrm{Re}} \mathbf{Q}_g \end{bmatrix}, \tag{44}$$

$$\mathbf{S} = \begin{bmatrix} 0 \\ \dfrac{1}{St}(\mathbf{u}_s - \mathbf{u}_g) \\ \dfrac{1}{St}(\mathbf{u}_s - \mathbf{u}_g).\mathbf{u}_s + \dfrac{\mathrm{Nu}}{EcPe}(T_s - T_g) \end{bmatrix}.$$

$$\partial_t \mathbf{U}_s + \nabla \cdot \mathbf{F}_s = -\mathbf{S},$$

$$\mathbf{U}_s = \begin{bmatrix} \alpha_s \rho_s \\ \alpha_s \rho_s \mathbf{u}_s \\ \alpha_s \rho_s E_s \end{bmatrix}, \quad \mathbf{F}_s = \begin{bmatrix} \alpha_s \rho_s \mathbf{u}_s \\ \alpha_s \rho_s \mathbf{u}_s \mathbf{u}_s \\ (\alpha_s \rho_s E_s)\mathbf{u}_s \end{bmatrix}.$$

Here the superscript * has been omitted for the sake of simplicity. The reference values for the length, pressure, temperature, and velocity are defined for each test case depending upon the problem of under investigation.

3.5.1 Dimensionless parameters and their physical interpretation

The substantial role of the dimensionless parameters in solving fluid dynamics problem aids in better understanding of governing physics. The introduced parameter in the previous section is tabulated in Table 7.

The Reynolds number is regarded as the ratio of inertial forces to viscous forces. Flow regimes with high Reynolds number can be modeled by inviscid Euler equations where it implies the dominance of inertial forces and the negligible effects of viscous terms. On

the other extreme, i.e., $\mathrm{Re} \ll 1$, comprises a class of flow regimes known as Stokes or creeping flow that can be modeled by Stokes equation (linearized Navier-Stokes).

The ratio of fluid velocity to the speed of sound in the medium is called Mach number and can be applied to characterize the compressibility effects. The Mach number equal to 0.3 is a criterion to distinguish compressible flow with the variation of density from the incompressible flow in conjunction with constant density.

The Prandtl number is the ratio of momentum dissipation to thermal conduction. $\mathrm{Pr} \gg 1$ implies the dominance of momentum diffusivity and $\mathrm{Pr} \ll 1$ represents the dominance of thermal diffusivity.

The Eckert number characterizing the heat dissipation in high speed flows for which dominance of viscous effects is remarkable, is supposed to be the ratio of kinetic energy to enthalpy (or heat dissipation to advective transport). When $Ec \ll 1$, viscous dissipation, pressure alters, and body forces in the energy equation can be ignored.

The Peclet number, defined as the ratio of adjective transport rate to diffusive transport rate. When $Pe \to \infty$, the heat diffusion can be neglected due to the small-time scale of the advection compared to the large time scale of the thermal diffusion.

The ratio of convective to conductive heat transfer is defined by the Nusselt number. $Nu \approx 1$ is known as slug flow. When Nu is large, conductive heat transfer (diffusion) is negligible.

Stokes number can be applied to characterize the response rate of the particles to changes in a fluid motion. When $St \ll 1$, particles can follow the career phase (one-way coupling) and when $St \gg 1$, particles have an impact on the carrier phase (two-way coupling). Froude number estimates flow inertia to the external field where the latter in most applications is the gravitational forces. $Fr \to \infty$ corresponds to a high-velocity flow in which gravitational force is negligible.

Table 7 Non-dimensional parameters and their physical interpretation

Dimensionless number	Definition	Mathematical equation
Reynolds number	Inertial forces / Viscous forces	$\mathrm{Re} = \frac{\rho_{ref} u_{ref} L}{\mu_{ref}}$
Mach number	Inertial forces / Compressibility forces	$M = \frac{u_{ref}}{a_{ref}}$
Prandtl number	Dissipation / Conduction	$\mathrm{Pr} = \frac{\mu_{ref} C_{p_{ref}}}{\kappa_{ref}}$
Eckert number	Kinetic energy / Enthalpy	$Ec = \frac{u_{ref}^2}{C_{p_{ref}} T_{ref}}$
Peclet number	Advection / Diffusion	$Pe = \frac{L u_{ref}}{\kappa_{ref}}$
Nusselt number	Convective heat transfer / Conductive heat transfer	$Nu = \frac{h_{ref} L}{\kappa_{ref}}$
Stokes number	Particle response time / Fluid characteristic time	$St = \frac{\tau_s}{t_{ref}}$
Froude number	Inertial forces / Gravitational forces	$Fr = \frac{u_{ref}}{\sqrt{gL}}$

3.6 Lagrangian approach

Another method to a model particle cloud in a fluid-particle flow is a Lagrangian approach, which can be divided into two groups of methods including discrete element and discrete parcel (particles). In those methods, the trace of individual particles or parcels of the particle are followed through the field, and the determination of the local properties are carried out by the particles or parcels features as they cross the point in the field.

The equations in DEM are applied to each particle in the field covering the body forces, contact, and fluid dynamic. The features of the cloud are described by solving simultaneously the motion and position of each element. This method benefits from taking into account the properties of particle-particle interaction. However, it contains drawbacks including lack of computational capability for solving a practical problem

with numerous particles as well as limitation of particle shapes which is constrained to the sphere.

The particle field in DPM is assorted to the group of particles called as parcels in which they have identical properties and move together. The parcel mobility is determined based on single particle motion in the parcel called “computational” particle. The motion equation of this model in dilute flows application is developed to take into account turbulent fluctuation of carrier phase, particle-particle collision, and particle-wall interaction. On the other hand, the equation of mobility of the computational particle for dense flow applications is extended in order to include particle-particle interaction based on the gradient of the solids stress. The most advantage of using DPM lies on breaking down the particle field into parcels, which results in computationally feasible in the modeling of gas-particle flows for practical problems. It can be referred as a disadvantage of the DPM that it suffers from the lack of the details for particle-particle interaction.

3.7 Erosion mechanism and modeling

The final significant challenge in the proposed strategy to take into consideration the multiphase effects in power descent phase of the lunar landing is surface erosion followed by particle influx into the flow field. An efficient erosion model must provide adequate information regarding location and time at which erosion appears as well as the rate and direction at which particles are lifted from the surface and in-fluxed into the domain. Thanks to the erosion of the surface, craters might be formed and alter the initial shape of the surface. This phenomenon might influence the final solution. However, the effect is not intense. In the current study, first, it is considered the effects of surface variation are negligible similar to what has been assumed in [51] secondly, a three-dimensional simulation has been done to observe how a crater (in this work, the crater is

positioned beneath the nozzle axis) can affect the particle trajectory. In case such effects are of interest the strategy of the simulation may be modified by applying Eulerian multiphase models in which the interface between solid and gas phases is modeled by solving another equation as in the volume of fluid or level set models. The more rigorous approach (considering microscopic scales) can be the application of Lagrangian models; nonetheless, it is worth mentioning that the computational cost would become much larger compared to the Eulerian counterpart. The following section provides, first, the erosion mechanisms. Next, some of the well-known erosion models which have been employed in solving the Lunar landing problem are presented, the relative merits and limitations of each model are explained, and the applied model is described.

3.7.1 Exerted forces on a stationary particle on the sediment bed

The at rest particle on a sediment bed undergoes several forces such as shear, pressure, interparticle and body forces. The particle will be mobilized if the aerodynamic forces are dominant about point P compared to the imposed gravitational and interparticle forces. A schematic of the exerted forces on an immobile particle is provided in Fig. 8.

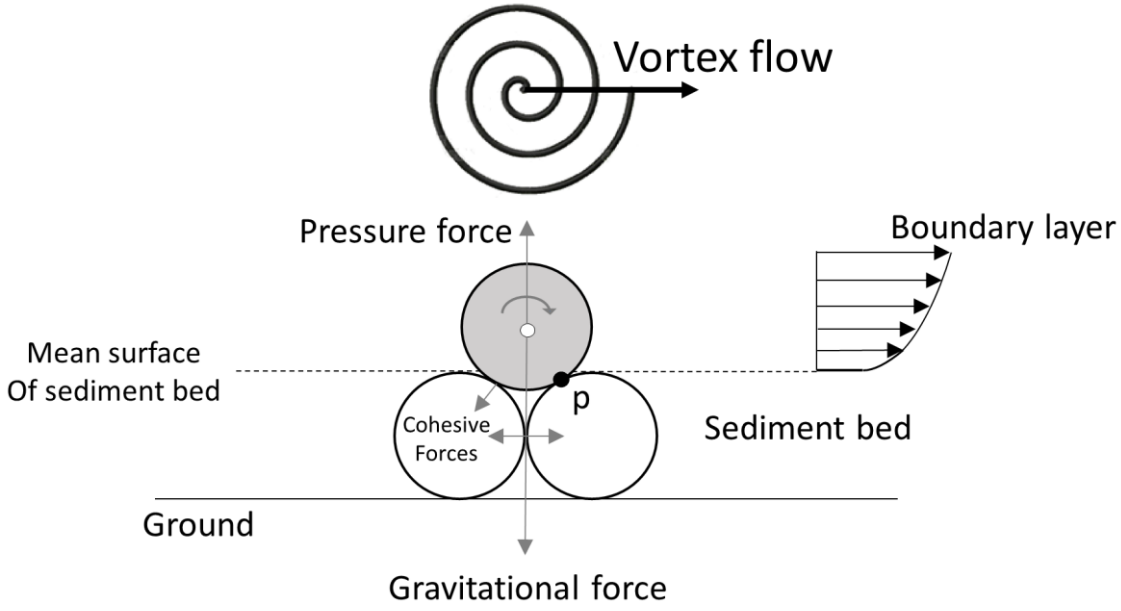

***Fig. 8** The various forces acting on particles on a sediment bed under the action of external flow. Modified from [126].*

3.7.2 Exerted forces on an entrained particle

The motion of an entrained particle in a flow filed may be influenced by several forces comprising the aerodynamic drag $\mathbf{F}_{\mathrm{d}}$, aerodynamic lift $\mathbf{F}_l$, the gravity force $\mathbf{F}_g$, the Magnus force due to the rotation $\mathbf{F}_m$, and the electric force $\mathbf{F}_E$. The effect of buoyancy upon the particle can be ignored because of the large density ratio defined as the ratio of particle density to air density. The gravitational force only acts on the vertical direction and is set equal to *-mg*, with *m* as particle mass, and *g* is the acceleration of gravity.

Fig. 9 illustrates the physical mechanism whereby aerodynamic drag is produced. Once the particle travels relative to the surrounding fluid, it will encounter a force opposed to the relative velocity by the fluid. This force is the well-known drag which is caused by the pressure difference in front of the particle and the wake behind it, as well as the viscous effects in which the momentum is transferred from fluid to the particle via molecular movements. The integration of total momentum flux (or total stress) over the particle surface is equal to the exerted force.

$$F_{di} = -\int_S p n_i \, dS + \int_S \sigma_{ij} n_j \, dS \tag{45}$$

The momentum transfer to the particle by the pressure forces (the first right-hand side term of the equation (45)) is independent of fluid viscosity. However, the second term is associated with fluid viscosity and is known as the frictional drag.

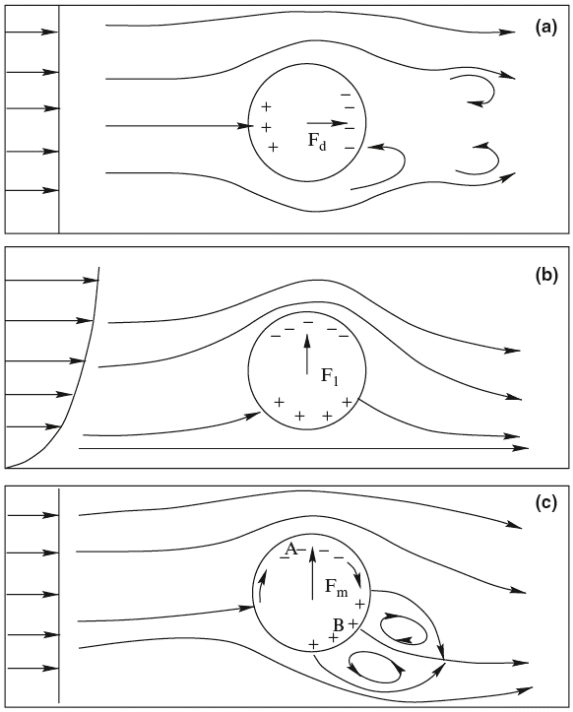

Fig. 9 The physical mechanism of a) aerodynamic drag force, b) aerodynamic lift force and c) Magnus force on a spinning particle. Reprinted from [127] with permission.

Because of the difficulty in calculating p and σ_{ij} distribution over the particle surface, equation (45) is not suitable for aerodynamic drag expression. As an other possible approach, it is depicted that the drag force is proportional to particle-to-fluid relative velocity $\mathbf{u_r}$;

$$\mathbf{F_d} = -\frac{1}{2} C_D \rho A \mathbf{u_r} U_r \tag{46}$$

In the above relation, the aerodynamic drag coefficient is shown by C_D. The particle cross-section in the direction of flow is denoted by A and for spherical particles, is equal to $\pi d^2/4$. U_r is the magnitude of $\mathbf{u}_\mathrm{r}$. Moreover, u_{pi} and u_i are the ith particle velocity and fluid velocity components, respectively, and the ith component of $\mathbf{u}_\mathrm{r}$ is as follows,

$$u_{ri} = u_{pi} - u_i \,. \tag{47}$$

Thus, U_r can be defined by

$$U_r = (u_{r1}^2 + u_{r2}^2 + u_{r3}^2)^{1/2}. \tag{48}$$

As the aerodynamic drag coefficient is a function of particle Reynolds number $\mathrm{Re}_p = U_r d / \upsilon$, the magnitude of the drag force is dependant upon the flow pattern. This function, $C_D(\mathrm{Re}_p)$, has been widely investigated by several experimental studies for various flow patterns. Fig. 10 shows the variation of the drag coefficient in terms of Reynolds number and flow patterns.

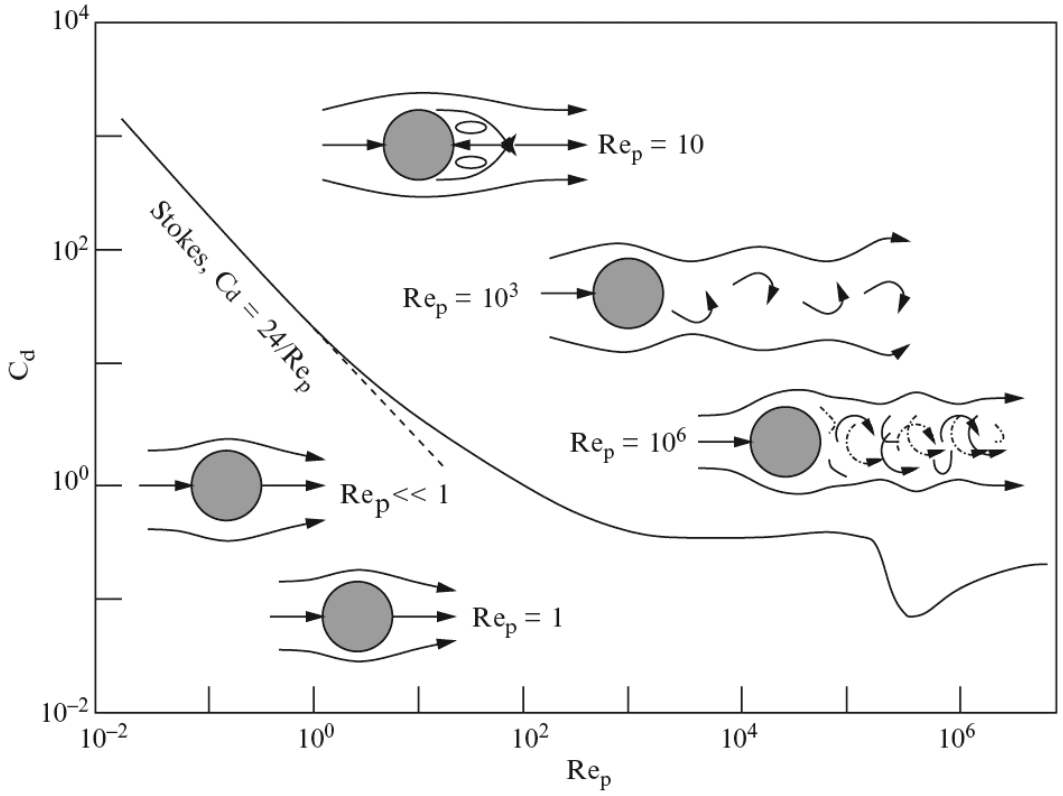

***Fig. 10** Aerodynamic drag coefficient for different flow regime in terms of the Reynolds number. Reprinted from [127] with permission.*

The Reynolds regimes depicted in Fig. 10 can be classified as follows:

$\mathrm{Re}_p \ll 1$ (known as Stokes region) corresponds to high viscous effects and negligible fluid inertia. The pressure and viscous stresses on the particle surface in this region were first determined analytically to be $C_D = 24/\mathrm{Re}_p$ [128] for Reynolds numbers smaller than 10.

When $10^3 < \mathrm{Re}_p < 3\times10^5$, the drag coefficient is close to 0.5 and relatively independent of Reynolds number. Moreover, viscous drag can be ignored compared to pressure-induced drag.

Lastly, for $\mathrm{Re}_p > 3\times10^5$, a significant decrement of drag coefficient from about 0.5 to approximately 0.1 can be observed due to the variation of pressure distribution over the particle surface, and a transition of the laminar boundary layer to turbulent boundary layer on the particle can be seen. In section 4.4.3, various relations for drag coefficients were provided.

The Bernoulli equation describes the aerodynamic lift mechanism shown in Fig. 9(b). This equation expresses that the total head produced by velocity head, pressure head, and gravity head along the streamline, is unvarying and can be derived from motion equations for inviscid barotropic flow in a steady-state condition.

$$\frac{1}{2}u^2 + \frac{p}{\rho} + gh = const. \tag{49}$$

u and *h* are the velocity of flow along the streamline and the height of streamline corresponding to reference level, respectively. The aerodynamic lift phenomenon is the result of the pressure gradient caused by shear in the flow. This pressure gradient is normal to the shear and in the direction of decreasing velocity. In other words, the faster-flow region over the upper surface induces lower pressure compared to the lower surface, which is exposed to lower velocity and higher pressure. The aerodynamic lift can be expressed by

$$\mathbf{F}_l = \frac{1}{2}C_l\rho A(\nabla U^2)d\,. \tag{50}$$

In the above equation, C_l corresponds to lift coefficient and is correlated to the drag coefficient, $C_l = 0.85C_D$ given by Chepil [129] and the gradient of $U \equiv |\mathbf{u}|^2$ is denoted as

∇U^2. Here, the shape of the particles plays a substantial role in defining $\mathbf{F}_l$. For instance, a spherical particle only when is placed in a strong shear flow can experience lift force, whereas in the case of a non-spherical particle, considerable lift force may take place even in the uniform flows due to the velocity gradient that geometry imposes, and hence the distribution of pressure on the surface.

As shown in Fig. 9(c), for a spinning particle, a force perpendicular to both direction of motion and rotation is generated, which is known as Magnus force. In order to explain Magnus force in terms of the Bernoulli equation, the viscous effects in relation to particle should be taken into account. The flow at the upper surface of the rotating particle (side A) undergoes pressure reduction due to an increase of the velocity which itself is a result of the same direction in the rotation of particle and fluid motion (in the presence of viscous forces). It is trivial that the opposite side experiences contrary conditions. The Magnus force is proportional to Re_p, and the ratio of circumferential speed to the magnitude of relative velocity, υ_s / U_r [130]. In works of [131, 132] regarding the motion of sands grains in the atmosphere, the following relation has been applied,

$$\begin{aligned} \mathbf{F_m} &= \pi\rho\frac{d^3}{8}\left(\mathbf{\Omega_p}\times\mathbf{u_r}\right), \quad \text{for low Re numbers} \\ \mathbf{F_m} &= C_m\pi\rho\frac{d^3}{8}\left(\mathbf{\Omega_p}\times\mathbf{u_r}\right), \quad \text{for high Re numbers} \end{aligned} \tag{51}$$

In the above equations, $\mathbf{\Omega_p}$ stands for angular particle velocity and C_m is a coefficient that accounts for the Magnus force dependency on Re_p and υ_s / U_r.

In the case of charged soil particles, the motion of windblown particles generates an Electric field near the surface [133]. These particles may experience an electric force $\mathbf{F_e}$ with the strength as large as the gravity force. According to Zheng *et al.* [133], only the vertical component can define the electric field, and the horizontal component can be

neglected. Accordingly, the electric force for a particle of mass m and the particle specific charge C_e (charge per unit mass) can be written as

$$\mathbf{F}_e = mC_e\mathbf{E}\,. \tag{52}$$

In summary, the equation of particle motion for a particle of mass m with velocity $\mathbf{u_s}$ can be expressed by the forces detailed above:

$$m\frac{d\mathbf{u_s}}{dt} = \mathbf{F_d} + \mathbf{F_l} + \mathbf{F_g} + \mathbf{F_m} + \mathbf{F_e}\,. \tag{53}$$

By using the definition of the forces we have

$$\begin{aligned} m\frac{d\mathbf{u_s}}{dt} &= -\frac{1}{2}C_d\rho A\mathbf{u_r}U_r + \frac{1}{2}C_l\rho A(\nabla U^2)d + mg \\ &+ \frac{1}{8}C_m\pi\rho d^3\left(\mathbf{\Omega_p}\times\mathbf{u_r}\right) + mC_e\mathbf{E}. \end{aligned} \tag{54}$$

In the case of a particle with the spherical shape, $m = \pi\rho_s d^3/6$ and $A = \pi d^2/4$, the above equation can be written in the following form:

$$\frac{d\mathbf{u_s}}{dt} = -\frac{3}{4}\frac{C_d\rho}{\rho_s d}\mathbf{u_r}U_r + \frac{3}{4}\frac{C_l\rho}{\rho_s}\nabla U^2 + g + \frac{3}{4}\frac{C_m\rho}{\rho_s}\left(\mathbf{\Omega_p}\times\mathbf{u_r}\right) + C_e\mathbf{E}\,. \tag{55}$$

3.7.3 Particle motion methodology during surface erosion phenomenon

Depend upon solid particles diameter, the various trend of motions can be followed by the particles belong to the same family size, some of which may also be observed in the Lunar landing problem. Bagnold [134] characterized the particle motion based on experimental observations into three categories: Suspension, saltation, and creep, which are schematically demonstrated in Fig. 11.

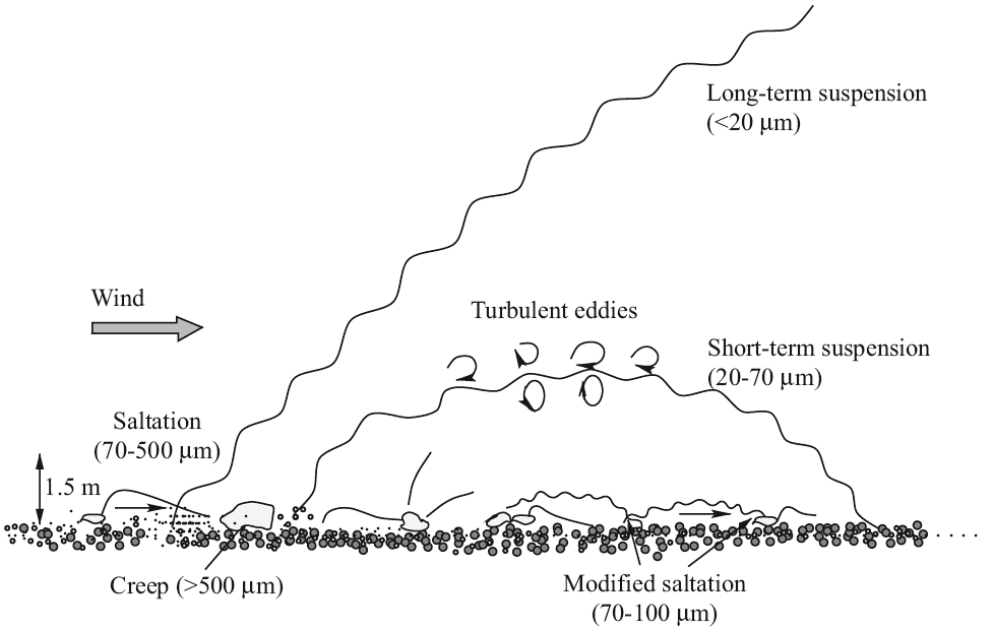

Fig. 11 Suspension, saltation, and creep of grains during wind erosion. Reprinted from [127] with permission.

Suspension

Suspension of the dust particles occurs owing to small terminal velocity, which is defined by the relative velocity of the particle to a fluid under negligible particle acceleration. The turbulence in the atmospheric boundary layer disperses the dust particles away from the surface, and the airborne grains can travel up to thousands of kilometers by means of the atmospheric circulation. The suspension is characterized into long-term and short-term based on the residence time of the dust grains, which is dependent on terminal velocity. According to the observations, the very fine dust particles (less than $20\mu m$) can be suspended for several days, which refers to a long-term suspension. The short-term suspension is covered by the particles with a diameter between 20 and $70\mu m$ that remain suspended for typically several hours. Since the Moon atmosphere is covered by semi-vacuum condition accordingly a less resistance time is expected, and also one can neglect the gravitational forces compared to the earth, the particles on the lunar would mostly experience long-term suspensions.

Saltation

The bouncing off action of the particles across the surface during erosion phenomena is called saltation. The particles are initially lofted off from the surface with the steep vertical ascent then traveled horizontally and eventually struck to the surface with the small impact angle. It is observed that the ascent angles are about 55° , and the striking angles are around 10°.

Creep

The last mechanism in the wind erosion is called creep; where, the heavy grains with a diameter larger than $1000\mu m$ are not able to be lifted from the surface under the typical atmospheric circumstances. They could only roll over the surface, owing to either wind force or the impact of the particles from the saltation process.

3.7.4 The lunar surface regolith erosion phenomenology

The soil erosion is a complex phenomenon which has been studied via various theoretical, computational, and experimental investigations from different viewpoints. The unique properties of the lunar environment and regolith make the issue even more complicated. Replicating the lunar environment for conducting experiments is almost impossible. Therefore experimental investigations are not sufficiently reliable. Theoretical and numerical studies are still in the development stage, and even with the significant effort which has been put in previous research studies [14, 20, 47-49, 65, 135, 136], a comprehensive model which can explain physics of the erosion even terrestrially is not available to date. These observations make one of the most critical shortcomings of solving the problem of Lunar landing from a theoretical point of view. Before selecting the erosion model, it is beneficial to know about the erosion mechanisms.

Four possible erosion mechanism to form craters have been identified by Metzger *et al.* [65], which are summarized as follows:

3.7.4.1 **Viscous erosion (VE)**

Viscous erosion takes place when the shear stress on the surface overcomes the critical cohesive strength of the soil and causes the solid particles to creep along the surface. The rolled particles elevate the possibility of particle-particle collision; accordingly, these collisions can lead to scattering of the particles into the flow field.

3.7.4.2 **Diffused gas eruption (DGE)**

The diffused gas eruption occurs when the gas penetrates a porous media and loosens the porous soil such that the soil layer could be fluidized. Therefore, it can be erupted at any location and cause the solid particles to be suspended along with it.

3.7.4.3 **Bearing capacity failure (BCF)**

When the pressure becomes higher than bearing capacity of the soil, a narrow cup shape is created, which has unstable circumstances and can easily collapse under the gravity force. Consequently, many solid particles would entrain to the flow field.

3.7.4.4 **Diffusion-driven flow (DDF)**

The drag force of fluid jet through the pore spaces of the soil reacts against the grains posing a distributed body force in the bulk of the soil, which can shear the material.

The dominant erosion mechanism on the lunar surface is viscous erosion. Due to the existence of a semi-vacuum, the soil layers are tightly packed; therefore, DGE, and DDF mechanisms are not in effect during the Lunar surface erosion. Besides, bearing capacity failure mechanism is negligible because of high packing density and bearing capacity of the Lunar regolith. However, some simulations results [41], which may represent the existence of this mechanism make this assumption subject to further investigations. Viscous erosion is associated with:

- aerodynamic entrainment in which aerodynamic forces are dominant compared to gravitational forces;
- saltation bombardment in which high-energy particles dislodge other particles by colliding;

- Aggregate disintegration in which particles get together due to thermal cycling and cohesion, then break apart when a significant force is exerted [127]. The contents above are summarized in Fig. 12.

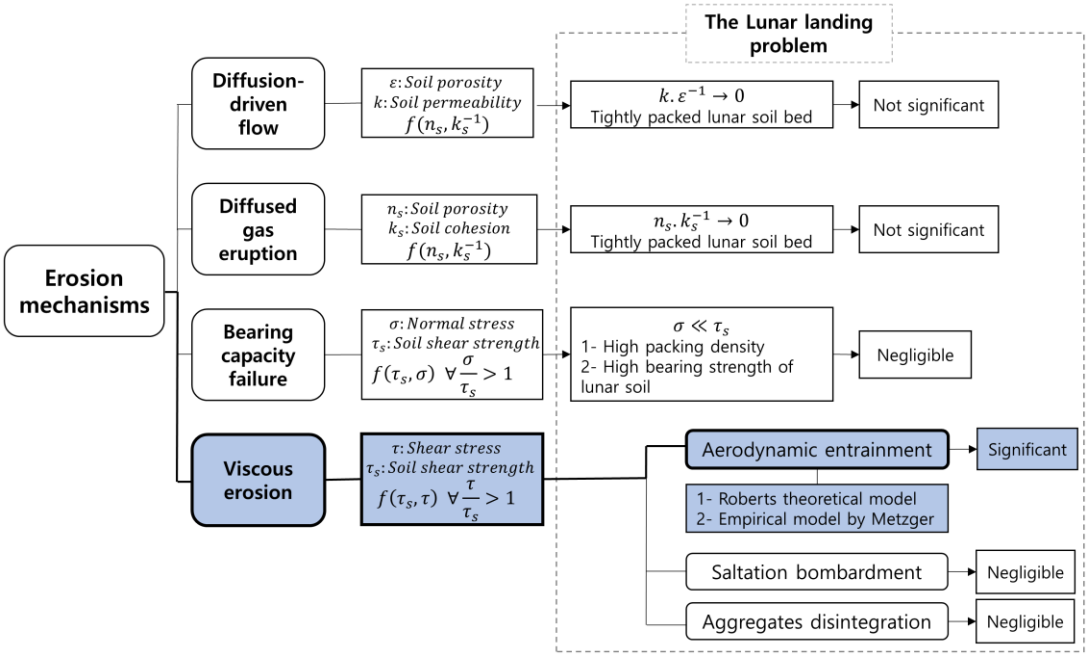

Fig. 12. Erosion mechanisms and their importance in lunar landing problem

A simplified yet potent model to simulate erosion on the surface is the Roberts' erosion model. According to Roberts [48], when the induced shear stress on the ground exceeds the threshold stress, erosion with a mass flux proportional to the excess shear will occur:

$$\frac{1}{2} au\phi = \tau - \tau_c \tag{56}$$

In the above equations, ϕ is erosion rate (mass flux), au is the fraction of gas velocity that the particles can obtain, τ is shear stress on the surface and τ_c indicates the threshold stress below which erosion does not occur defined as

$$\tau_c = C + P\tan\varphi. \tag{57}$$

Here, C, P and φ are cohesive stress, gas static pressure on surface and friction angle, respectively. The coefficient a is

$$a = \left[\frac{1}{2} + \sqrt{\frac{1}{4} + \frac{1}{\zeta}} \right]^{-1}, \tag{58}$$

where,

$$\zeta = \frac{18\mu_c h}{\rho_s \sqrt{RT_c \left(4 + k_h\right)}} \left[\frac{1}{d^2} + \frac{1}{d} \frac{\left(4 + k_h\right) C_D F}{72e\sqrt{2RT_c}\mu_c} \right]. \tag{59}$$

From the above relations, it is clear that the coefficient a is dependent on various parameters. In the equation (59), μ_c and T_c are the engine chamber viscosity and temperature, h is the hover altitude, ρ_s and D are particle density and the particle diameter of regolith, k_h is the hypersonic factor which is defined by $\gamma\left(\gamma - 1\right)M_n^2$, where γ is the ratio of specific heats and the Mach number at nozzle exit plane is specified by M_n. Further, ζ in the above equation is related to R gas constant as well as drag coefficient, C_D (set equal to the constant value of 0.2 by Roberts) and engine thrust, F.

Less sophisticated models can be derived from an analogy from the sediment beds research area. More sophisticated models based on wind erosion are also available; However, the dependency of these models on regolith properties which are mostly unknown (or at best, limited) makes the use of these models impractical. Moreover, empirical relationships to take into account the particle density, diameter and gas density and velocity, and gravity are provided by [49, 135, 136].

Chapter 4. Numerical approach

4.1 The basics of the numerical simulation

After the selection of an appropriate mathematical model to describe and comprise the governing physics of the problem, the next step is applying discretization of the equation based on available methods. One should bear in mind that the choice of an efficient discretization method should take into account the accuracy and the computational cost while compromising these two simultaneously.

Two steps discretization are involved: space discretization and equation discretization.

Space discretization is initiated to provide a mesh regarding continuum space approximation where the domain is divided into a finite number of grids to determine the solution values. Next, the equations are discretized by transforming the differential or integral equations into algebraic relations whereby the unknown values are determined.

4.1.1 Categories of discretization methods and their characteristics

The most well-known methods for discretization in CFD are as follows: finite difference method (FDM), Finite volume method (FVM), and the finite element method (FEM). Another class of discretization methods which are gaining popularity in fluid dynamics field from fundamental fluid mechanics problems to more sophisticate wave-based problems of computational electromagnetics are the so-called high order —higher than second-order—spectral methods

The simplest approach among all three is the finite difference, which takes advantage of Taylor series expansions. The highlighted features of FDM can be stated as being easy to code, capable of providing high-order accurate solutions and can be benefitted from *hp*-additivity.

On the other hand, it cannot be used in complex geometries and unstructured grids. The next widely used method of discretization is referred to FVM, which directly solves the conservation laws in physical space by applying an integral form of the laws above. Also, to be a flexible tool of calculating surface fluxes over the control volume, the FVM is also capable of handling any arbitrary mesh as well as geometries. The main weakness of the FVM is the difficulty associated with the computation of high order solutions, especially on unstructured grids, which makes finite volume method limited to second-order accuracy in most applications. The finite element method, which was originated from the field of structural analysis, was first applied in fluid dynamics problem in the late 70's and continued its development till date. It is based on variational methods, can reach any order of accuracy and is applicable on an unstructured grid. In FEM, the reconstruction data are employed from within the element. One of the main drawbacks of the FEM method is the inability of providing the explicit semi-discrete form. In other words, the method is inherently implicit; Nevertheless, it can be explicit with major modifications.

The final category, so-called as high-order methods with the purpose of providing a high-order conservative scheme that has a compact formulation and can deal with complex geometries in a computationally efficient manner. In these methods, high order solution can be obtained by increasing the polynomial order, and some of the popular subcategories include spectral difference (SD), spectral volume (SV), and flux reconstruction/correction procedure via reconstruction (FR/CPR) and discontinuous Galerkin (DG) method. In spectral (finite) volume method to achieve a higher order of accuracy, each spectral volume is further subdivided into control volumes, and the high-order reconstruction is based on cell-averaged state variables from these control volumes [137]. In the spectral difference method, the concept of discontinuous and high-order

local representations is utilized to achieve conservation and high accuracy in such a way similar to the DG and SV methods. The difference is the application of the simpler finite-difference formulation to increase efficiency [138]. Flux reconstruction method employs the differential form of the equation identical to what is done in SD.

Nonetheless, in the FR method, the reconstruction of flux polynomial is achieved via a more general scheme compared to the interpolation procedure used by SD. The extension of the FR approach [139] to simplex elements provided lifting collocation penalty (LCP) framework [140]. The FR and LCP schemes are later renamed to CPR by their creators as both the methods provide the same final formulation. Interested readers are referred to the review papers of Ekaterinaris [141] and Wang [142] for more details regarding the comparison of high-order spectral methods.

In discontinuous Galerkin formulation in comparison with the continuous counterpart, discontinuous basis functions are applied (local elemental mass matrix of the finite element formulation versus globally coupled mass matrix of continuous finite element method). The discontinuous feature of the basis functions makes the DG method more flexible. For instance, arbitrary triangulation with hanging nodes can be allowed. *P* adaptivity can be obtained as the polynomial degree, or even the basis functions can be defined for individual elements independent from neighbor elements. Embarrassingly high parallel efficiency is also achievable due to extremely local data structure [143].

These types of methods are known to benefit from the advantages of FVM and FEM at the same time. In the current thesis, a DG discretization is applied due to high order capability of the method, which is desirable in most of the investigated problems, as well as the consistency of the selected mathematical model with some inherent features of the scheme which will be discussed in the following sections.

4.2 Modal discontinuous Galerkin (DG) method on unstructured grid

The DG method was introduced by Reed and Hill [144] for the first time, and during last decades further developed by [145-147], it has become an outstanding tool for solving the fluid dynamics governing equations. While the DG method has been successfully applied to various classes of problems such as compressible and incompressible flows, aeroacoustics, magneto-hydrodynamics, and many more [148], it has recently also found its way into the multiphase problem.

Sun and Wheeler [149] applied primal DG to solve the coupled system of flow and reactive transport in porous media. In other work, Klieber and Rivière [150] proposed new DG schemes by adaptive techniques in space and time and showed that the methods on heterogeneous media are robust. Franquet and Perrier [151] adopted the systems from Baer and Nunziato and developed a robust high order DG method for compressible multiphase flows and reported good validated results. Later, they also applied the extended method to reactive multiphase flows [152]. The DG method extended to interphase capturing in Multiphase flow by Owkes and Desjardins [153]. It was revealed by Lu *et al.* [154] that the DG method is able to boost the resolution near discontinuities in the single medium and material interfacial vicinities. They applied the Runge-Kutta DG method along with the front tracking to solve two-medium gas-gas and gas-liquid flows. By using the Mie-Grüneisen family of equations of state, de Frahan *et al.* [155] obtained the DG solution for multiphase flows. Recently, Dumbser and Loubère [156] proposed a rigorous nonlinear a posteriori stabilization of the DG method and applied the method to the Baer-Nunziato model in two-dimensional space. Applying a solution of Navier-Stokes-Korteweg equations for compressible liquid-vapor multiphase flow with

phase transition using the local discontinuous Galerkin (LDG) method is done by Diehl *et al.* [157]. It was observed that LDG can provide reliable and efficient solutions in two and three space dimensions.

Although the studies above showed the capability of applying the DG method to the diverse multiphase flow problems, few mathematical models have been investigated the inherent features of the DG method for various categories of multiphase flow. *To the best knowledge of the author, there is no previous work on applications of a high order DG method to solve a two-fluid model of dusty gas flows*. Moreover, existence of stiff source terms in equations owing to the coupling effects in the two-fluid model and strong discontinuities in the flow, the mere application of high-order methods without appropriate manipulation of numerical artifacts or without proper treatment of the non-homogeneous part of the partial differential equation will generally results in divergence, an oscillatory solution or in the best scenario a enormous computational costs, caused by small time steps.

Discretization of dusty-gas flow equations, which are explained in the earlier sections has been applied by using modal DG method. In the following section, the most important parts of the developed modal unstructured DG method, including high order accuracy and positivity/monotonicity preserving property are summarized. For a more detailed discussion on general DG methods, readers are referred to [145-148], for DG implementations, and [158-161] for limiter-related issues.

4.2.1 Definition of the problem in the DG method framework

The compact form of the mathematical model along with source terms can be written as follows:

$$\partial_t \mathbf{U} + \nabla \cdot \mathbf{F}_{\text{inv}}(\mathbf{U}) + \nabla \cdot \mathbf{F}_{\text{vis}}(\mathbf{U}, \nabla \mathbf{U}) = \mathbf{S}(\mathbf{U}) \qquad \text{in} \left[(t, \Omega) \middle| t \in (0, \infty), \Omega \subset \mathbb{R} \right], \tag{60}$$

At the first step, we consider the convection dominated problem; where the formulation is reduced to

$$\partial_t \mathbf{U} + \nabla \cdot \mathbf{F}_{\text{inv}}(\mathbf{U}) = \mathbf{S}(\mathbf{U}) \qquad \text{in} \left[(t, \Omega) \middle| t \in (0, \infty), \Omega \subset \mathbb{R} \right], \tag{61}$$

where Ω denotes a bounded domain, and $\mathbf{U}$, $\mathbf{F}_{\text{inv}}$, $\mathbf{S}$ are conservative variables vector, inviscid flux vector, and source terms vector, respectively. The solution domain can be decomposed by a group of non-overlapping elements, $\Omega = \Omega_1 \cup \Omega_2 \cup ... \Omega_{ne}$, in which *ne* is the number of elements. The partial differential equation of (61) cannot allow for solutions with discontinuities. By multiplying a weighting function ϕ_i into the conservative laws (61) and integrating over the control volume for each element, the following formulation can be derived:

$$\int_{\Omega_k} \left[\partial_t \mathbf{U} \phi(\mathbf{x}) + \nabla \cdot \mathbf{F}_{\text{inv}}(\mathbf{U}) \phi(\mathbf{x}) - \mathbf{S}(\mathbf{U}) \phi(\mathbf{x}) \right] d\Omega = 0 . \tag{62}$$

In order to construct a discretized system of the conservation laws, the global spatial domain Ω can be approximated by Ω_h where $\Omega_h \rightarrow \Omega$ as $h \rightarrow 0$. The approximated domain, which is a tessellation of the space by bounded elementary control volumes, $\mathcal{T}_h = \{\Omega_k\}$, is filled with *ne* number of the non-overlapping elements $\Omega_k \in \mathcal{T}_h$. The exact solution of the governing equations can be approximated by the numerical solution in every local element as

$$\mathbf{U}(\mathbf{x}, t) \approx \mathbf{U}_h = \sum_{e=1}^{ne} \mathbf{U}_h^e(\mathbf{x}, t) \equiv \mathbf{U}_h^1 + \ldots + \mathbf{U}_h^n . \tag{63}$$

By splitting the integral over Ω_h into series of the integrals over the sub-elements and applying the integration by part as well as divergence theorem to the equation (62), the elemental formulation reads as

$$\begin{aligned} &\int_{\Omega_k} \partial_t \mathbf{U}_h \phi_i(\mathbf{x}) \mathrm{d}\Omega_k + \oint_{\partial\Omega_k} \phi_i(\mathbf{x}) \mathbf{F}_{\text{inv}}(\mathbf{U}_h) \cdot \hat{n} d\sigma - \int_{\Omega_k} \nabla \phi_i(\mathbf{x}) \cdot \mathbf{F}_{\text{inv}}(\mathbf{U}_h) \mathrm{d}\Omega_k \\ &= \int_{\Omega_k} \phi_i(\mathbf{x}) \mathbf{S}(\mathbf{U}_h) \mathrm{d}\Omega_k , \end{aligned} \tag{64}$$

where $\hat{n}$ is the outward normal vector of the element interface and $\mathbf{U}_h$ is the p-exact polynomial approximated solutions of the $\mathbf{U}$ on the discretized domain of Ω_h. $\mathbf{U}_h$ can be expressed as the polynomial field that sums the multiplication of local degree of freedom with the corresponding smooth polynomials of degree P in the standard element:

$$\mathbf{U}_h = \sum_i^P U_i(t)\phi_i(\mathbf{x}) . \tag{65}$$

Here $U_i(t)$ and $\phi(\mathbf{x})$ denote the local degree of freedom and the basis function, which can be chosen to be any continuous polynomial function, respectively.

In the one-dimensional case, the orthogonal scaled Legendre functions were selected as basis functions, while a linear mapping function was used for mapping from the physical space to the standard element. In the two-dimensional case, the PDK polynomials [162] were selected as basis functions, while a collapsed coordinate transformation was used to transfer the triangles in the physical domain to the standard square elements, Ω_e, in which the coordinates (a, b) are bound by constant limits

$$\mathscr{R} = \{(a,b) \big| -1 \le a,b \le 1\} . \tag{66}$$

Another transformation was introduced to transfer the triangle in the physical space into the computational space where the new local coordinates have independent bounds, as depicted in Fig. 13. A suitable coordinate system, which describes the triangular region between constant independent limits, can be defined by the following inverse transformation:

$$r = \frac{(1+a)(1-b)}{2} - 1, \quad w = b . \tag{67}$$

New local coordinates (r, w) can then define the standard triangular region as follows:

$$\mathscr{T} = \{(r,w) \big| -1 \le r, w; r + w \le 0\} . \tag{68}$$

For more details on the various transformations used in the DG method, readers are referred to subsection 4.3 and the text book [163].

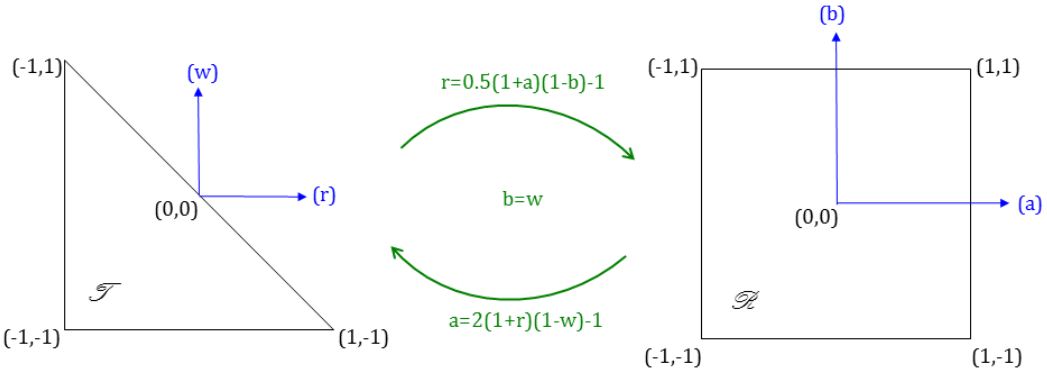

Fig. 13 Coordinate transformation, adapted from [7]

The simple and efficient local Lax-Friedrichs (LLF) flux function, commonly used in the DG method, is applied to all the multiphase test cases in the present study. Despite the dissipative nature of the numerical flux, it improves the linear stability of the DG numerical approximation. The dimensionless form of the LLF flux is defined as

$$\mathbf{F}_{\text{inv}}(\mathbf{U}_h) \approx \hat{\mathrm{f}}_{i,\text{inv}}\left(\mathbf{U}_h^-, \mathbf{U}_h^+\right) = \frac{1}{2}\left[\mathbf{F}_{i,\text{inv}}\left(\mathbf{U}_h^-\right) + \mathbf{F}_{i,\text{inv}}\left(\mathbf{U}_h^+\right) - C\left(\mathbf{U}_h^+ - \mathbf{U}_h^-\right)\right], \tag{69}$$

where C is the maximum modulus of the eigenvalues of the Jacobian matrix, $\max_{\min(U^-,U^+)\le u\le\max(U^-,U^+)} |\mathrm{F}'_{i,\text{inv}}(U)|$, and for convex fluxes, it reads as $C = \max\left(\left|v^-\right| + a_S^-, \left|v^+\right| + a_S^+\right)$. Here $a_S = \sqrt{T}/M$ is the speed of sound at an elemental interface, and the superscripts (+) and (–) denote the inside and outside of an elemental interface, respectively.

Moreover, a third-order accurate, three-stage total-variation-diminishing Runge-Kutta method was employed for time integration, owing to its simplicity, efficiency, and robustness. In order to minimize the temporal discretization error, the time step was set in such a way that the Courant-Friedrich-Levy (CFL) criterion is always satisfied. The

Gauss-Legendre quadrature rule was used to calculate the volume and surface integrals in (64), which are proved to be 2*P* and 2*P*+1 order accurate, respectively.

As can be seen in (60), when the solution of viscous flows is of interest, an approach for estimation of the derivatives of the conserved variable which appear in the viscous flux terms should be applied. In this regard. These first-order derivatives will change into second-order derivatives when the viscous fluxes are evaluated. These terms cannot be accommodated directly in a weak variational formulation using a discontinuous space function. One possible approach is the addition of a set of separate equations to regard the gradient of the conservative variables as an auxiliary set of unknowns, as proposed by Bassi and Rebay [164]. In this work, **A** is chosen to be the derivatives of the conserved variables **U**, i.e., $\mathbf{A} = \nabla \mathbf{U}$. This approach is known as mixed DG formulation and will result in a coupled system

$$\begin{aligned} &\mathbf{A} - \nabla \mathbf{U} = 0, \\ &\partial_t \mathbf{U} + \nabla \cdot \mathbf{F}_{\text{inv}}(\mathbf{U}) + \nabla \cdot \mathbf{F}_{\text{vis}}(\mathbf{U}, \nabla \mathbf{U}) = \mathbf{S}(\mathbf{U}). \end{aligned} \tag{70}$$

Then the solution of the primary and auxiliary variables can be approximated as,

$$\mathbf{U}_h = \sum_i^P U_i(t)\varphi_i(\mathbf{x}) \text{ and } \mathbf{A}_h = \sum_i^P A_i(t)\varphi_i(\mathbf{x}). \tag{71}$$

where $A_i(t)$ denotes the local degree of freedom for the auxiliary variable. By following the similar procedure outlined above for an inviscid system of equations (multiplying a weighting function into the conservative laws and integrating over the control volume for each element) then the formulation can be derived:

$$\int_{\Omega_k} \left[\mathbf{A}\varphi(\mathbf{x}) - \nabla \mathbf{U}\varphi(\mathbf{x})\right] d\Omega = 0 \tag{72}$$

$$\int_{\Omega_k} \left[\partial_t \mathbf{U}\varphi(\mathbf{x}) + \nabla \cdot \mathbf{F}_{\text{inv}}(\mathbf{U})\varphi(\mathbf{x}) + \nabla \cdot \mathbf{F}_{\text{vis}}(\mathbf{U})\varphi(\mathbf{x}) - \mathbf{S}(\mathbf{U})\varphi(\mathbf{x})\right] d\Omega = 0 \tag{73}$$

$$\int_{\Omega_k} \varphi_i(\mathbf{x}) A_h \mathrm{d}\Omega_k - \oint_{\partial\Omega_k} \varphi_i(\mathbf{x}) \mathbf{U}_h \cdot \hat{n} d\sigma + \int_{\Omega_k} \nabla \varphi_i(\mathbf{x}) \cdot \mathbf{U}_h \mathrm{d}\Omega_k = 0, \tag{74}$$

$$\int_{\Omega_k} \partial_t \mathbf{U}_h \varphi_i(\mathbf{x}) \mathrm{d}\Omega_k + \oint_{\partial\Omega_k} \varphi_i(\mathbf{x}) \mathbf{F}_{\mathrm{inv}}(\mathbf{U}_h) \cdot \hat{n} d\sigma - \int_{\Omega_k} \nabla \varphi_i(\mathbf{x}) \cdot \mathbf{F}_{\mathrm{inv}}(\mathbf{U}_h) \mathrm{d}\Omega_k$$
$$+ \oint_{\partial\Omega_k} \varphi_i(\mathbf{x}) \mathbf{F}_{\mathrm{vis}}(\mathbf{U}_h) \cdot \hat{n} d\sigma - \int_{\Omega_k} \nabla \varphi_i(\mathbf{x}) \cdot \mathbf{F}_{\mathrm{vis}}(\mathbf{U}_h) \mathrm{d}\Omega_k = \int_{\Omega_k} \varphi_i(\mathbf{x}) \mathbf{S}(\mathbf{U}_h) \mathrm{d}\Omega_k, \tag{75}$$

The process of estimation of surface and volume integrals are analogous to the inviscid system procedure. However, for the auxiliary terms, a central flux splitting scheme is applied.

$$\mathbf{F}_{\mathrm{vis}}(\mathbf{U}_h) \approx \hat{\mathrm{f}}_{i,\mathrm{vis}}\left(\mathbf{U}_h^-, \mathbf{A}_h^-, \mathbf{U}_h^+, \mathbf{A}_h^+\right) = \frac{1}{2}\left[\mathbf{F}_{i,\mathrm{vis}}\left(\mathbf{U}_h^-, \mathbf{A}_h^-\right) + \mathbf{F}_{i,\mathrm{vis}}\left(\mathbf{U}_h^+, \mathbf{A}_h^+\right)\right]$$
$$\mathbf{U} \approx \hat{\mathrm{f}}_{i,\mathrm{aux}}\left(\mathbf{U}_h^-, \mathbf{U}_h^+\right) = \frac{1}{2}\left[\mathbf{U}_h^- + \mathbf{U}_h^+\right] \tag{76}$$

4.2.2 Elemental transformation to computational space

For th purpose of numerical integrations of equation (75), it is necessary to describe the bases over the standard elements for surface and volume integrations that include basis functions as well.

4.2.2.1 **One-dimensional elemental transformation**

The following mapping relation transfers the local element Ω_h in space coordinate x to standard element Ω_e in one-dimensional problems,

$$\eta = 2\frac{x - x_i}{x_{i+1} - xi} - 1 \quad \forall \eta \in \Omega_h \tag{77}$$

where the inverse relation is as follows,

$$x = \frac{1-\eta}{2} x_i + \frac{1+\eta}{2} x_{i+1} \quad \forall x \in \Omega_e \tag{78}$$

Fig. 14 shows schematic transformation in one-dimension where the range of the master element is $(\eta) \in [-1,1]$

The transfer Jacobians will be,

$$\mathbf{J}_{x\to\eta}=\frac{\partial x}{\partial \eta}=\Delta x,\ \mathbf{J}_{\eta\to x}=\frac{\partial \eta}{\partial x}=\Delta x/2. \tag{79}$$

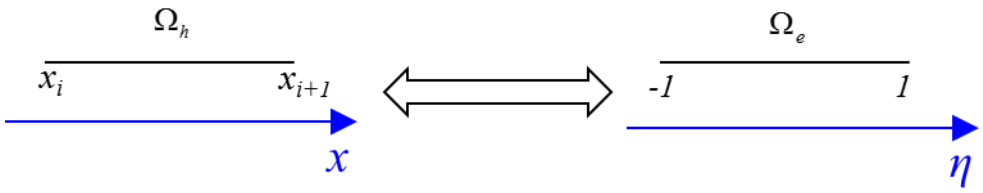

Fig. 14 Schematic diagram of the linear mapping of the 1D element.

4.2.2.2 **Two-dimensional elemental transformation**

Quadrilateral elements

It is possible to extend the transformation above to two-dimension from cartesian coordinate (*x*, *y*) to a standard quadrilateral element $(\eta_1,\eta_2)\in[-1,1]$ through following relations,

$$\begin{aligned}x&=\frac{(1-\eta_1)(1-\eta_2)}{4}x_1+\frac{(1+\eta_1)(1-\eta_2)}{4}x_2+\frac{(1+\eta_1)(1+\eta_2)}{4}x_3+\frac{(1-\eta_1)(1+\eta_2)}{4}x_4\\ y&=\frac{(1-\eta_1)(1-\eta_2)}{4}y_1+\frac{(1+\eta_1)(1-\eta_2)}{4}y_2+\frac{(1+\eta_1)(1+\eta_2)}{4}y_3+\frac{(1-\eta_1)(1+\eta_2)}{4}y_4\end{aligned} \tag{80}$$

The transfer Jacobian form *xy*-coordinate to $\eta_1\eta_2$-coordinate can be written as,

$$J_{xy\to\eta_1\eta_2}=\frac{\partial(x,y)}{\partial(\eta_1,\eta_2)}=\begin{bmatrix}\dfrac{\partial x}{\partial \eta_1} & \dfrac{\partial x}{\partial \eta_2}\\ \dfrac{\partial y}{\partial \eta_1} & \dfrac{\partial y}{\partial \eta_2}\end{bmatrix} \tag{81}$$

where,

$$\frac{\partial x}{\partial \eta_1} = \frac{1}{4}\left[(1-\eta_2)(x_2-x_1)+(1+\eta_2)(x_3-x_4)\right]$$
$$\frac{\partial y}{\partial \eta_1} = \frac{1}{4}\left[(1-\eta_2)(y_2-y_1)+(1+\eta_2)(y_3-y_4)\right]$$
$$\frac{\partial x}{\partial \eta_2} = \frac{1}{4}\left[(1-\eta_1)(x_4-x_1)+(1+\eta_1)(x_3-x_2)\right] \quad (82)$$
$$\frac{\partial y}{\partial \eta_2} = \frac{1}{4}\left[(1-\eta_1)(y_4-y_1)+(1+\eta_1)(y_3-y_2)\right]$$

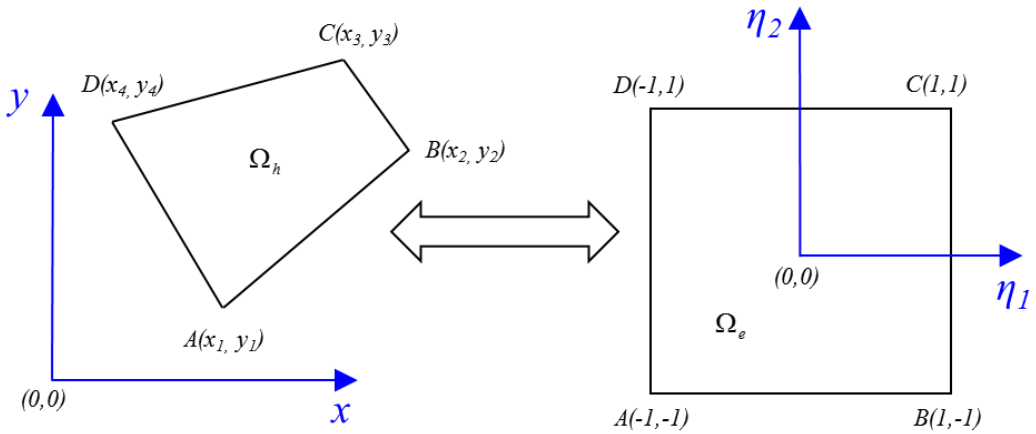

Fig. 15 Schematic diagram of the linear mapping of the 2D quadrilateral element.

Triangular elements

Extra effort is needed in the case of triangular elements, in order to map from physical element to the standard one. The two-step transformation is introduced here as a *collapsed coordinate*, which is shown in Fig. 16 and includes the following steps:

1. Transformation of an arbitrary triangle into the canonical (right triangle) element by the following,

$$x = -\left(\frac{\xi_1+\xi_2}{2}\right)x_1 + \left(\frac{1+\xi_1}{2}\right)x_2 + \left(\frac{1+\xi_2}{2}\right)x_3$$
$$y = -\left(\frac{\xi_1+\xi_2}{2}\right)y_1 + \left(\frac{1+\xi_1}{2}\right)y_2 + \left(\frac{1+\xi_2}{2}\right)y_3 \quad (83)$$

Here,

$$J_{xy\to\xi_1\xi_2}=\frac{\partial(x,y)}{\partial(\xi_1,\xi_2)}=\begin{bmatrix}\dfrac{\partial x}{\partial\xi_1} & \dfrac{\partial x}{\partial\xi_2}\\ \dfrac{\partial y}{\partial\xi_1} & \dfrac{\partial y}{\partial\xi_2}\end{bmatrix}=\frac{1}{2}\begin{bmatrix}x_2-x_1 & x_3-x_1\\ y_2-y_1 & y_2-y_1\end{bmatrix}=\text{Area}/2 \tag{84}$$

2. Mapping of the right triangle element Ω_e^t the standard square element Ω_e by the following transformation

$$\eta_1=2\frac{1+\xi_1}{1-\xi_2}-1,\quad \eta_2=\xi_2. \tag{85}$$

for which,

$$J_{\xi_1\xi_2\to\eta_1\eta_2}=\frac{\partial(\xi_1,\xi_2)}{\partial(\eta_1,\eta_2)}=\begin{bmatrix}\dfrac{\partial\xi_1}{\partial\eta_1} & \dfrac{\partial\xi_1}{\partial\eta_2}\\ \dfrac{\partial\xi_2}{\partial\eta_1} & \dfrac{\partial\xi_2}{\partial\eta_2}\end{bmatrix}=\frac{1-\eta_2}{2} \tag{86}$$

To apply the collapsed coordinate transformation, the master triangular and quadrilateral elements should be assumed as follows,

$$\begin{aligned}\Omega_e^t&=\left\{(\eta_1,\eta_2)\middle|-1\le\eta_1,\eta_2;\eta_1+\eta_2\le 0\right\},\\ \Omega_e^q&=\left\{(\xi_1,\xi_2)\middle|-1\le\xi_1,-1\le\xi_2\right\}.\end{aligned} \tag{87}$$

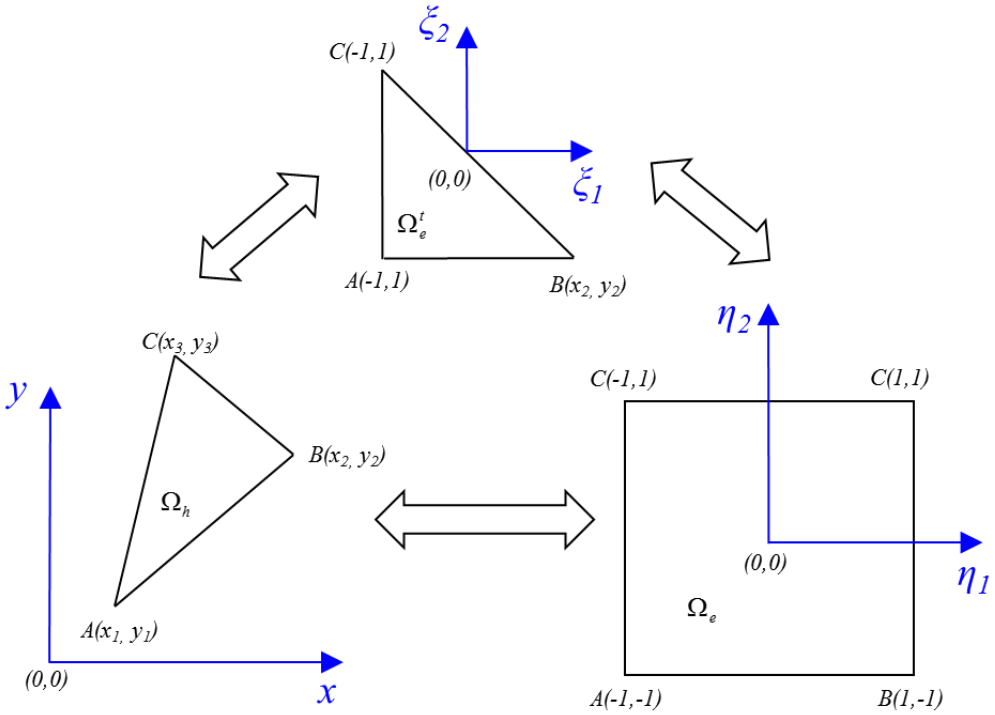

Fig. 16 Schematic diagram of the linear mappings of the 2D triangular element.

4.2.2.3 **Three-dimensional elemental transformation**

In the case of three-dimensional transformation, for mapping of the tetrahedron elements in physical space to the canonical master element $\Omega_e^c = \{(\eta_1, \eta_2, \eta_3) | 0 \le \eta_1 \le 1; 0 \le \eta_2 \le 1-\eta_1; 0 \le \eta_3 \le 1-\eta_1-\eta_2\}$ (indicated in Fig. 17), the employed linear transformations are as follows,

$$\begin{aligned} x &= (1-\eta_1-\eta_2-\eta_3)x_1 + \eta_1 x_2 + \eta_2 x_3 + \eta_3 x_4 \\ y &= (1-\eta_1-\eta_2-\eta_3)y_1 + \eta_1 y_2 + \eta_2 y_3 + \eta_3 y_4 \\ z &= (1-\eta_1-\eta_2-\eta_3)z_1 + \eta_1 z_2 + \eta_2 z_3 + \eta_3 z_4 \end{aligned} \tag{88}$$

$$J_{xyz\to\eta_1\eta_2\eta_2} = \begin{bmatrix} \frac{\partial x}{\partial \eta_1} & \frac{\partial x}{\partial \eta_2} & \frac{\partial x}{\partial \eta_3} \\ \frac{\partial y}{\partial \eta_1} & \frac{\partial y}{\partial \eta_2} & \frac{\partial y}{\partial \eta_3} \\ \frac{\partial z}{\partial \eta_1} & \frac{\partial z}{\partial \eta_2} & \frac{\partial z}{\partial \eta_3} \end{bmatrix} = 6 \times \text{Volume} \tag{89}$$

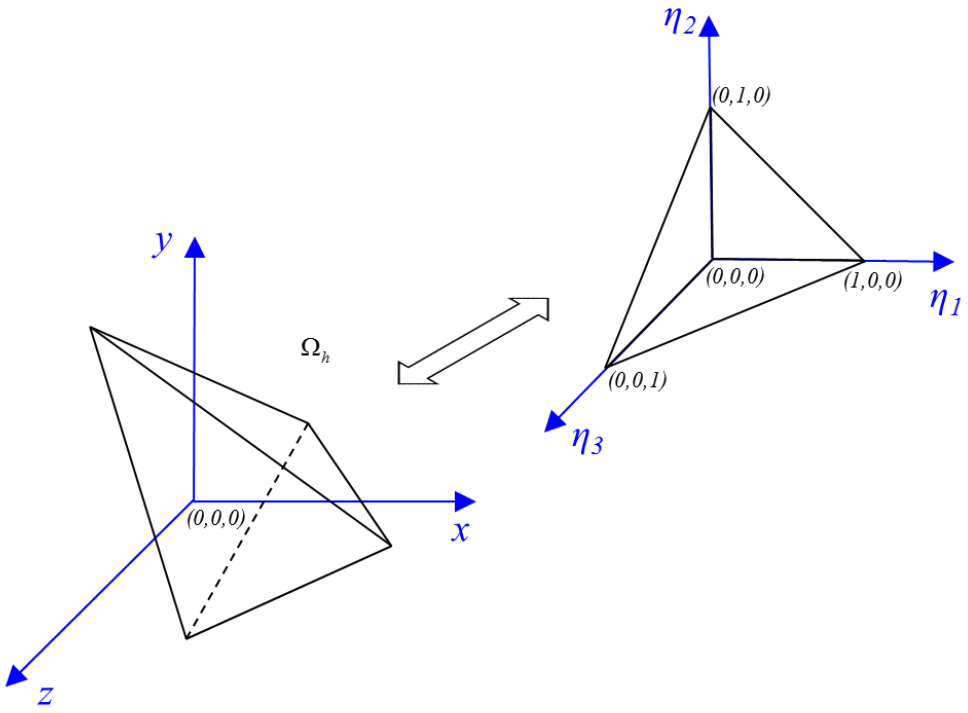

Fig. 17 Schematic diagram of the linear mapping of the 3D tetrahedron element

4.2.3 Foundation of basis functions

The structure of basis function in order to use for polynomials of degree *P* on standard reference elements is introduced in this section. Two well-known class of polynomials are continually applied in discontinuous finite element methods: Lagrange polynomial as a non-hierarchical basis and hierarchical basis called Legendre polynomial. The former (eigenfunctions of a particular Sturm-Liouville problem) is particularly useful as an interpolation basis, and the latter is a particular form of orthogonal Jacobi polynomial. The orthogonality feature benefits from useful properties, including solving efficiently the block matrices. The mentioned above advantage will be handy in treating the source terms, which will be discussed in coming sections in more details.

The use of the *nodal* basis will depict a non-hierarchical expansion associated with a set of nodes; nonetheless, the *modal* basis will typically represent a hierarchical expansion.

The reason behind calling these bases as modal is that the coefficients of the expansion functions, which are also called as modes are unknown.

A schematic of the mass matrices computed by Lagrange and Legendre basis is depicted in Fig. 18.

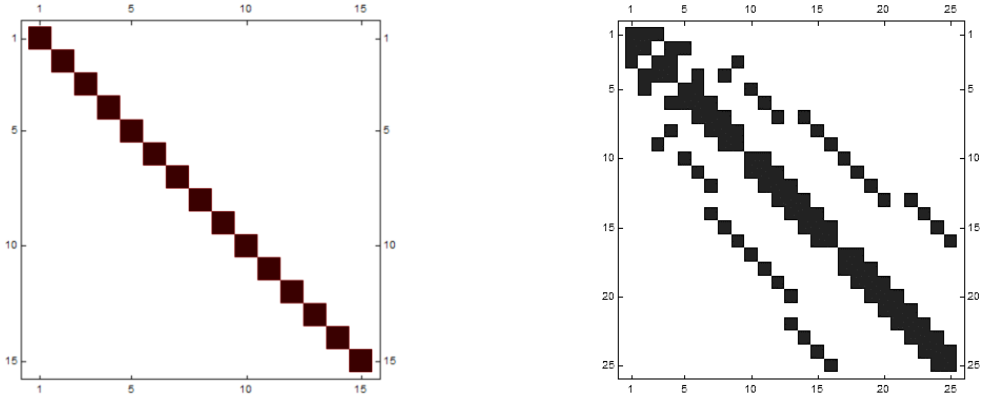

Fig. 18 Comparison of typical mass matrices corresponding to Lagrange (right) and Legendre (left) bases, adapted from [7]

Because of desired features including recursion and orthogonality, the Legendre polynomials are used as basis functions in this study, which will be outlined for one, two, and three-dimensional space in the following subsections. These functions are solutions to the Legendre differential equation. The nth -order Jacobi- polynomial $P_n^{\alpha,\beta}(\mathrm{x})$ is given by

$$P_n^{\alpha,\beta}(\mathrm{x}) = \frac{(-1)^n}{2^n n!}(1-\mathrm{x})^{-\alpha}(1+\mathrm{x})^{-\beta}\frac{d^n}{dx^n}\left[(1-\mathrm{x})^{\alpha+n}(1-\mathrm{x})^{\beta+n}\right] \qquad \alpha,\beta>1 \tag{90}$$

4.2.3.1 **Basis functions for the one-dimensional problem**

Legendre basis function in one-dimension can be derived by using Rodrigue's formula, and it is defined by $P_n(\eta)$,

$$P_n(\eta) = \frac{1}{2^n n!}\frac{d^n}{d\eta^n}\left(\eta^2-1\right)^n . \tag{91}$$

The orthogonality feature of Legendre polynomials can be identified as:

$$\int_{-1}^{1} P_i(\eta)P_j(\eta)d\eta = \begin{cases} 0 & \text{if} \quad i \neq j \\ C_{mn} & \text{if} \quad i = j \end{cases} \tag{92}$$

The modes of the Legendre basis functions are depicted in Fig. 19 and also the polynomials up to 6th order of accuracy are shown as below:

$$\begin{aligned}
&\varphi_0(\eta) = P_0(\eta) = 1 \\
&\varphi_1(\eta) = P_1(\eta) = \eta \\
&\varphi_2(\eta) = P_2(\eta) = \frac{1}{2}\left(3\eta^2 - 1\right) \\
&\varphi_3(\eta) = P_3(\eta) = \frac{1}{2}\left(5\eta^3 - 3\eta\right) \\
&\varphi_4(\eta) = P_4(\eta) = \frac{1}{8}\left(35\eta^4 - 30\eta^2 + 3\right) \\
&\varphi_5(\eta) = P_5(\eta) = \frac{1}{8}\left(63\eta^5 - 70\eta^3 + 15\eta\right)
\end{aligned} \tag{93}$$

Scaled Legendre polynomials are defined as: $\wp_n(\eta) = \dfrac{2^n (n!)^2}{(2n)!} P_n(\eta)$

$$\begin{aligned}
&\varphi_0(\eta) = \wp_0(\eta) = 1 \\
&\varphi_1(\eta) = \wp_1(\eta) = \eta \\
&\varphi_2(\eta) = \wp_2(\eta) = \eta^2 - \frac{1}{3} \\
&\varphi_3(\eta) = \wp_3(\eta) = \eta^3 - \frac{3}{5}\eta^2 \\
&\varphi_4(\eta) = \wp_4(\eta) = \eta^4 - \frac{6}{7}\eta^2 + \frac{3}{35} \\
&\varphi_5(\eta) = \wp_5(\eta) = \eta^5 - \frac{10}{9}\eta^3 + \frac{5}{21}\eta
\end{aligned} \tag{94}$$

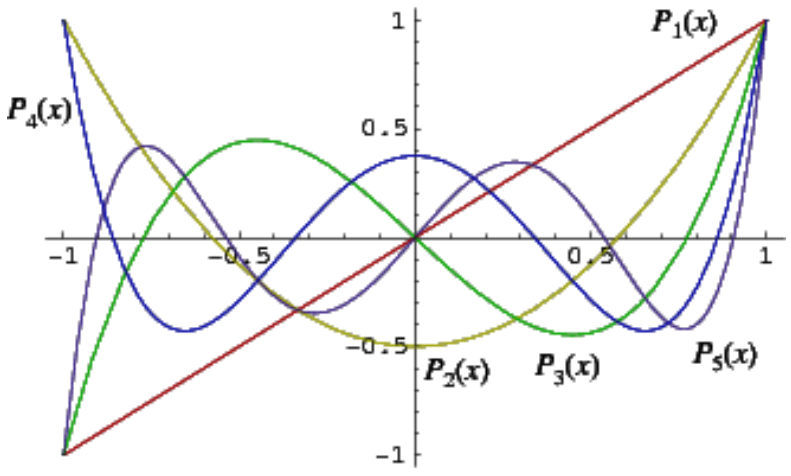

Fig. 19 Legendre polynomial space

4.2.3.2 **Basis functions (rectangular and triangular bases) for the two-dimensional problem**

Rectangular basis

The structure of the basis functions can be established in each coordinate direction via the tensorial product of the Legendre polynomials. The polynomial function of order *N*, is defined as $\varphi_k(\eta_1,\eta_2) = L_p(\eta_1).L_q(\eta_2)$ with: $k = p+q(N+1); \quad 0 \le p;\ q \le N.$

where, φ_k is the single indexed multidimensional basis which sorts all the modes of the principal functions (*P* and *Q*). It is worth mentioning that owing to the applied bilinear mapping [163], these polynomials on rectangular elements cannot provide a diagonal mass matrix.

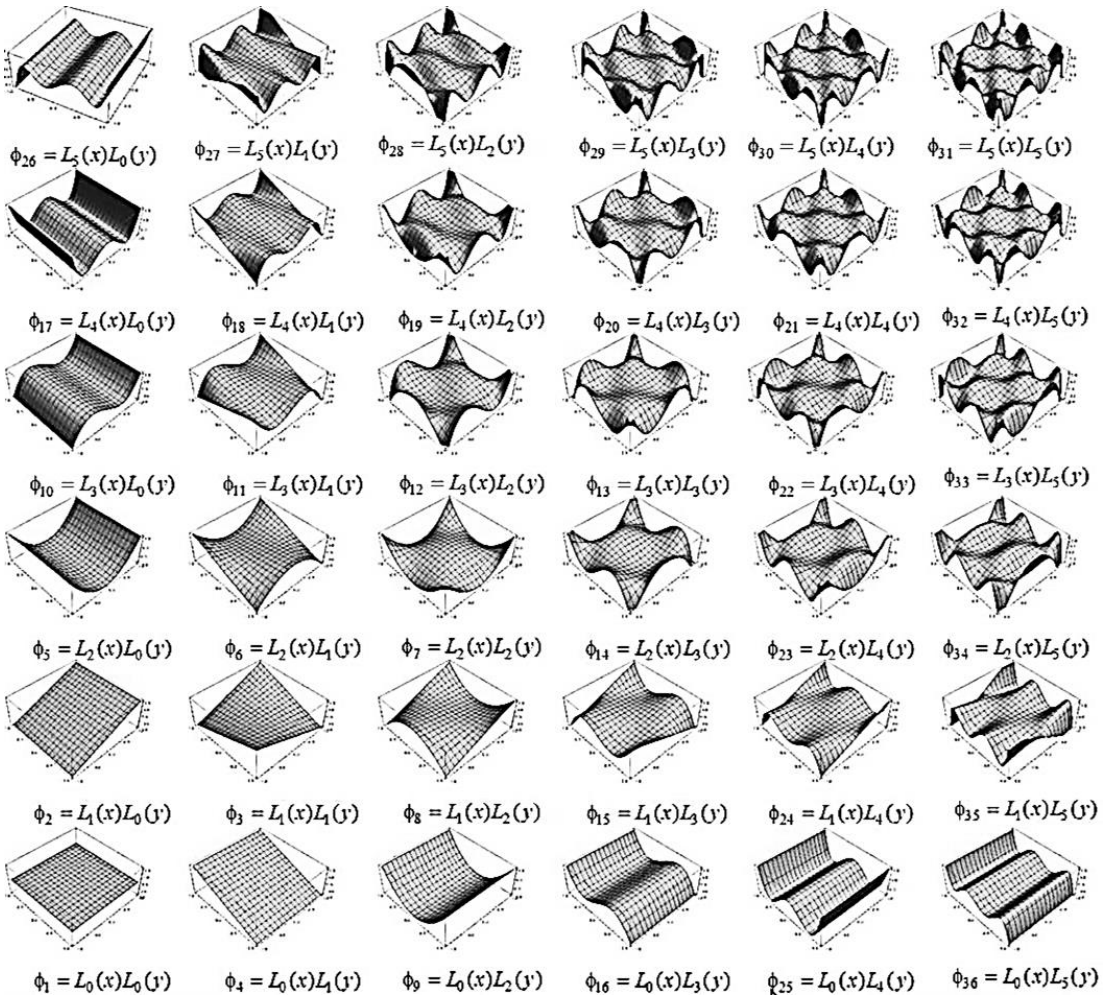

Fig. 20 Scaled Legendre polynomial space, based on Pascale' triangle for standard rectangular elements (up to polynomial order of P=6), adapted from [7]

Triangular basis

Orthogonal basis functions can be constructed over Ω_e^t by tensorial product of the Legendre polynomials (principal functions) in the region Ω_e^q.

$$\varphi_k(\xi_1,\xi_2) = P_p^{0,0}(\eta_1)\left(\frac{1-\eta_2}{2}\right)^p P_q^{2p+1,0}(\eta_2) \tag{95}$$

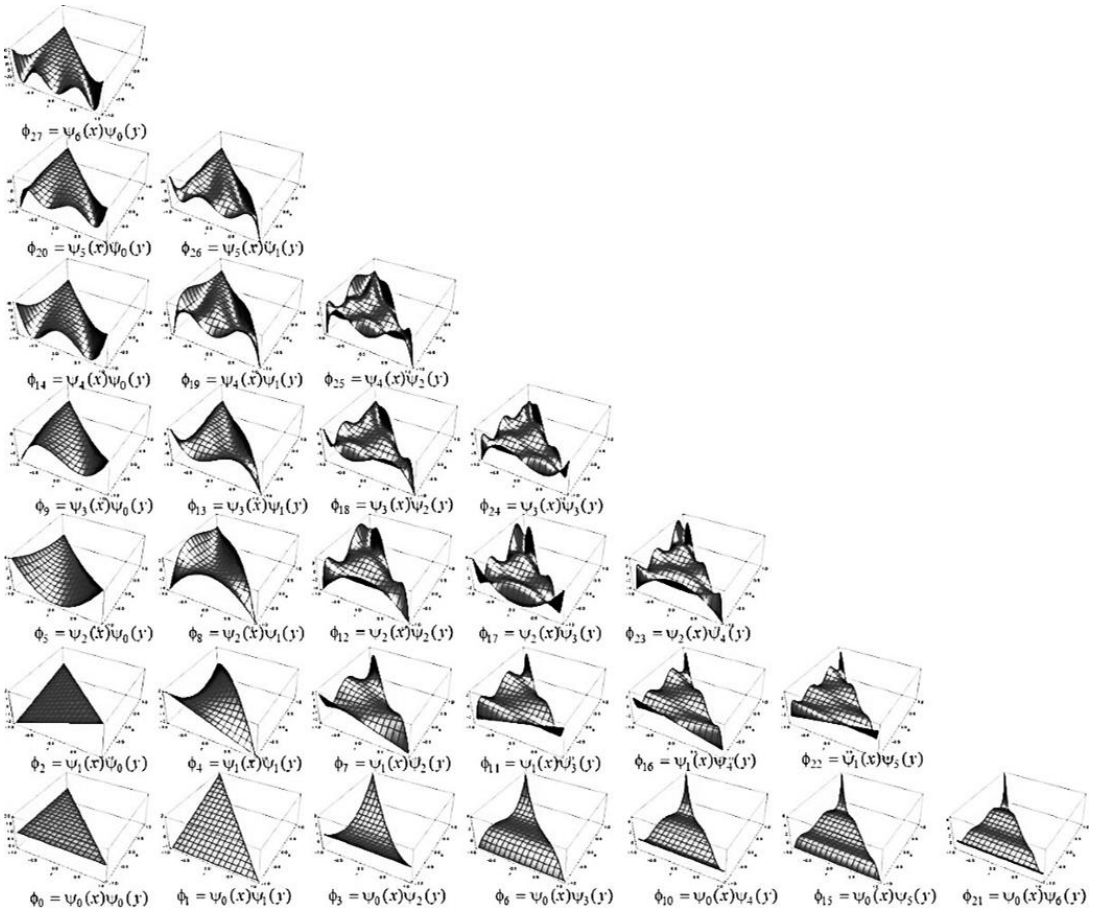

Fig. 21 Scaled Legendre polynomial space, based on Pascale' triangle for standard triangular elements (up to polynomial order of P=6)), adapted from [7].

4.2.3.3 **Basis functions for three-dimensional problem**

In three-dimensional space, by applying an orthogonal basis functions over Ω_e by tensorial product of the Legendre polynomials (principal functions) in the region Ω_e^c; An orthogonal mass matrix is obtained, the formulation can be written as,

$$\varphi_k(\eta_1,\eta_2,\eta_2) = P_p^{0,0}\left(\frac{2\eta_3}{1-\eta_1-\eta_2}-1\right)\left(-\frac{4\eta_1}{1-\eta_2}\right)^p P_q^{2p+1,0}\left(1-\eta_2\right)^{p+q} P_r^{2p+2q+2,0}(2\eta_2-1). \quad (96)$$

4.2.4 Numerical integration in the computational domain

Numerical integration is applied to the distinct local weak form of governing equations with the purpose of calculating the surface and volume integrals. Among various procedures that are widely used in finite element and discontinuous Galerkin methods, numerical quadrature (in one-dimensional problems and sometimes it can be used as a genaral method) or cubrature (in two- and three-dimension) is the most well-known algorithm in which one can approximates the integrals by weighted sum of function evaluations. Existence of strong discontinuities or turbulence effects which results in aliasing instabilities makes the selection of a rule for integration extremely difficult. In the current work Gauss-Legendre algorithm as a sub-category of Gauss quadrature procedure is employed. Since it is defined in the range of -1 to 1, a transformation of physical coordinate to standard ones is needed. The integration approximation for various elements in different dimension is tabulated as below. Moreover, the graphical illustrations of the position and required number of quadrature points are depicted in Fig. 22 and Fig. 23

Table 8 The integration approximation for various elements in 1D/2D and 3D

1D element	$\int_a^b f(x)dx \approx \sum_{i=1}^{n} w_i f(x_i)$, $\int_{-1}^{1} f(\eta)d\eta \approx \sum_{i=1}^{n} w_i f(\eta_i)$
2D quadrilateral element	$\int_{-1}^{-1}\int_{-1}^{1} f(\eta_1,\eta_2)d\eta_1 d\eta_2 \approx \sum_{i=1}^{n}\sum_{j=1}^{n} w_i w_j f(\eta_i,\eta_j)$ $\Omega_e^q = \{(\eta_1,\eta_2) \mid -1 \le \eta_1,\eta_2 \le 1\}$
2D triangular element	$\int_{-1}^{1}\int_{-1}^{1-\eta_1} f(\eta_1,\eta_2)d\eta_1 d\eta_2 \approx \sum_{i=1}^{n}\sum_{j=1}^{n} w_i w_j f(\eta_i,\eta_j) \approx \frac{1}{2}\sum_{i=1}^{n} w_i f(\eta_i,\eta_j)$ $\Omega_e^t = \{(\eta_1,\eta_2) \mid -1 \le \eta_1,\eta_2,\eta_1+\eta_2 \le 1\}$
3D tetrahedron element	$\int_{-1}^{1}\int_{-1}^{1-\eta_1}\int_{-1}^{1-\eta_1-\eta_2} f(\eta_1,\eta_2,\eta_3)d\eta_1 d\eta_2 d\eta_3 \approx \frac{1}{6}\sum_{i=1}^{n} w_i f(\eta_i,\eta_j,\eta_k)$ $\Omega_e^c = \{(\eta_1,\eta_2,\eta_3) \mid 0 \le \eta_1,\eta_2,\eta_1+\eta_2+\eta_3 \le 1\}$

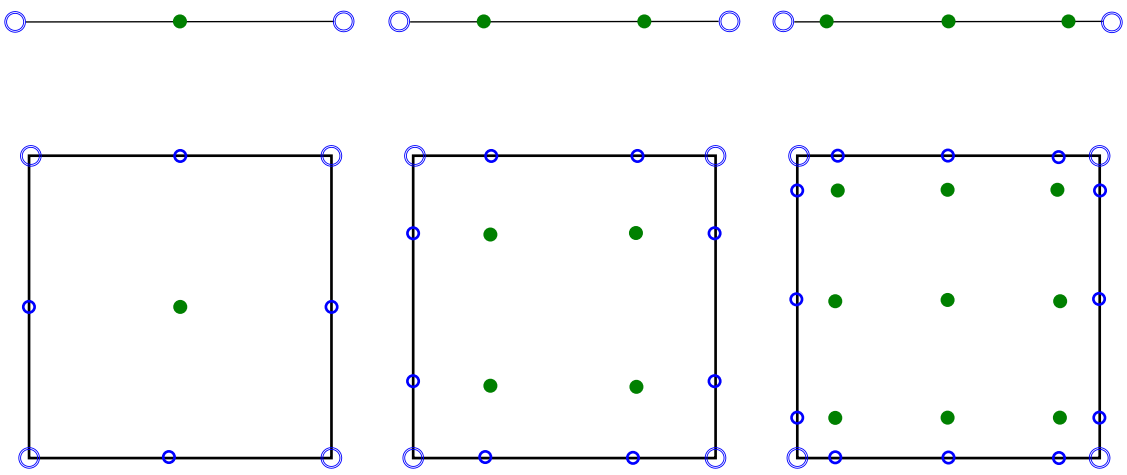

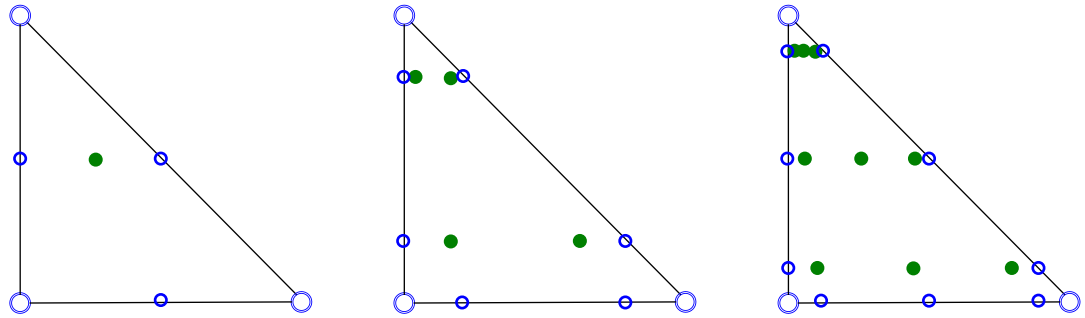

Fig. 22 Schematic representation of number and location of required quadrature points used in numerical integration for (a) 1D elements, (b) 2D quadrilateral elements, (c) 2D triangular elements, adapted from [7]

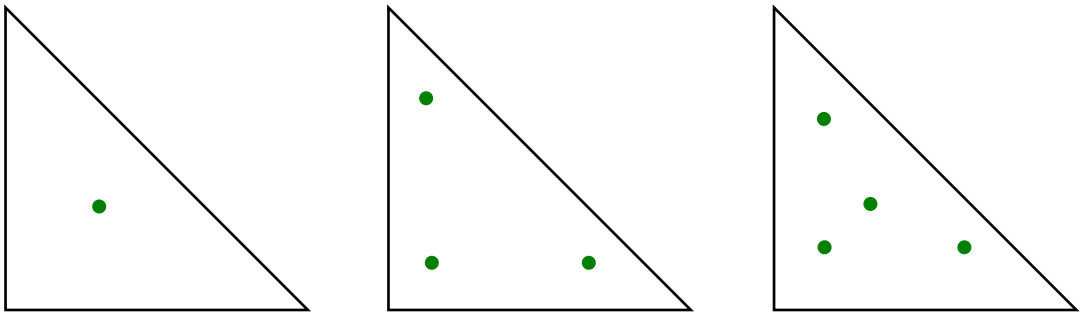

(a) Surface quadrature points

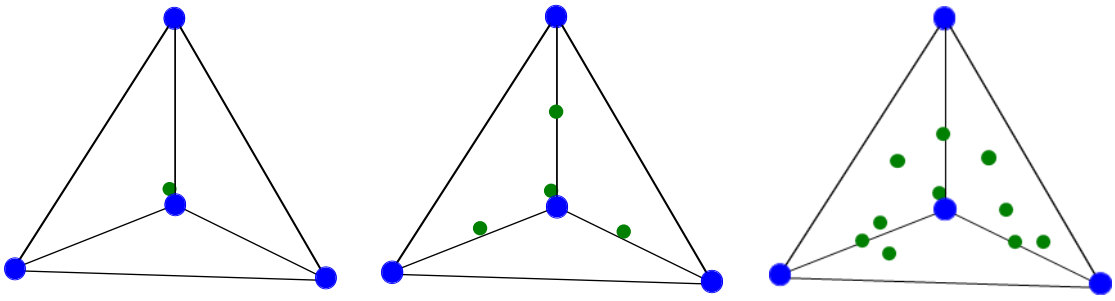

(b) Volume quadrature points

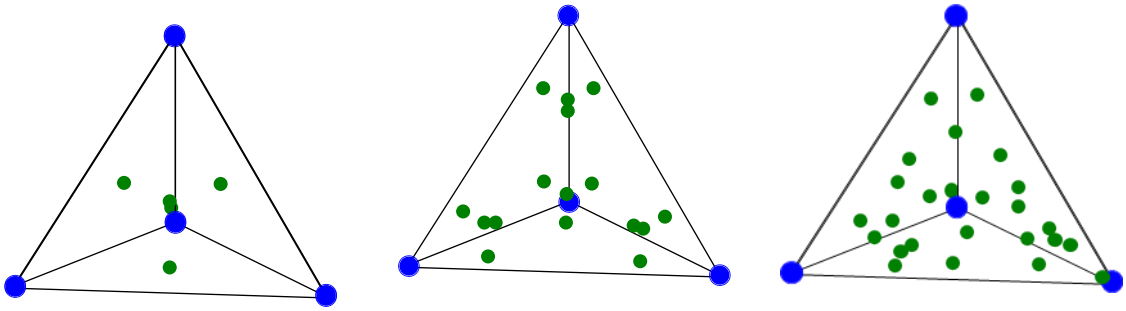

(c) Surface and volume quadrature points together

Fig. 23 Schematic representation of number and location of required quadrature points used in numerical integration in a 3D tetrahedron element, adapted from [7]

4.2.5 Numerical flux functions

A factor that plays important role from in the stability of numerical simulation is an appropriate numerical flux. These fluxes can also determine the accuracy of the solution. A proper numerical flux should feature from consistency and conservative as well.

Consistency conveys the idea that for smooth continuous inter-element boundary values, the solution of the numerical flux is identical to the analytic flux function. Furthermore, conservative implies a single-valued flux on the inter-element boundaries. The inviscid numerical flux calculation can be classified into two general methods as flux difference splitting (FDS) methods and flux vector splitting (FVS) methods. These numerical approaches are taking advantage of using the upwind direction identification schemes which are referred to as the *Riemann approach* or *Boltzmann approach*. These schemes are broadly presented in the classical review paper of Harten *et al.* [165] and other references [166-169]. Observation of using the FVS approach reveals that this method is more straightforward and more efficient compared to Godunov-type methods of FDS class. In current dissertation, to circumvent the complexity of implementation and avoiding the carbuncle errors in the numerical simulation Rusanov [170] (or local Lax-Friedrichs) and Rotated-RHLL [171] fluxes are applied depending on the problem

interests. The implementation of the inviscid numerical flux is exactly analogous to the well-established FVM procedure, and the details of the implementation are skipped.

Extra effort is required to compute the viscous numerical flux in DG framework. Accurate mathematical derivation of viscous numerical flux for the problem of pure elliptical equations (Laplace problem) can be referred to in [172, 173]. The integrated of some numerical flux introduced by [173] is presented in

Table 9. The definition of the operators such as $\{\ \}$ and for scalar variable *s* and vector quantity $\vec{v}$ is depicted as follows

$$\begin{aligned} s &= s^+\vec{n}^+ + s^-\vec{n}^- = \vec{n}\left(s^+ - s^-\right) \\ \{s\} &= \frac{1}{2}\left(s^+ + s^-\right) \\ \vec{v} &= \vec{v}^+.\vec{n}^+ + \vec{v}^-.\vec{n}^- = \vec{n}\left(\vec{v}^+ - \vec{v}^-\right) \\ \{\vec{v}\} &= \frac{1}{2}\left(\vec{v}^+ + \vec{v}^-\right) \end{aligned} \tag{97}$$

Table 9 Comparison of some the numerical schemes for viscous flux. Adapted from [173].

Method	$\hat{u}$	$\hat{\sigma}$
Bassi and Rebay [164] (BR1)	$\{u_h\}$	$\{\sigma_h\}$
Brezzi *et al.* [174]	$\{u_h\}$	$\{\sigma_h\}-\alpha_r\left(\ u_h\ \right)$
Cockburn and Shu [175] (LDG)	$\{u_h\}-\beta.[u_h]$	$\{\sigma_h\}+\beta\ \ \sigma_h\ \ -\alpha_j\left(\ u_h\ \right)$
Douglas and Dupont [176] (IP)	$\{u_h\}$	$\{\nabla_h u_h\}-\alpha_j\left(\ u_h\ \right)$
Bassi *et al.* [177] (BR2)	$\{u_h\}$	$\{\nabla_h u_h\}-\alpha_r\left(\ u_h\ \right)$

In the above table, the penalty terms are defined as,

$$\begin{aligned} &\alpha_j(\varphi) = \mu\varphi = \eta_e h_e^{-1}\varphi, \\ &\alpha_r(\varphi) = -\eta_e\{r_e(\varphi)\}, \end{aligned} \tag{98}$$

where, η_e is a positive number and h_e is an indicator of element size (e.g., circumscribed circle radius of the element), and $\int_\Omega r_e(\varphi).\tau dx = -\int_e \varphi.\{\tau\}ds$.

In most of the computations in this thesis, BR1 is applied, where central discretization is employed for both auxiliary and viscous fluxes. It should be mentioned that it keeps the order of accuracy to only *P* (polynomial degree) for odd ansatz [175]. Also, the stencil is known to be spread. These drawbacks motivated the application of the LDG method in which one-sided fluxes in opposite directions for the auxiliary and viscous fluxes are utilized. In this thesis, β is set equal to zero when LDG flux is employed yielding to an *upwind-downwind* (also known as *alternating flux*) scheme.

4.2.6 Positivity preserving scheme

High order conservative schemes, including the DG scheme introduced in the previous section, usually suffer from the non-physical negative density or pressure. This situation leads to the ill-posedness of the system and numerical breakdowns in consequence. On the other hand, in the case of conservation laws with source terms which are added to account for chemical reactions, gravity or the interaction of phases, as in the present case, the possibility of encountering negative density or pressure during numerical simulation increases. Therefore, the application of an efficient positivity preserving schemes is necessary to prevent the numerical breakdown. In the present work, the positivity preserving scheme of Zhang and Shu [178] for compressible Euler equations were applied to ensure the positivity of density and pressure fields, while maintaining the higher order accuracy. The general implementation of the scheme can be outlined as follows.

Limiting the higher order coefficients for density was achieved first by computing the minimum value of the density amongst all quadrature points, $\rho_{\min}$. The coefficients for the density expansion were then modified as $\tilde{a}_i^{\rho} = \theta_1 a_i^{\rho}$ with $\theta_1 = \min(\frac{a_0^{\rho} - \varepsilon}{a_0^{\rho} - \rho_{\min}}, 1)$. Here the *i* index accounts for all the bases, and the zero indexes represent the mean solution.

Also, the value ε is determined by $\varepsilon = \min(10^{-13}, a_0^{\rho}, \bar{p})$ where $\bar{p}$ denotes the mean element pressure.

For the modification of pressure, the following procedures were used. First, we set **s** as

$$\mathbf{s} = (1-t)\bar{\mathbf{w}} + \beta\bar{\mathbf{q}}, \tag{99}$$

where $\bar{\mathbf{w}}$ and $\bar{\mathbf{q}}$ are the cell average and conservative variables, respectively. β can be calculated as follows

$$\beta = \begin{cases} 1 & \text{if } p(\mathbf{q}) \geq \varepsilon \\ \text{the solution of } p(\mathbf{s}) = \varepsilon, & \text{if } p(\mathbf{q}) < \varepsilon \end{cases} \tag{100}$$

Finally, the coefficients are modified by $\tilde{a}_i^{\rho} = \theta_2 a_i^{\rho}$ with $\theta_2 = \min(\beta, 1)$.

The application of this limiter was proved to provide stable schemes for unstructured triangular meshes with favorable results [161]. We report the first application of this type of limiter to the two-fluid model of dusty gas flows. Our numerical experiments on all the test cases show that application of a positivity preserving limiter is necessary to obtain converged solutions without compromising the accuracy of the solution.

4.2.7 Monotonicity preserving scheme

Our numerical investigations show that simple application of the positivity preserving scheme is not enough to develop a stable scheme, especially in the presence of strong shock waves. The situation deteriorates when the multiphase system with source terms is being solved. In the present study, the limiter of Zhang and Shu [179] for one-dimensional cases and the limiter of Barth and Jespersen [158], which was initially devised for the finite volume framework are applied. It is important to note that any TVD/MUSCL type scheme can degrade the order of accuracy in the smooth regions of the solution unless a pragmatic shock detection scheme is introduced.

According to Barth and Jespersen [158], the limiting procedure of slopes should be done in a way that the solution at the integration points is confined to the range spanned by the neighboring solution averages. The limited solution can then be written as

$$U(\mathbf{x},t) = a_0(t)\varphi_0(\mathbf{x}) + \lambda_{\min}\sum_{i>0}^{p} a_i\varphi_i(\mathbf{x}), \tag{101}$$

where $\lambda_{\min} = \min\max(\lambda_1, 0),$

$$\lambda_1 = \begin{cases} \min(1, \dfrac{U_{\max} - U_i}{\Delta_2}), & \text{if } \Delta_2 > 0 \\ \max(1, \dfrac{U_{\min} - U_i}{\Delta_2}), & \text{if } \Delta_2 < 0 \\ 1, & \text{otherwise} \end{cases} \tag{102}$$

Here $\Delta_2 = U_j(\mathbf{x}_i^*) - U_j$ and $U_{\max}$ and $U_{\min}$ are the maximum and minimum solution averages on the elements sharing edges, respectively.

4.2.8 Boundary conditions

The implementation of boundary conditions in two-fluid or multi-fluid systems requires a different set of conditions for each phase. The benchmark problems considered in this paper are free from boundary effects, except the compression corner test case, in which an adiabatic, impermeable, inviscid wall boundary condition is applied for both phases (Kim and Chang [116]. Other boundary conditions choices like the adherence condition or reflection conditions are also viable for the solid phase [180]. When the viscous system of conservation laws (e.g., Navier-Stokes-Fourier) is considered, it is necessary to use a non-slip boundary condition for the gas phase and a slip boundary condition for the solid phase.

Some of the applied boundary conditions for the gas phase are summarized below.

4.2.9 Novel source terms treatment

It was well-known that the stiff relaxation terms in balance laws (i.e., strictly hyperbolic systems with source terms) lead to disparate relaxation times, which in turn results in severe numerical difficulties. In the case of the two-fluid model, in addition to the time scale related to the convection, a much smaller relaxation time scale exists that inevitably imposes smaller time steps on the numerical solver. The use of a slower time scale in such problems can cause severe numerical instability.

The most well-known methods for removing this limitation are the operator splitting and zero-relaxation limit; however, as reported in Béreux [181], the range of validity of each method is very limited, to the product of relaxation time and the acoustic wave pulsation. Moreover, spurious solutions may arise when the effects of the source terms are not properly resolved [182]. Finally, it is well established that the convergence rate of the first-order finite difference methods for conservation laws will be no better than $O(h^{1/2})$ [183]. Here we demonstrate that the inherent feature of the new DG scheme bypasses the need to apply such inefficient treatments in conventional methods.

For a single variable u_h, the elemental formulation (64) reduces to

$$\frac{d}{dt}\int_{\Omega_k} u_h\varphi_i(\mathbf{x})\mathrm{d}\Omega_k + \oint_{\partial\Omega_k} F(u_h)\cdot\hat{n}\varphi_i(\mathbf{x})d\sigma - \int_{\Omega_k} F(u_h)\cdot\nabla\varphi_i(\mathbf{x})\mathrm{d}\Omega_k = \int_{\Omega_k} S(u_h)\varphi_i(\mathbf{x})\mathrm{d}\Omega_k. \tag{103}$$

Taking **U** as the global vector of degrees of freedom, this equation can be written in a matrix form:

$$
\begin{aligned}
&\mathbf{M}\frac{d\mathbf{U}}{dt}-\mathbf{K}\mathbf{U}+\widehat{F}(u_h)\mathbf{\Theta}-S(u_h)\mathbf{\Theta}'=0\\
&\frac{d\mathbf{U}}{dt}-\mathbf{M}^{-1}\mathbf{K}\mathbf{U}+\widehat{F}(u_h)\mathbf{M}^{-1}\mathbf{\Theta}-S(u_h)\mathbf{M}^{-1}\mathbf{\Theta}'=0\\
&\frac{d\mathbf{U}}{dt}=L(\mathbf{U})\\
&\mathbf{U}=(U^{(1)},U^{(2)},...,U^{(N)})^T\\
&L(\mathbf{U})=\mathbf{M}^{-1}\mathbf{K}\mathbf{U}-\widehat{F}(u_h)\mathbf{M}^{-1}\mathbf{\Theta}+S(u_h)\mathbf{M}^{-1}\mathbf{\Theta}'
\end{aligned}
\tag{104}
$$

Here, **M** and **K** are the mass and stiffness matrixes, and **Θ** and **Θ′** are the vectors that incorporate the contributions of the boundary and source terms, respectively. The matrixes are defined as follows:

$$
\begin{aligned}
&\mathbf{M}=\int_{\Omega_k}\varphi_i(\mathbf{x})\varphi_j(\mathbf{x})\mathrm{d}\mathbf{\Omega}_k \quad \forall \quad 1\le i\le j\le n\\
&=\begin{bmatrix}
\int_{\Omega_k}\varphi_1(\mathbf{x})\varphi_1(\mathbf{x})\mathrm{d}\mathbf{\Omega}_k & \int_{\Omega_k}\varphi_1(\mathbf{x})\varphi_2(\mathbf{x})\mathrm{d}\mathbf{\Omega}_k & ... & \int_{\Omega_k}\varphi_1(\mathbf{x})\varphi_n(\mathbf{x})\mathrm{d}\mathbf{\Omega}_k\\
\int_{\Omega_k}\varphi_2(\mathbf{x})\varphi_1(\mathbf{x})\mathrm{d}\mathbf{\Omega}_k & \int_{\Omega_k}\varphi_2(\mathbf{x})\varphi_2(\mathbf{x})\mathrm{d}\mathbf{\Omega}_k & ... & \int_{\Omega_k}\varphi_2(\mathbf{x})\varphi_n(\mathbf{x})\mathrm{d}\mathbf{\Omega}_k\\
\vdots & \vdots & \ddots & \vdots\\
\int_{\Omega_k}\varphi_n(\mathbf{x})\varphi_1(\mathbf{x})\mathrm{d}\mathbf{\Omega}_k & \int_{\Omega_k}\varphi_n(\mathbf{x})\varphi_2(\mathbf{x})\mathrm{d}\mathbf{\Omega}_k & ... & \int_{\Omega_k}\varphi_n(\mathbf{x})\varphi_n(\mathbf{x})\mathrm{d}\mathbf{\Omega}_k
\end{bmatrix},
\end{aligned}
\tag{105}
$$

Owing to the orthogonal property of the basis functions, $\mathbf{M}=\begin{cases}C_{ij} & i=j\\ 0 & i\ne j\end{cases}$

$$
\begin{aligned}
&\mathbf{K}=\int_{\Omega_k}\nabla\varphi_i(\mathbf{x})\varphi_i(\mathbf{x})\mathrm{d}\mathbf{\Omega}_k\\
&=\begin{bmatrix}
\int_{\Omega_k}\nabla\varphi_1(\mathbf{x})\varphi_1(\mathbf{x})\mathrm{d}\mathbf{\Omega}_k & \int_{\Omega_k}\nabla\varphi_1(\mathbf{x})\varphi_2(\mathbf{x})\mathrm{d}\mathbf{\Omega}_k & ... & \int_{\Omega_k}\nabla\varphi_1(\mathbf{x})\varphi_n(\mathbf{x})\mathrm{d}\mathbf{\Omega}_k\\
\int_{\Omega_k}\nabla\varphi_2(\mathbf{x})\varphi_1(\mathbf{x})\mathrm{d}\mathbf{\Omega}_k & \int_{\Omega_k}\nabla\varphi_2(\mathbf{x})\varphi_2(\mathbf{x})\mathrm{d}\mathbf{\Omega}_k & ... & \int_{\Omega_k}\nabla\varphi_2(\mathbf{x})\varphi_n(\mathbf{x})\mathrm{d}\mathbf{\Omega}_k\\
\vdots & \vdots & \ddots & \vdots\\
\int_{\Omega_k}\nabla\varphi_n(\mathbf{x})\varphi_1(\mathbf{x})\mathrm{d}\mathbf{\Omega}_k & \int_{\Omega_k}\nabla\varphi_n(\mathbf{x})\varphi_2(\mathbf{x})\mathrm{d}\mathbf{\Omega}_k & ... & \int_{\Omega_k}\nabla\varphi_n(\mathbf{x})\varphi_n(\mathbf{x})\mathrm{d}\mathbf{\Omega}_k
\end{bmatrix},
\end{aligned}
\tag{106}
$$

$$
\mathbf{\Theta}=\begin{bmatrix}
\int_{\Omega_e}\varphi_1(\mathbf{x})\left|J\right|\mathrm{d}\mathbf{\Omega}_e\\
\int_{\Omega_e}\varphi_2(\mathbf{x})\left|J\right|\mathrm{d}\mathbf{\Omega}_e\\
\vdots\\
\int_{\Omega_e}\varphi_n(\mathbf{x})\left|J\right|\mathrm{d}\mathbf{\Omega}_e
\end{bmatrix},
\tag{107}
$$

$$\boldsymbol{\Theta}' = \begin{bmatrix} \int_{\Omega_e} \varphi_1(\mathbf{x}) \left| J' \right| \mathrm{d}\boldsymbol{\Omega}_e \\ \int_{\Omega_e} \varphi_2(\mathbf{x}) \left| J' \right| \mathrm{d}\boldsymbol{\Omega}_e \\ \vdots \\ \int_{\Omega_e} \varphi_n(\mathbf{x}) \left| J' \right| \mathrm{d}\boldsymbol{\Omega}_e \end{bmatrix}. \tag{108}$$

The choice of orthogonal basis functions greatly simplifies the contribution of the high order moments of the polynomial approximate solution to the source-term related vector $\boldsymbol{\Theta}'$ in equation (30). Once the basis functions (Legendre polynomials), $\varphi_n(\mathbf{x})$, are multiplied by the transformation Jacobian ($\left| J' \right| = (1-b)/2$), the integration in the interval [-1 1] will vanish for all the terms except the first term, due to the orthogonal property of the basis functions and a coincidental relation $\varphi_1(\mathbf{x}) = 1$; that is,

$$\boldsymbol{\Theta}' = \begin{bmatrix} \int_{\Omega_e} \varphi_1(\mathbf{x}) \left| J' \right| \mathrm{d}\boldsymbol{\Omega}_e \\ \int_{\Omega_e} \varphi_2(\mathbf{x}) \left| J' \right| \mathrm{d}\boldsymbol{\Omega}_e \\ \vdots \\ \int_{\Omega_e} \varphi_n(\mathbf{x}) \left| J' \right| \mathrm{d}\boldsymbol{\Omega}_e \end{bmatrix} = \begin{bmatrix} 2 \\ 0 \\ \vdots \\ \vdots \\ 0 \end{bmatrix}. \tag{109}$$

Note that, in this novel method, the source term treatment is greatly simplified, the same as the first-order (P^0) case. In other words, the contribution of the cell average solutions is dominant in the source terms in the DG framework, although the left-hand side of equations (64) and (25) is calculated by the high order polynomial approximation.

4.2.10 Linear approximation for solving constitutive equations

The solution of these equations will provide viscous stress, excess stress, and heat flux, which are essential in defining the numerical viscous flux on cell interfaces. The non-conserved variables can be approximated and called as first-order Boltzmann-based equations by using Newtonian law for defining shear, bulk viscosity and Fourier law of heat conduction as follows,

$$\mathbf{\Pi}_0 = -2\mu\left[\nabla\mathbf{u}\right]^{(2)}, \quad \Delta_0 = -2\mu_b \nabla.\mathbf{u}, \quad \mathbf{Q}_0 = -\kappa\nabla \ln T \tag{110}$$

The readers are referred to [7, 184, 185] for more details regarding an extension of approximation of constitution equations to second-order Boltzmann-based in continuum framework.

4.3 Finite volume (FV) method applied on carrier phase

In this section, FV method adopted flux function, and viscosity assumption is briefly explained since some of the numerical simulations are conducted by commercial software. The computational domain is divided using a finite set of control volumes to approximate the conservation equations of mass, momentum, and energy, utilizing the finite volume method (FVM). The FVM is a robust and efficient method for solving a hyperbolic system of equations [186]. The flux on a cell surface was determined by the advection upstream splitting method plus (AUSM+). The AUSM+ scheme shows excellent capabilities for resolving discontinuities and providing entropy-satisfying and positivity-preserving solutions. The density-based approach in the ANSYS FLUENT (version 17.2) CFD code was employed. The viscosity for the ideal gas assumption was calculated using Sutherland's law to take into account the dependency on temperature.

4.4 Discrete phase model (DPM) applied on dust particle in the Lagrangian framework

4.4.1 Survey on applications and limitations

The following options are available while applying by the discrete phase trajectory which gives the users the capability to simulate a wide range of problems including particle separation and classification, aerosol dispersion, spray drying, liquid fuel combustion, coal combustion, and bubble stirring of liquids.

i. For both steady and unsteady flows, the formulation of Lagrangian is included with the discrete phase inertia, hydrodynamic drag, and the force gravity.
ii. Estimation of the influence of turbulence on the dispersion of particles owing to the existence of turbulent eddies in the carrier phase.
iii. Calculation of energy exchange of the discrete phase
iv. Applying vaporization and boiling of liquid droplets
v. Coupling option to take into consideration the effect of particles on the continuous phase
vi. Breaking up/coalescence of the droplet

The trajectory model similar to any methods is subjected to some drawbacks which limit the application of this approach. Some of those disadvantages are listed below:

i. Since the dispersed phase is sufficiently dilute, the continuous phase can be considered free from the effects of particle-particle interactions as well as volume fraction. These issues convey an idea that the volume fraction of the discrete phase must appear at low magnitudes usually less than 10-12%.
ii. The governing physics of the explained steady-particle Lagrangian DPM is suited for flows in which the initial conditions, as well as exit conditions, are well-defined. These circumstances imply that the Lagrangian model has poor functionality once the particles are suspended for an unspecified period in the carrier phase. Such phenomena can be found in solid suspension through closed systems including mixing vessels or fluidized bed.

4.4.2 Calculation of particle trajectory

In the current study, the trajectory and the behavior of the scattered particles in continuous phase are modeled in a Lagrangian framework using the discrete phase model (DPM) by integrating the force balance over each particle. In this model, the assumption of neglecting particle-particle interaction is valid, since the volume fraction of the

dispersed phase compared to the continuous phase is significantly low (less than 10%). The DPM can be expressed in a way that makes a simulation of the heat and momentum exchange feasible, by conducting two-way coupling with the Eulerian frame of gas. The force balance equation can be written in the *x*-direction for simplicity, as follows:

$$\frac{du_p}{dt} = F_D(u - u_p) + \frac{g_x(\rho_p - \rho)}{\rho_p} + F_x \tag{111}$$

In the ordinary differential equation, the source term F_x can be any additional force, which acts on the particle. Furthermore, F_D is the drag force per unit mass and can be expressed as

$$F_D = \frac{18\mu}{\rho_p d_p^2}\frac{C_D Re}{24} \tag{112}$$

Here u, ρ, μ, and d, are velocity, density, viscosity, and diameter, respectively. The subscript p represents the property of the particle. g is the gravitational acceleration, and Re is the relative Reynolds number defined as

$$Re = \frac{\rho d_p \left| u - u_p \right|}{\mu} \tag{113}$$

where the drag coefficient C_D is given by

$$C_D = a_1 + \frac{a_2}{Re} + \frac{a_3}{Re^2} \tag{114}$$

Here a_1, a_2 and a_3 represent constant coefficients for smooth spherical particles [187, 188].

4.4.3 Dispersal and continuous phases coupling

The solver follows the exchange of conserved variables such as mass, momentum, and heat by the particle stream as the trajectory of the particles is calculated. The variables mentioned above can be accommodated in the calculation of the subsequent gas phase.

Moreover, this phenomenon implies that not only the continuous phase impacts the discrete phase but also the particle's trajectories can affect the gas phase as well. Therefore, two-way coupling computation is terminated after solving alternatively the discrete phase and gas phase once the solutions in both phases become stabilized, and no further alteration observed.

Chapter 5. Numerical experiments on inviscid flows including Euler-type systems of equation

In this chapter, we present the results for some of the well-known benchmark problems in one- and two-dimensional space. To verify the code and estimate the order of accuracy of the numerical scheme, we first solve a smooth problem with analytical solutions. We then investigate the widely studied Sod's shock tube problem in dusty gas flows with special emphasis on the complex wave behaviors therein. Finally, we solve

two two-dimensional multiphase flows—explosion and compression corner problems—to highlight the effects of the dispersed phase (solid dust) on the multi-dimensional dusty gas flow. In all test cases, the ratio of the specific heats of air (γ) and the ratio of the specific heats of the two phases (c_m/c_v) are set equal to 1.4 and 1.0, respectively. Unless otherwise mentioned, the following values are used for particle properties:

diameter, d=10 μm;

mass density, ρ_s=2,500 kg/m^3;

specific heat, c_m=718 J/kg-K.

5.1 One-dimensional dusty gas flows

5.1.1 Verification study in the single-phase case (1-D)

The propagation of a smooth sine wave (known as the entropy waves problem) was considered for verification of the code. The periodic boundary conditions were applied at both sides of the domain. For the following initial condition,

$$\begin{cases} u(x,0)=1, \\ \rho(x,0)=1.0+0.2\sin(\pi x), \\ p(x,0)=1, \end{cases} \tag{115}$$

the corresponding exact solutions can be written as

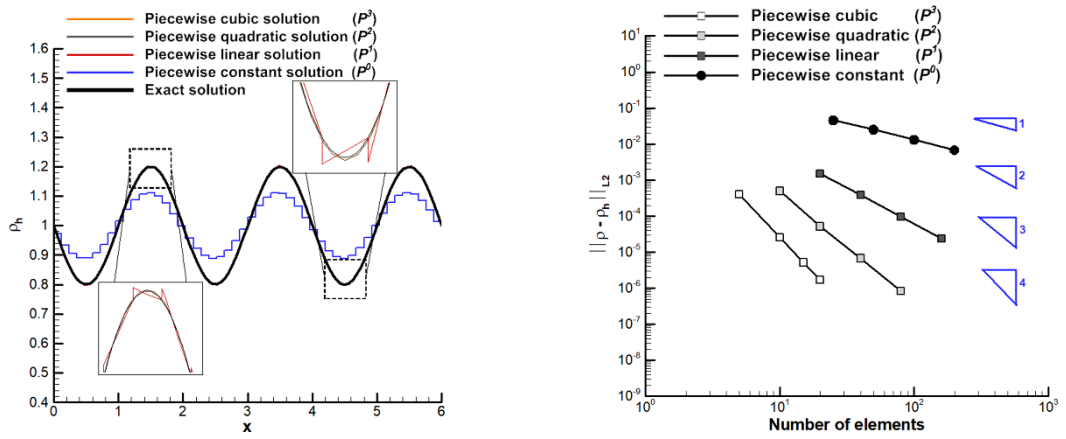

Roe flux function

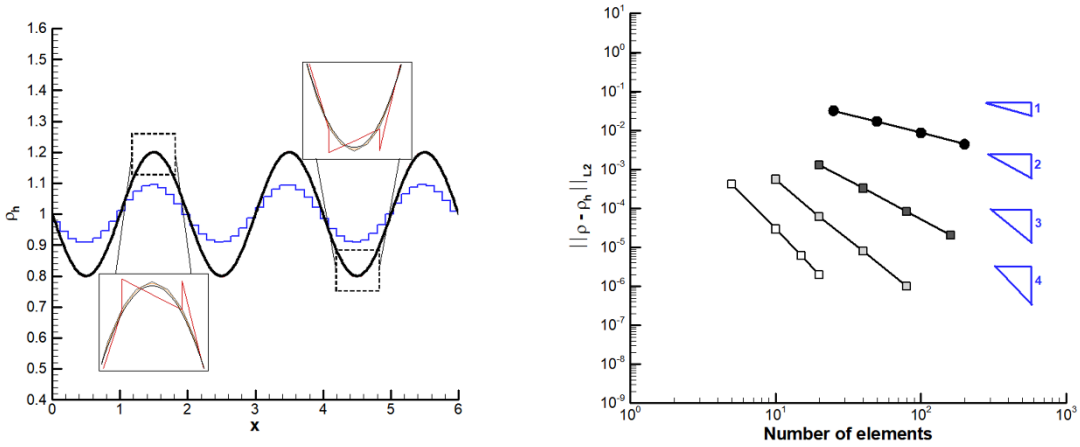

HLL flux function

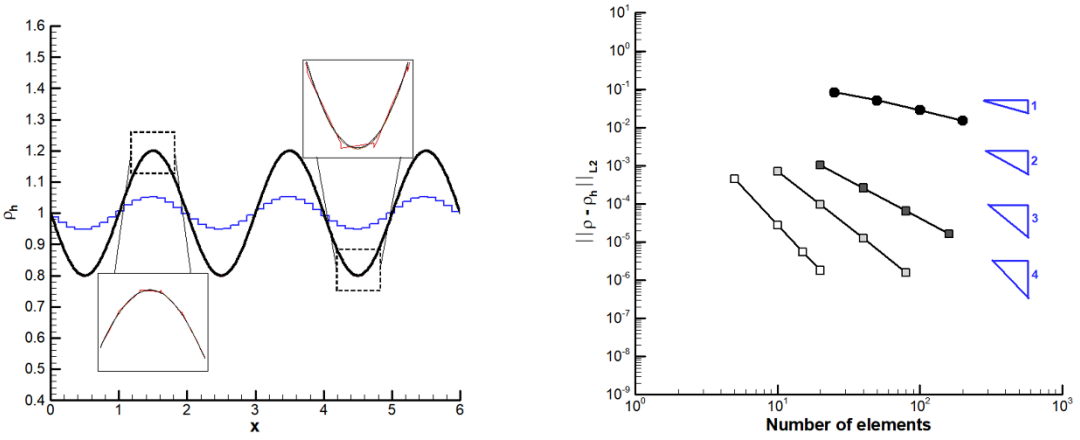

Rusanov (LLF) flux function

Fig. 24. Comparison of various numerical fluxes for the smooth solution of Euler equation; (left) profile, (right) Euclidean norm of density [18]

$$\begin{cases} u(x,t)=1, \\ \rho(x,t)=1.0+0.2\sin(\pi(x-t)), \\ p(x,t)=1. \end{cases} \tag{116}$$

In order to measure the order of accuracy of the DG method for various flux functions, the density distribution of the solution was obtained for different orders of accuracy (P^{χ}, with χ indicating the polynomial order) and the results are shown in Fig. 24. It can be seen that numerical deviation from the analytical solution is large in the first-order piecewise constant case (P^0); however, the application of more sophisticated numerical fluxes such as Roe and HLL can improve the accuracy of the piecewise constant solution.

In order to evaluate the performance of the numerical scheme in more detail, the numerical errors and the order of accuracy were calculated based on the density solution. The results were found to be consistent with the observations of Qiu *et al.* [189]. Moreover, it was confirmed that all numerical fluxes lead to the expected order of accuracy of P+1. It is worth noting that each flux function shows different behavior in performance for different orders of a polynomial function, and thus drawing a general conclusion is not possible.

5.1.2 Sod shock tube problem in dusty gas flows

Fig. 25 depicts the shock tube problem in single phase (pure gas) and multiphase (dusty gas). The evolution of various types of waves and discontinuities from the initial Riemann data can provide the essence of dusty gas flows; as, for example, the supersonic flows formed by the interaction of rocket plume and lunar dust. Moreover, the shock tube problem is ideal for examining the feasibility and validity of the new numerical methods, since it is free from boundary effects or other numerical complexities. The scheme tested in the one-dimension problem can also be extended to the multi-dimensional situation afterward.

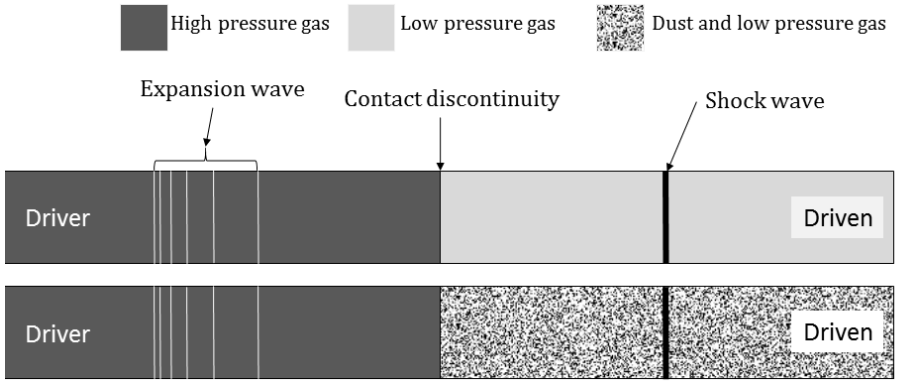

Fig. 25. Schematic of the shock tube problem in dusty gas (pure gas versus dusty gas) (computational domain length: 100L)

In order to obtain solutions without spurious oscillations, the positivity-preserving scheme was used in conjunction with the monotonicity-preserving limiter. It should be emphasized again that no extra effort is necessary for handling the source terms, thanks to the special feature associated with the orthogonal basis functions introduced in the new DG scheme, as explained in subsection 4.2.9. That is, the present DG method is immune to the artifact that may arise from splitting the source terms, or the complexity incurred by application of the fractional step approach [86, 190] or the random choice method [114] to cope with the source terms.

Table 10. The initial condition for the Sod's shock tube problem

Non-dimensional variable	Driver section	Driven section
Pressure	10.0	1.0
Gas density	10.0	1.0
Particle concentration	0.00001	1.0
Gas velocity	0.0	0.0
Dust velocity	0.0	0.0

The results of the dusty shock tube problem with the initial condition summarized in Table 10 are presented in Fig. 26. It can be seen that the numerical solutions of the pure gas are in good agreement with the analytical solutions of the shock tube problem. In the

figures, the term ‘dusty gas’ implies the carrier gas phase. This problem has been previously investigated by Saito [80], Saito *et al.* [81], and Pelanti and LeVeque [85]. Comparison with these previous results can be used as verification of the present computational model of two-fluid dusty gas. The multiphase solutions demonstrate the profound effects of the inertia of the dust particles on the flow properties. The gradual response of the dust particles to the diaphragm rupture was observed, especially in the velocity and temperature profiles. Interestingly, the strength of the right-running shock wave front was found to be much smaller than that of pure gas, which is due to the absorption of momentum and heat from the gas molecules by the dust particles. In addition, the deceleration of the shock wave front was observed from the velocity profile, inducing compression waves behind the shock wave. This phenomenon was identified in the pressure profiles as well.

5.1.3 Composite wave structures in the Sod problem of dusty gas flows

In contrast to a single-phase flow, dusty gas flows can show some striking wave structures, which have no counterpart in classical theory. The physical explanation of these phenomena in dusty gas flows has rarely been addressed in the literature. In this section, we provide a detailed discussion on the underlying physics forming these abnormal waves.

Various wave structures that are formed in the shock tube problem of dusty gases are schematically illustrated using the *x*-*t* diagram in Fig. 27 (a) describes the case in which the contact discontinuity of gas and the boundary path of a particle are located at the same position, while Fig. 27 (b) describes the case in which the boundary path of a particle is located at a distance from the contact discontinuity of gas. When a shock wave impinges on a cloud of particles in dusty gas flows, it will be reflected as an expansion or shock wave, depending on the ratio of the specific heats of the solid particle and gas, and

the particulate loading of the mixture [72]. In this diagram, the case of reflected rarefaction waves was not considered, since the properties of the test case of the mixture corresponding to the case of shock wave reflection. Since solid particles with non-negligible inertia cannot follow the abrupt changes of flow, a relaxation zone attached to the shock wave forms and the shock wave front decelerates until a new equilibrium condition is reached. The size of the relaxation zone is affected by the diameter of the solid particle, density, and heat capacity. As mentioned before, a finite time is required for the particles to fully attain the speed of the gas. During this period, reflected compression waves are generated from the boundary path of the particle, eventually forming a weak left-running shock wave, as illustrated in Fig. 27 (a).

For better clarification, we investigated in detail how the evolution of those waves is affected by the concentration of dust particles. We identified three abnormal behaviors based on the density profile: 1) the tale of the left-running rarefaction waves; 2) the region before the contact discontinuity, and 3) the tale of the right-running shock wave. It is well known that, after the diaphragm ruptures, a right-running compression wave and left-running rarefaction waves will start to propagate in the background medium. On the other hand, dust particles with different density ratios on each side of the diaphragm will lead to the existence of an extra contact discontinuity (in solid phase) compared to the case of pure gas. We refer to this discontinuity as the dust contact discontinuity (DCD).

The first composite wave structure, marked as number (1) in Fig. 28, was observed at the tail of the rarefaction waves in the density profile. This exotic structure should be distinguished from the numerical artifacts that may be found in high order methods when they are not appropriately treated. Due to the presence of dust particles, the rarefaction waves weaken, and their propagation speed decreases as well. Therefore, gas will accumulate in

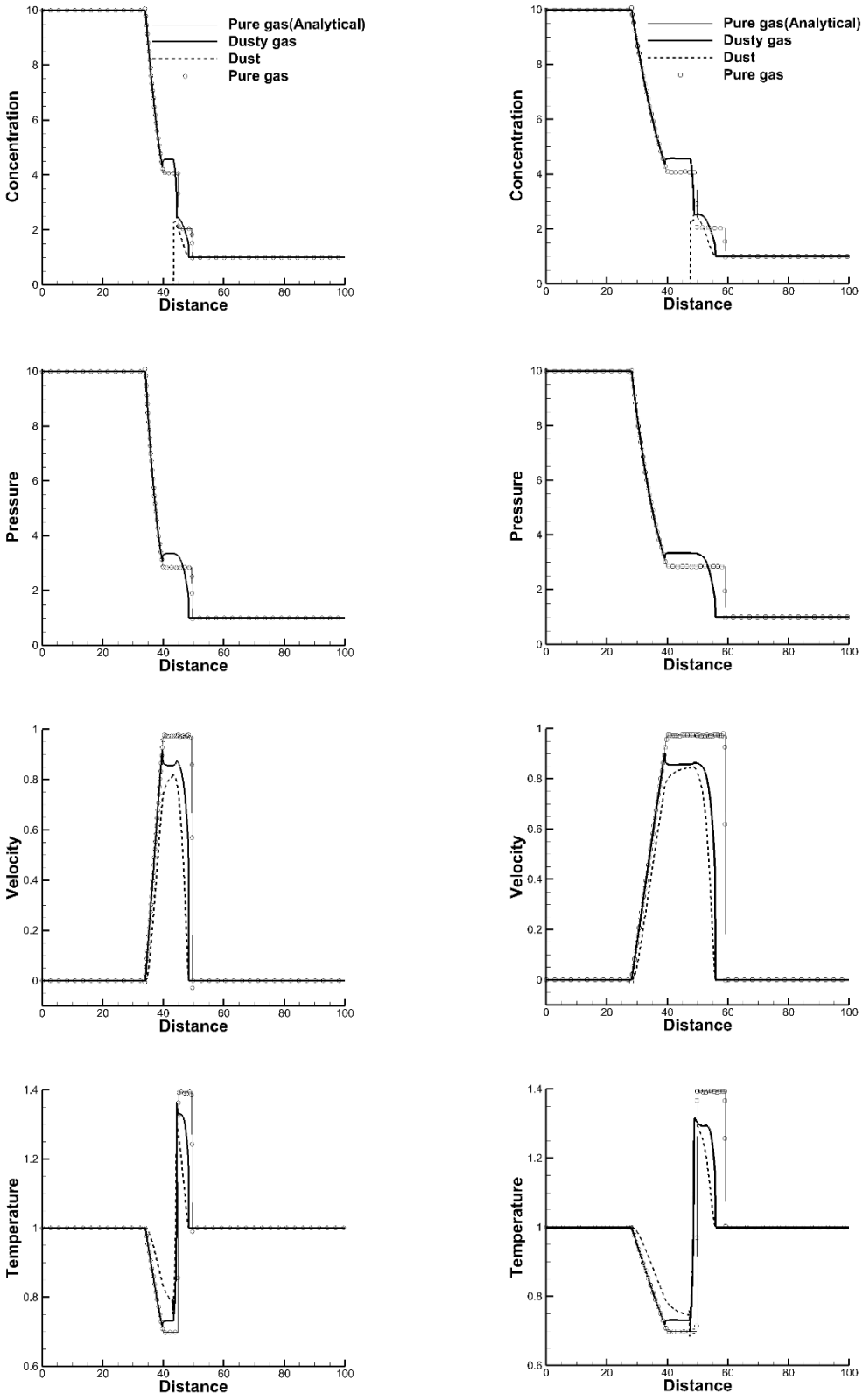

t=5 *t=10*

Fig. 26. Solutions of the Sod's shock tube problem in dusty gas for two different time steps (P1 solution) [18]

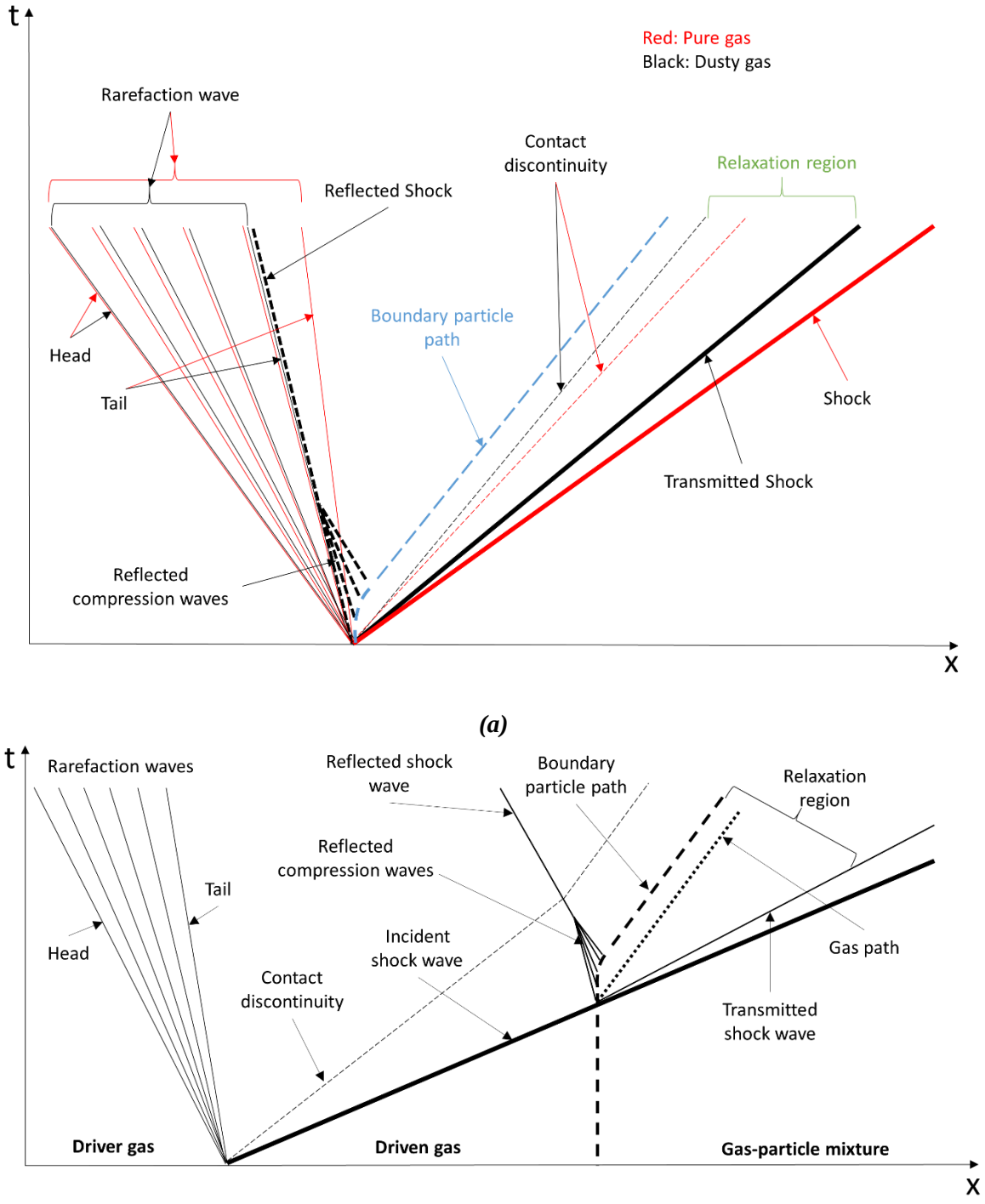

Fig. 27. Schematic of various wave structures in the 1-D dusty gas flow: (a) The gas contact discontinuity and boundary particle path is initially located at the same position, (b) The particle boundary path is located at a distance from the gas phase contact discontinuity [18]

The region close to the tail of the rarefaction waves and the reflected compression waves generated from the boundary path of the dust particle will form a weak shock wave attached to the tail of the left-running rarefaction waves, as observed in Fig. 28 (a).

This weak shock wave is directly related to the presence of the DCD, and it will be strengthened when the dust concentration increases. It will be shown in a later figure that, when there is no DCD, i.e., when both the high and low-pressure sections are filled with the same dust concentration, this composite wave structure will disappear. In passing, it should be mentioned that this type of composite waves is different from the generic compound waves observed in magneto-hydrodynamics, due to the non-convexity and the non-strict hyperbolicity [191], and the present waves should be called composite waves or pseudo-compound waves, rather than compound waves.

In another region, marked number (2) in Fig. 28, the presence of dust induces an increase in pressure (and a decrease in velocity) in the middle region, leading to higher density compared to the case of pure gas. It turns out that this increase in density is dependent on dust concentration, as well as the location of the DCD.

A second composite wave structure, marked number (3) in Fig. 28, was observed at the tail of the shock wave. It consists of a right-running shock wave followed by a relaxation zone. When there is no particle, the shock wave is steep and strong as expected. When particles are present, however, the shock wave weakens substantially, and the relaxation zone forms instead, due to the coupling effects between the two phases. We can see that a higher particle concentration leads to a larger relaxation zone and a reduction in the propagation speed of the shock wave. It will be shown in the next figure that the location of the DCD changes the position where the shock wave forms, but does not affect the size of the relaxation zone.

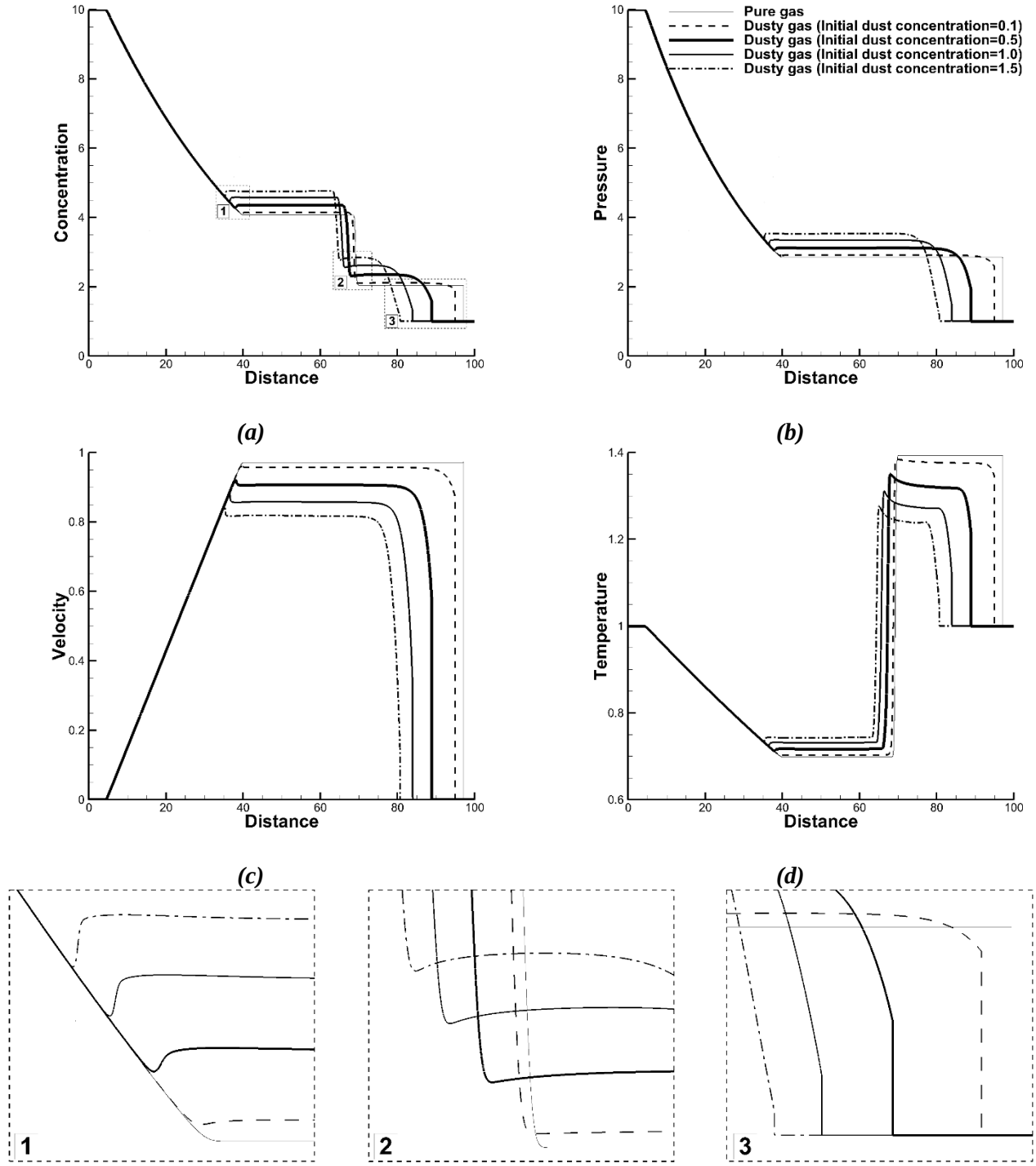

Fig. 28. Effects of initial dust concentration on the Sod's shock tube in the dusty gas (P^1 solution) (RW: rarefaction wave, RS: reflected shock, CD: contact discontinuity, RZ: relaxation zone, SW: shock wave) [18]

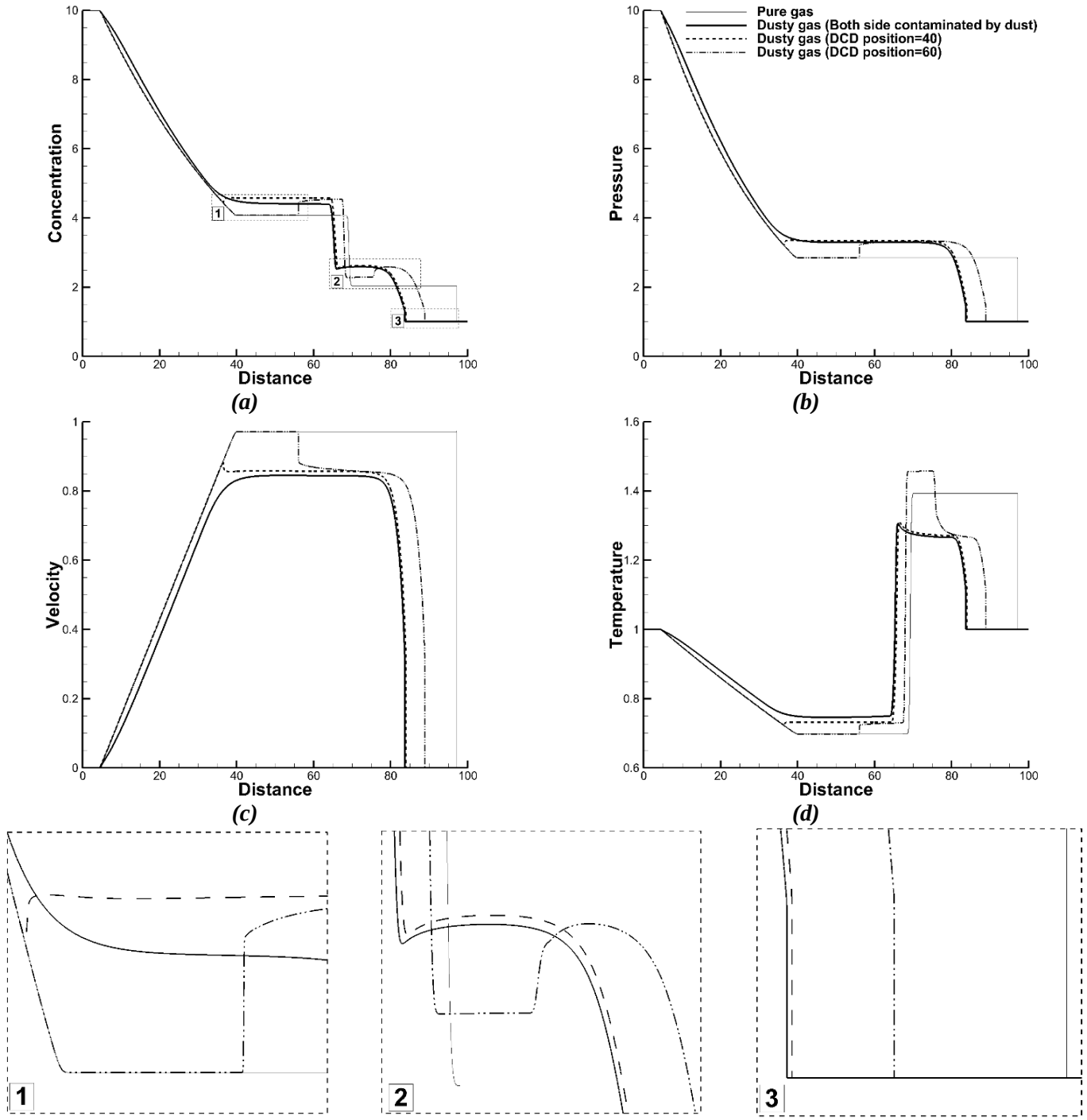

Pseudo compound wave made up of RW-RS

CD attached/detached to/from RZ

RZ attached to SW

Fig. 29. Effects of location of the initial dust contact discontinuity (DCD) on the Sod's shock tube in the dusty gas at t=30 (P^1 solution)
(RW: rarefaction wave, RS: reflected shock, CD: contact discontinuity, RZ: relaxation zone, SW: shock wave) [18]

In order to investigate how the DCD would affect wave patterns in the dusty gas flows, additional cases were simulated by varying the position of the DCD (from x=40 to x=60) while maintaining the same dust concentration, as shown in Fig. 29. The other profiles in this figure correspond to the pure gas and the dusty gas case of the previous figure. In all cases, the dust concentration is assigned with the same value ($\alpha_0\rho_0$=0.1). In the region marked number (1), the weak discontinuity in density, pressure, and temperature profiles discussed in Fig. 28 vanishes when there is no DCD. When the DCD is shifted towards the right end of the tube (x=60), the discontinuity is detached from the rarefaction waves and is shifted to the right as well.

In the region marked number (2), the shifted DCD seems to produce yet another contact discontinuity (around x=70) attached to the relaxation zone. When putting together with adjacent waves, there seems to be a new composite wave structure, consisting of three waves—a contact discontinuity, the relaxation zone, and a shock wave. On the other hand, as can be seen in region number (3), the strength of the right-running shock wave and the size of the relaxation zone remain the same for all dusty gas cases, though the position of the waves is shifted as expected.

5.2 Two-dimensional dusty gas flows

5.2.1 Verification study in the single-phase case (2-D)

In order to examine the order of the accuracy of the developed method, the propagation of a smooth sine wave in a two-dimensional domain was considered. The periodic boundary conditions were applied at all sides of the square domain, as shown in Fig. 30(a). For the following initial condition,

$$\begin{cases} u(x,y,0)=1, \\ v(x,y,0)=1, \\ \rho(x,y,0)=1.0+0.2\sin\left[\pi(x+y)\right], \\ p(x,y,0)=1. \end{cases} \tag{117}$$

the corresponding exact solutions can be written as

$$\begin{cases} u(x,y,0)=1, \\ v(x,y,0)=1, \\ \rho(x,y,0)=1.0+0.2\sin\left[\pi(x+y-t)\right], \\ p(x,y,0)=1. \end{cases} \tag{118}$$

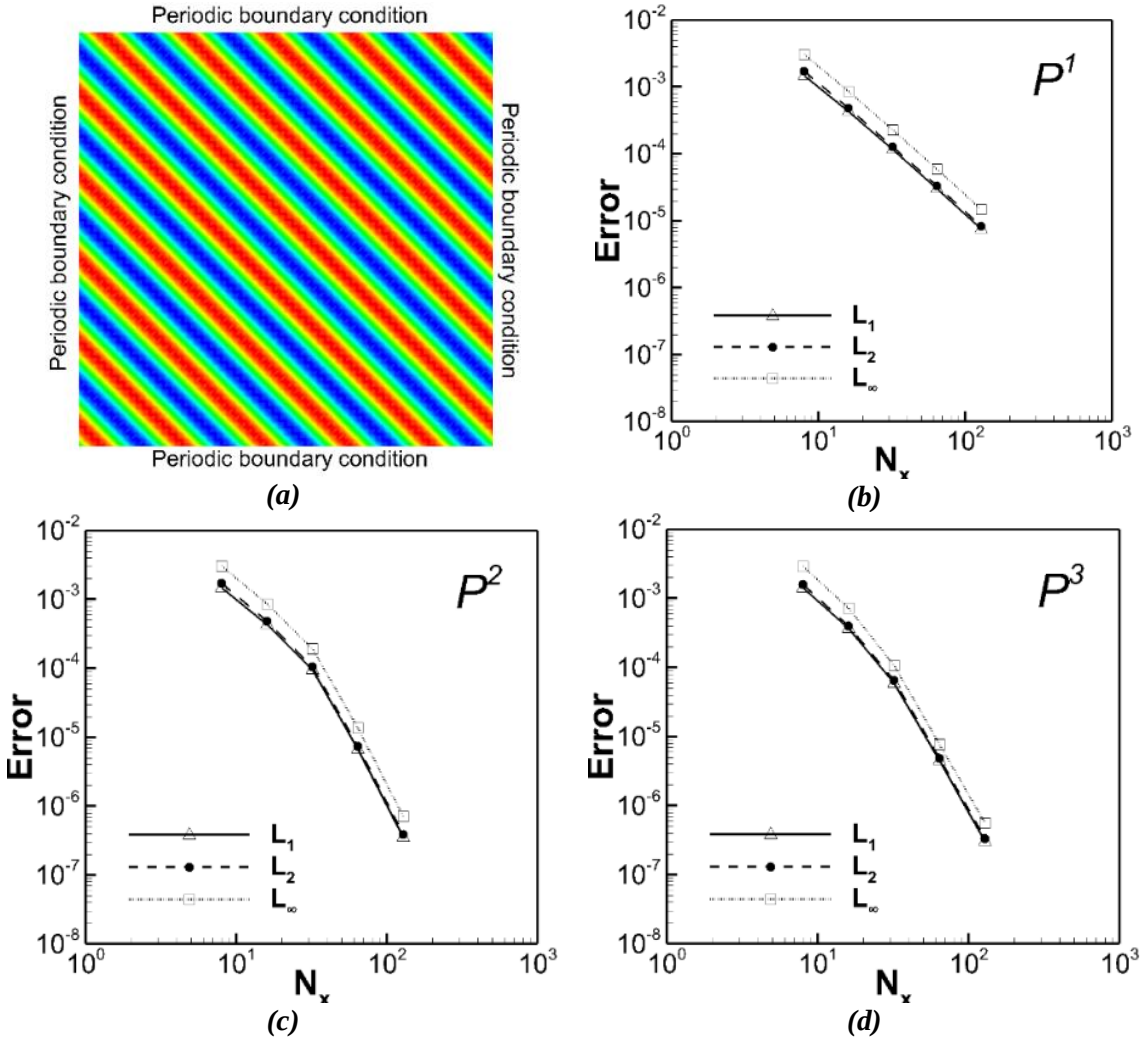

Fig. 30 Analysis of the order of the accuracy of the two-dimensional code for a smooth sine function problem [18]

The error norms for density solutions up to fourth-order accuracy (P^3) are calculated and summarized in Fig. 30 (b-d) Table 11. It can be seen that the desired order of accuracy is achieved. For fine grids, the actual order is shown to be higher than the nominal order of accuracy.

Table 11 Accuracy analysis for 2D entropy waves [18].

P^1

ΔX	N_x	L_1 error	L_2 error	L_∞ error	L_1 order	L_2 order	L_∞ order
1.25	8	1.47E-03	1.72E-03	3.09E-03	-	-	-
0.625	16	4.33E-04	4.84E-04	8.65E-04	1.764	1.829	1.835
0.3125	32	1.16E-04	1.29E-04	2.30E-04	1.896	1.912	1.914
0.15625	64	3.01E-05	3.31E-05	5.92E-05	1.951	1.955	1.956
0.078125	128	7.64E-06	8.40E-06	1.50E-05	1.979	1.980	1.980

P^2

ΔX	N_x	L_1 error	L_2 error	L_∞ error	L_1 order	L_2 order	L_∞ order
1.25	8	1.47E-03	1.72E-03	3.09E-03	-	-	-
0.625	16	4.33E-04	4.84E-04	8.65E-04	1.764	1.830	1.835
0.3125	32	9.60E-05	1.06E-04	1.92E-04	2.174	2.197	2.172
0.15625	64	6.77E-06	7.44E-06	1.38E-05	3.827	3.825	3.801
0.078125	128	3.55E-07	3.91E-07	7.06E-07	4.251	4.249	4.286

P^3

ΔX	N_x	L_1 error	L_2 error	L_∞ error	L_1 order	L_2 order	L_∞ order
1.25	8	1.43E-03	1.59E-03	2.90E-03	-	-	-
0.625	16	3.69E-04	4.03E-04	7.30E-04	1.959	1.980	1.990
0.3125	32	5.90E-05	6.50E-05	1.09E-04	2.643	2.633	2.744
0.15625	64	4.47E-06	4.91E-06	7.75E-06	3.725	3.728	3.813
0.078125	128	3.06E-07	3.37E-07	5.68E-07	3.866	3.863	3.771

5.2.2 2-D compression corner problem in dusty gas flow

As the second two-dimensional benchmark problem, we investigated the compression corner problem for both the single and multi-phase applications. This problem is far more complicated due to the presences of boundary effects and the intrinsic complexity of the flow. The incident shock Mach number M_s, the wall inclination angel θ_w, and the initial condition of driven and driver sections define the governing physics of the shock-wave diffraction. The schematic of the compression corner problem is illustrated in Fig. 31.

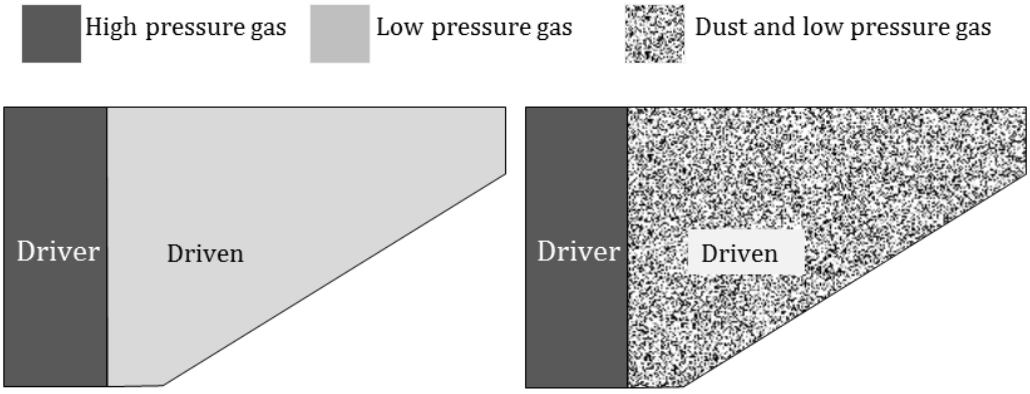

Fig. 31. Schematic of the pure gas (left) and dusty gas (right) 2-D compression corner problems (computational domain size: 5L×4L)

As a validation study, we compared our numerical solutions with the experimental results obtained by [113] for the case of a single Mach reflection (SMR). The initial condition is for both the single-phase and multiphase cases are provided in Table 12.

Table 12.The initial condition for the single Mach reflection problem

Non-dimensional variable	Driver section	Driven section
Pressure	4.64	1.0
Gas density	2.71	1.4
Particle concentration	0.1	0.1
Gas velocity (*x*-direction)	1.51	0.0
Gas velocity (*y*-direction)	0.0	0.0
Dust velocity (*x* and *y* -directions)	0.0	0.0

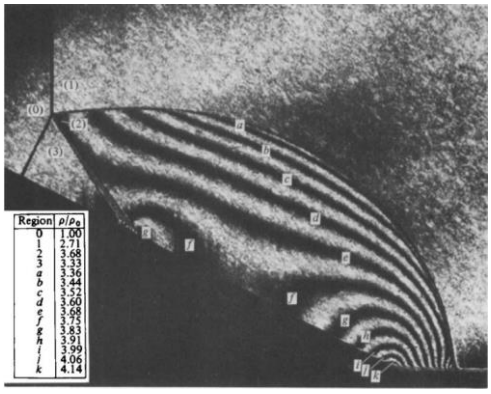

Experimental image [113]

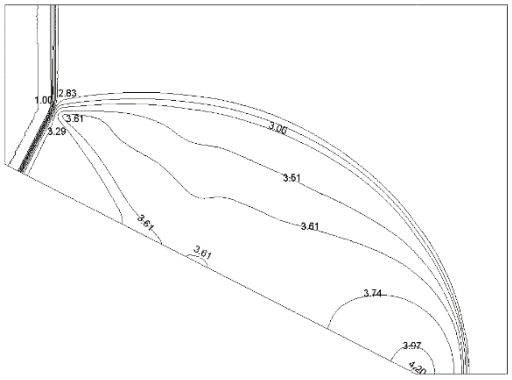

P^0 *soloution*

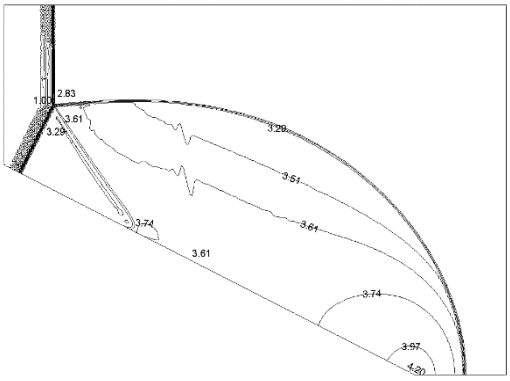

P^1 *solution*

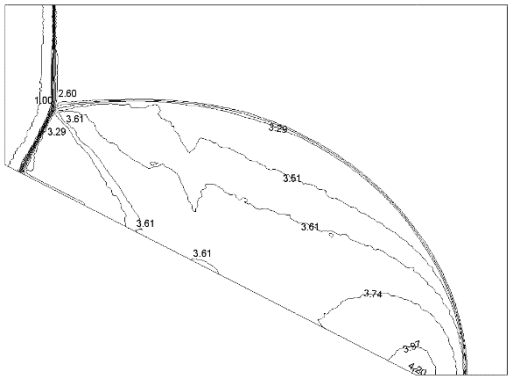

P^2 *solution*

A

B

C

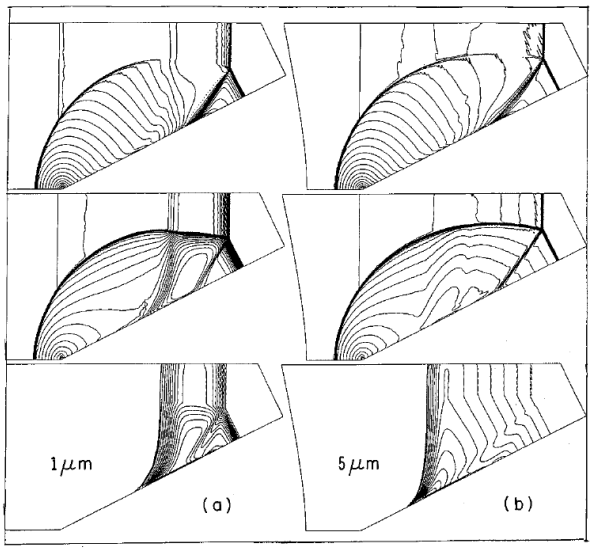

Ben-Dor et al. [106]

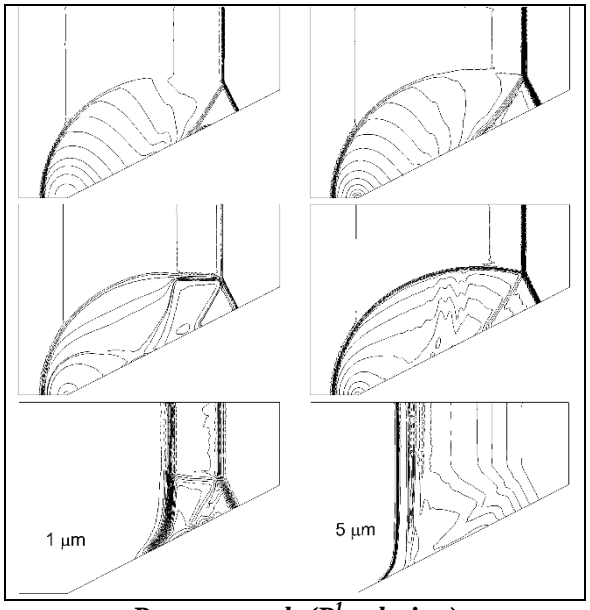

Present result (P^1 solution)

Fig. 32. Validation of pure gas case (Isopycnics for single Mach reflection: M_s=2.03 and θ_w=27°) and verification of dusty gas case (A-constant flow Mach number contours, B-constant gaseous phase density contours, and C-constant dust phase spatial density) [18]

The incident shock Mach number is set to 2.03, and the corner wedge angel is given by 27°. Numerical solutions, up to the third order of accuracy, were in good agreement with experimental data, as shown in Fig. 32. We confine our validation to a single-phase SMR case since no experimental data are available in the case of dusty gas flows. The comparison shows that the solutions up to third order accuracy (P2) are in good agreement with the experimental data. Also, we verified the dusty gas results with the solutions of [106] for two particle diameters (1 μm and 5μm) in the case of SMR. The comparison of Mach contours, as well as isopycnic surfaces of gas and dust densities, indicates a good agreement.

Furthermore, a very strong shock wave case studied by Woodward and Colella [192] was investigated. The problem, a strong Mach 10 shock impinging on a wall inclined at 30°, was known to lead to a complicated double Mach reflection (DMR). The initial conditions for both the single-phase and multiphase cases are summarized in Table 13.

Table 13.The initial condition for the double Mach reflection problem

Non-dimensional variable	Driver section	Driven section
Pressure	116.5	1.0
Gas density	8.0	1.4
Particle concentration	0.1	0.1
Gas velocity (*x*-direction)	8.25	0.0
Gas velocity (*y*-direction)	0.0	0.0
Dust velocity (*x* and *y* -directions)	0.0	0.0

In Fig. 33 (a), a study on grid independency was done for solutions with the second order of accuracy (P^1). A grid resolution with h=1/100 was found to provide almost identical results with h=1/120, and hence the grid with h=1/100 was used throughout. The density and Mach contours at non-dimensional time t=200, as shown in Fig. 33 (b) and (c), indicated that the present DG scheme successfully resolves all the important flow

features: slip lines, Mach stem, secondary Mach stem, reflected shock wave, and the formation of supersonic flow in the delta region. A weak jetting effect reported in Ben-Dor *et al.* [106] was also observed.

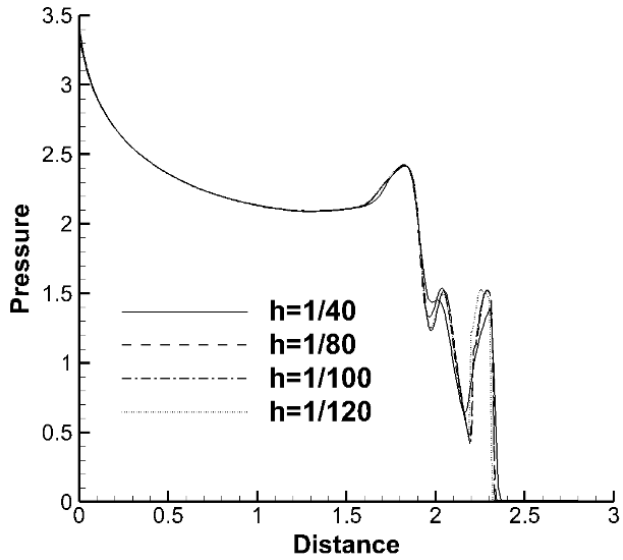

(a) Grid independency study: Pressure distribution along the reflecting wedge surface

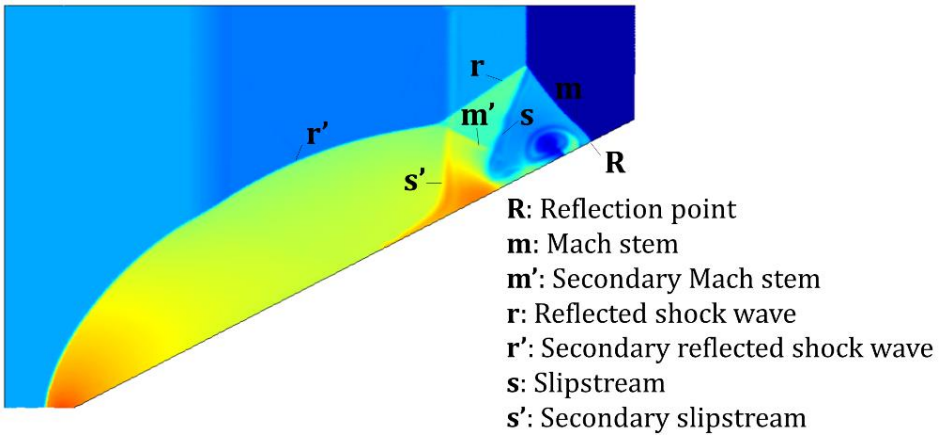

(b) Density contour

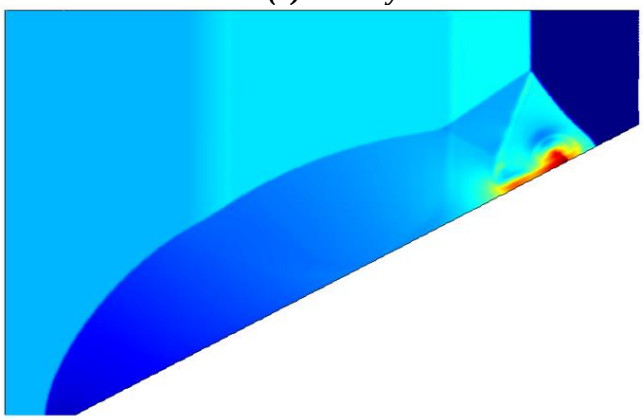

(c) Mach contour

Fig. 33. Verification study: Double Mach reflection (pure gas P^1 solution) [18]

The effects of polynomial order on numerical solutions were analyzed in Fig. 34. It can be seen that the first-order solution with h=1/100 cannot resolve the expected flow feature properly. However, higher order solutions can provide a satisfactory resolution to accurately explain the important physical features of the flow. It can also be seen that there is no drastic change in solutions when increasing the polynomial order from one (P1) to two (P2). It should be mentioned that the application of the positivity preserving scheme is necessary to prevent numerical instabilities in this high Mach number flow.

In order to understand the effects of dust particles on the time evolution of the flow, the single-phase and multiphase solutions (pure gas, dusty gas, and dust concentration) are summarized in Fig. 35 for two different time steps. One of the main features of the dusty gas flows is that the transition region in the shock waves is much thicker than that of the pure gas. In the multiphase flow, as the shock front is decelerated due to interaction with particles, a longer time is required for the shock front to reach the same location when there is no particle in the flow field. It is also evident that the presence of the particles can lead to attenuation of the incident shock wave. It should be mentioned that both the positivity and monotonicity preserving limiters were applied in the simulation of multiphase flows to prevent the numerical breakdown.

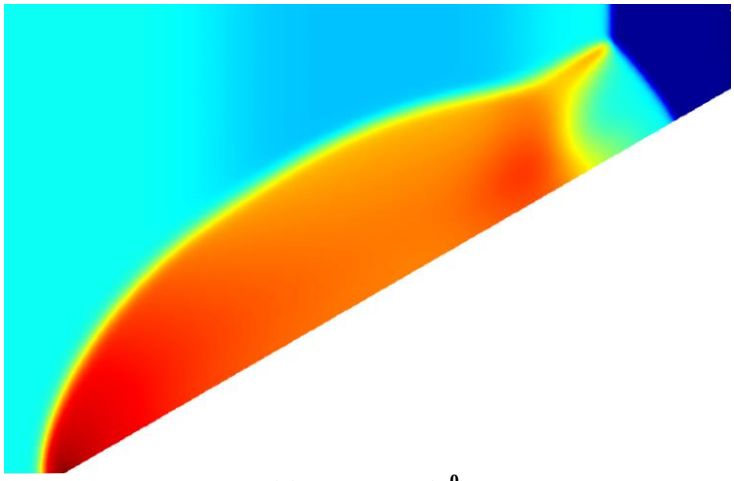

(a) Pure gas (P^0)

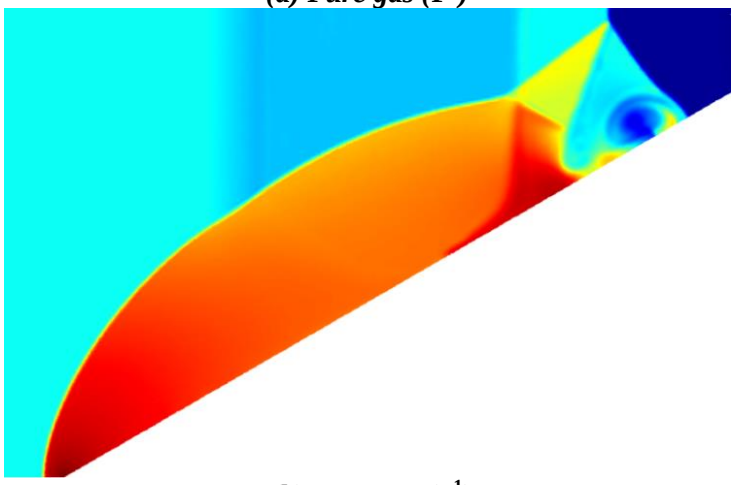

(b) Pure gas (P^1)

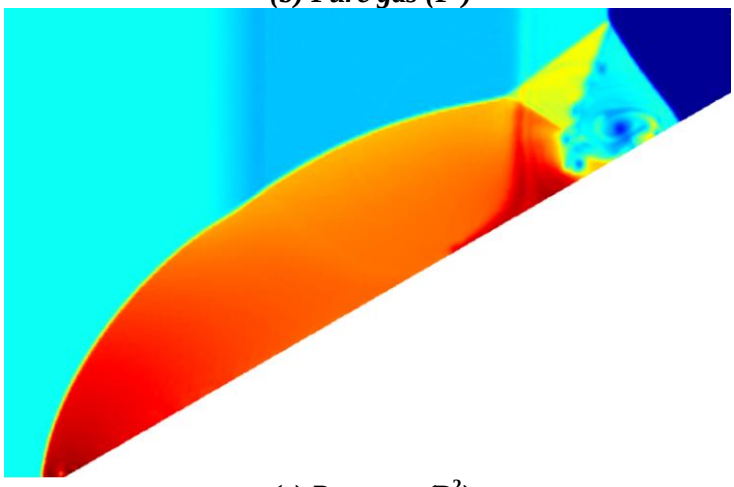

(c) Pure gas (P^2)

Fig. 34. Effects of polynomial orders on the density contours [18]

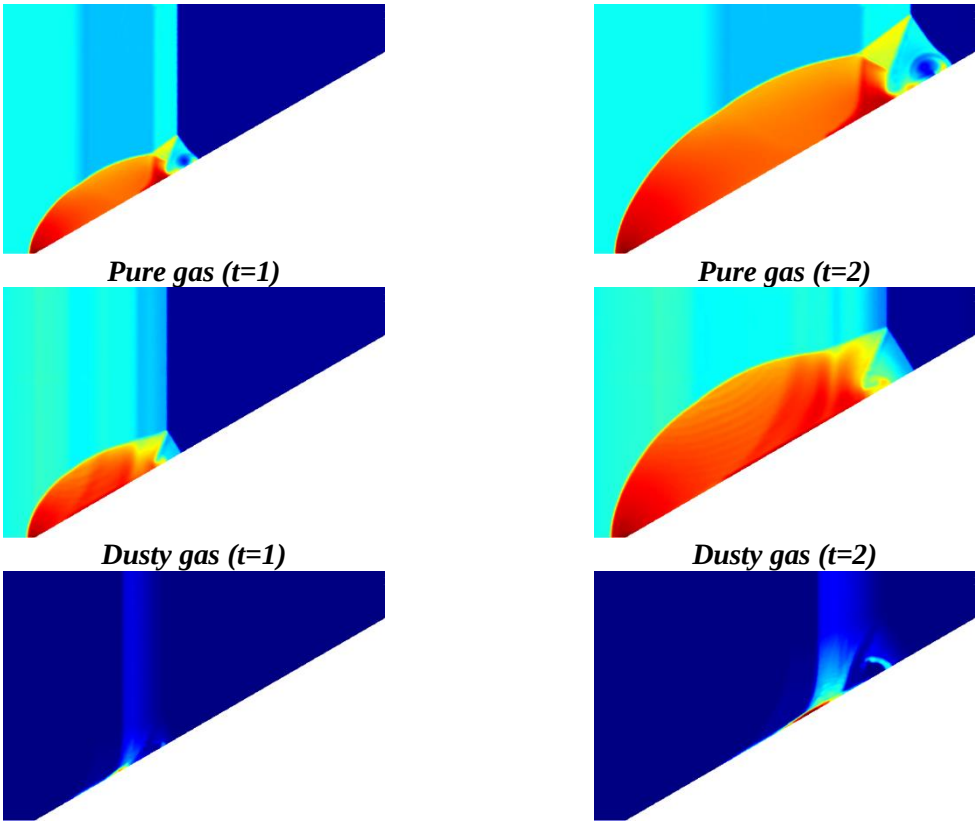

Fig. 35. Time evolution of density contours in the compression corner (double Mach reflection) problem (P^1 solution) [18]

The effects of dust particles on the structure of the DMR were also investigated, as summarized in Fig. 36. The convex shape of the Mach stem in the pure gas simulation is due to the front of the curled slipstream reaching the Mach stem [193]. The presence of particles, however, decelerates the velocity of the slipstream front and does not allow the slipstream to catch up with the Mach stem, as shown in Fig. 36 (b) of the multiphase case with a particulate loading β=0.1 and a particle diameter 10 μm. As a result, the Mach stem forms almost perpendicular to the reflecting wall surface in the dusty gas case. The secondary reflected shock wave and slipstream are severely distorted so that they are not identified. Moreover, the secondary triple point configuration, in which the secondary reflected shock wave, Mach stem, and slipstream coincide undergoes a significant change so that such a point is almost indistinguishable.

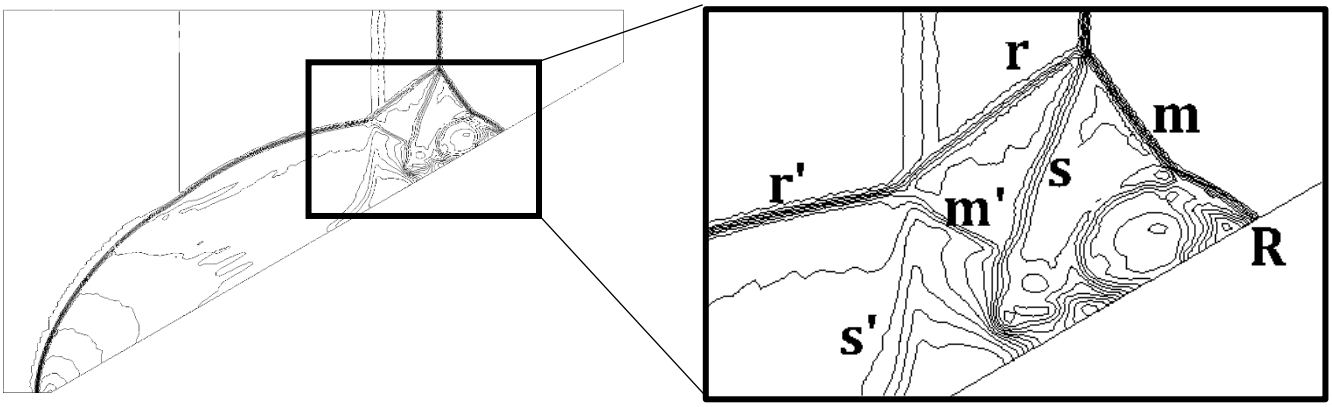

(a) Pure gas

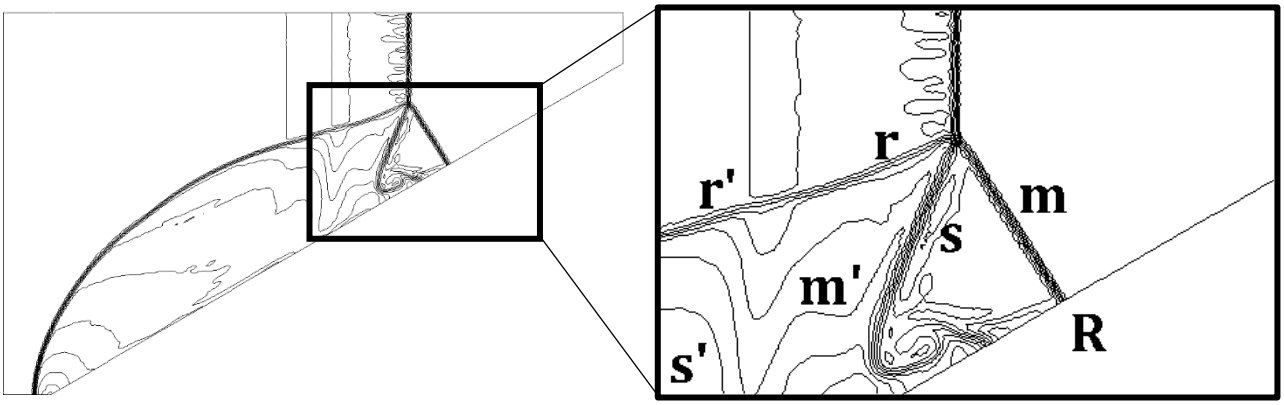

(b) Dusty gas: β=0.1, d=10.0 μm

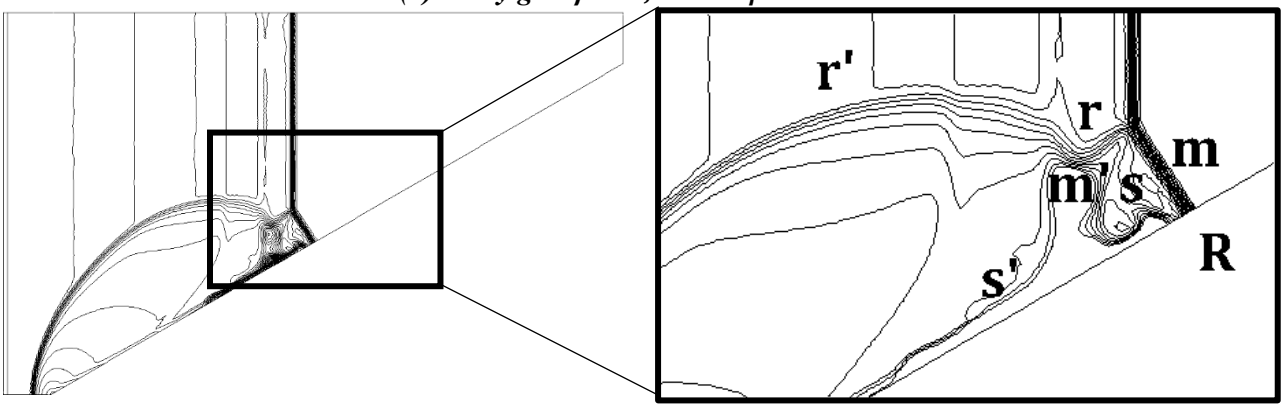

(c) Dusty gas: β=0.5, d=0.5 μm

Fig. 36. Change of the DMR structure in the presence of dust particles (P^1 solution) [18]

Another dusty gas case with a particulate loading β=0.5 and a particle diameter 0.5 μm were considered. Such a setting leads to a greater number of particles in the domain compared to the previous case. It can be seen in Fig. 36 (c) that, unlike the previous case in which only the secondary triple point is subject to major change, both the primary and

secondary triple points are affected by dust particles. Note also that the incident shock front is significantly decelerated in this case with high dust concentration.

Finally, a more detailed parametric study on the effects of particulate loading and particle diameter size was summarized in Fig. 37. Isopycnic surfaces, that is, surfaces with a constant density of gas phase in the dusty gas indicate that the particulate loading will substantially affect the configuration of the triple points. This change is more significant in the case of larger dust particles. Moreover, when the particulate loading increases, the incident shock front greatly decelerates, especially in the case of smaller dust particles. Furthermore, it can be seen that the height of the Mach stem shortens in dusty gas flows. Due to the increased momentum and thermal interactions, the height of the Mach stem shortens more in the case of a smaller dust particle. Also, it can be observed that the particle diameter affects the curvature and slope of the secondary and primary reflected shock waves. The larger the particle diameter is, the less is the curvature of the secondary reflected wave. Also, the primarily reflected shock gets more aligned with the secondary reflected shock as the diameter increases. In the case of large particles and high mass loadings, the reflected shocks are completely distorted. Furthermore, it can be seen that the slipstreams are affected by the increase of particulate loading. The slipstreams are found highly distorted in case of smaller particles. In summary, it can be inferred that the increase of particle diameter and mass loading would lead to blurrier flow patterns of reflected waves and slipstreams. The surfaces of the constant density of solid phase in the dusty gas, shown in Fig. 37 (b), imply that smaller particles can follow the gas phase closely, but larger particles cannot follow the gas phase so that the structure of isopycnic surfaces becomes drastically different from that of the corresponding gas.

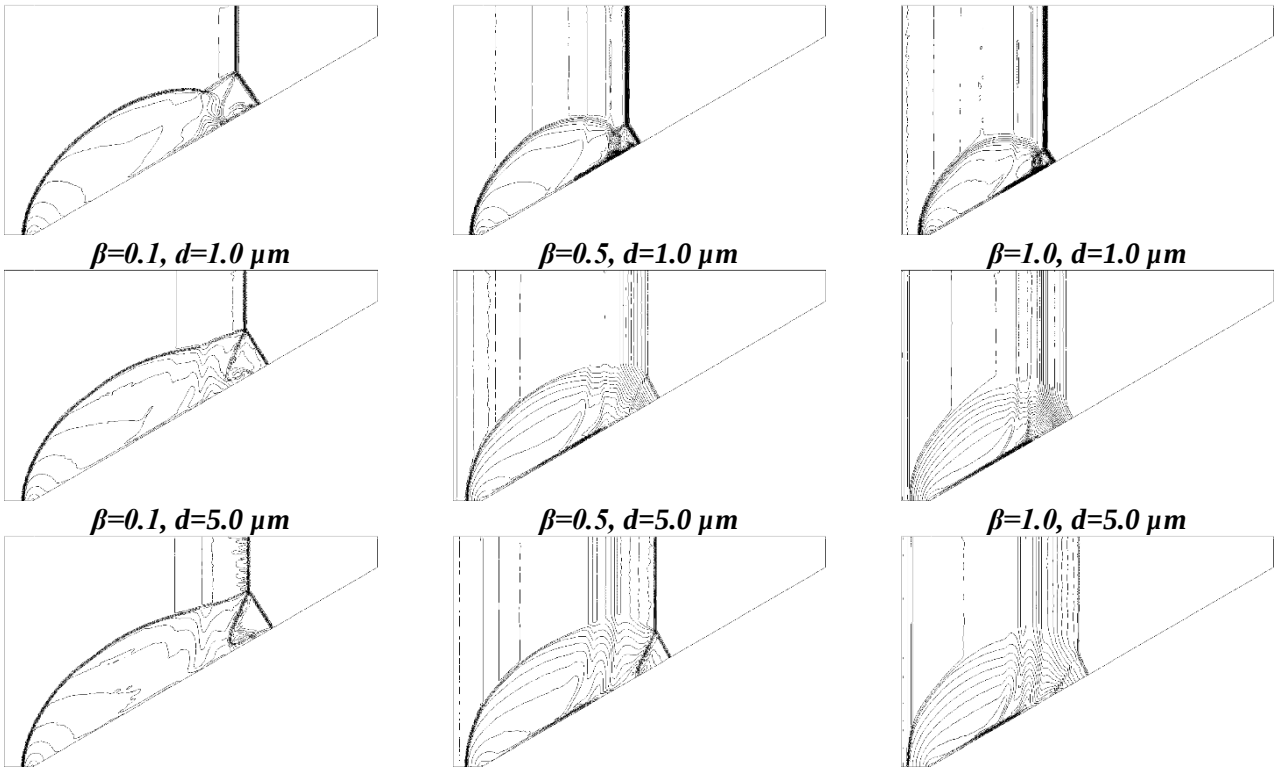

β=0.1, d=1.0 μm *β=0.5, d=1.0 μm* *β=1.0, d=1.0 μm*

β=0.1, d=5.0 μm *β=0.5, d=5.0 μm* *β=1.0, d=5.0 μm*

β=0.1, d=10.0 μm *β=0.5, d=10.0 μm* *β=1.0 , d=10.0 μm*

(a) Gas phase

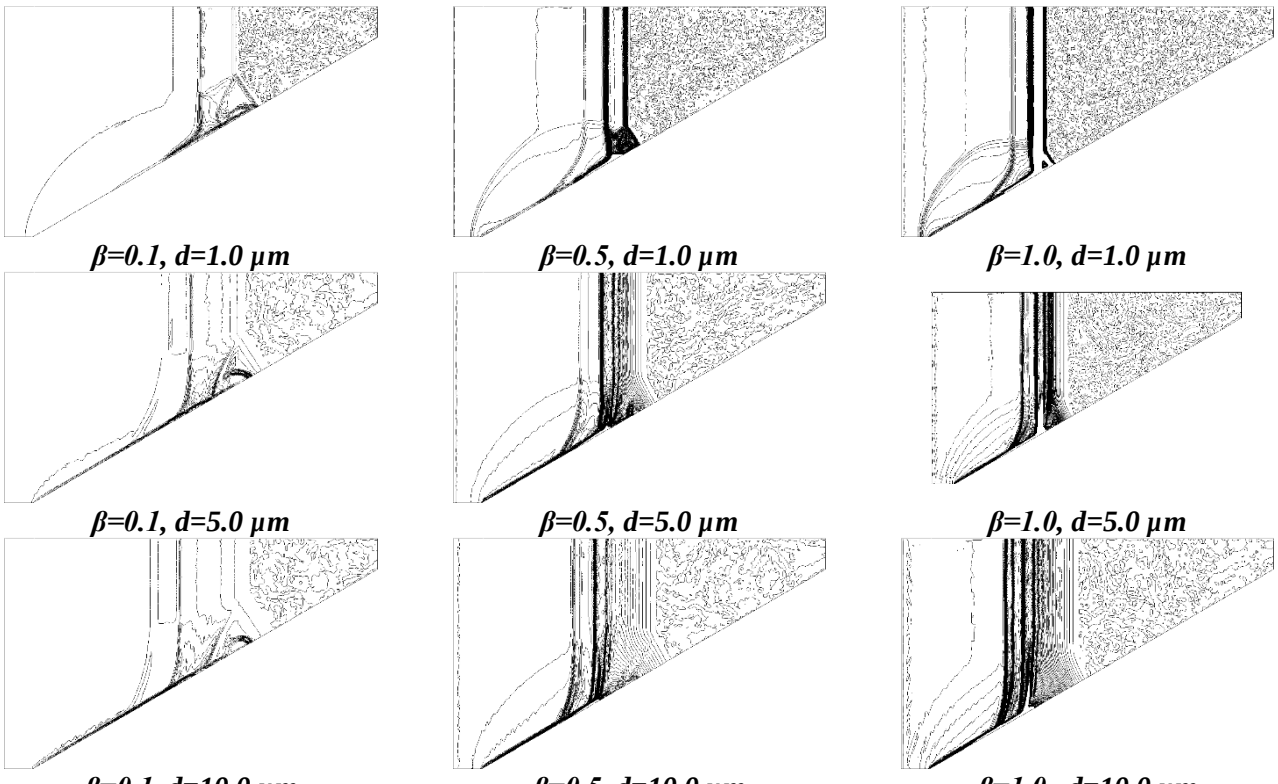

β=0.1, d=1.0 μm *β=0.5, d=1.0 μm* *β=1.0, d=1.0 μm*

β=0.1, d=5.0 μm *β=0.5, d=5.0 μm* *β=1.0, d=5.0 μm*

β=0.1, d=10.0 μm *β=0.5, d=10.0 μm* *β=1.0 , d=10.0 μm*

(b) Solid phase

Fig. 37. Parametric study on particulate loading and particle diameter in the double Mach reflection problem (P^1 solution) [18]

5.2.3 The pattern of waves in shock-vortex interaction in Schardin's problem

As an extension study on two-dimensional dusty gas flows, and as it was shown in the previous section, one can investigate the influence of particle grains on complicated wave patterns after the passage of shock incident from the wedge tip under the certain condition which leads to the occurrence of two counter-rotating vortices. Shardin's problem is an important benchmark problem for studying shock-vortex interaction. In this work, we consider the dusty gas Shardin's problem for studying the shock-vortex interaction in a dusty medium. To this end, a modal discontinuous Galerkin method is developed for solving the two-fluid model of the dusty gases. The simulation results reveal that some dynamics of the shock-vortex interaction in a dusty medium is different from that of the pure gas counterpart.

5.2.3.1 **Verification of single-phase solver over time evolution**

The interaction of shock and vortex–two fundamental fluid mechanics phenomena–has been a topic of interest for decades. The interaction is important due to various technological and environmental applications. Some of the well-known applications include noise generation in supersonic jets, shock-enhanced mixing (especially in non-premixed supersonic combustion), strake-wing configurations, and compressors operating near their stability limits [194-198].

Fig. 38 depicts the schematic of the various types of discontinuities and other compressible flow features that are observed in the Shardin's problem. As the result of the impingement and subsequent reflection and deflection of the planar shock on the wedge, structures such as Mach stem, slip lines, Mach triple points, vortices and vortexlets would emerge. In the following subsections, after validating the developed

solver, we will investigate the effects of the presence of dust particles on the behavior of these structures.

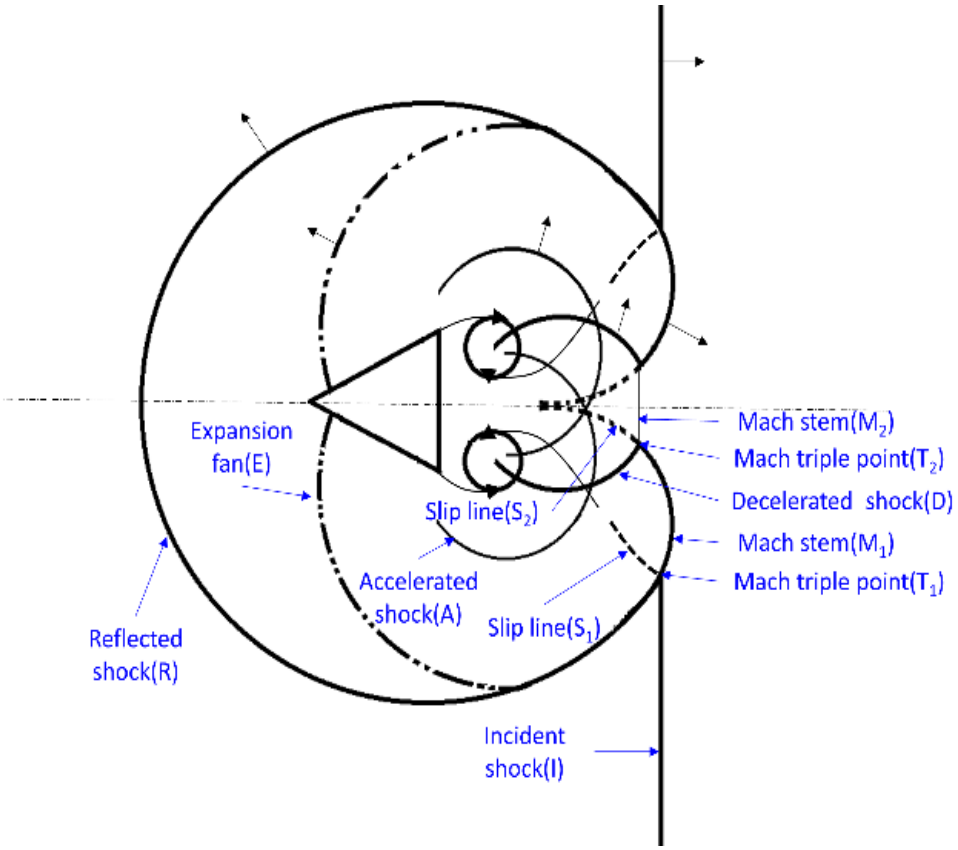

Fig. 38 Schematic of the compressible flow features observed in Shardin's problem

The developed solver has been extensively verified and validated in various problems for both pure gas and dusty gas models in [18, 199]. In Fig. 39, and Fig. 40 the numerical Schlieren photos of the pure gas model are compared with the experimental results of [200] for different time steps. The basic flow structures including the two splits shock after impingement on the vortex (one in and the other against the direction of vortex circulation) and the V-shaped decelerated deflected shock are well captured in the numerical solutions.

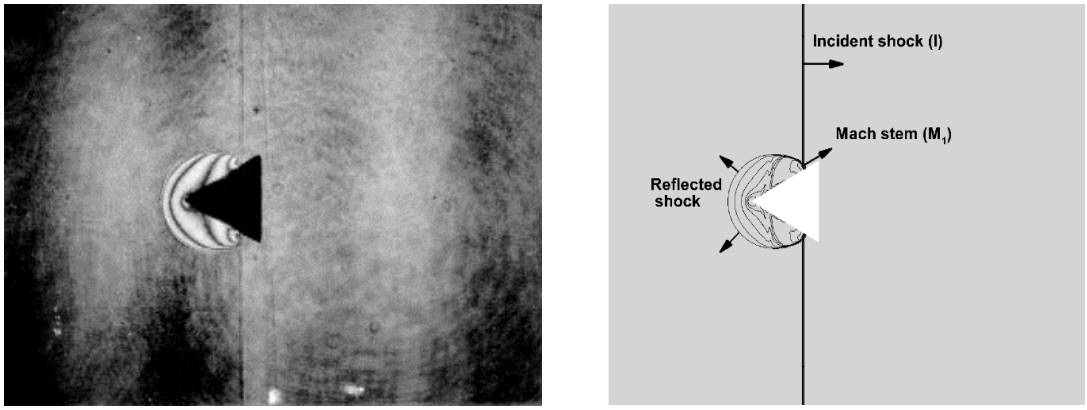

a) $t = 28\mu s$

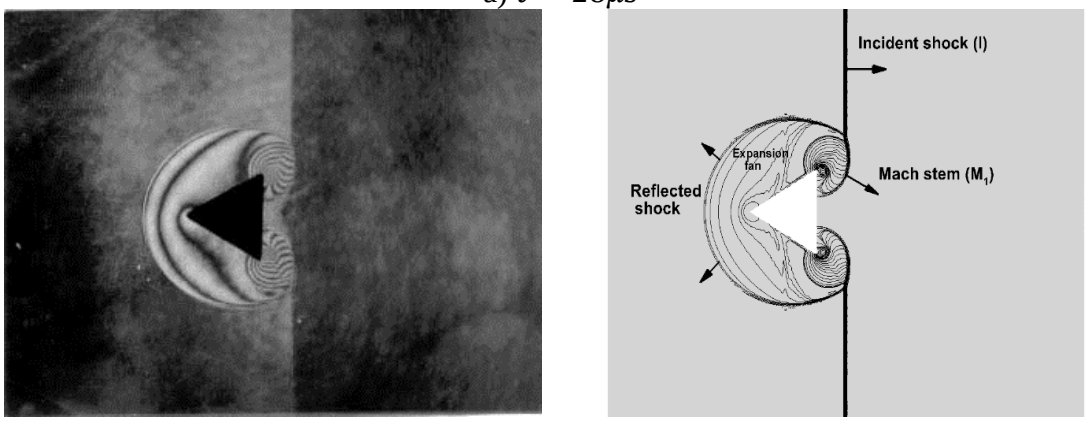

b) $t = 53\mu s$

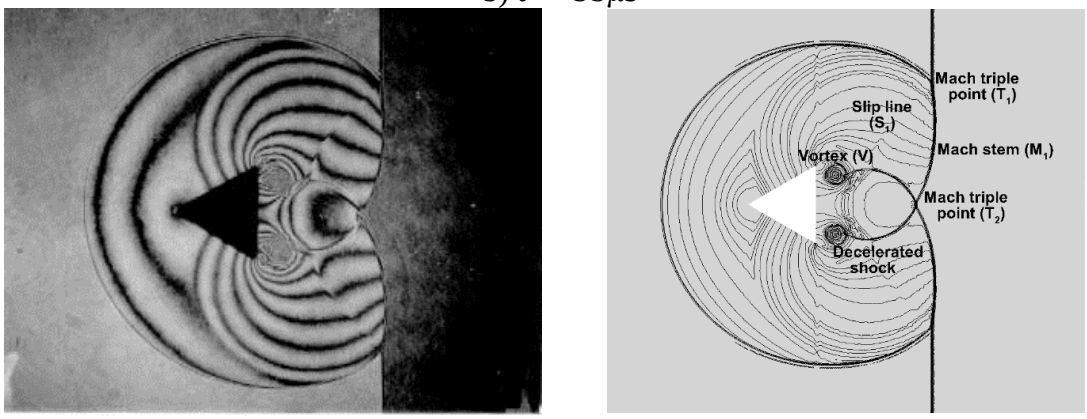

c) $t = 102\mu s$

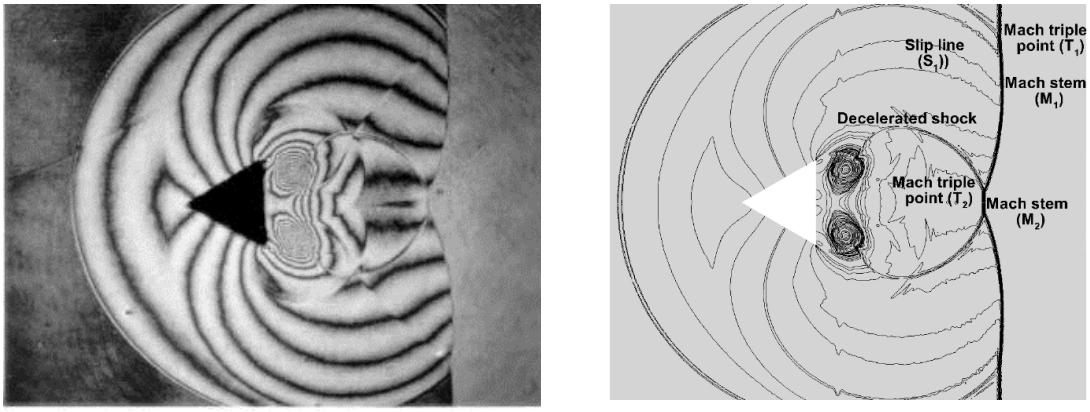

d) $t = 130\mu s$

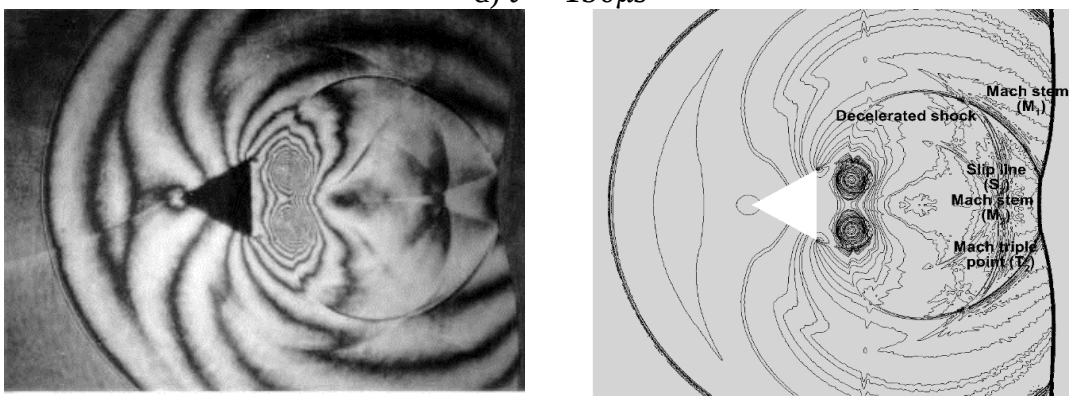

f) $t = 172\mu s$

Fig. 39 Density contours: Left) experimental data adopted from [200] right) present numerical simulation. Time evolution of incident shock impinges to the prism

More precise wave patterns are depicted in Fig. 41 right after the prisom. The only feature which is not resolved in the numerical solutions is the vortexlets string emerging in the slip layer of the main vortex due to Kelvin–Helmholtz instability. This feature may be captured if a much finer grid or higher order polynomials are applied as it is shown in Fig. 42 where superfine grid is employed. However, as the main purpose of the current work is to investigate the effects of the presence of dust particles, the investigation of such details is deferred to future works.

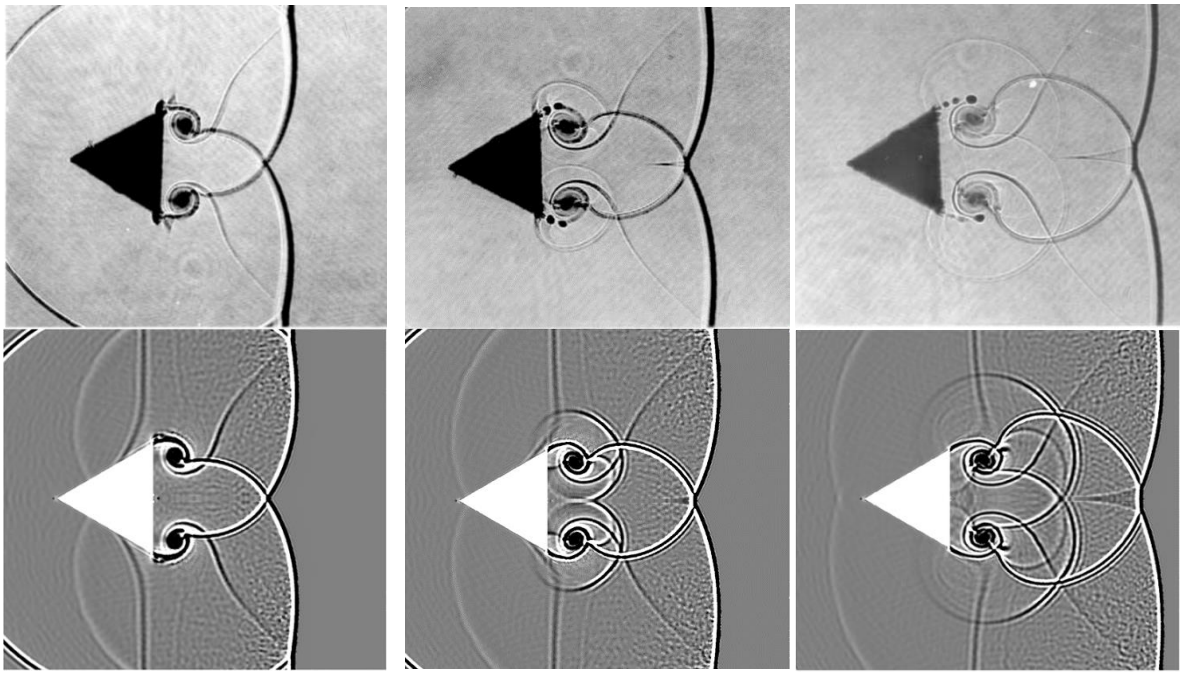

t=91 μs *t=108 μs* *t=128 μs*

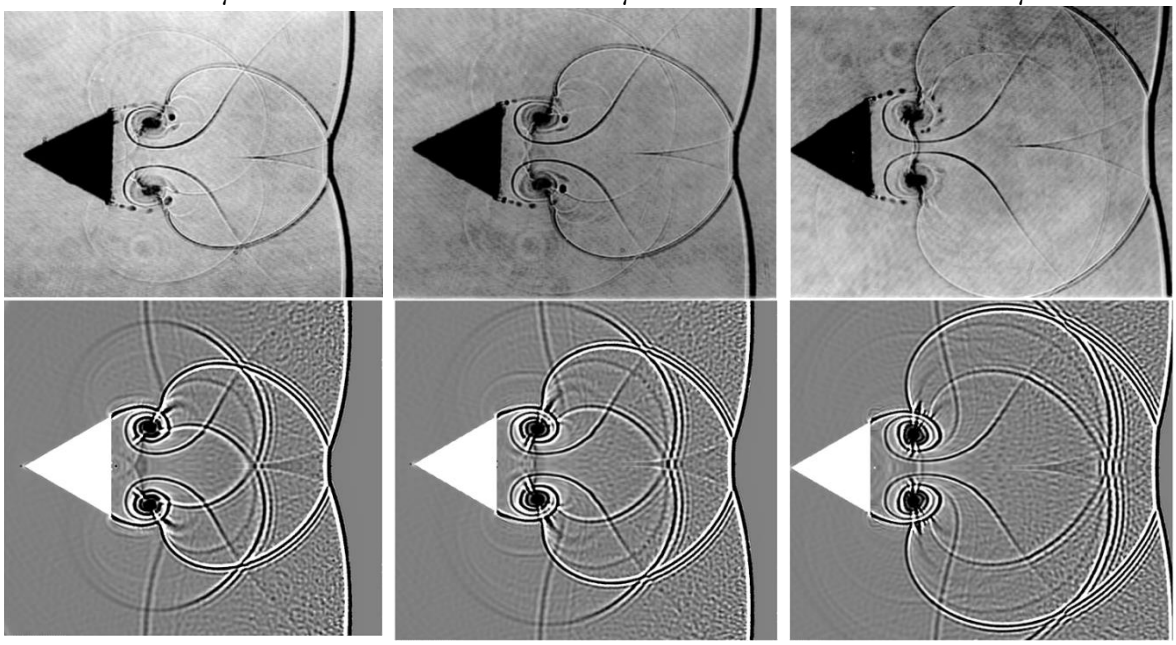

t=138 μs *t=151 μs* *t=178 μs*

Fig. 40 Comparison of the numerical Schlieren photos (bottom) with experimental results of [200] (top)

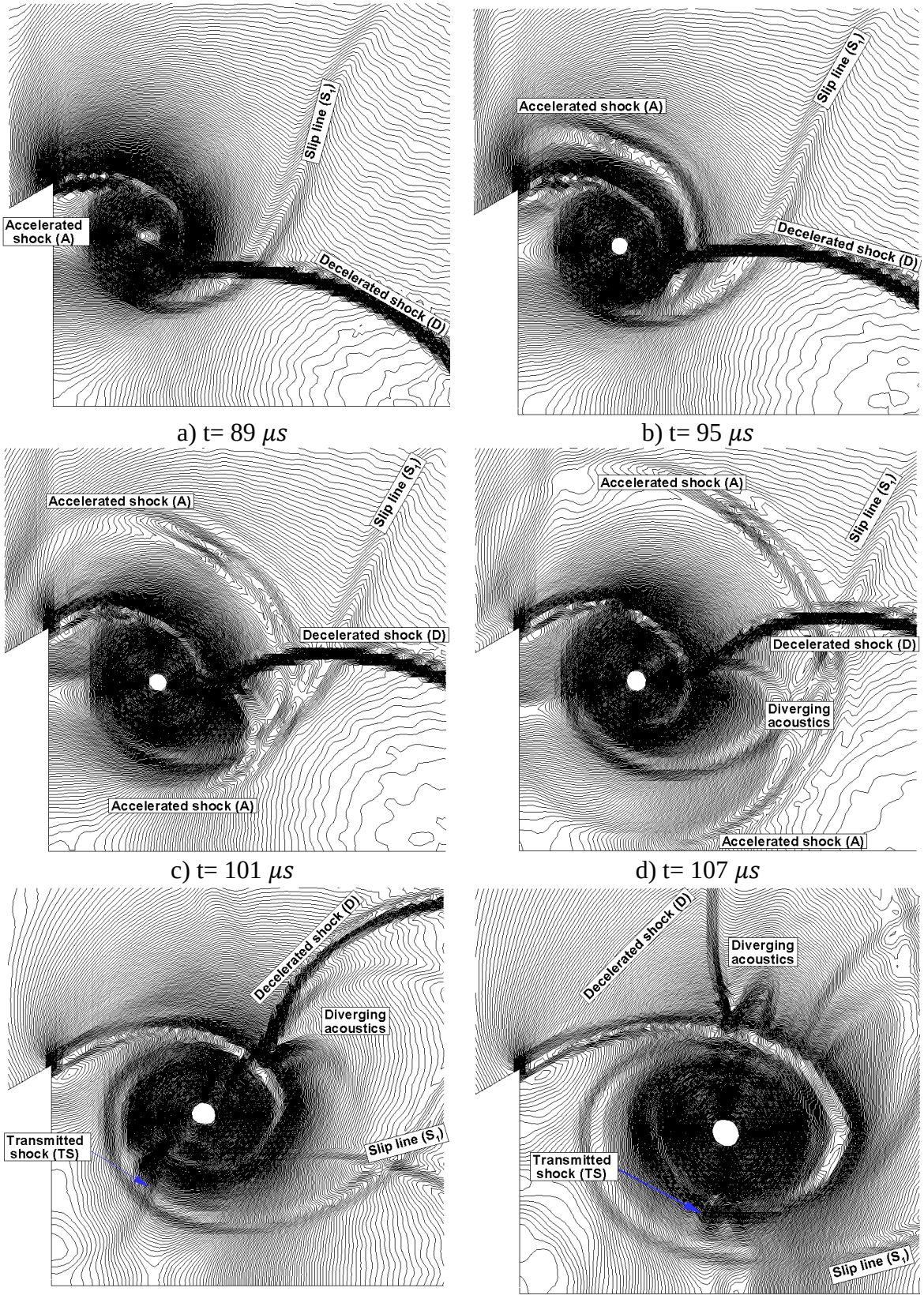

a) t= 89 μs b) t= 95 μs

c) t= 101 μs d) t= 107 μs

e) t= 130 μs f) t= 172 μs

Fig. 41 Time evolution numerical simulation for shock-vortex interaction

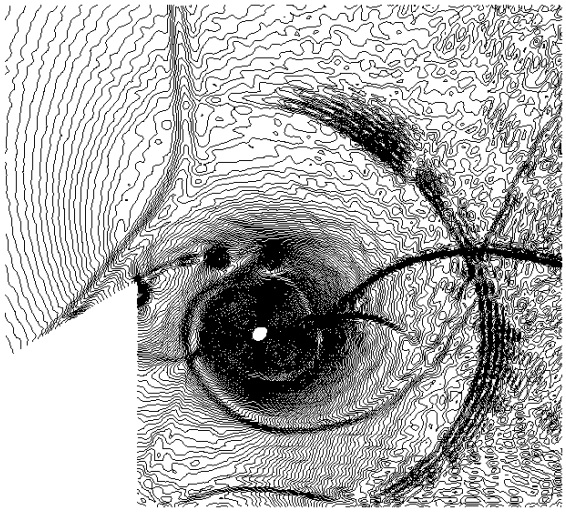

Fig. 42 Capturing vortexlets by using superfine grid

5.2.3.2 **Schardin's problem in the presence of particle-laden flow**

The importance and complexity of the problem have motivated various experimental and numerical works. When shocks and vortices form in a dusty environment, the dust-gas interaction can significantly affect the dynamics of the flow. However, the interaction of shocks and vortices in a dusty environment has rarely been investigated in the past. In this work, the so-called Shardin's problem in the presence of dust particles (which hereafter will be referred to as the dusty gas Shardin's problem) is considered with a focus on the effect of particulate phase on the shock-vortex interaction.

It is well-known that particles inside a vortex will follow a pattern from the vortex core and concentrate on the edges of the vortex. Moreover, in dusty gas flows, presence of relaxation regions and complex mechanisms of wave patterns including pseudo-compound wave (a reflected shock attached to the rarefaction wave) as well as composite wave (a contact discontinuity attached to the relaxation zone) can be observed. In the Shardin's problem, a traveling shock wave passes by a compression corner forming different types of Mach reflections depending upon the shock Mach number and wall inclination angle. When the shock front passes the wedge, two counter-rotating vortexes will be created behind the triangular prism and will interact with the shock wave.

Different scenarios for defining the dusty gas Shardin's problem can be considered. The dust can be initialized uniformly in both side of the diaphragm, or it can be present only on the right-hand side of the membrane. It is also possible that the domain is initialized with dust just after the compression corner where the vortex starts to form. The initialization may affect the evolution of flow structures. In this work, however, we select the case where the whole domain is initialized with uniform distribution of dust grains.

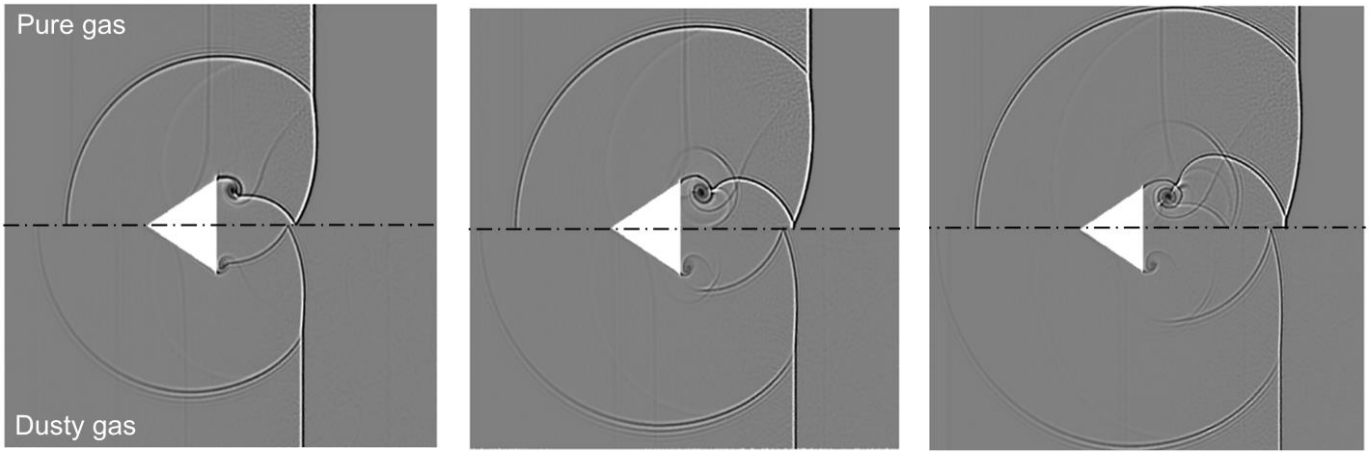

t=89 μs *t=107 μs* *t=130 μs*

Fig. 43 Time evolution of numerical shadowgraphs; pure gas (top half) compared with dusty gas (bottom half) (d=10 μm, β=10)

Fig. 43 demonstrates the effects of the presence of particles on the flow. In the test case, glass beads with a diameter of 10 μm and a density of 2,500 kg/m^3 are distributed uniformly in the whole domain. The particulate loading (β) is set equal to 10. It can be seen that all the basic structures observed in the pure gas case are also present in the dusty gas case; however, all the discontinuities are either decelerated or accelerated when dust particles are added. More specifically, the left running discontinuities, i.e., reflected shock wave and rarefaction waves are accelerated, and all the other right-running discontinuities including slip lines, incident, and accelerated shocks are decelerated compared with the case of pure gas. Some discrepancies between the case of pure gas and dusty gas in the vicinity of the vortex become obvious as the particles are transferred from the vortex core towards the vortex edges.

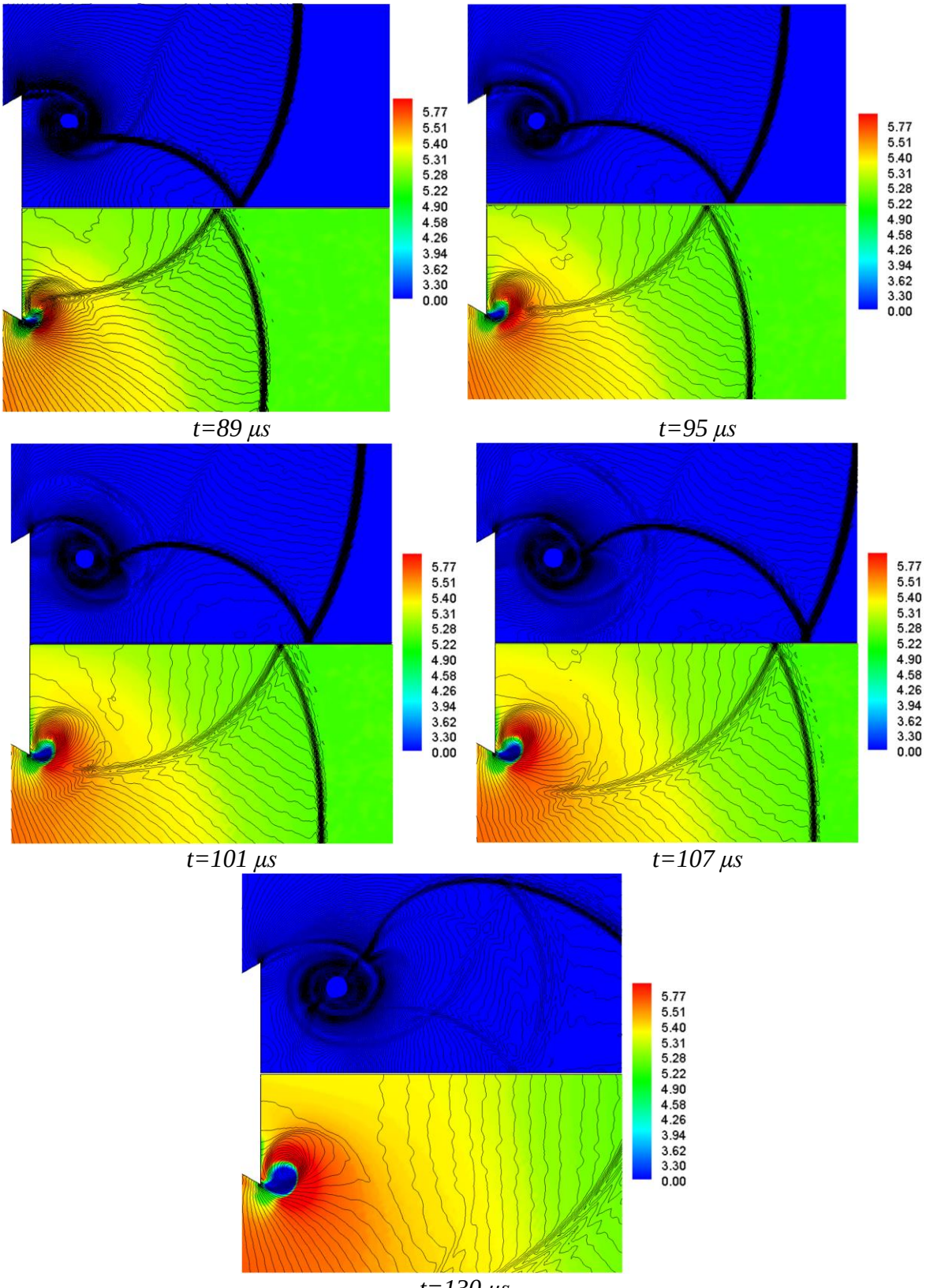

Fig. 44 Comparison of gas density contour lines overlaid on dust phase contours for pure gas (top half) and dusty gas (bottom half)

Accumulation of dust particles and the formation of a particle-free region in the center of the vortex over time evolution are demonstrated in Fig. 44. It can be seen that the dust particles are converted towards the edges of the vortex and form a low-density region in the core of the vortex. The accumulation of the particles diminishes the slip layer and slip line. Moreover, it can be observed that the waves not only are decelerated but also attenuated.

Chapter 6. Numerical experiments on viscous flows including conservation law equations along with first-order constitutive relations

In this chapter, simulation results for a few problems where the first-order Boltzmann-based constitutive relations (NSF) govern the flow are presented. In the investigated problems, the viscous effects find importance and application of zeroth-order Boltzmann-based constitutive relations (Euler) is not sufficient for prediction of this category of problems.

6.1 Axisymmetric under-expanded jet flow

Supersonic jets issuing from underexpanded nozzles are observed in various practical engineering applications ranging from plumes of aircraft and rockets to supersonic combustors. On the other hand, this type of flows is a suitable benchmark problem for studying the complex wave patterns due to the interaction of shock waves with particles [18]. An essential parameter pertinent to the problem of the underexpanded jet is the prediction of the location of the Mach disk. From a physics point of view, understanding this feature is key in the fundamentals of gas dynamics. Moreover, this property is essential in predicting the structure of the plume of the nozzle (an important system design requirement). Therefore, such studies can be crucial in various engineering applications based on the concept of jet under-expansion. Examples include jet propulsions, natural gas pipeline blowdowns, and radio jets. This parameter has long been investigated experimentally [201-206] and numerically [207-210]. A comprehensive review regarding the Mach disk position, diameter, and apparition of free underexpanded jets in the quiescent medium can be found in the paper by Franquet *et al.* [211]. The

schematic of the problem defined as a supersonic jet expanding from a high-pressure chamber into a low-pressure ambient is illustrated in Fig. 45.

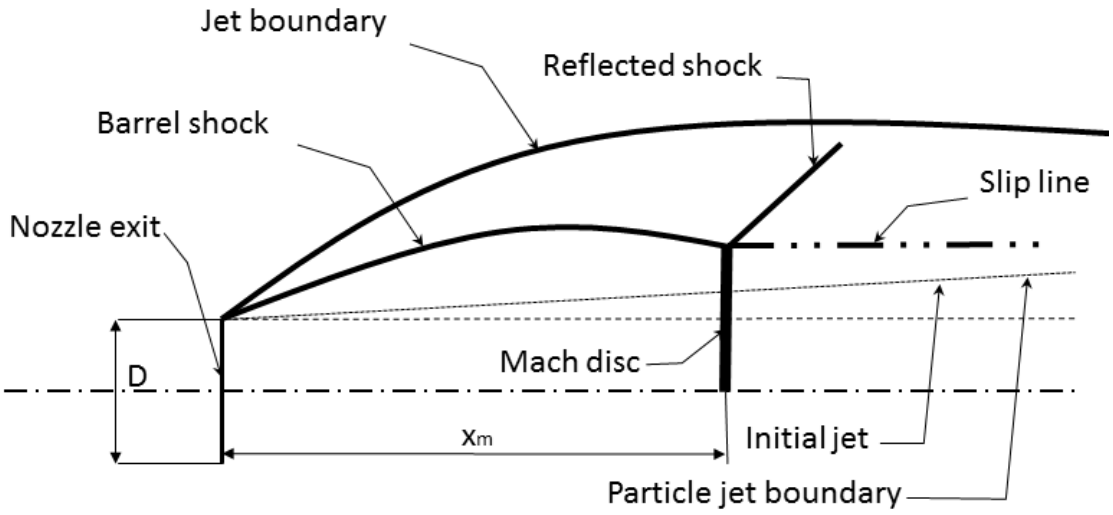

Fig. 45 Schematic of the under-expanded jet of particle-laden gas (computational domain size: 5D×10D)

In some applications such as in solid propellant rocket boosters, injection of powder fuel into the combustion chamber or volcanic eruptions, the presence of particles can subsequently change the dynamics of the flow. Even though the gas-only flow of the underexpanded jets has been studied from different perspectives in an abundant number of works, the particle-laden underexpanded jets are addressed only in a limited number of researches. Sommerfeld [212] studied the effect of particle diameter and ambient pressure on the structure of the underexpanded jets with the use of a discrete particle methods and a piecewise linear method. In another work, Sommerfeld [213] applied Lagrangian formulation on structured grids to investigate supersonic two-phase gas-particle flows. Hayashi *et al.* [214] applied a Eulerian formulation to investigate the dynamics between a gas phase and a solid phase in terms of the size and loading ratio of solid particles. Ishii *et al.* [115] comprehensively investigated the underexpanded supersonic free-jet flows and supersonic flows around a truncated cylinder of gas-particle mixtures using a Eulerian-Lagrangian framework. In the numerical dusty gas flows studies mentioned

above, a downstream movement of the Mach disk location was predicted which is in contradiction with the early experimental results of [201, 215] and more recent experiment of [117]. In the latter, a combined experimental and numerical study was conducted by which a correlation for the inlet velocity of the gas phase was established. The current work aims to expand upon the counter-intuitive trend (downstream vs. upstream movement of the Mach disk) by using a high-order accurate numerical approach, i.e., discontinuous Galerkin method. Previous studies only considered the effect of variation of particles diameter on the behavior of the underexpanded jets. However, the parameter that explains the interaction of the dust and gas phase is the Stokes number. We hypothesize that besides particle diameter all the other parameters present in the Stokes number relation, including dust particle microscopic density, gas viscosity and reference values of velocity and characteristic length would affect the movement of the Mach stem. To the best knowledge of the authors, this is the first time that details of such phenomena are being investigated. Here, after verification and validation of the numerical method and demonstration of the counter-intuitive behavior for different particle diameters, we analyze the role of the Stokes number independently for various particulate loadings.

Before numerical investigations, the validity of numerical solutions is examined. The numerical tool has been extensively validated for the inviscid gas flows in [18]. For the purpose of validation of the viscous solver in the problem of underexpanded jet, the location of Mach disk in the absence of particles (in a pure gas) for different pressure ratios (p_0/p_∞) is first studied for validation of the pure gas solver. This parameter has been experimentally studied by various researchers in the past [117, 202, 203, 216]. Recently, Franquet *et al.* [211] presented an extensive review of experimental works dealing with free under-expanded jets. The comparison of the Mach disk location with

experimental results is shown in Fig. 46. Generally, the results are in good agreement with experimental data of Avduevskii *et al.* [203] for mid-range pressure ratios. In the case of pressure ratios of 2 and 100, our predictions are more close to the experimental results of Lewis and Carlson [216].

It can be seen that when first-order polynomials (P^0) are applied to the location of the Mach disk is slightly underestimated compared to the second order solution (P^1).

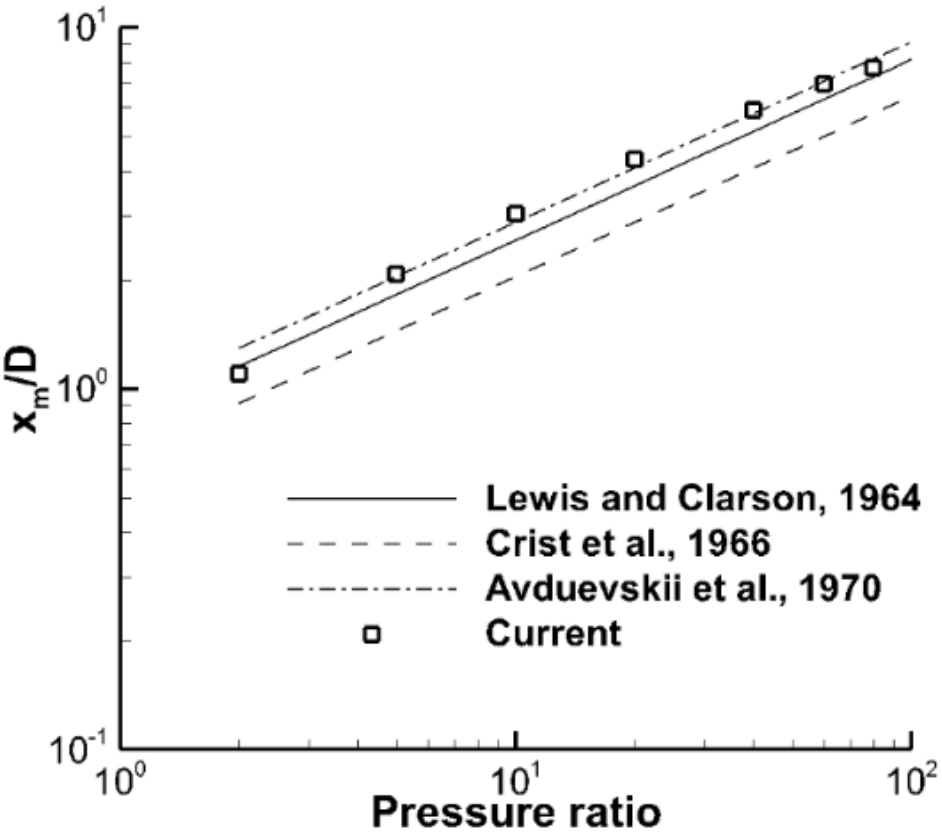

Fig. 46 Comparison of prediction of Mach-disc location depending on the pressure ratio for the pure gas flow with previous experimental results

In Fig. 47, a comparison of the Mach contour with schlieren image of an experimental test case reported in [117] where $\frac{p_0}{p_\infty} = 29.8$ is provided, which demonstrates a good qualitative agreement in terms of prediction of the geometrical shape of the jet with experimental results. Moreover, a qualitative validation for the case of dusty gas can be

found in [18]. Further, for all the simulations, the second order (P^1) polynomials were applied.

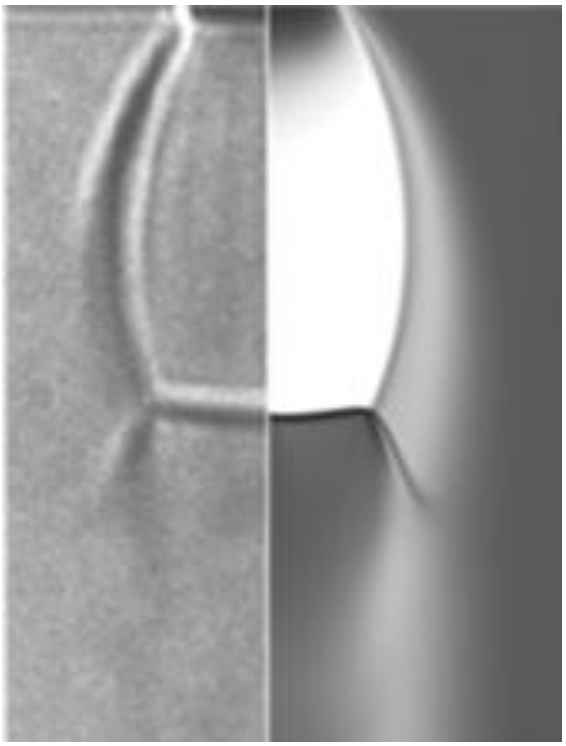

Fig. 47 Comparison of the Mach contour with schlieren image of an experimental test case reported in [117] where p_0/p_∞=29.8

6.2 Axisymmetric particle-laden under-expanded jet

One of the few experimental studies on the interaction of particles with shock waves is the case of under-expanded supersonic jets of gas and particle. In this subsection, we investigate the problem of supersonic jets of particle-laden gas [117]. In order to implement the axisymmetric formulation in the present computational framework, the source terms in the system of governing equations should be modified. The axisymmetric equations can be easily derived by following previous studies [85, 115, 117]. The problem is defined as a supersonic jet which is expanded from a high-pressure chamber into a low-pressure chamber, as illustrated in Fig. 45.

A comparison of dusty gas solutions with experiments of Sommerfeld [117] is shown in Fig. 48. Here, particle properties are set equal to the values of diameter 45 μm and

mass density 2500 kg/m^3. In this problem, one of the critical flow features is the upstream movement of Mach disk as a consequence of the interaction of gas phase with particles. As reported in [117], when the particle loading increases, the Mach disk gets closer to the nozzle exit and the wave patterns observed in the downstream of the Mach disk becomes more pronounced. The phenomena of movement of Mach disk has also been reported in [201] and [215]. As can be seen in Fig. 48 (b), even though an exact match with experimental results are not achieved, a close agreement in the qualitative trend of upstream movement of the Mach disk is found. There were, nonetheless, some differences between the numerical solutions and the experimental shadowgraphs; for example, the curvature of the Mach disk and the width of the jet boundary. While experiments show that the Mach disk tends to straighten as the particle loading increases, the numerical simulation cannot predict this feature. Also, the width of the jet boundary is over-predicted in the numerical solutions compared to experimental results. Such deviations may arise from the difference in considering the effect of a nozzle. In the present investigation, for the sake of simplicity, the computationthe is set up to simulate expansion of a circular jet from a hole into ambient condition without considering a nozzle. Apparently, further in-depth investigation will be necessary for capturing all the detailed features observed in experiments.

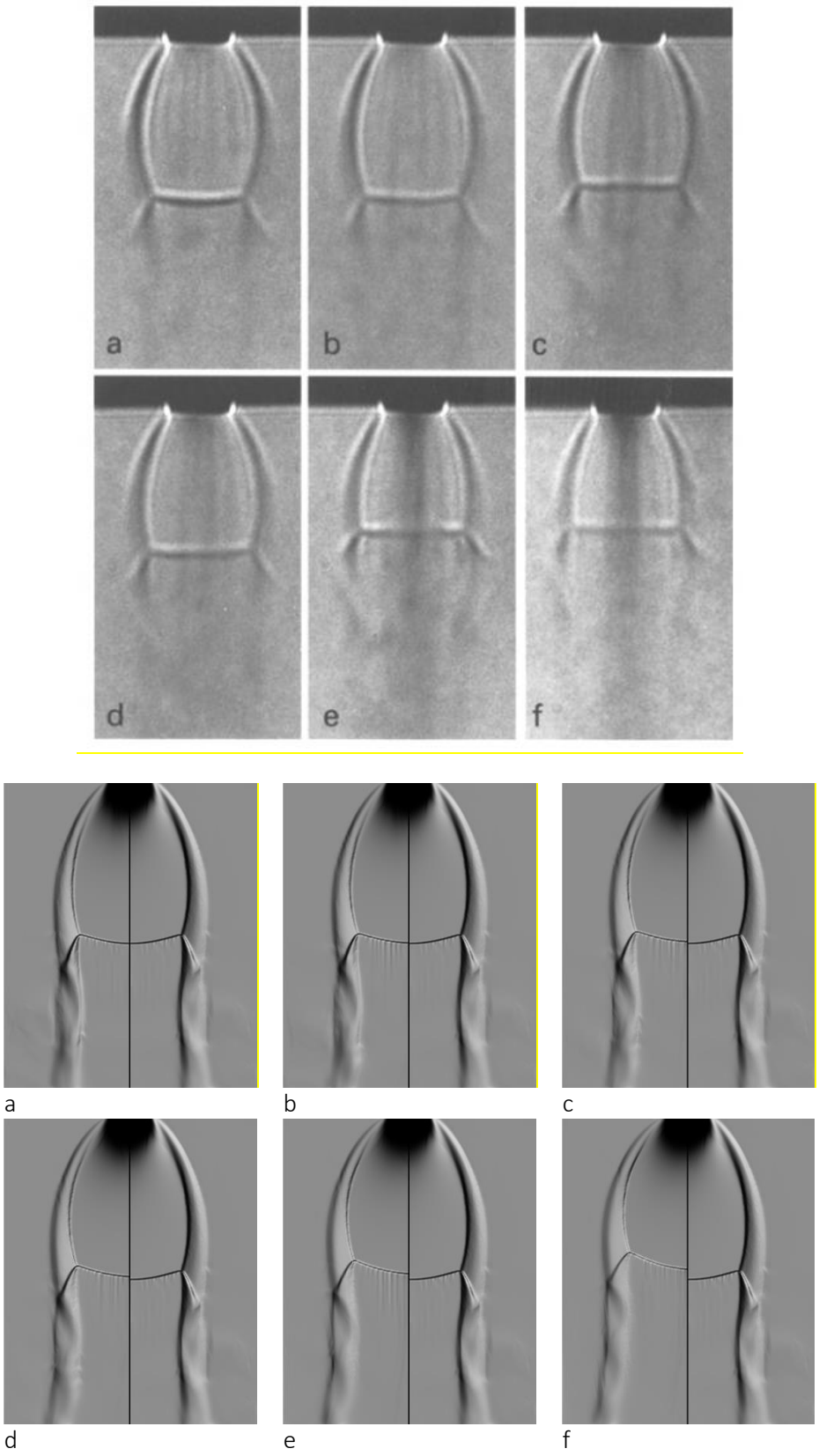

Fig. 48 Shadowgraphs of the under-expanded gas-particle [117] (top) and density contours of pure gas solution (right) with dusty gas (left) jet for different particle loadings (bottom): a) β= 0.0; b) β= 0.11 ; c) β= 0.24; d) β= 0.35; e) β= 0.64; f) β= 1.07 (P_0 = 0.31MPa, P_0/P_∞ = 29.8, d = 45μm) (P^1 solution)

The crucial parameter in fluid-particle flows to characterize the response rate of the particles to changes in fluid motion or to evaluate the kinetic equilibrium of the particles with the carrier gas is the Stokes number, defined as

$$St = \frac{\tau_V}{t_{ref}} \tag{119}$$

Here t_{ref} is a reference time defined as characteristic length (often nozzle diameter in the literature) divided by the characteristic speed and, τ_V is the momentum (velocity) response time of the particles given by

$$\tau_V = \frac{\rho_s d^2}{18\mu_g} \tag{120}$$

$St \ll 1$ implies that the response time of the particles is much less than the characteristic time of the flow. In this case, the particles have enough time to equilibrate with the carrier phase leading to nearly equal velocities. These types of flow can be accurately simulated with a one-way coupled model. On the other extreme, when $St \gg 1$, the response time of the particles is much more than that of the carrier phase. Consequently, particle velocity is little affected by the fluid velocity change. A two-way coupling algorithm should thus take into account the back-influence of the particle phase on the carrier fluid.

6.2.1 The counter-intuitive trend in the movement of the Mach disk

While all the previous experimental results indicate an upstream movement of the Mach disk, in some of the numerical reports, the trend contradicts the experiments. This counter-intuitive behavior is observed for small-diameter particles. Here, the effect of particle diameter on the movement of the Mach disk is studied for two different particle diameters, i.e., $d = 1 \ \mu m$ and $d = 100 \ \mu m$. Glass beads with the macroscopic density of 2500 *kg/m*^{3} are simulated. The characteristic length (in the Stokes relation) is

set equal to 0.01 and air with the viscosity of 1.65×10^{-5} $\mathrm{P}a.s$ at 273.15 *K* is selected as the carrier phase. The corresponding Stokes numbers are 0.27 and 2776 for 1- and 100-micron particles, respectively. As shown in Fig. 49 for smaller particles the Mach disk shows a downstream movement while for larger particles the movement of the Mach disk is upstream-wise compared to the pure gas case. It is interesting to note that the experimental results of [117] indicate an upstream motion for particles with a diameter of 45 μm.

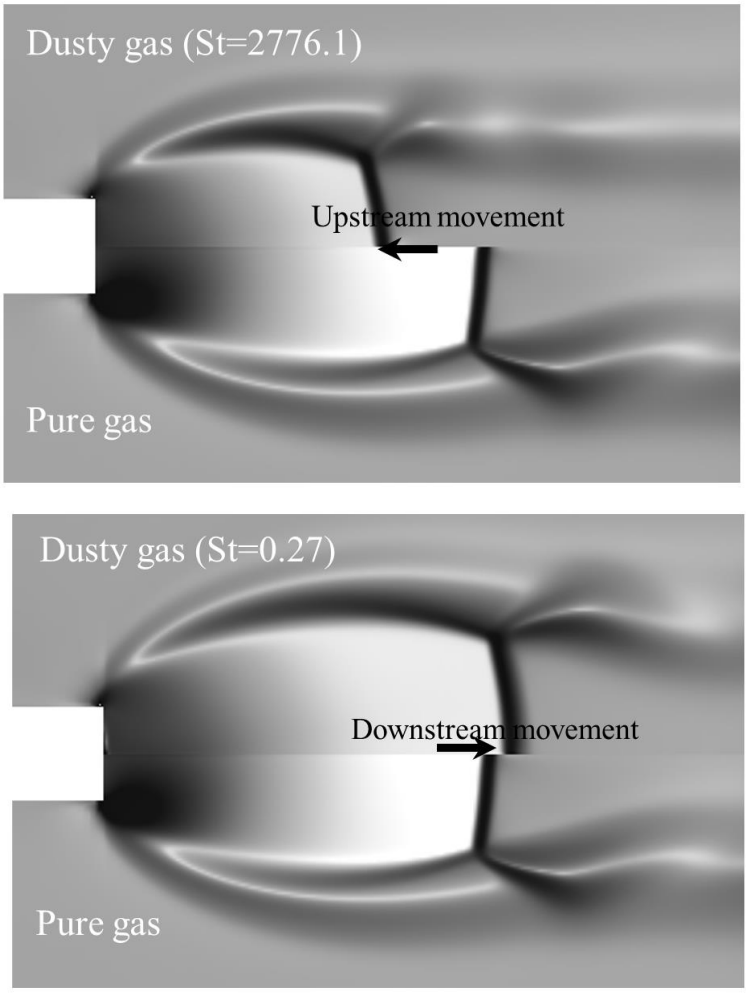

Fig. 49 Effects of addition of dust particles with different diameters on Mach disk location

6.2.2 Effects of Stokes number with a characteristic length

According to equation (119) and (120), the Stokes number can be assigned by variation of different parameters including particle diameter, the density of the particle phase, the viscosity of the carrier phase or characteristic time of the flow. Here Stokes number is artificially assigned by multiplying a constant coefficient to the source terms so that only coupling effects are investigated. It has been demonstrated through experiments of Sommerfeld [117] that the Mach disk location moves towards the jet exit plane by the increase of the particulate loadings. However, in Fig. 49 a counter-intuitive behavior is observed in case of low Stokes number flows. Fig. 50 demonstrates more detailed analysis of the role of Stokes and particulate loading (β, defined as the mass of particles per unit volume of the carrier phase) on the location of the Mach disk. Here the Mach contours of the dusty gas flow are compared with the pure gas case. The Mach disk displacement trend changes from an upstream movement to a downstream movement when the Stokes number decreases. This transition can be observed around the Stokes number of 1. It should be noted that the particulate loading has an effective role in the Stokes number at which this transition occurs. The higher the particulate loading, the more is the Mach disk displacement (either upstream or downstream). In the case of $\beta = 1.07$, upstream to downstream transition is observed even for higher Stokes number ($St = 2.77$). For all the simulated test cases in Fig. 50, the streamlines of the particles overlaid on density contours of the dust phase are plotted in Fig. 51. As it can be seen from the figure, the streamlines depict an identical qualitative trend for similar Stokes number. In low Stokes number flows, dust particles can follow the gas streamlines closely; However, in higher Stokes number flows, the dust particles show a more independent movement, as shown in Fig. 51. This figure can partially justify the counter-intuitive Mach disk location displacement. For the case of $St = 2776.1$ and $\beta = 1.07$, as

the particles do not follow the gas phase streamline closely, a high concentration region near the jet exit can be observed. Therefore, there is a noticeable change of local particulate loading in the radial direction, leading to the formation of curved Mach disk as evident in Fig. 50.

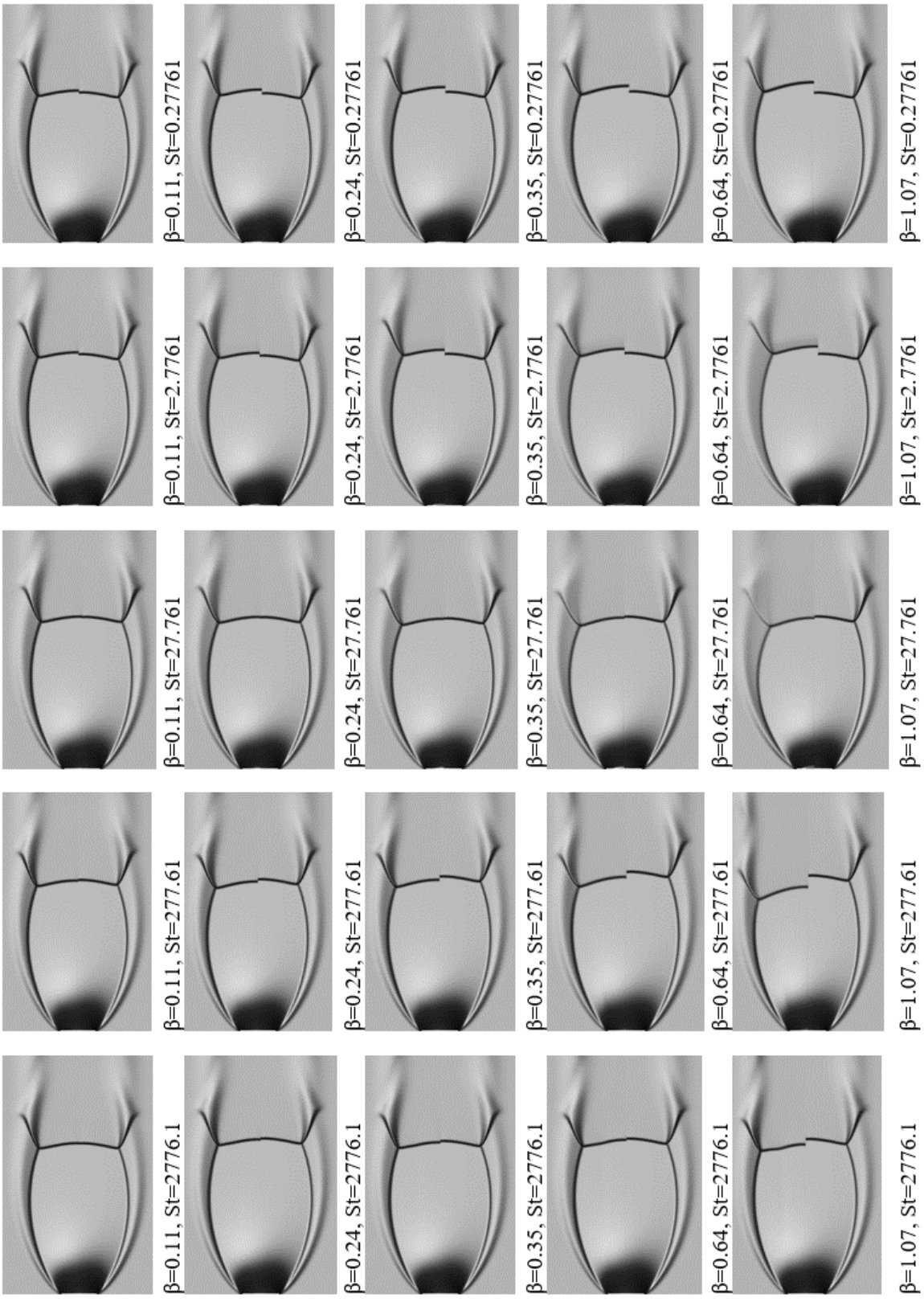

Fig. 50 Effect of variation of particulate loading and Stokes number on Mach contours in the under-expanded jet problem(p_0/p_∞=29.8)

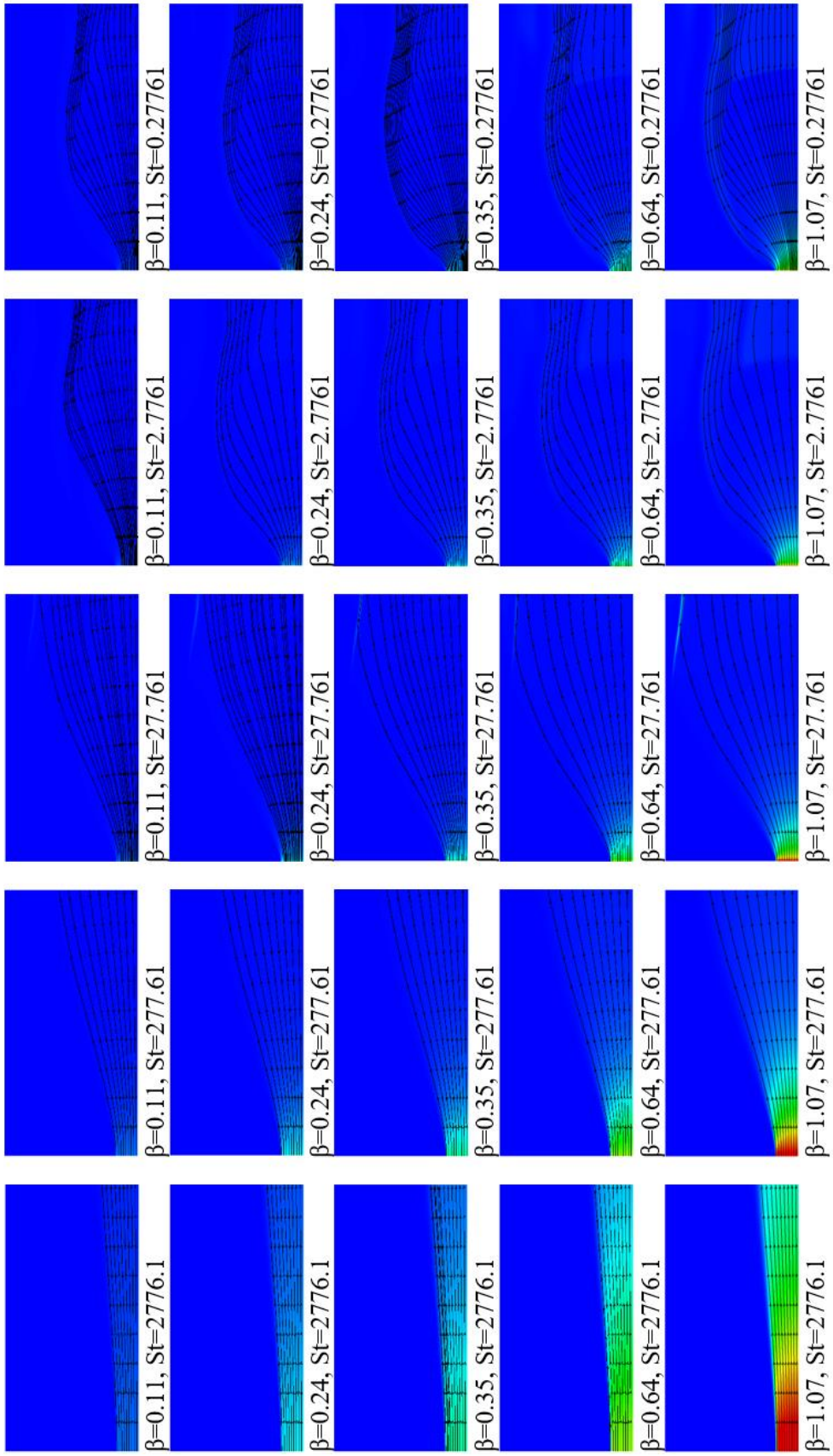

Fig. 51 Effect of variation of particulate loading and Stokes number on density contours and particles streamlines the under-expanded jet problem(p_0/p_∞=29.8)

6.2.3 Non-equilibrium effects at the exit plane

Even though numerical results confirm the downstream movement of the Mach disk, there is no experimental result which confirms this trend. Sommerfeld [117] showed that the numerical solution gives a 25% over-prediction in particle velocity compared to the experimental measurements. This is partly due to consideration of rarefaction and compressibility effects in drag correlations. On the other hand, Sommerfeld [117] suggested that a reduced gas velocity equal to the equilibrium sound speed of the gas-particle mixture should be assigned at the inlet to make the simulation results closer to the experiments. Presence of dust particles decelerate the gas front, delay the gas phase expansion leading to lower exit jet velocities. While this is the actual condition in a dusty gas underexpanded jet, in our calculations we assumed that the gas obtains sonic speed at the exit. Therefore, the influence of particles inside the nozzle (before the jet exit plane) is neglected. According to [117], the ratio of the equilibrium sound speed of the gas-particle mixture to the sound speed of the pure gas is given by

$$\frac{u^*}{a^*} = \sqrt{\frac{\gamma_e}{\gamma}\frac{1}{1+\beta}} \tag{121}$$

where u^* and a^* are the velocity and speed of sound at the exit plane. γ_e is the specific heat ratio of the gas-particle mixture equivalent gas. A series of simulation has been conducted in order to evaluate the level of the agreement of each approach with experimental results. The results are summarized in Table 14. As can be observed in the table, 10 to 50% over-prediction (with a direct relationship to particulate loading) is observed. However, when the equivalent mixture speed is applied at the exit plane, the maximum deviation of the results compared to experiments is 14% for the case of $\beta = 1.08$. In Fig. 52, the Mach contours of dusty gas flow are compared with the pure gas contours. Here the equivalent mixture speed is assigned on the exit plane. As

demonstrated in the figure, even when small particle diameters are added to the flow, the Mach disk movement is only towards upstream.

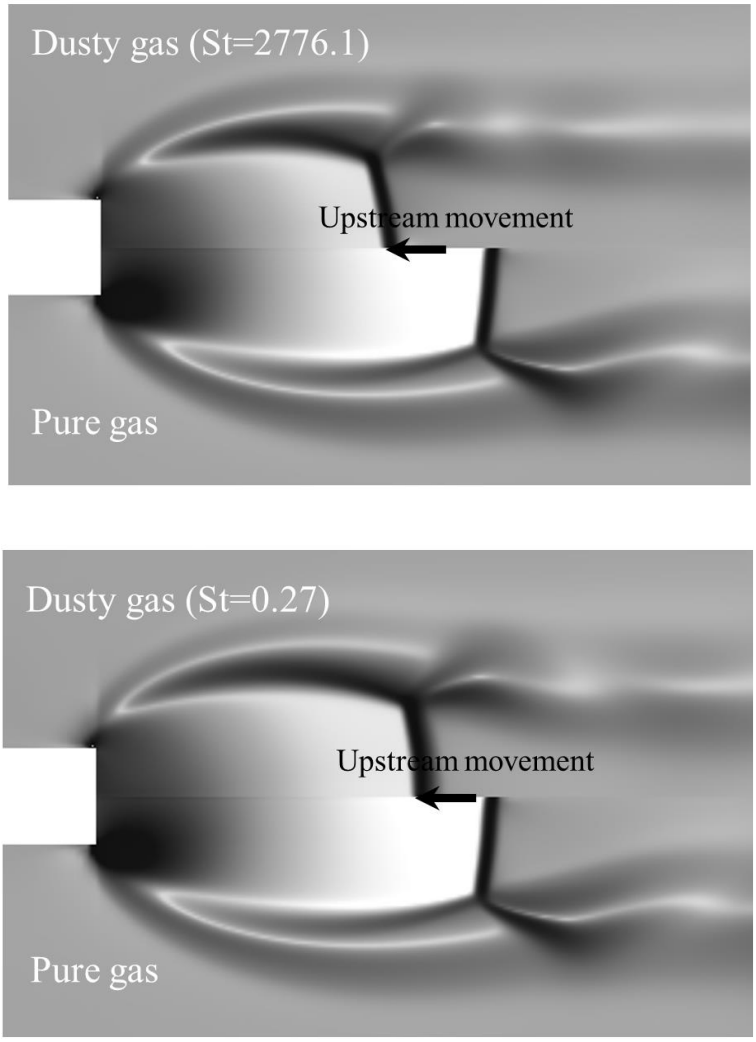

Fig. 52 Effects of addition of dust particles with different diameters on Mach disk location

Table 14 Comparison of the Mach disk location prediction with experimental results ($d = 26\mu m, St = 187.9$)

β / X_m/D	**Experimental**	**Numerical (Sonic speed at exit plane)**	**Numerical (Equivalent speed at exit plane)**
0.0	3.8	3.73	3.73
0.26	3.54	3.845	3.45
0.38	3.15	3.815	3.33
0.66	2.8	3.755	3.094
1.08	2.5	3.695	2.85

Chapter 7. A numerical experiment on near-field plume-surface interaction and regolith erosion in the descending phase of the lunar landing

7.1 Survey on the Lunar landing problem

Moon has a tremendously different environment compared to that of the earth. The extremely weak gravity on the Moon cannot hold an atmosphere. Therefore, only the heavy gas particles that rarely collide with one another would form an exosphere (100 molecules per cubic centimeter compared to 100 billion molecules per cubic centimeter on Earth's atmosphere at sea level). In such a rarefied atmosphere where the Sunlight would not be blocked, and heat cannot be trapped, temperature variations are also significant (i.e., 123 Celsius in the daytime and -233 Celsius at night). As explained before, during the final stages of a *soft landing* on the Moon, when the Lunar Lander approaches the dusty surface of the Moon, the interaction of engine plume and Lunar regolith cause a surface erosion and consequently dispersion of particles into the flow-field. This interaction would lead to some severe consequences, including the pilot's vision reduction, damage to the descent module or previously established sites on the Moon, false instrument readings, to name a few. Apart from the rarefied condition and presence of dust particles there exists a number of other complexities (e.g., mixed subsonic-supersonic regimes, shock-expansion interaction, shear layers) which make the simulation of descent phase an exciting subject from CFD point of view. In this section, we first introduce the prevailing physics observed in a Lunar landing problem, then our methodology for the simulation will be outlined, and finally, some simulation results will be presented.

7.2 Prevailing physics

In Fig. 53 the schematic of the problem (descent phase of Lunar Lander) is illustrated. To explain the physical phenomena that govern the flow, some of the regions of the domain with essential features are marked by numbers on the figure. Region 1 shows the formation of the expansion fan at the lip of the nozzle. Region 2 marks the continuum flow exhausting from the descent engine characterized by high Mach and low Knudsen numbers. Number 3 defines the surface through which continuum assumption breaks down. Due to the presence of a surface opposing the exiting jet, a strong stand-off bowl-shaped shock (number 4) forms and gradually weakens by deviation from the axis. The location of this shock wave will largely depend upon the external ambient pressure or exit to ambient pressure ratio. Right after the normal shock and exactly underneath the nozzle, the flow re-compresses to a near-continuum condition in the stagnation region marked by number 5. The virtual diverging channel formed by the stand-off shock and the Lunar surface expands the flow in the radial direction. The flow after reaching to the sonic speed at the sonic line (number 6) gains supersonic speeds and expands further into the near vacuum condition. In a region in the proximity of the sonic line, a supersonic boundary layer forms causing dynamic pressure, which is the source of viscous erosion to maximize. Hence peak of the mass flux of the eroded particles can be observed at somewhere near this point. The entrained particles then gain supersonic velocities and can travel significant distances away from the landing site as negligible drag force of rarefied atmosphere cannot impede the debris particles seriously.

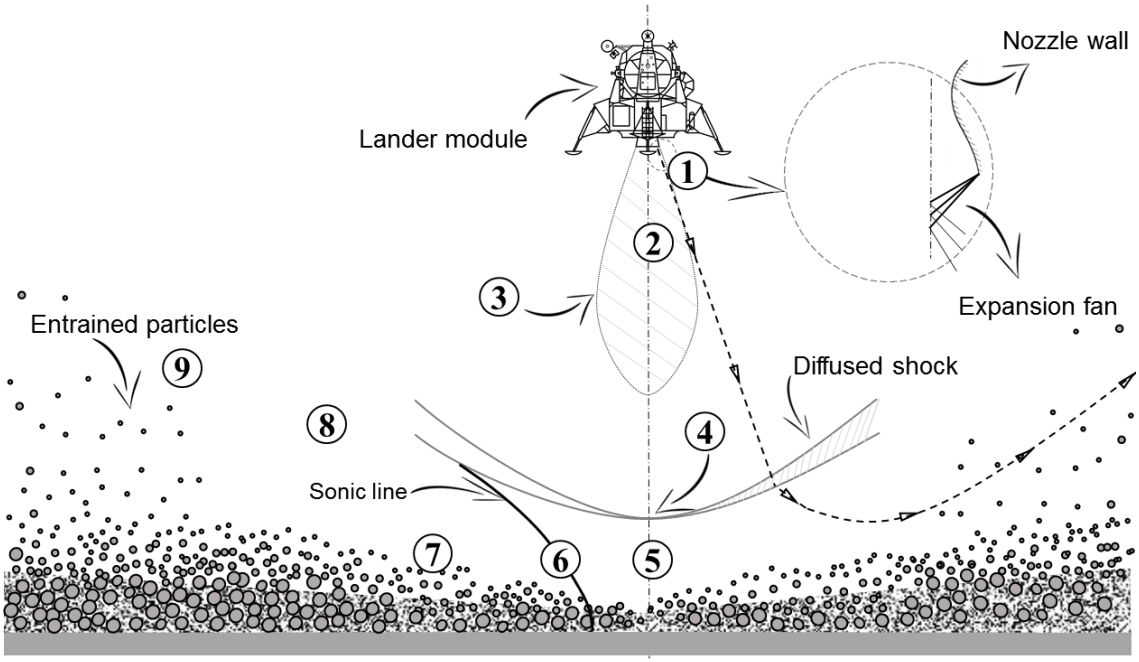

Fig. 53 The prevailing physics in the descent phase of a Moon landing

7.3 Verification and validation of the numerical method for the carrier gas phase

Due to the lack of experimental results for the proposed lunar lander, the Apollo 11 nozzle was considered to verify the numerical simulation. The internal flow inside the nozzle was simulated by assuming the working gas to be a polyatomic water vapor (which is a good representation of the actual exhaust gas), and the solutions at the nozzle exit were compared with the results of the DPLR code developed at the NASA Ames research center [217]. As shown in Fig. 54, the velocity, density, and temperature profiles were found to be in good qualitative agreement, except for some deviations in temperature due to the different type of gas.

The impingement of the rocket motor plume on the lunar surface in a hovering altitude of 5m was also investigated. Surprisingly, the solutions of the current work (NSF) were found to be in good agreement with the DSMC solutions of Morris [217], including pressure contours as low as 20 Pa, as depicted in Fig. 55. An internal shock, formed

inside the nozzle, is reflected from the axis of symmetry and interacts with the stand-off shock near the lunar surface. These discontinuities are well resolved by the present CFD method and the hybrid CFD-DSMC method [217] in which the gas flow near the nozzle is solved by a CFD approach.

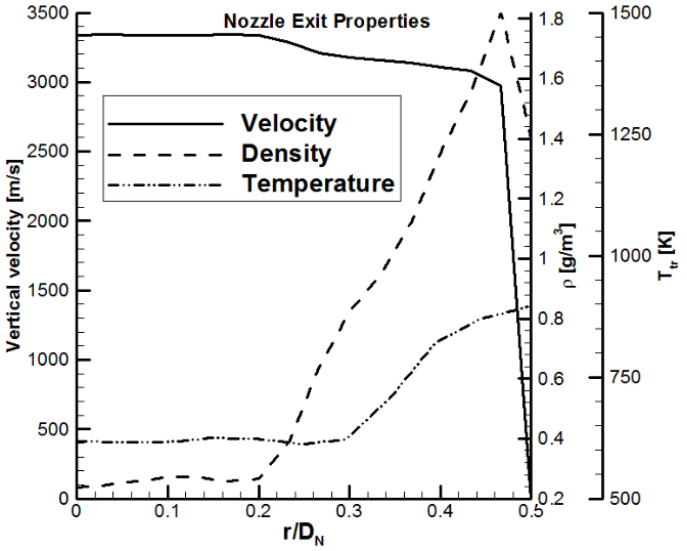

(a) Present results

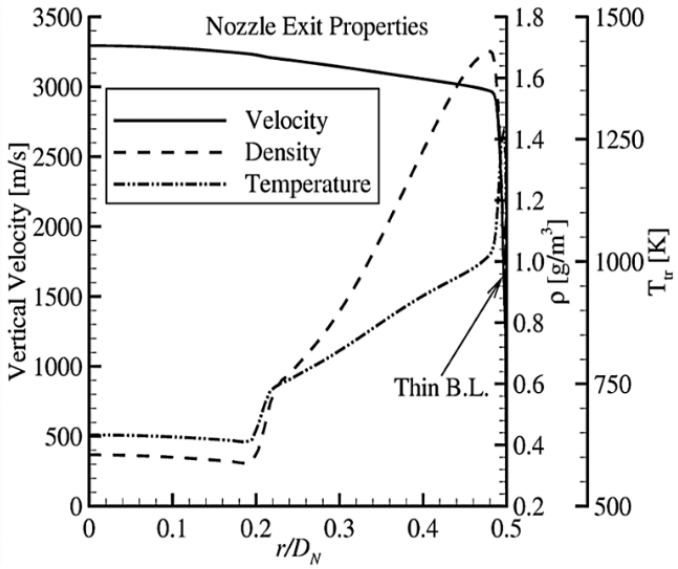

(b) Continuum-based CFD code results (DPLR)[217]

Fig. 54. Verification of numerical solutions for the gas phase at the nozzle exit

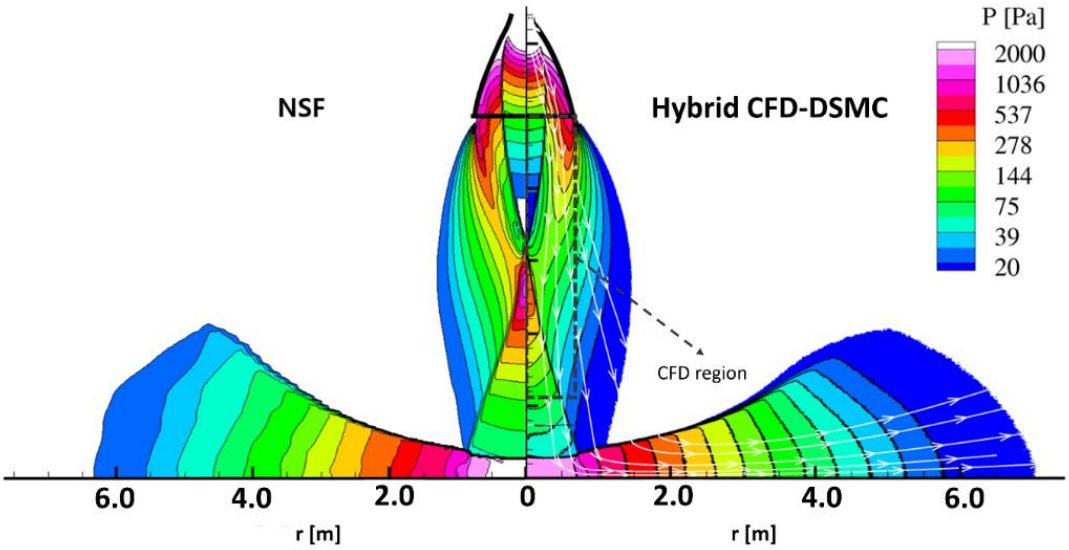

Fig. 55. Verification of numerical solutions (pressure): present work (left); DSMC [217] (right)

In order to elaborate on the validity of the present findings, a non-equilibrium quantifier based on a combination of the Knudsen (Kn) and Mach (M) numbers was introduced to evaluate the degree of deviation that might be present in the first-order NSF constitutive laws. As noted first by Tsien in 1946 [218, 219] 'the order of magnitude of the additional second-order heat flux or stresses is $\mathrm{Kn}\cdot M$,' rather than Kn alone, and therefore the degree of non-equilibrium in the moving gases should be the ratio of the viscous force to the pressure, since the viscous force is a direct consequence of the thermal non-equilibrium [218, 219]. In this context, it should be mentioned that the Knudsen number is a pure thermodynamic quantity without any reference to the average velocity of gas molecules. A non-equilibrium quantifier to incorporate the average velocity of gas molecules, N_δ, is then expressed as $N_\delta=\mathrm{Kn}M(2\gamma/\pi)^{0.5}$. Since the quantifier N_δ in the *moving* gases represents the relative magnitude of off-diagonal terms in the second-order rank tensor of the stress, the value N_δ =1.0 means that the magnitude of the

off-diagonal terms (viscous stress) is comparable to the diagonal term (hydrostatic pressure), implying a high degree of non-equilibrium.

The contours of the local non-equilibrium quantifier in a dynamic flow field are plotted along with the local Knudsen and Mach numbers in Fig. 56(a)-(c). Seven representative locations in the computational domain are marked with numbers to classify flow regimes according to the degree of non-equilibrium depicted in Fig. 56(d). Among the marks shown in Fig. 56(d), regions 1 to 3 fall very close to the equilibrium regime, and region 4 belongs to a state near equilibrium. Regions 5 and 6 belong to a state slightly deviated from equilibrium, while region 7 belongs to a regime considerably deviated from equilibrium.

However, none of these regions approach a highly non-equilibrium state, since N_δ values rarely exceed 0.1, as shown in Fig. 56(c),(d). Moreover, due to the presence of the lunar surface in front of the gas expansion, even these maximum non-equilibrium states are formed only in very narrow region 7 and in regions far from standoff shocks, making most of the near-field regions near- or slightly deviated from equilibrium. This observation explains the physical reason behind the good agreement of the NSF solutions with the DSMC solutions in the present flow problem.

7.4 Implementation of erosion models using a User Defined Function (UDF)

To simulate the eroded particles that are injected into the flow field, the DPM module was used. The erosion mass flux as a function of axial direction was calculated by implementing an erosion model via the UDF feature of the FLUENT code. To compute the mass flow rate of injected particles via equation (56), the shear stress on the regolith surface should be estimated. The DEFINE_DPM_INJECTION_INIT function [188] is

applied to initialize a particle's injection properties, including location, diameter, and velocity. The above macro is called at the beginning of each step in which particles are injected. The computed quantities, such as the particle mass flow rate, need to be post-processed to interpret the computational results. For this purpose, a memory storage command C_UDMI was applied.

Once the steady state solution of the carrier gas phase is computed, the erosion model UDF outlined above is called in the case of a one-way algorithm. The equation of motion of particles is then integrated based on the local time step. Next, particles are tracked, and their final location is determined. On the other hand, when the two-way coupled algorithm is employed, the source terms of the Eulerian phase should be updated to take into account the coupling effects. The loop is terminated after meeting the convergence criteria for the steady-state solution. The algorithm of the solution is illustrated in Fig. 57.

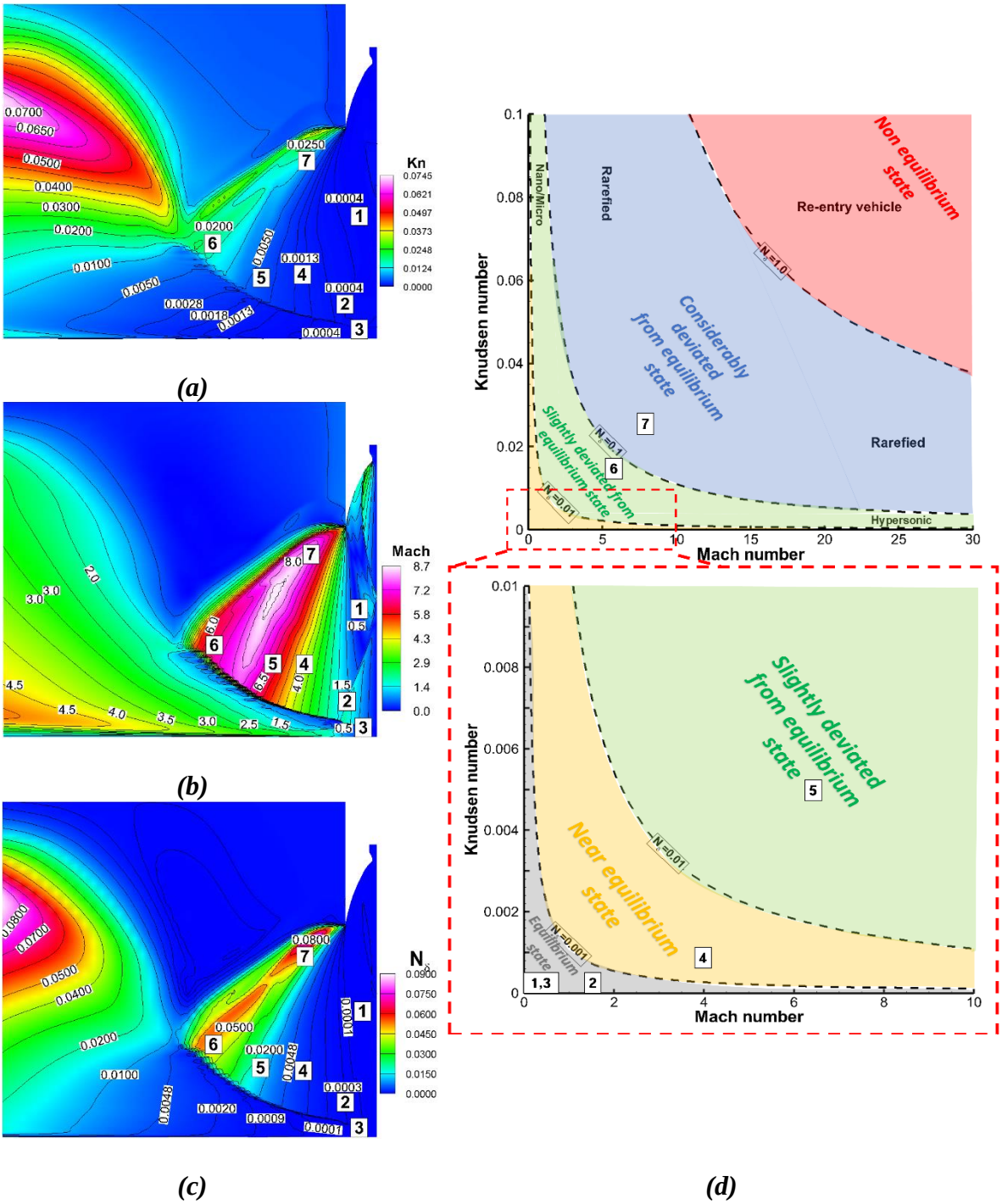

Fig. 56. Flow classification based on Kn, M and N_δ for the Apollo nozzle flow problem

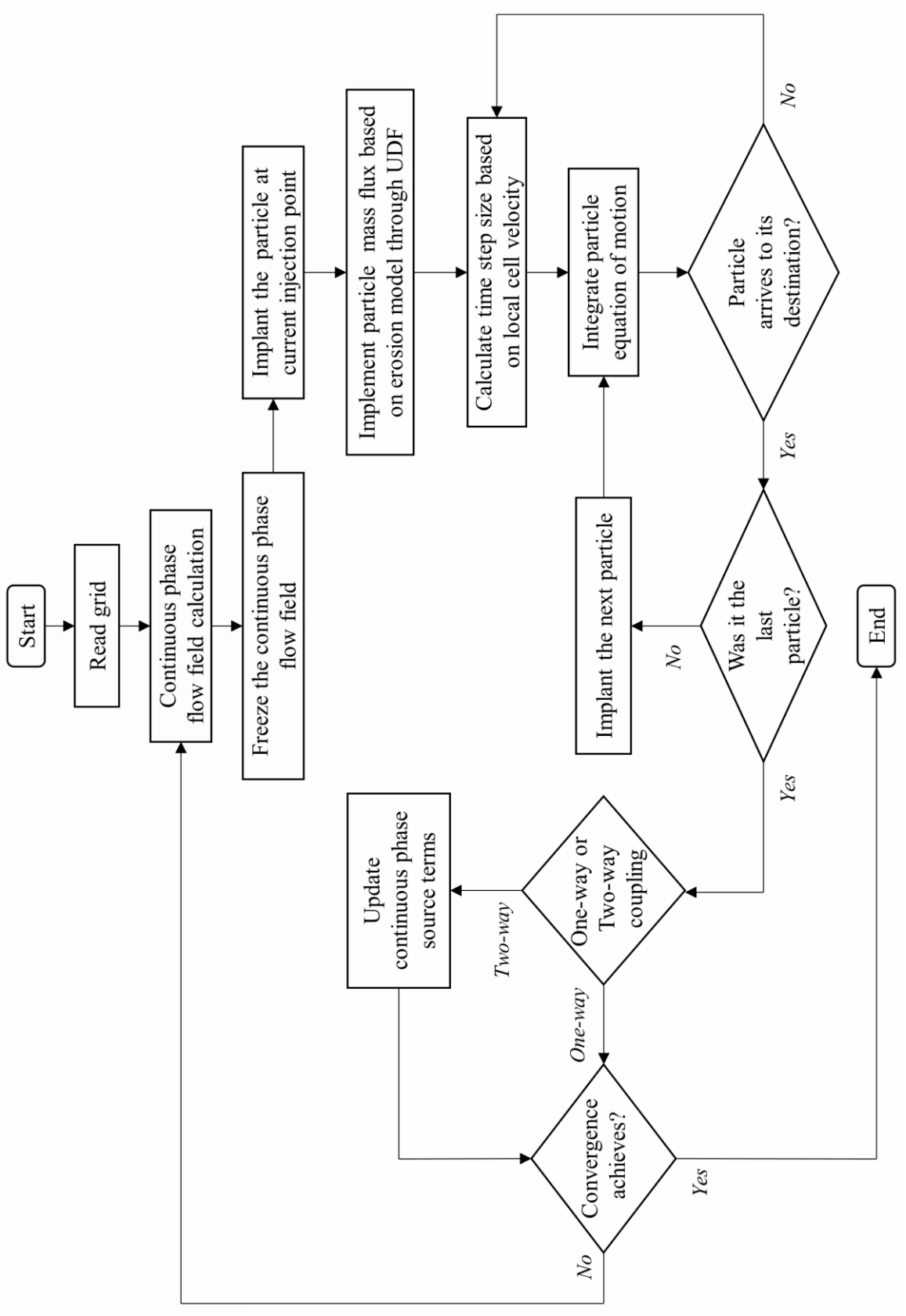

Fig. 57 Solution algorithm in steady flow demonstrating the step at which the erosion model UDF is called

7.5 Results and discussion: plume impingement, regolith erosion, and particle dispersal

7.5.1 Nozzle plume impingement on the lunar surface

Before investigating the complicated multiple nozzle/plume flow field, a single equivalent nozzle with the same mass flow rate and thrust was considered. The on-design operating condition of the descent engine of the proposed lunar lander was considered to study the near-field plume-surface interaction. The nozzle throat and exit diameters were 11.35 mm and 80.26 mm, respectively. The lander was assumed to hover at an altitude of 1m in all simulations. The axisymmetric boundary condition was applied to the nozzle axis to take 3D effects into account. Due to the geometrical symmetry of the nozzle, only half of the domain was solved. The computational domain assumed 60 and 30 times the nozzle exit diameter in the axial and radial directions, respectively. The working gas was assumed to be a polyatomic water vapor (which is a good representation of the actual exhaust gas). The boundary conditions and prescribed values are summarized in Table 15.

Table 15. Boundary conditions in the axisymmetric simulation

Pressure inlet	**Chamber pressure**	1378.946 (kPa)
	Chamber temperature	876.33 (K)
Pressure outlet	**Ambient pressure**	5 (Pa)

As illustrated in Fig. 58, the gas flow emanates from the nozzle exit and expands into the low-pressure atmosphere, forming an under-expanded jet plume. According to the definition of slip lines [220], the pressure across the jet boundary must be maintained

constant. Therefore, the pressure of the jet boundary along its entire region must be close to the ambient pressure. As the gas is further expanded into the vacuum, the exit pressure becomes higher than the back pressure. Hence, the expansion waves are reflected from the jet boundary to adjust the exit pressure with the ambient pressure. As a free boundary, the jet boundary can vary in size and direction. The incident expansion waves after reflection from the free boundary convert to compression waves and later form a shock wave. This phenomenon is in contrast to reflection from a solid boundary, where the expansion waves reflect as expansion waves.

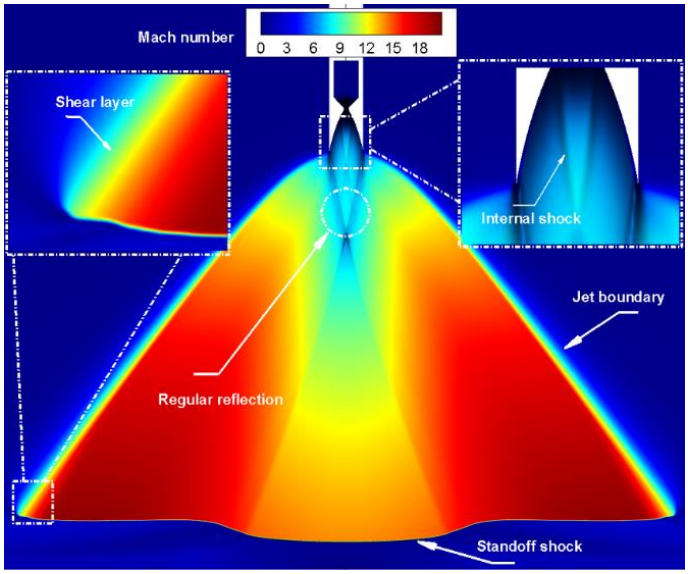

(a)

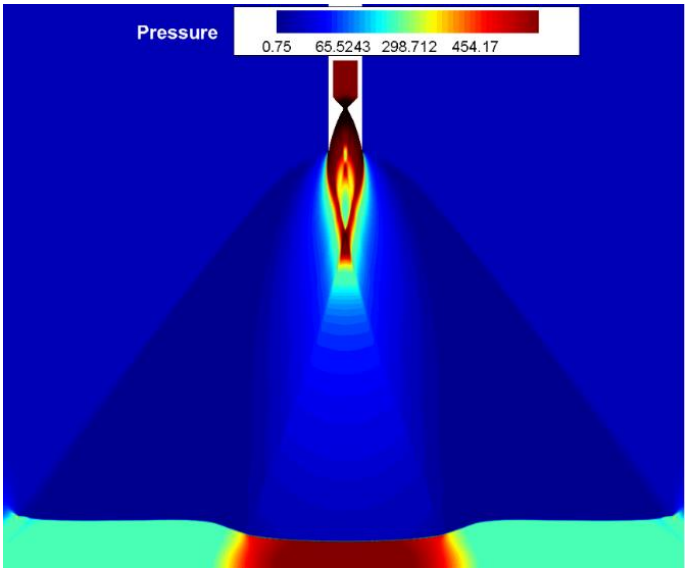

(b)

Fig. 58. Solutions of axisymmetric nozzle plume and surface interaction: a) Mach number, b) pressure

When the plume impinges on the surface, a bowl-shaped stand-off shock is formed which turns the flow radially outward. Moreover, the flow stagnates exactly underneath the nozzle axis so that the stagnation condition with maximum pressure is found at the intersection point of the nozzle axis and the surface. As the radial distance from the stagnation point increases, the static pressure on the surface decreases. The bowl-shaped shock and the impingement surface resemble a diverging nozzle in which the flow is accelerated from zero velocity at the stagnation point to supersonic velocities while the density continually decreases.

As was done for the Apollo nozzle case, seven representative locations in the computational domain, marked with numbers in Fig. 59, were considered to evaluate the degree of non-equilibrium in the moving gases. As shown in Fig. 59(a) illustration of the degree of non-equilibrium, region 5 falls very close to the equilibrium regime, and regions 1, 2, 3, 6, 7 belong to a state slightly deviated from equilibrium. On the other hand, region 4 inside a triangle defined by the jet boundary, the weak central wave, and the standoff shock belongs to a regime considerably deviated from equilibrium.

Nonetheless, the regime with the maximum N_δ value of 0.33 (<<1.0) may be still considered within the NSF framework.

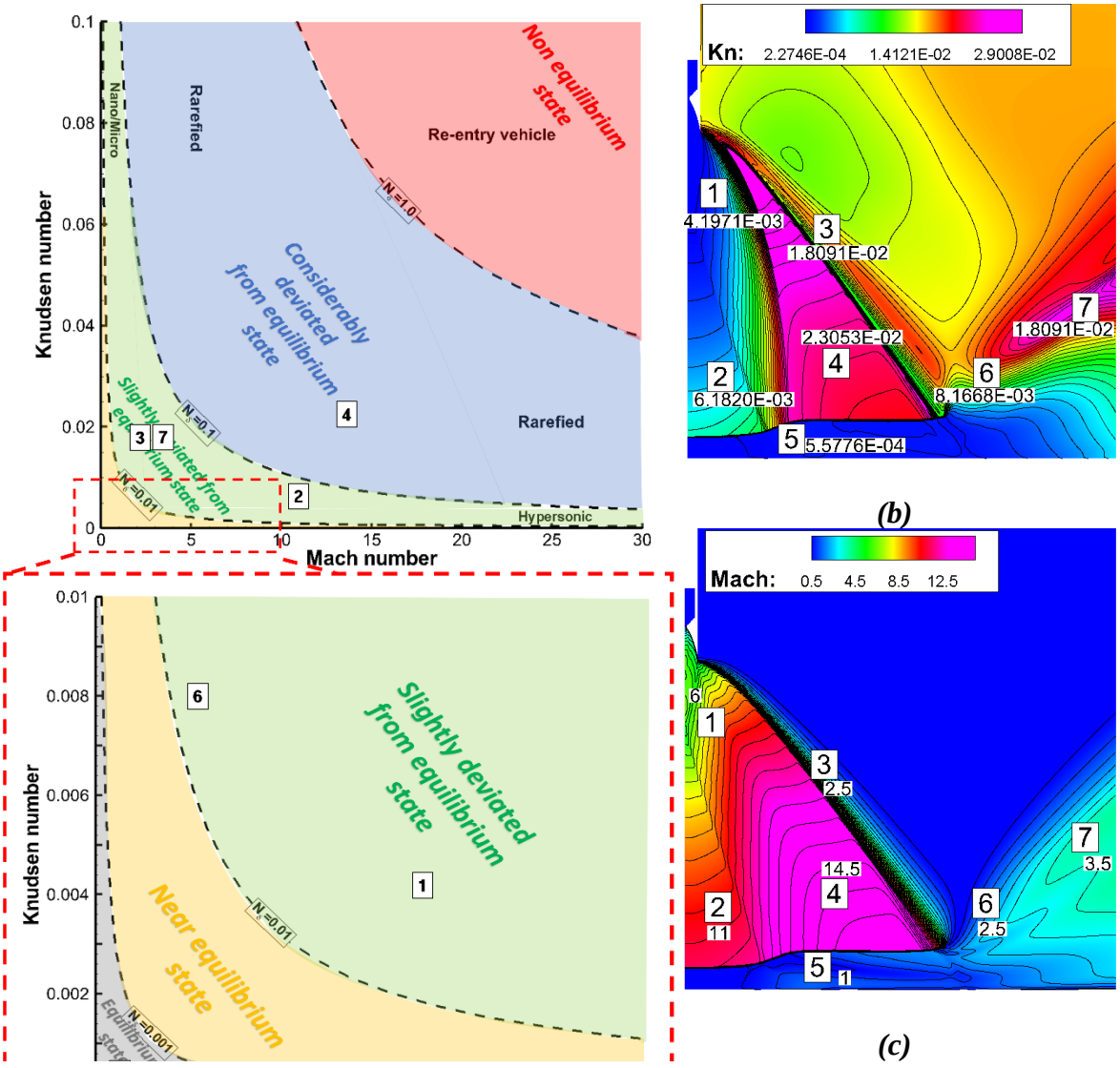

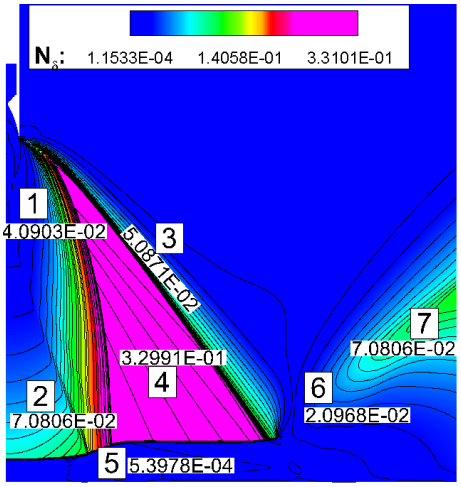

(d)

(a)

Fig. 59. Flow classification based on Kn,* M *and* N_δ *for a single nozzle jet case

As the next step, the complicated plume flow-field of multiple (five) nozzles was investigated. Due to the symmetric geometry of the five-nozzle configuration, a quarter of the physical domain was simulated as depicted in Fig. 60. In this three-dimensional simulation, not only the plume-surface/plume-plume interaction but also pressure distribution and thermal influences on the components of the lunar lander, including legs, were investigated.

To obtain a better understanding of the plume-plume interactions, the Mach number and pressure on two cross-sections A and B (one along the three aligned engines and the other one rotated 45° compared to the first one) are plotted in Fig. 61. In Fig. 61(a), (c), (e), the Mach number contours on these cross-sections besides the 3D Mach iso-surface for certain Mach numbers are plotted. As can be seen, the Mach number is higher in section A-A compared to section B-B, due to interactions with the landfall legs which also lead to alteration of the plume shape—hindering the gas propagation. Similarly, Fig. 61(b), (d), (f) shows the pressure contours on two cross-sections besides the 3D pressure iso-surface.

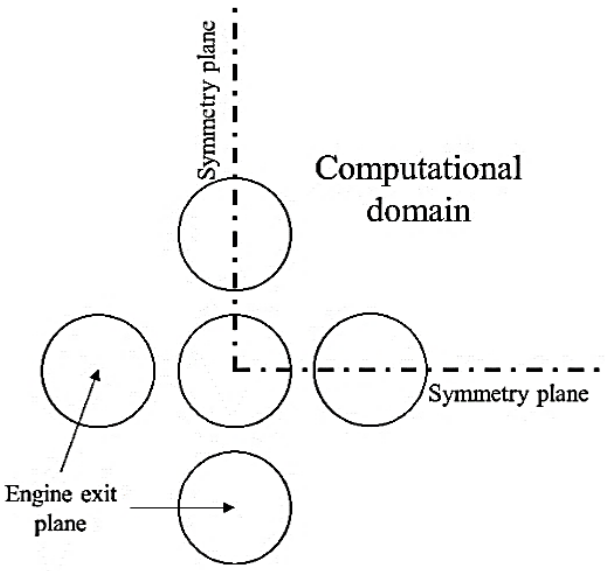
Symmetry plane
Computational domain
Symmetry plane
Engine exit plane

(a)

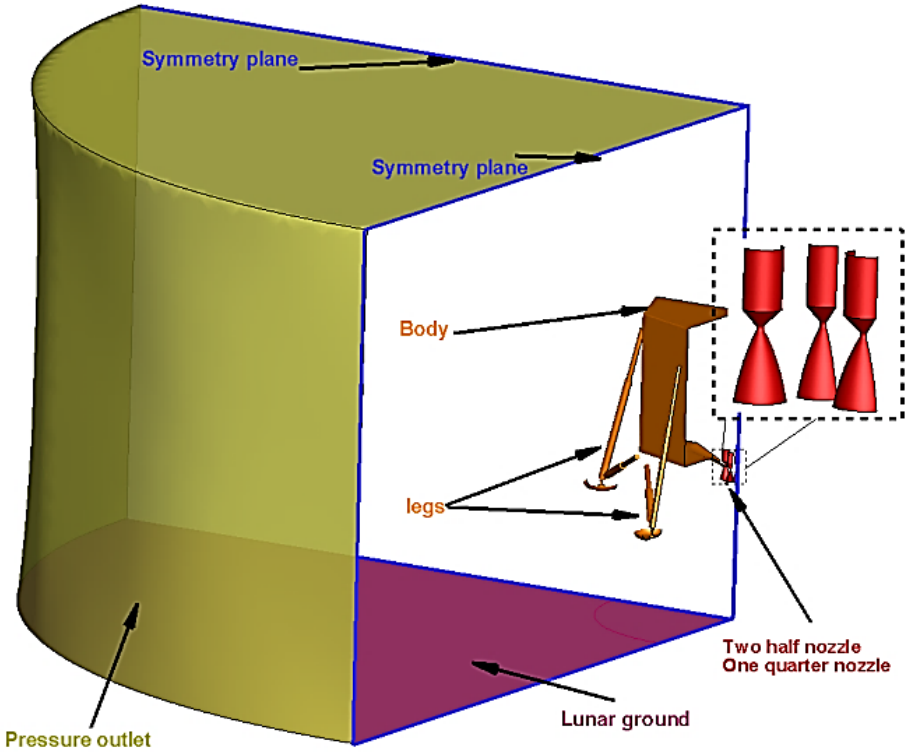

(b)

Fig. 60. Schematic of the computational domain for the five-nozzle configuration and symmetry planes

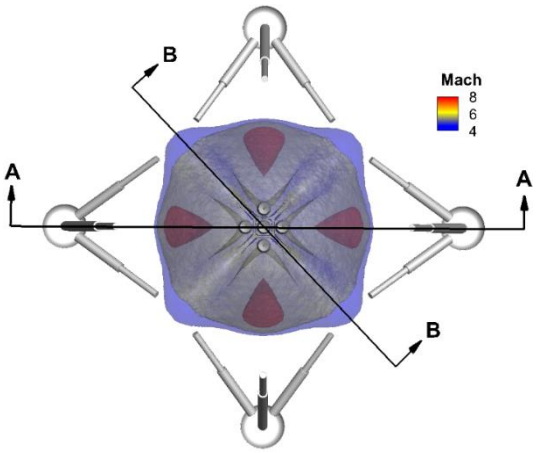

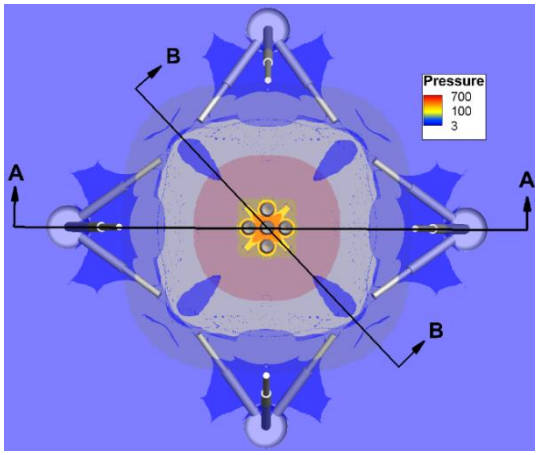

(a) Upper view of 3D iso-surface for certain Mach numbers

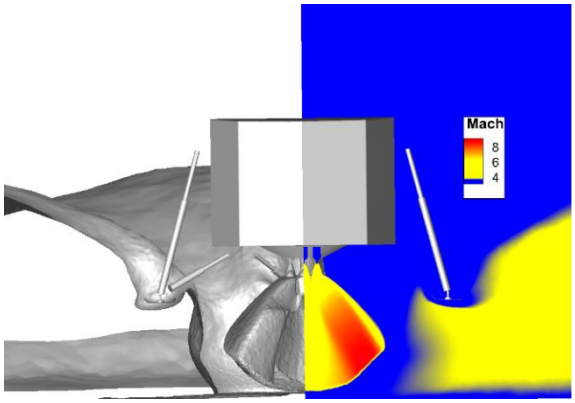

(b) Upper view of 3D iso-surface for certain pressure values

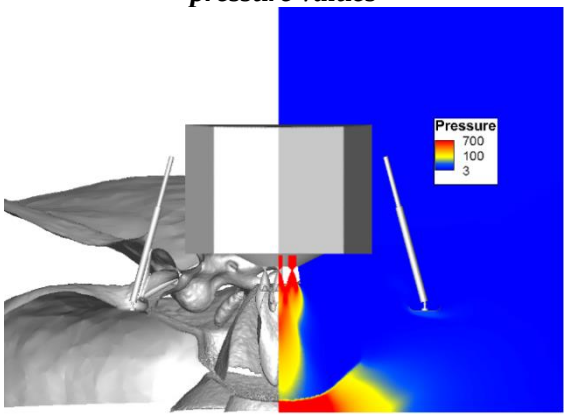

(c) Mach number contours at A-A slice

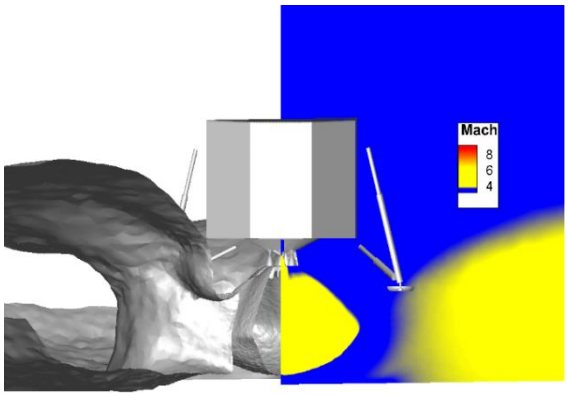

(d) Pressure iso-surface and contours at A-A slice

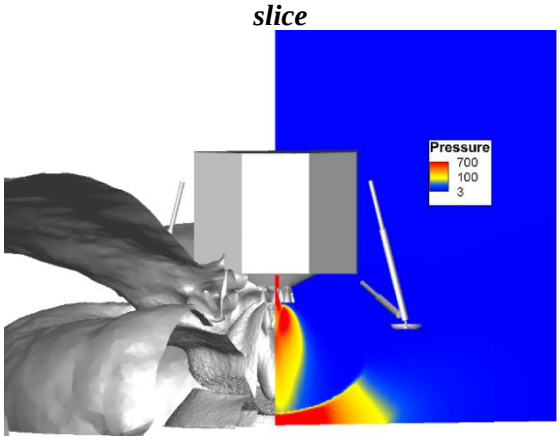

(e) Mach number contours at B-B slice

(f) Pressure iso-surface and contours at B-B slice

Fig. 61. 3D solutions of local Mach number and pressure

Mach number and temperature contours are also illustrated in Fig. 62. The essential features of the under-expanded jet impingement on a surface, including exhaust gas expansion, jet boundary, regular shock reflection, and standoff shock, are visible. For further illustration, two cross sections were selected, A-A, slightly below the nozzle exit, and B-B, moderately above the standoff shock. As shown in the A-A section, a regular shock reflection exists downstream of the nozzle exit. In contrast, the reflected shock has

been eliminated in the B-B section. Compared to the axisymmetric engine (single nozzle engine), the plume expands further into the ambient region. Interestingly, no significant change in shock standoff distance was observed. Owing to strong plume-plume interaction, the Mach number for the five-engine configuration is significantly lower compared to the equivalent single nozzle case. Fig. 62(b) shows a substantial temperature increase—approximately one-third of the chamber initial temperature—right after the shock reflection region.

In the current work, it was possible to estimate the thermal influences and the effects of the aerodynamic force on the module components. Such analysis may have an essential role in the proper design of the lander configuration and the selection of materials for module components. The configuration of the proposed lunar lander consists of an octagonal body, four bumpers, four landfall legs, and eight connectors.

Fig. 63 shows the pressure contours on a cross section passing the three aligned nozzles and on the body surface of the explorer. From Fig. 63(a), three spots can be identified as a stagnation point; one at the intersection of the nozzle axis and the lunar surface, and the other two at the bottom of the landfall legs. At these points, the static pressure is much higher than the surrounding region. Moreover, the landfall legs create an obstacle and result in higher pressure distribution on the bottom surface of the bumper. The lower surface of the bumper connectors also experiences higher pressure, since it is directly exposed to the reflected gas flow from the lunar surface. The bottom of the module at four regions, marked by dash-dot circles, also experienced higher pressure compared to other areas on the explorer body, due to the presence of the four landfall legs, as shown in Fig. 63(b).

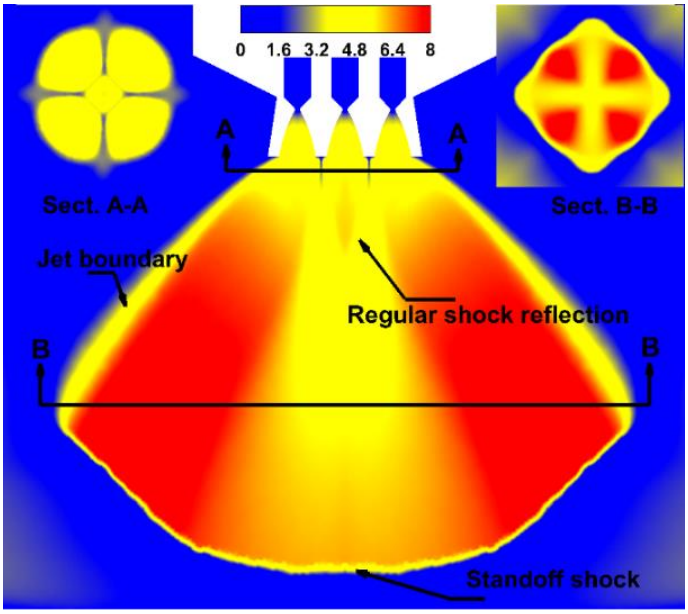

(a) Mach number contours

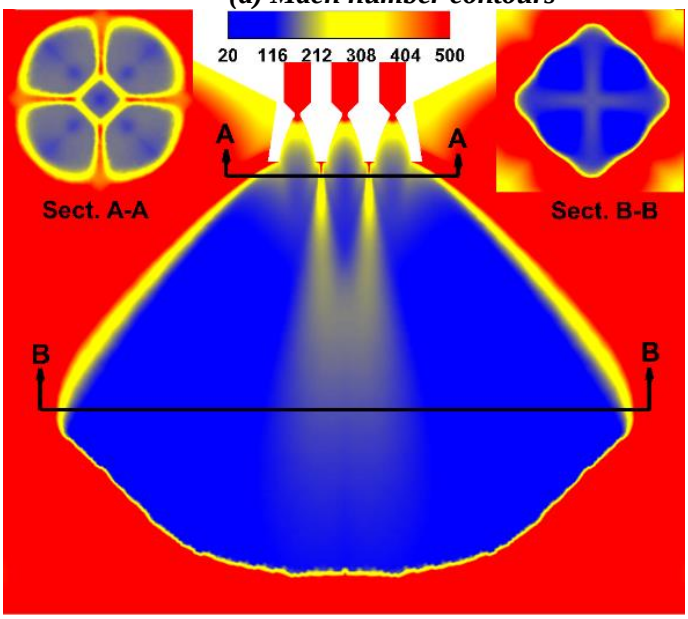

(b) Temperature contours

Fig. 62. Mach number and temperature contours on a cross section along three aligned nozzles in the five-nozzle configuration

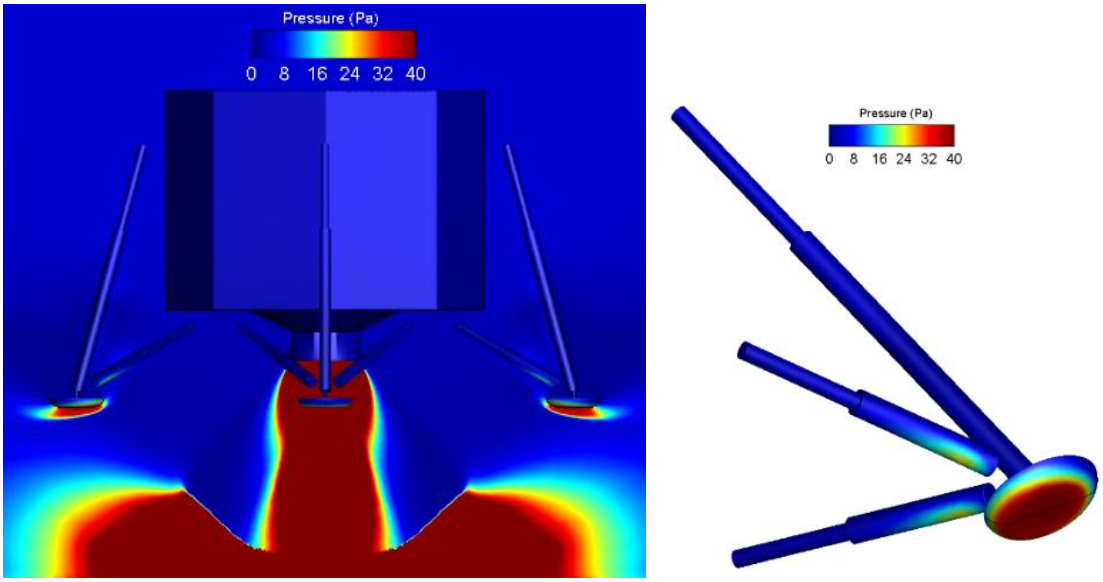

(a) Cross-section through three aligned nozzle and 3D view of the landfall leg

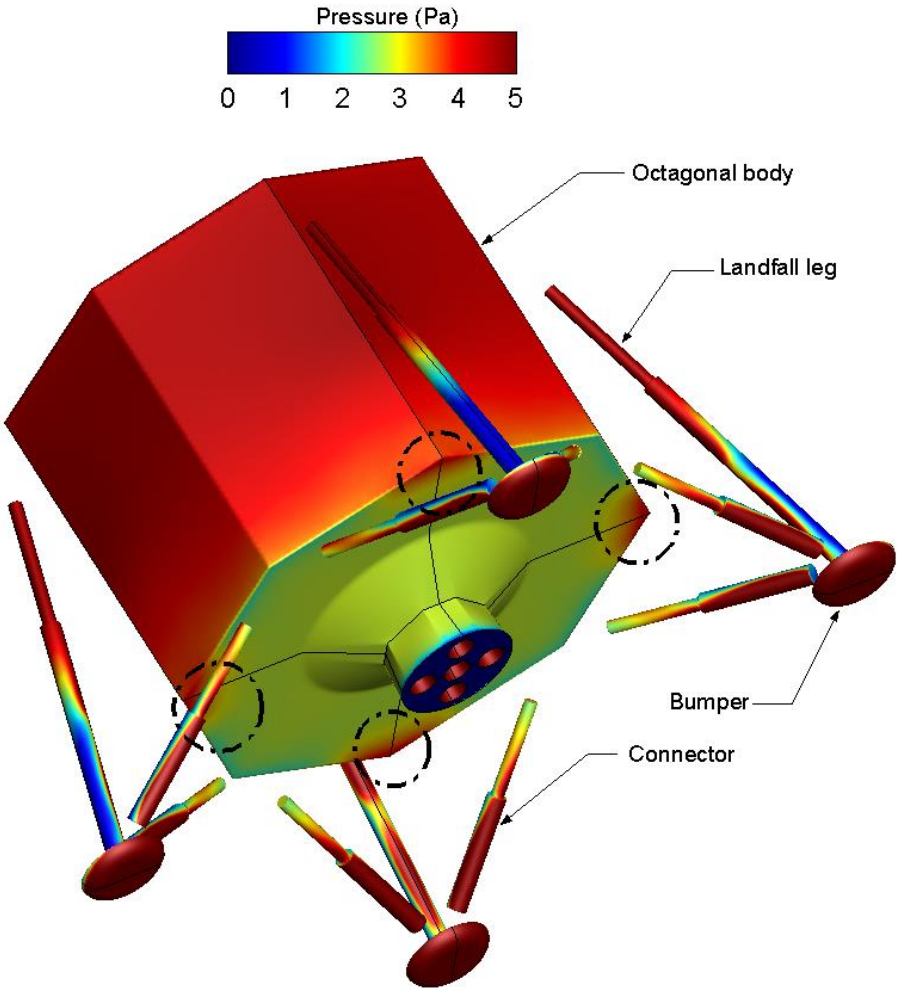

(b) Perspective view of the lunar module

Fig. 63. Pressure distribution on lunar lander components

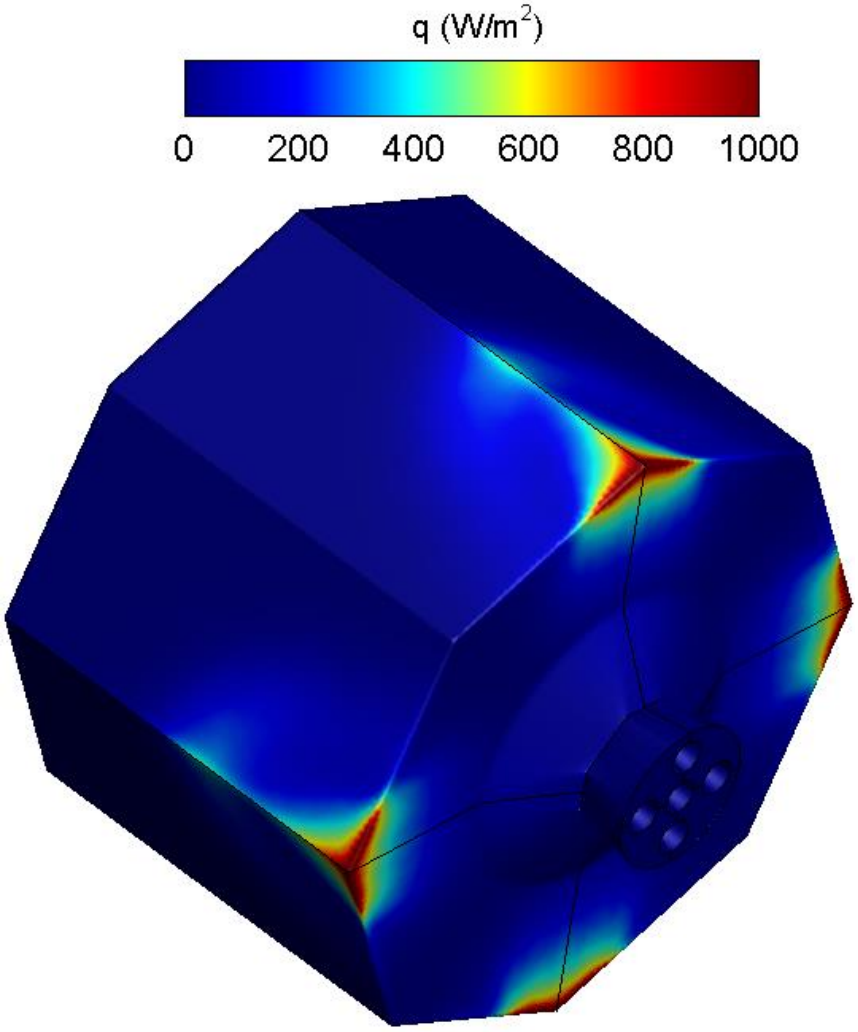

(a) Perspective of the lunar module

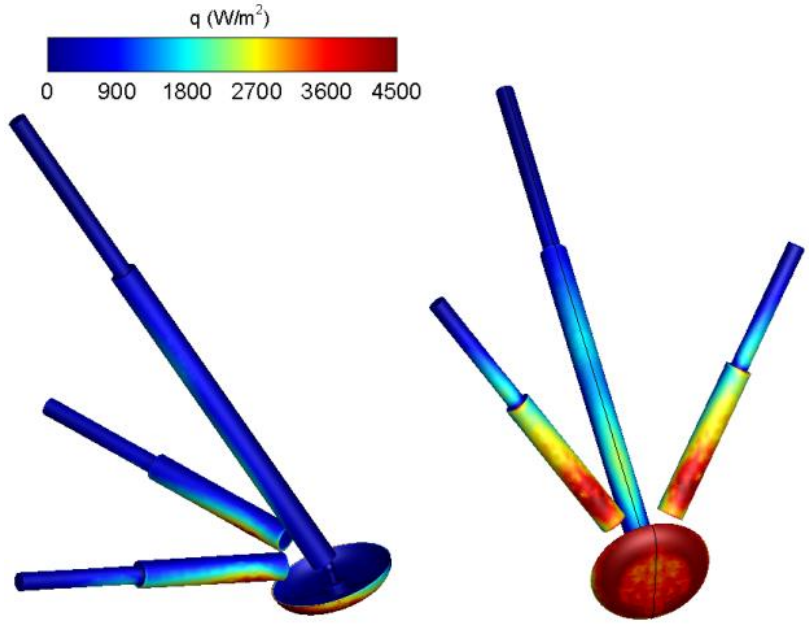

(b) Different 3D views of the landfall leg

Fig. 64. Heat flux distribution on lunar lander module components

The reflected gas plume from the lunar surface causes high pressure on not only exposed surfaces but also high temperature through convection. As shown in Fig. 64, the heat flux distribution follows a trend similar to that of the pressure distribution. The maximum heat flux was observed on the four corners of the hexagonal body that face the bumpers.

The significant effect of plume-plume interaction in multi-nozzle configuration compared to a single nozzle can be seen in Figs. 65 and 66. Regions 1, 2, 3, 4 and 7 on both the A-A and B-B slices fall very close to the equilibrium regime, and region 8 belongs to a near equilibrium state. On the other hand, regions 5 and 6 belong to a state slightly deviated from equilibrium. Nonetheless, most of the regions near the nozzles are either in equilibrium or near equilibrium. In fact, the maximum N_δ value of 0.06 in Fig. 66(d) is far smaller than the N_δ value of 0.33 in Fig. 59(d) of the single nozzle case, implying multi-nozzle configuration leads to a reduction in the degree of non-equilibrium.

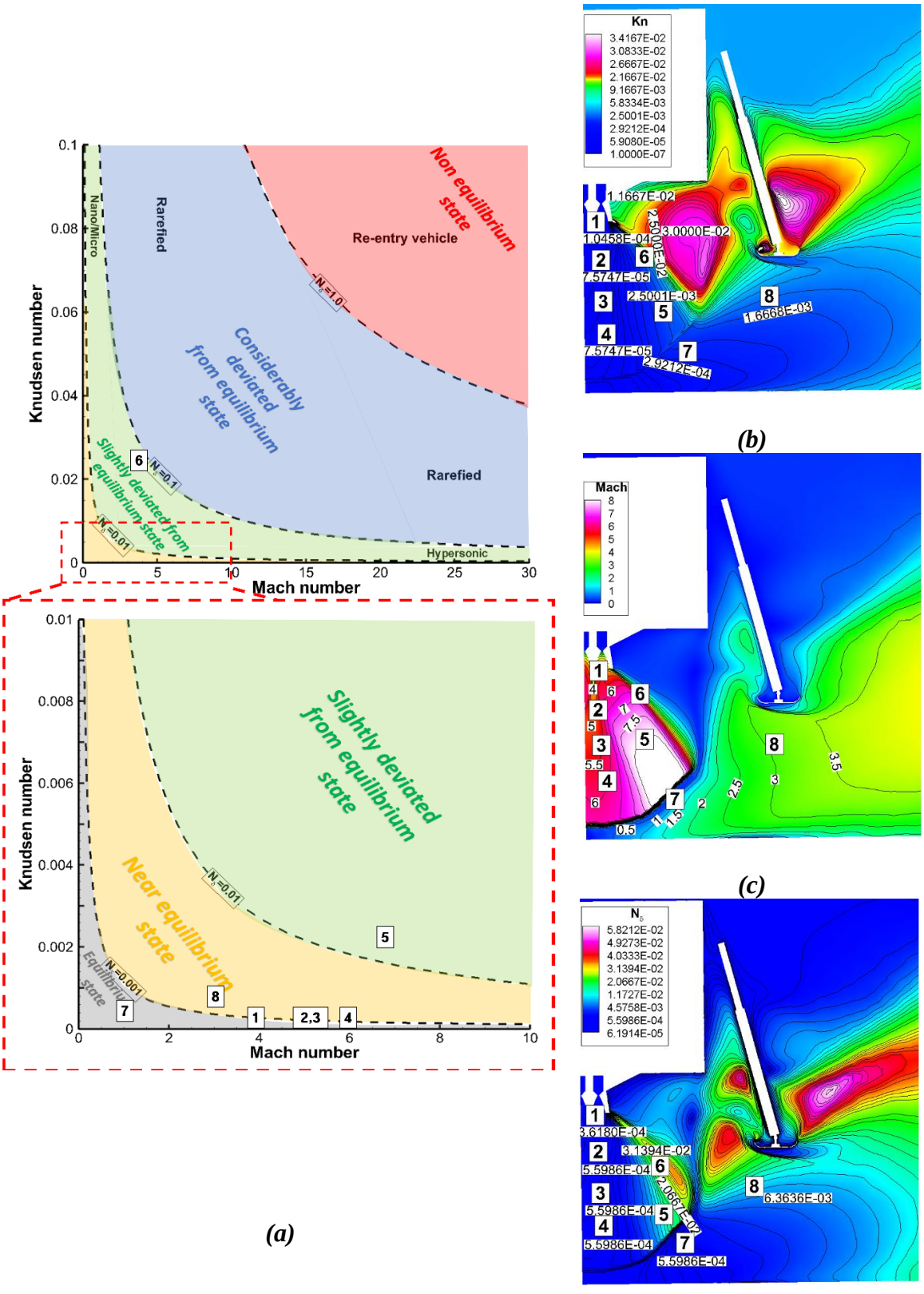
Knudsen number
Mach number
Non equilibrium state
Re-entry vehicle
Rarefied
Nano/Micro
Considerably deviated from equilibrium state
Slightly deviated from equilibrium state
Rarefied
Hypersonic
N_5=1.0
N_5=0.1
N_5=0.01
Slightly deviated from equilibrium state
Near equilibrium state
Equilibrium state
N_5=0.01
N_5=0.001
Kn
Mach
N_5
(a)
(b)
(c)
(d)

Fig. 65. Flow classification based on Kn, M and Nδ for five nozzles in operation at A-A slice

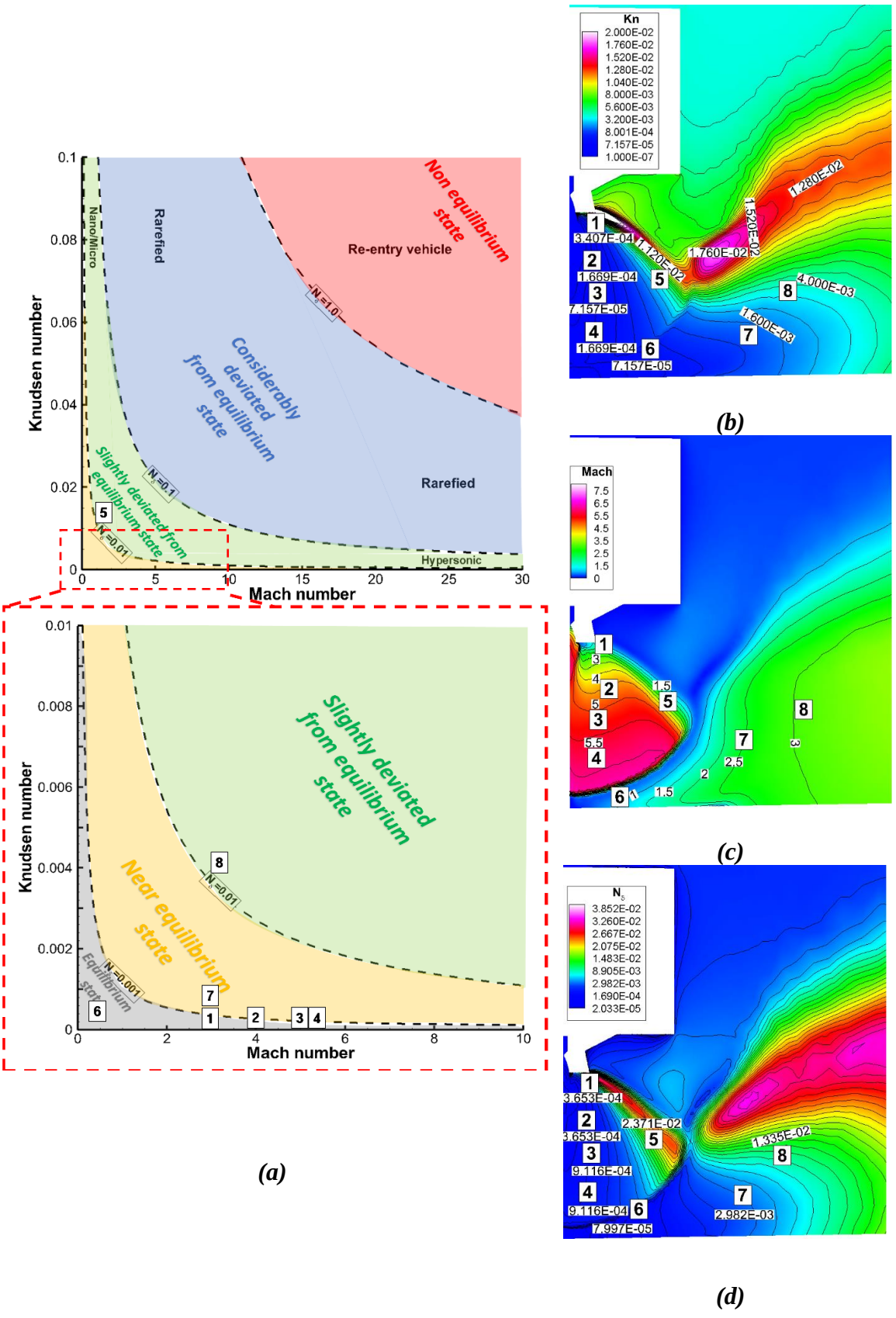

Fig. 66. Flow classification based on Kn,* M *and* N_δ *for five nozzles in operation at the B-B slice

At this stage, it may be instructive to investigate the degree of non-equilibrium in the dynamic flow field in more detail, in particular, based on a non-equilibrium measure derived from the Rayleigh-Onsager dissipation function. Until now, the local N_δ, M and Kn numbers have been computed to estimate the degree of non-equilibrium. The analysis based on these numbers revealed that most of the flow fields in the Apollo and five-nozzle configurations are either in equilibrium or near equilibrium. This observation can be justified in the case of a *low hover altitude with increasing ground effect* and *plume-plume interaction.* In the case of low hover altitude, the plume-surface interaction generates a strong standing shock near the lunar surface, and the initial high-speed flow from the nozzle is highly compressed along the core of the plume and is further decelerated to zero velocity at the stagnation point. As a result, the near-field flows are dominated by low speed (low M) near the surface and high pressure (low Kn) in the core of the plume, forming flow-fields in a continuum or near continuum. In the case of plume-plume interactions, because of momentum and energy exchange, the velocity and temperature are accordingly substantially decreased, and the local N_δ, M and Kn numbers become much lower than the single-nozzle configuration, and a wider area of the flow field is in near equilibrium.

Nonetheless, there is still room to refine the present analysis of the degree of non-equilibrium in the moving gases. It should be noted that the effect of heat flux is completely omitted in the local N_δ, M and Kn numbers, though heat flux will definitely play a physical role in thermal non-equilibrium. A better non-equilibrium measure can thus be derived based on the Rayleigh-Onsager dissipation function, which is a vital component in the theory of irreversible thermodynamics and is directly related to entropy

production in non-equilibrium processes. A measure based on the energy dissipation arising from molecular collisions was introduced in [12] and can be expressed as follows:

$$\hat{R}^2 = \hat{\mathbf{\Pi}} : \hat{\mathbf{\Pi}} + \hat{\mathbf{Q}} \cdot \hat{\mathbf{Q}}, \tag{122}$$

where $\hat{\mathbf{\Pi}} \equiv \frac{N_\delta}{p}\mathbf{\Pi}$, $\hat{\mathbf{Q}} \equiv \frac{N_\delta}{p}\frac{\mathbf{Q}}{\sqrt{T/(2\varepsilon)}}$, $\varepsilon = \frac{1}{\mathrm{Ec}\,\mathrm{Pr}}\frac{1}{T_r/\Delta T}$, $\mathrm{Ec}=(\gamma\text{-}1)M^2(T_r/\Delta T)$.

Note that the measure $\hat{R}$ is basically a combination of the global parameters N_δ, ε, and the local conserved properties p, T, and the local non-conserved viscous shear stress $\mathbf{\Pi}$ and heat flux $\mathbf{Q}$. And the second term in (122), a combination of ε, T and $\mathbf{Q}$, represents the thermal and heat flux effects in the entropy production in non-equilibrium processes, overcoming the limitation of the simple measure N_δ.

Fig. 67 shows the local non-equilibrium measure $\hat{R}$ in regions where the flow experiences sudden changes and the degree of non-equilibrium is higher than other parts of the computational domain. Moreover, a comparison of Fig. 67(a) (the Apollo lander nozzle) and Fig. 67(b) (the proposed lunar lander nozzle) reveals that a more substantial portion of the domain considerably deviates from equilibrium in the proposed lunar lander case. In fact, the non-equilibrium measure $\hat{R}$ is approximately ten times higher than the Apollo lander case in almost every region of the domain.

On the other hand, a comparison of Fig. 67(b) (the single nozzle configuration) and Fig. 67(c), (d) (the five-nozzle configuration) indicates that a greater portion of the domain in the five-nozzle configuration is either in equilibrium or near equilibrium. Therefore, based on the present in-depth analysis, it can be said that even the first-order constitutive relationships, namely the NSF equations, in conjunction with the physical conservation laws, can provide a fairly reasonable prediction of the near-field interaction of the plume (in particular, multiple plumes) and the lunar surface in meter scale low altitude hover.

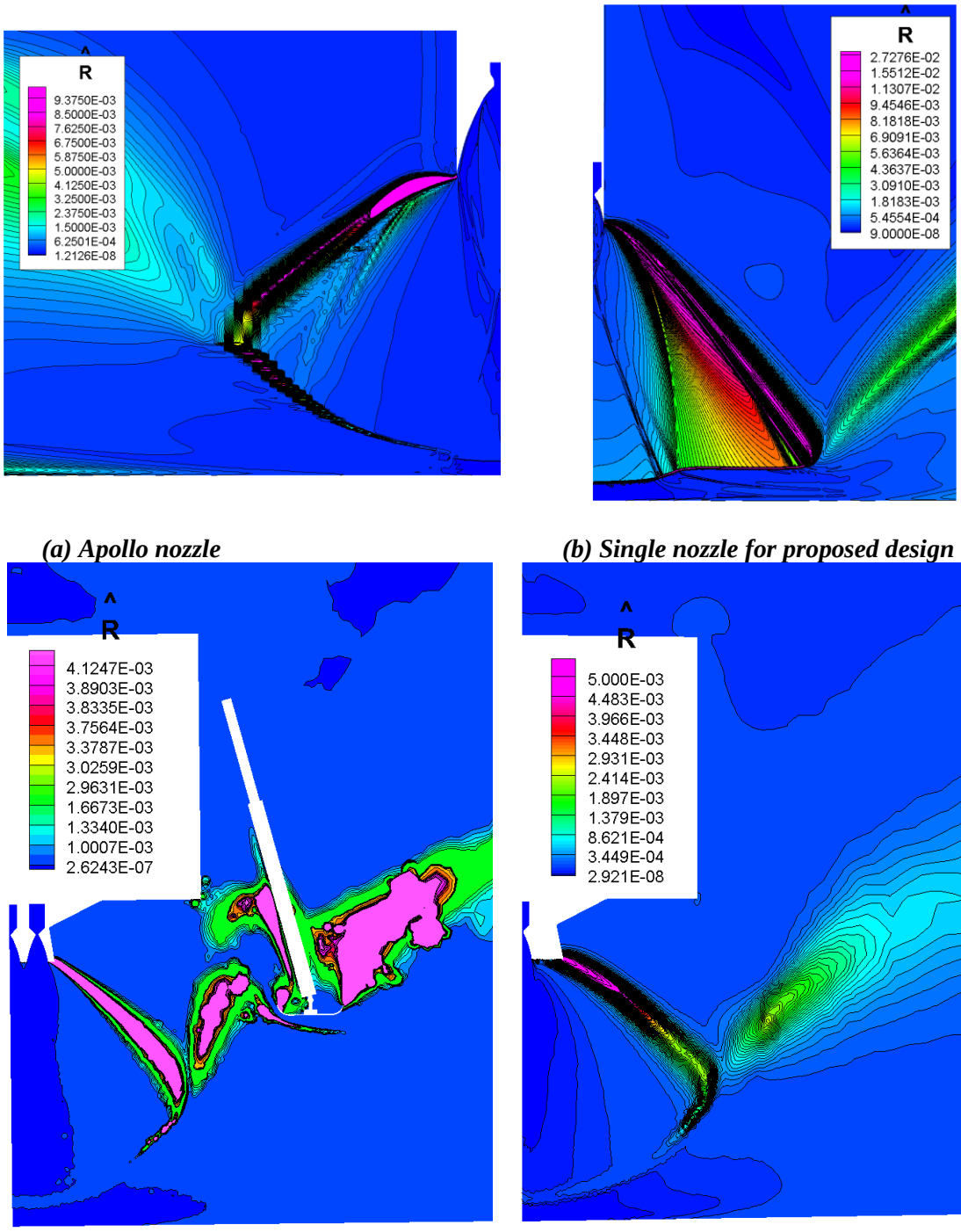

(a) Apollo nozzle *(b) Single nozzle for proposed design*

(c) Five-nozzle configuration at A-A slice *(d) Five-nozzle configuration at B-B slice*

Fig. 67. Distribution of the non-equilibrium measure $\hat{R}$ based on the entropy production for different nozzles

7.5.2 Simulation of erosion on the lunar surface

To simulate the surface erosion phenomena and the consequent entrainment of regolith grains, particles were injected from the surface based on the eroded mass flux via DPM. The present simulation methodology was first verified by using the DSMC solution for ammonia gas of Morris *et al*. [50]. An axisymmetric jet with uniform properties impinging on a dusty surface was simulated. A constant wall temperature of 1000K was imposed on the lunar surface. A schematic of the problem and boundary conditions is illustrated in Fig. 68(a).

The cohesive stress and the fraction angle were assumed to be 100Pa and 30°, respectively. It was noted in [50] that shear stress could be computed by assuming either a laminar or turbulent boundary layer if the roughness of the surface is small compared to the boundary layer thickness. On the other hand, if the roughness is high enough, the shear stress can be estimated by the local dynamic pressure at a distance slightly above the boundary layer. This is the most conservative way to obtain shear stress and leads to a much higher value than the shear stress in the laminar/turbulent boundary layer [221].

Weak (one-way) coupling between the dust and carrier gas phases was considered. The simulated particle diameter and particle density were assumed to be 30μm and 3000 kg/m^3, respectively. The simulations were performed for hover altitudes of 5m and 10m. A schematic of the particle injection based on the erosion rate is illustrated in Fig. 68(b). It is worth noting that the application of the UDF is necessary to simulate the non-uniform mass flow rate that the erosion model provides. The eroded particles were then injected into the flow field as a stream from each surface element.

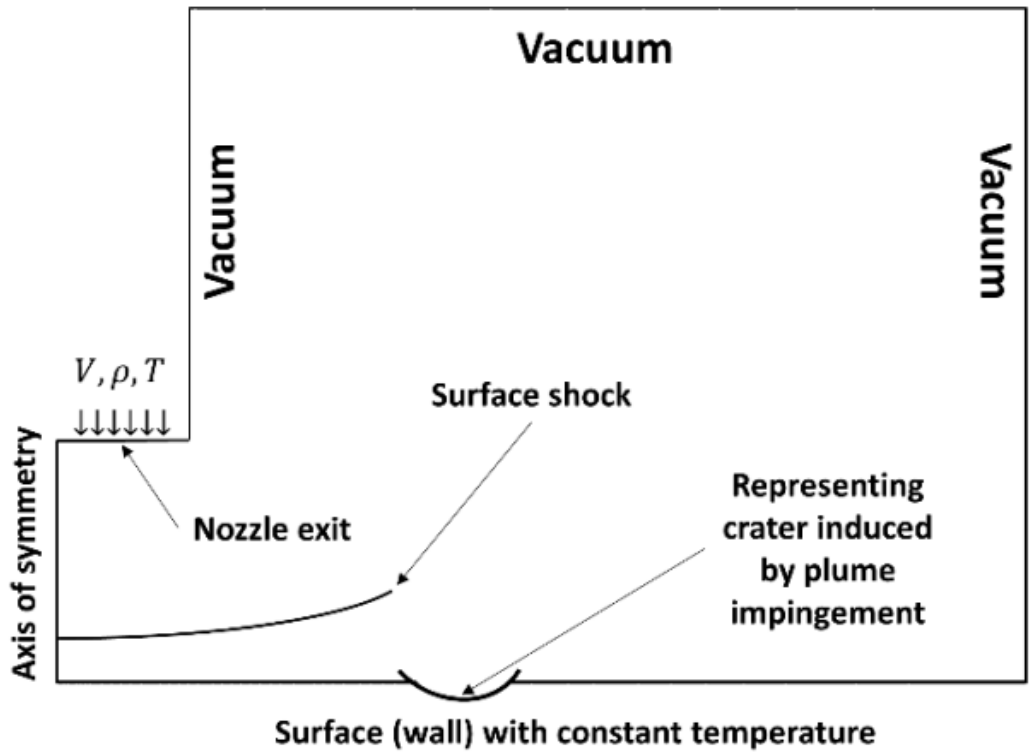

(a)

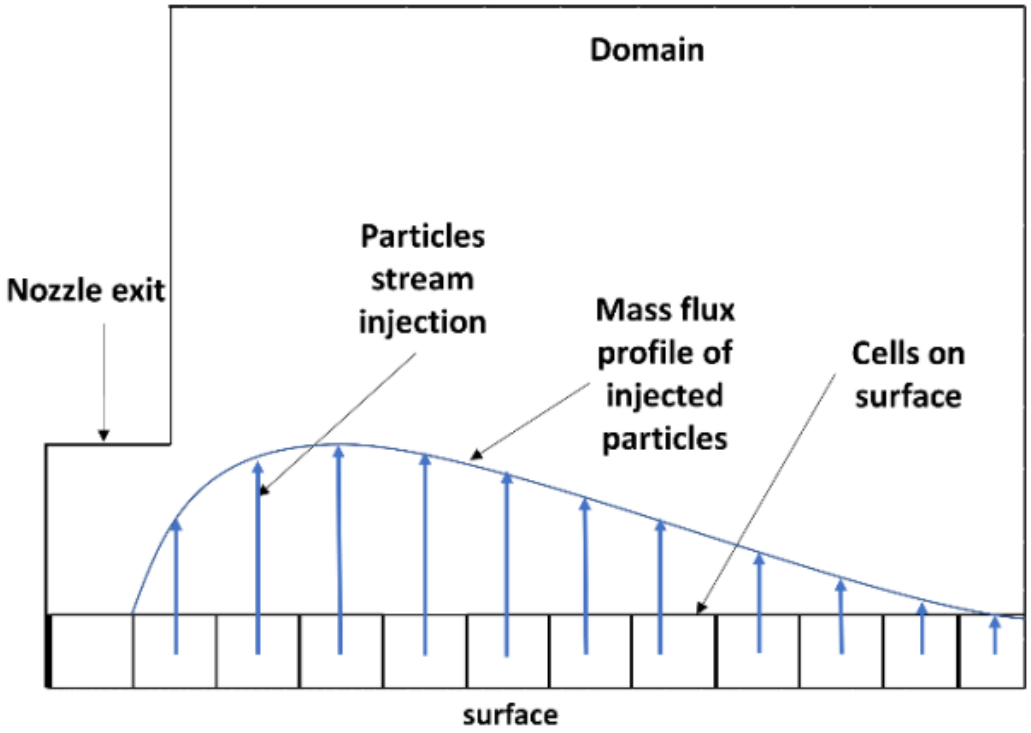

(b)

Fig. 68. Schematic of a) flow field and b) particle influx from the lunar surface representing eroded particles

A comparison of the computed shear stress and erosion rate with the DSMC solution of Morris *et al*. [50] is illustrated in Fig. 69. The simulation results were found to be in qualitative agreement with each other for both the shear stress and mass flux of particles. As shown in Fig. 69(b), the mass flow rate of the particles increases radially and reaches a maximum after a certain distance (about 2m) from the jet axis where the dynamic pressure is at its peak. The deviation observed in the shear stress is due to the difference in treatment; the local dynamic pressure was calculated at 5cm above the boundary layer in the DSMC solution [50], while it was calculated at 5cm above the surface in the present study, leading to a lower local velocity and dynamic pressure.

The streamlines of expanded gas from the nozzle along with the trajectories of eroded particles from the surface are overlaid on the radial gas velocity in Fig. 70. It can be noticed that the motions of grains in the present problem depend largely on the local flow condition. The reason is that when the velocity equilibration length—the distance required for particle velocity to reach that of the carrier gas—is much smaller than the characteristic length ($\lambda_v \ll L$) [222], a particle has enough time to conform to the local carrier phase motion.

Moreover, in

Table 16, the maximum particle velocity and the maximum inclined angle of the lofted particles for a hovering altitude of 5m are compared with the DSMC solution [50]. The present results were found to be in qualitative agreement with the DSMC solutions, including the general pattern of trajectories and the inclined angle of eroded particles. Some deviations can be attributed to the different treatment of the local dynamic pressure in the erosion model; 5cm above the boundary layer in the DSMC solutions versus 5cm above the surface in the present study.

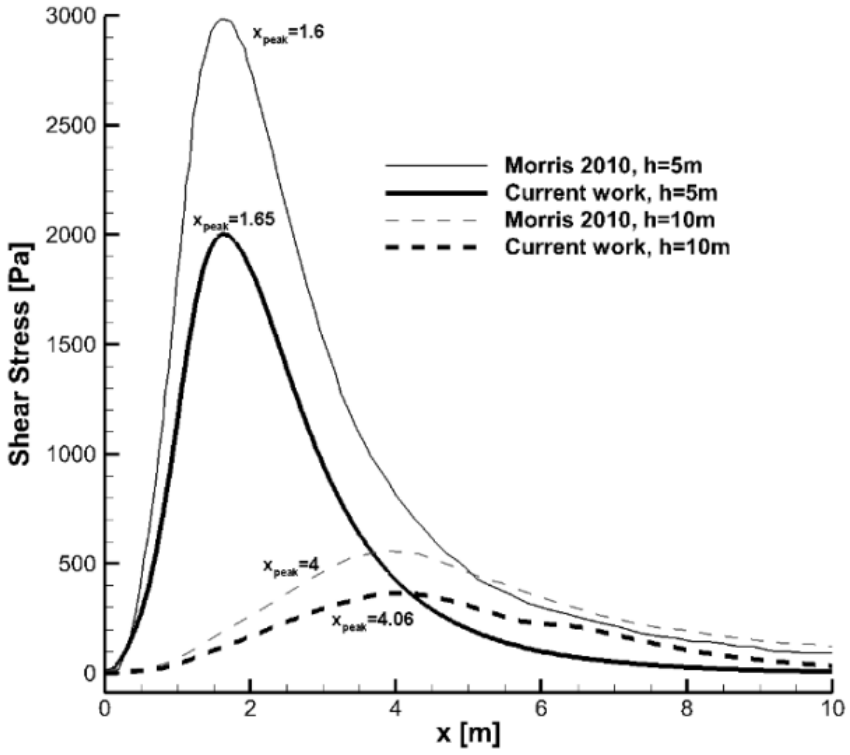
3000
2500
2000
1500
1000
500
0
0
2
4
6
8
10
Shear Stress [Pa]
x [m]
x_{peak}=1.6
x_{peak}=1.65
x_{peak}=4
x_{peak}=4.06
Morris 2010, h=5m
Current work, h=5m
Morris 2010, h=10m
Current work, h=10m

(a) Shear stress

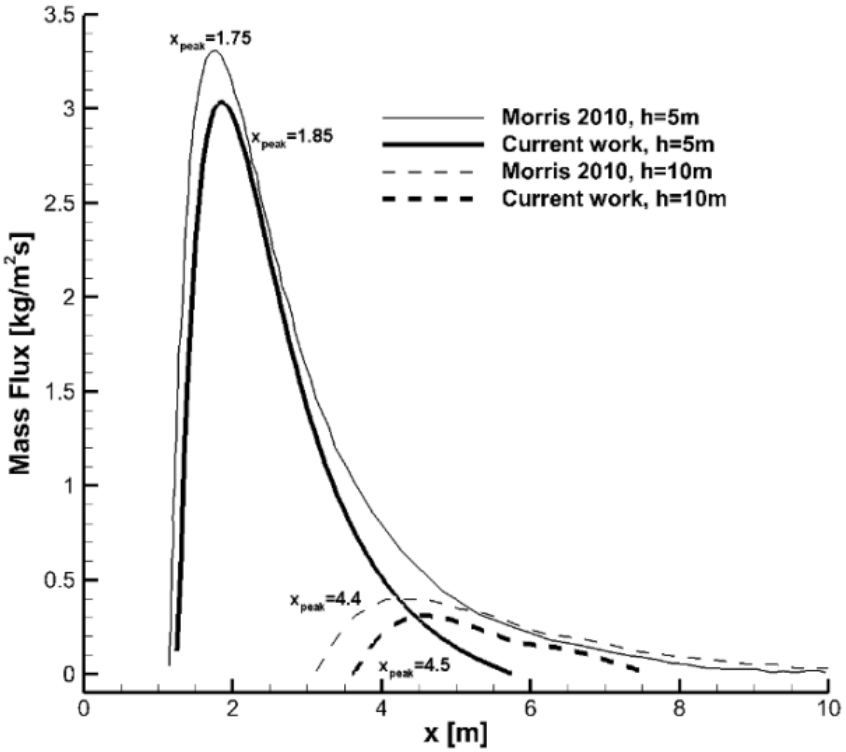

(b) Particle mass flux

Fig. 69. Comparison of erosion modeling parameters with DSMC [50] for different hover altitudes

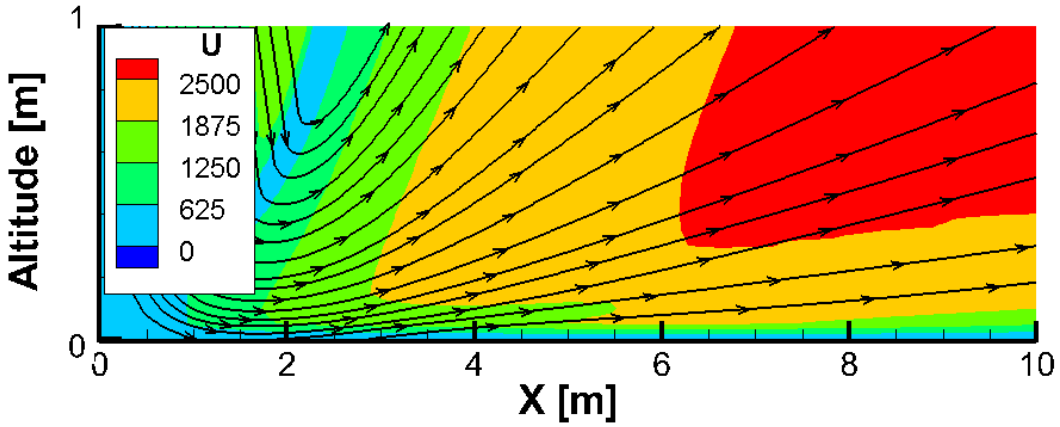

(a) Streamlines of exhaust gas from nozzle overlaid upon the radial gas velocity

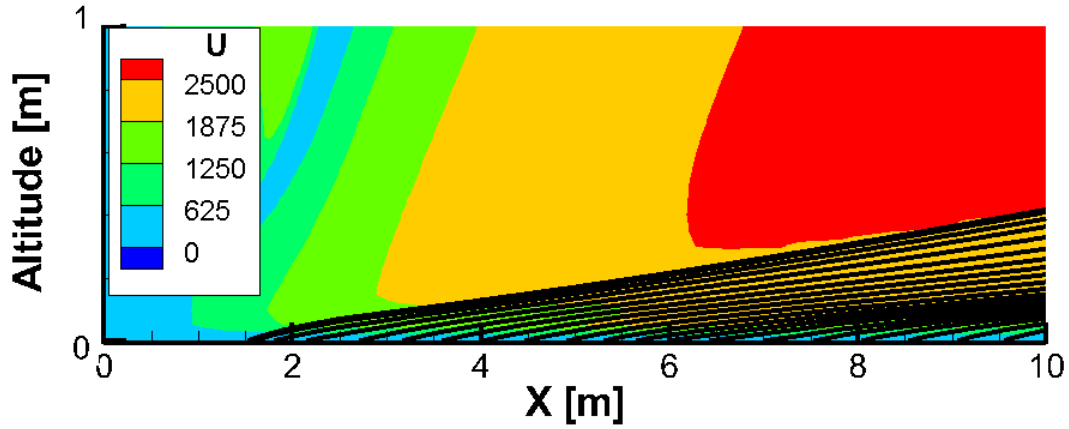

(b) Trajectories of eroded particle overlaid upon the radial gas velocity

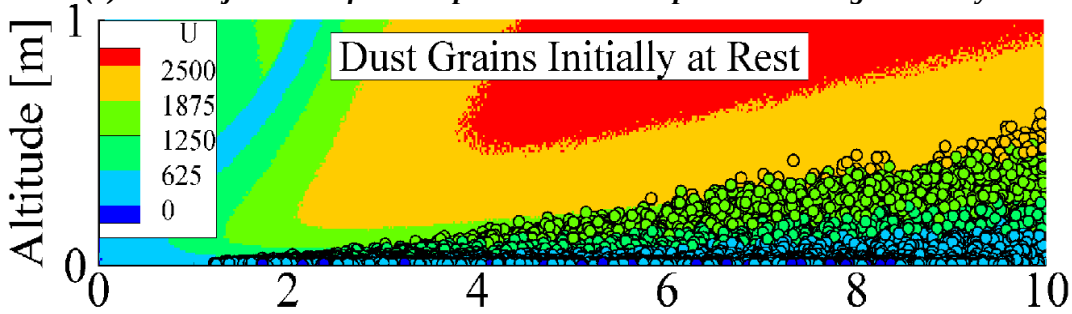

(c) Injected particles in DSMC solution [50]

Fig. 70. Dust grains overlaid upon radial velocity ($D_p = 30\mu m, h = 5m$)

Table 16. Comparison of maximum surface shear stress, maximum particle velocity and maximum particle inclined angle from the surface at a 10m radial distance from the nozzle axis ($D_p = 30\mu m$, hover altitude $= 5m$)

	Max. shear stress (Pa)	**Max. particle velocity (m/s)**	**Max. particle inclined angle**
DPLR [50]	2995	1700	2.8°
Present work	2000	1640	2.0°

To obtain better insight regarding the role of the critical parameter an in Roberts' theory—the fraction of velocity that the particles gain from the carrier phase—a sensitivity analysis based on the equations (56)-(59) was conducted. In Fig. 71, the parameter a for a given threshold shear stress is plotted for varying particle diameter, hover altitude, Mach number of flow, and the number density of particles. For very small particle diameters, the value of parameter a becomes close to one, which implies the velocities for dust and carrier phase are identical. On the other hand, as the diameter of

the grains increases, the particles move more slowly than the gas phase due to the larger drag force.

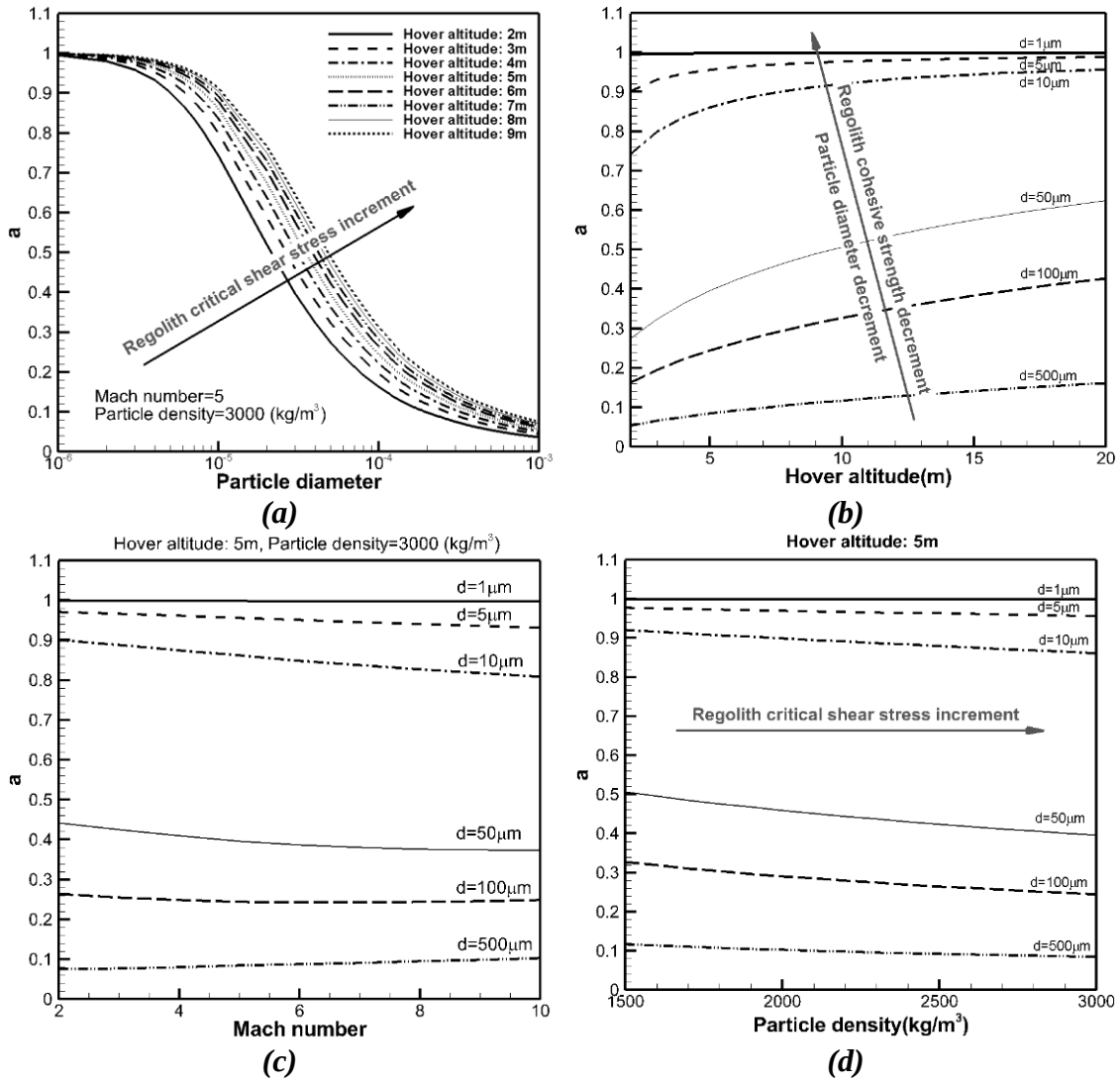

Fig. 71. Parametric study on the fraction velocity in the Roberts erosion model

A series of simulations were also conducted to investigate the effect of hover altitude and particle diameter on surface erosion. From Table 17, it can be shown that the maximum particle velocity decreases with increasing particle diameter. This trend remains the same irrespective of hover altitudes and coupling models. Moreover, the maximum velocity of particles in the strongly-coupled two-way case phase is predicted to be lower than that in the loosely-coupled one-way case.

Interestingly, a counter-intuitive trend was found for the maximum inclined angle; the initial decrease was followed by an increase with increasing particle diameter. Apparently, the maximum inclined angle is highly dependent on the Stokes number. When the Stokes number was smaller than 1, the trend decreased, but it increased when the Stokes number was larger than 1.

Table 17. Comparison of maximum particle velocity and maximum particle inclined angle from the surface at a 10m radial distance from nozzle axis in terms of different hover altitudes and particle diameters

Hover altitude (m)	**Particle diameter (μm)**	**Coefficient a**	**Max. velocity (m/s)**		**Max. inclined angle**		**Stokes number**
			One-way	**Two-way**	**One-way**	**Two-way**	
5	1	0.998	2500	2390	1.4°	2.28°	0.07577
	10	0.86	2350	1460	1.2°	2.13°	0.7577
	30	0.54	1640	1050	2.0°	3.14°	2.2732
	50	0.39	1170	800	2.75°	3.86°	3.7887
10	1	0.999	1870	1720	0.47°	0.57°	0.07577
	10	0.92	1780	1625	0.41°	0.53°	0.7577
	30	0.66	1280	1170	1.02°	1.24°	2.2732
	50	0.51	930	860	1.7°	1.93°	3.7887

7.5.3 Dispersal simulation of the eroded particles from the induced crater

Small craters can be formed in the lunar surface either by natural processes, like the impact of an object or by the impingement of the rocket motor plume on the surface. Predicting the trajectories of eroded particles in such circumstances can be useful for the engineering design of a lunar lander. Fig. 72(a) shows a schematic of the lunar lander

module hovering above a small crater induced by plume-surface interaction. The crater dimension in the present simulation was chosen based on the experimental results reported in [223].

Particles with two different diameters, 100 μm, and 1μm, which correspond to St=757 and St=0.0757, respectively, were injected from the surface. As shown in Fig. 72(b), (d), particles with a high Stokes number move with a higher inclined angle, surrounding the lander module, and with a much higher possibility that the eroded particles will strike the lander components. On the other hand, as shown in Fig. 72(c), (e), particles with a low Stokes number move with lower inclined angle, so may not strike the module. Consequently, with increasing particle diameter or Stokes number, more careful consideration will be required to protect the module components from particle impact.

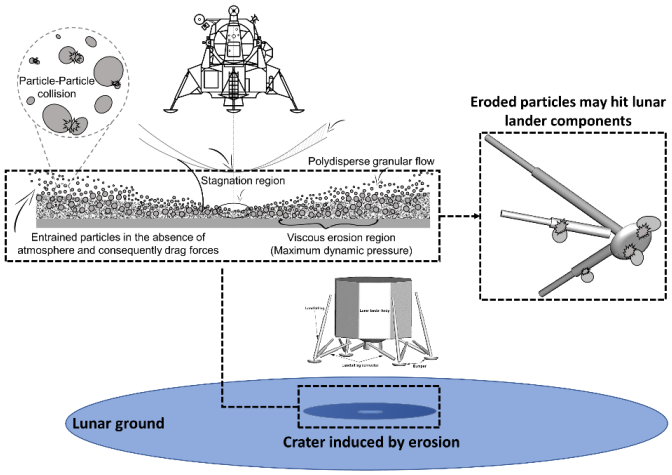

(a) Schematic of the lunar lander module and induced crater

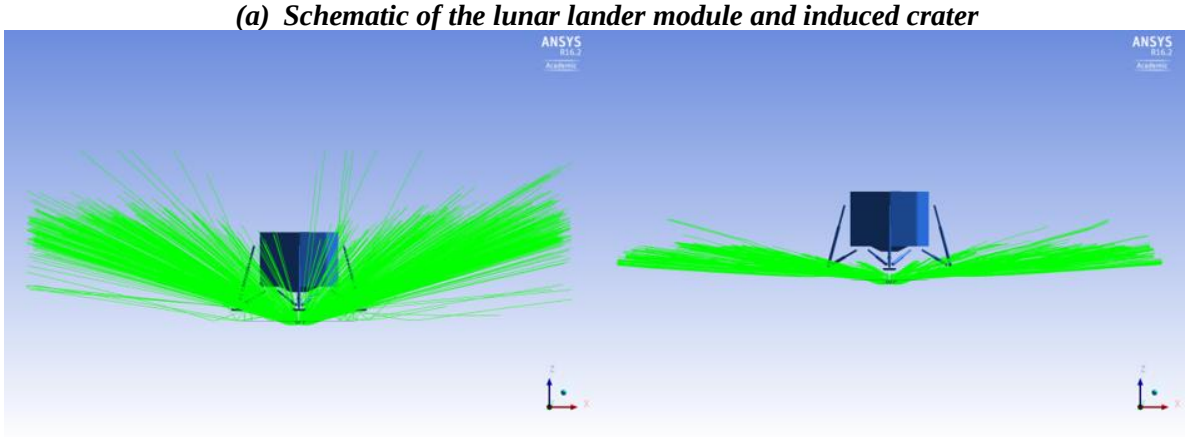

(b) Injected particles with diameter $100\mu m$ *and* $St = 757$

(c) Injected particles with diameter $1\mu m$ *and* $St = 0.0757$

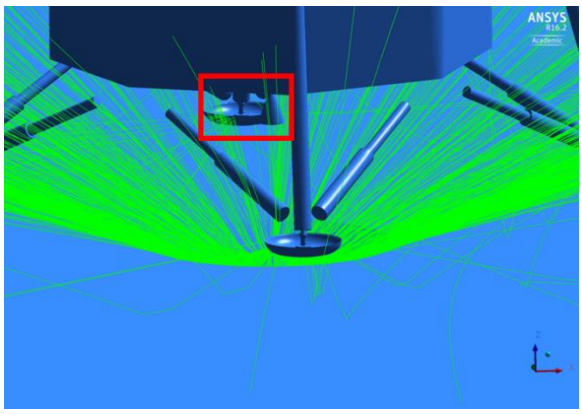

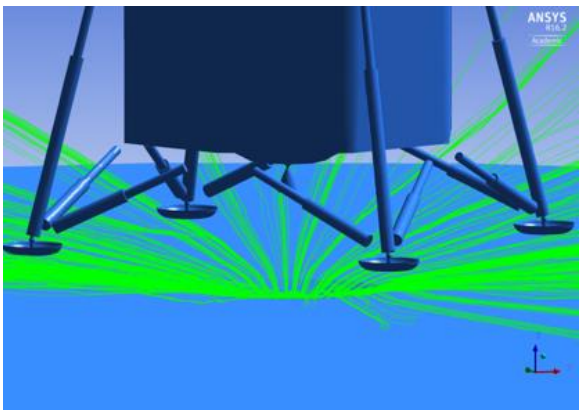

(d) Impingement of particles to the bumper $(100\mu m)$

(e) No impingement of particles to the bumper $(1\mu m)$

Fig. 72. Particle injection from an induced crater underneath of the jet for particle diameters $(100\mu m, 1\mu m)$

Chapter 8. Application of near-vacuum (near-continuum state) conditions in semiconductor fabrication industries

The process of producing the integrated circuits that are used in everyday electrical and electronic devices is called semiconductor device fabrication. The integrated circuit is composed of two critical parts: a tiny and very fragile silicon chip (die) and a package which is designed to afford protection to the internal silicon chip and to provide users with a practical way of handling the component. The process of semiconductor fabrication consists of multiple-step sequence including photolithographic and chemical reaction steps during which electronic circuits are gradually formed on a wafer composed of pure semiconducting material. Semiconducting material that is used mostly is Silicon;

however, depend upon the application different compound semiconductors can be employed.

It is estimated that the whole manufacturing mechanism takes six to eight weeks from beginning to packed chips ready for shipment. The process is performed under highly accurate procedures and is conducted by highly specialized facilities called foundries or fabs. In the case of more sophisticated semiconductor devices, such as modern 14, 10, 7 nm nodes, the fabrication process may last up to 15 weeks; Where, all the steps in producing such devices are completely automated and took place in a hermetically sealed, surrounded by nitrogen environment to improve the products (number of working microchips versus the number of microchips made in a wafer) with FOUPs. Furthermore, the transportation of wafers from a machine to another one is conducted by automated material handling systems.

8.1 Applications and field of use

Semiconductors are made up of materials that have electrical conductivity between conductors such as most metals and nonconductors or insulators such as ceramics. Based on materials and the mixture content, it is possible to estimate the magnitude of electricity conducted by the semiconductor. They can play an insulator role in low temperatures and conversely as a conductor in high temperatures.

These materials are the bases of modern-day electronics such as radio, computers, and mobile phones. The semiconductor material is applied in the manufacturing of electrical components and used in electronic devices such as transistors and diodes. These materials can be divided into two major classes known as intrinsic semiconductors and extrinsic semiconductors. An intrinsic semiconductor material, which is a single element not mixed with anything else, is very pure and characterized with poor conductivity. On the

other hand, the extrinsic semiconductor material is contaminated by small amounts of impurities through a process called doping, which causes changes in the conductivity of this material. The process of contamination generates two groups of semiconductors, which are known as the negative charge conductor called as n-type and the p-type, which is a positive charge conductor.

The conductivity of semiconductors can be altered by temperature changes as well as the impurity content. Such properties may be helpful in producing devices with certain electrical features by combining various semiconductors, which provides electrical signal control. It is challenging to imagine a world without electronics if semiconductor materials were not explored. Although the vacuum tubes can be used as an alternative for them, employing semiconductors has made electronics faster, reliable, and a lot smaller in size. Also, they have provided the opportunity of manufacturing different electrical devices with distinguished capabilities which can be used for various purpose. For instance, temperature sensors used in air conditioners are made with semiconductors. The temperature is precisely controlled in rice cookers because of the semiconductors. Personal computers operation which is handled by CPUs also consists of the semiconductors. Several digital consumer products in everyday life, such as mobile phones, smartphones, digital cameras, televisions, washing machines, refrigerators, LED bulbs, and OLED displays also employ semiconductors.

8.2 Processes of fabricating semiconductors

In the manufacturing of the semiconductor devices, the various steps of the process are divided into four general groups, including deposition, removal, patterning, and modification of electrical properties.

A deposition is called to a process in which the materials are transferred, grown, or coated onto a surface known as substrate/wafer. This process can be conducted by

available technologies such as physical vapor deposition (PVD), chemical vapor deposition (CVD), electrochemical deposition (ECD), and molecular beam epitaxy (PVD). Moreover, recently, the industries tend to use a new technique known as atomic layer deposition (ALD). Indeed, a better definition of deposition is the formation of the oxide layer by thermal oxidation. For instance, local oxidation of silicon (LOCOS) is a process in which a thin layer of silicon dioxide is grown on a silicon wafer.

In the *removal* process, the surface of the wafer has been cleaned from any materials the following examples are falling into this category: etch processes (either wet or dry) and chemical-mechanical planarization (CMP).

The interest shape and formation of the deposited materials are defined in the *patterning* process, which is generally referred to as lithography. As an example can be given in conventional lithography where a chemical coated wafer known as photoresist is passed through a stepper machine. In this step, the stepper machine moves a mask from the exposing selected surface of the wafer below to short wavelength light. Then, the exposed regions are washed away by using a developer solution. If still, some photoresist is remaining, plasma ashing removes the rest.

Modification of electrical properties has comprised of doping transistor sources and drains in which the process is conducted via diffusion furnaces and ion implantation. This process is extended to the reduction of a material's dielectric constant in low-k insulators by being exposed to ultraviolet light in UV processing. The modification of electrical properties is constantly obtained by oxidation by which it is possible to produce semiconductor-insulator junctions. A clear example would be local oxidation of silicon in order to manufacture metal oxide field effect transistors.

8.3 Organic light emitting dude (OLED)

An OLED is a solid-state device or electronic device that typically made up of organic thin films sandwiched between two thin film conductive electrodes. The emission of bright light appears once the electrical current is applied. Owing to use of carbon-based designer molecule, an OLED emits light when an electric current pass through it. This phenomenon is known as electro phosphorescence.

The dimension of such thin layered system is estimated less than 500 nm or about 200 times smaller than a human hair. Generating self-luminous displays by OLED technology is free of using backlighting results in more energy efficient. These features not only make the displays thin and compact but also, they are capable of providing low power requirement for displays, i.e., only 2-10 volts.

OLED technology benefits from using substances that emit red, green, blue, or white light. OLED materials just by applying the substances above and without any other source of illumination, they present bright, clear video and images that are visible at almost any angle. It is observed that one can control the brightness of an OLED by applying certain amount of power to the system. Therefore, one way to handle the brightness and the color of light is to enhance the organic material.

An OLED consists of the following parts:

Substrate (clear plastic, glass, foil)-The substrate is a place where organic materials are deposited on it.

Anode(transparent)- when current flows through the device, it removes electrons (adds electron holes).

Organic layers- These layers are composed of organic plastic molecules that transport holes from the anode. A conducting polymer is used in OLEDs known as polyaniline.

Emissive layer- It is made of organic plastic molecules (different ones from the conducting layer) that transport electrons from the cathode; this is where light is made. The polymer that is used in the emissive layer is polyfluorene.

Cathode (may or may not be transparent depending on the type of OLED) -The cathode injects electrons when current flows through the device.

8.4 Applying organic materials into the substrate

The major part of manufacturing OLEDs is applying the organic layers to the substrate. This technique can be conducted through three methods:

8.4.1 Vacuum deposition or vacuum thermal evaporation (VTE):

In a vacuum chamber, the evaporated organic molecules are allowed to condense as thin films onto cooled substrates. This process is suffered from high cost and inefficiency.

8.4.2 Organic vapor phase deposition (OVPD)

In low pressure, hot-walled reactor chamber, a carrier gas transports evaporated organic molecules onto cooled substrates, where they condense into thin films. The advantage of using a carrier gas is that it increases efficiency and provides low-cost OLED manufacturing. In the OVPD process, an inert carrier gas is employed in order to precisely transfer films of organic material onto a cooled substrate in a hot-walled, low pressure chamber. It should be mentioned that the organic materials are stored in external, separate, thermal-controlled cells. When evaporated from these heated cells, the materials are entrained and transported by an inert carrier gas such as nitrogen. This process can be controlled by using a gas flow rate, pressure, and temperature. The materials deposit down onto the cooled substrate from a manifold located

only several centimeters above the substrate.

Higher deposition rates: compared to the conventional processes, i.e., VTE, OVPD benefits from high deposition rates, which could be several times higher than the rate in counterpart. The reason is that the deposition rate in the OVPD process is primarily controlled by the flow of the carrier gas.

Higher materials utilization: In the OVPD process, since the organic materials do not deposit on the heated surfaces of the chamber, materials' utilization is much higher compared to VTE, where the materials are deposited everywhere.

Better device performance: The OVPD process can provide satisfactory film thickness control and uniformly over larger areas compared to the VTE. By using three variable process control, OVPD offers more precise deposition rates and doping control at very low levels. Consequently, sharper or graded layer interfaces can be more effortlessly obtained. Furthermore, it provides co-deposition of multiple materials in one chamber without the cross-contamination problems which has been observed in VTE systems.

Shadow mask patterning: OVPD offers higher shadow mask-to-substrate distance control than is possible with VTE up-deposition. Because the mask is above, instead of below the substrate, its thickness can be dictated by the desired pattern shape rather than the need for rigidity. Hence, rigorous reproducible pixel profiles can be achieved.

Larger substrate sizes: Since the Aixtron AG-proprietary showerhead can be modeled to maintain a constant source-to-substrate distance, OVPD may be more readily scaled to larger substrate sizes.

8.4.3 Inkjet printing

With inkjet technology, OLEDs are sprayed onto substrates just the same as the process of spraying the ink onto paper during printing. Inkjet technology significantly declines the cost of OLED manufacturing and allows OLEDs to be printed onto very large dims for large displays like 80-inch TV screens or electronic billboards.

8.5 Vacuum deposition processes

Vacuum deposition is a process of surface engineering treatment where layers of materials are deposited onto a substrate. The thin layers on the surface could be included as metal coatings (e.g., copper, nickel) and nonmental coatings (e.g., ceramic matrix composites of carbon/carbon).

Vapor deposition is called to a technology that put materials into a vapor state by condensation, chemical reaction, or conversion. A well-known technique which is called physical vapor deposition (PVD) is one of the subsets of vapor deposition technology. In this process, the vapor phase is generated by condensation from a liquid or solid source. On the other hand, the process is known as chemical vapor deposition (CVD) when the vapor phase is produced by chemical reaction. The above-mentioned technologies are typically carried out in a vacuum condition with or without the use of plasma (i.e., extracted particle by ionized gas), which provide kinetic energy to the surface instead of adding thermal energy. It also allows for processing temperature decrement.

8.5.1 Advantages of the vacuum environment

The vacuum condition provides the following desirable features:

i. *Long mean free path for collision by reducing the particle density*
ii. *Reducing the particle density of contaminants (undesirable atoms and molecules)*
iii. *Serving low-pressure condition*
iv. *Handling gas and vapor composition*
v. *Handling the mass flow into the processing chamber*

In the vapor deposition technology, the energy, as well as material, are added onto the surface. By doing so, the bulk of the object is relatively kept cool without any changes.

Consequently, surface features are generally refined free from significant alteration to the underlying microstructure of the substrate.

8.5.2 Different types of vacuum deposition

The main subsets of the vacuum deposition are as follows:

8.5.2.1 **Physical vapor deposition (PVD)**

The important characteristic of this method is that deposition of coating layers onto a surface is not restricted to a certain area, but it will cover the entire object. The whole hard deposition processes of PVD is combined in:

i. A method for coating the metal
ii. An active gas including nitrogen, oxygen, or methane
iii. A dense and hard coating is the result of plasma bombardment of the substrate

The PVD technology can be classified into four different methods such as ion plating, ion implantation, sputtering, and laser surface alloying. The consequence of each method would vary in metals and plasma. It is worth mentioning that no chemical reaction occurs during the process, and the gasified material condenses on the surface to produce the desired thin film.

8.5.2.2 **Chemical vapor deposition (CVD)**

The deposition of material takes place on substrate in such a way that a chemical reactant gas mixture, which contains carrier gas and vapor material, interacts with the surface. Like it, a vapor is delivered by what is known as a precursor. It can be formed as a gas, liquid, or solid. Under normal pressure and temperature, the gas form can be transferred to the chamber. However, the solids and liquids are fed to the chamber under high temperature and low-pressure condition.

It is possible to accelerate or assist the decomposition of the gas mixture on the surface via the use of heat, plasma, or other methods. The processes in chemical vapor deposition

are comprised of sputtering, ion plating, plasma-enhanced, low-pressure CVD, laser-enhanced CVD, active, reactive evaporation, ion beam, laser evaporation, and other variations. The major difference in the processes mentioned above arises from the initiated chemical reactions and also the classification of operating pressure.

i. High vacuum (below 10^{-6} Pa)
ii. Low-pressure at sub-atmospheric pressures
iii. Atmospheric pressure

The following steps take place in the CVD process, once the energy is transferred to the substrate in order to assist the progress of coating reaction with the carrier gas.

i. Generation of the reactive gas mixture
ii. Transportation of the mass the reactant gas through a boundary layer to the substrate
iii. Adhesion of the reactants on the substrate
iv. Deposit formation owing to reaction of the absorbents

The deposition reactor chamber must be free from any contamination such as dust and moisture. Moreover, it must be clean and leak tight. In addition to the chamber's concern, the substrate itself requires pretreatment including mechanical and/or chemical cleaning (e.g., ultrasonic cleaning and/or vapor degreasing) followed in some test cases by vapor honing (to enhance adsorption).

The most common applications of the CVD technology can be found in electronics optical, optoelectrical, photovoltaic, and chemical industries.

8.6 Numerical analysis of simulating simplified geometry

Simulation of the coating process in OLED deposition is challenging due to the variation in length scale, pressure changes, and a high number of degrees of freedom. The

numerical simulations of OLED deposition in CVD process under near-vacuum/vacuum condition were mostly conducted by the DSMC method. Since in the above-mentioned technology the process is dealing with heavy molecules (e.g., Sio_2, Alq_3) the degree of freedom (*f*) plays an important role in DSMC calculations. In this work, we tend to initiate a new approach where the gas mixture in the condition of near-vacuum/vacuum is going to be solved by a continuum-based equation solver.

8.6.1 Physical properties of gas species

Due to the lack of experimental information, the physical properties of the gas species, particularly in the case of heavy molecules employed in the CVD process, can be calculated from kinetic theory. The density ρ_i of a gas species *i* which considered as ideal gas can be defined as

$$\rho_i = \frac{p_i m_i}{RT} \tag{123}$$

where *m* and *R* are molecular mass for each gas species and the universal gas constant, respectively. Calculation of transport properties, including thermal conductivity and dynamic viscosity are highly temperature dependence and free from pressure effects in CVD. These parameters can be estimated via kinetic theory for less common gases while experimental data are available for well-known gases such as Ar, N_2, and He. To this end, some assumptions on the intermolecular potential energy function $\varphi(r)$ are required. The Lennard-Jones potential was proposed as an accurate intermolecular potential energy function as well as commonly used for non-polar molecules in which the potential energy of interaction between two non-bonding atoms or molecules based on their distance of separation is described:

$$\varphi(r) = 4\varepsilon[(\frac{\sigma}{r})^{12} - (\frac{\sigma}{r})^{6}] \tag{124}$$

where σ the collision diameter of the molecules, r is the distance between the molecules, and the maximum energy of attraction is defined by ε. Using the Lennard-Jones potential, the gas species i is classified by three factors including the mole mass m_i, the collision diameter σ_i, and the maximum energy of attraction usually shown as $(\varepsilon/k)_i$ with dimension in kelvin. In this formula, k represents the Boltzmann's constant. The value of these parameters for some gases which are used in the CVD process is provided in Appendix D.

As it is mentioned in [224] a reduced temperature is defined by T^* as

$$T_i^* = \frac{T}{(\varepsilon / k)_i} \tag{125}$$

Moreover, a temperature dependence integral function $\Omega_\mu(T^*)$ is provided where the polynomials calculation of Ω_μ can be found in Appendix D. Therefore, it is possible to determine the dynamic viscosity and thermal conductivity of the gas species as follows:

$$\mu_i = 2.6693\times10^{-6}\frac{(m_i T)^{1/2}}{\sigma_i^2 \Omega_\mu(T_i^*)} \tag{126}$$

$$\kappa = \frac{R}{m_i}[\frac{15}{4} + 1.32(\frac{C_{pi} m_i}{R} - \frac{5}{2})]\mu_i \tag{127}$$

Physical properties of some of CVD gases are tabulated in Table 18 by which the preliminary numerical simulation can be conducted.

Table 18 Physical properties for some CVD gases at T=294 (K)

	Molecular weight (m) [kg/kmol]	Specific heat ratio (γ)	Bulk viscosity ratio (f_b)	Prandtl number (Pr)	Viscosity index (s)	Gas constant (R) [J/(kg.K)]	Heat capacity (c_p) [J/(kg.K)]	Viscosity coefficient [kg/(m.s)]	Thermal conductivity (k) [w/(m.K)]
Ar	39.948	1.667	0	0.667	0.81	208.24	521.93	2.25E-05	1.76E-02
N_2	28.0134	1.4	0.8	0.7368	0.74	296.91	1041.716	1.74E-05	2.62E-02
SiF_4	104.0791	1.128	N/A	0.8758	N/A	79.886	703.9742	1.58E-05	1.52E-02
WF_6	297.83	1.0753	N/A	0.9195	N/A	27.917	398.818	1.71E-05	9.19E-03

8.6.2 Physical properties of the gas mixture

The characteristics of the gas mixture, including thermodynamic properties, are essential to be estimated. One of the key features of the thermodynamic properties, which must be defined, is the ratio of the heat capacity know as Gamma (γ). To determine the Gamma, two methods are suggested as follows:

The *first approach* is taking care of Gamma calculation by knowing the exact value of the degree of freedom. As it is shown for the ideal gas, the relation between heat capacity ratio and degree of freedom can be written as

$$\gamma = 1 + \frac{1}{f} \tag{128}$$

Thus, based on the above formulation for a monoatomic gas, with three degrees of freedom γ=1.666. While for a diatomic gas, with five degrees of freedom γ=1.4.

The Gamma of a mixture where a chemical reaction takes place (e.g., CVD process) can be defined as the *second approach* by calculating the equivalent heat capacity in constant pressure and the gas constant.

Consider a homogeneous mixture of gases where reactants and products associated with several moles to balance the equation. Suppose the number of moles of products is n_i where i indicates each product. The summation of the product moles is $n = \sum_i n_i$. Therefore, the mole fraction of each constituent can be written as $y_i = n_i/n$. Hence, the equivalent heat capacity in constant pressure can be defined by either

$$C_{p,m} = \frac{1}{n}\sum_i n_i c_{p_i} \tag{129}$$

Or

$$C_{p,m} = \sum_i y_i c_{p_i} \tag{130}$$

Where c_{pi} is the heat capacity for each product.

The Gamma of the mixture is determined in terms of the gas constant and equivalent heat capacity as follows:

$$\gamma = \frac{1}{1 - \frac{R}{C_{p,m}}} \tag{131}$$

Calculation of the viscosity has been extended by the kinetic theory of Chapman and Enskog for low-pressure multicomponent gas-mixtures, but since they are quite complicated and rarely used, here, we just describe the simplified rigorous theoretical expression including Wilke's method [225] which is tabulated in Table 19. The empirical relation of thermal conductivity in the low-pressure condition is defined in the form of the theoretical relation that has been proposed for mixture viscosity by Wassiljewa equation [226]. The formulations are summarized in Table 19. The other features of gas-mixture that should be defined is bulk viscosity, particularly since the constituents are not monoatomic gases. In such circumstances, mechanical pressure differs from thermodynamic pressure as it is shown below:

$$p_{mech} = p_{therm} - (\lambda + \frac{2}{3}\mu)\, div\mathbf{V} \tag{132}$$

In the current study, three-dimensional simplified test cases are adopted to produce a preliminary solution for OLED deposition. In order to validate the three-dimensional DG inhouse code, a lid-driven cavity problem was investigated. In the next step, cylindrical Couette flow along with slip and temperature jump boundary condition was studied by taking advantage of ANSYS FLUENT. Lastly, flow on a simplified rotating substrate which was exposed to a flow came from inlet boundary was investigated to check the uniformity of flow on the substrate by adopting three-dimensional DG inhouse code and ANSYS FLUENT.

Table 19 Defining thermodynamic properties and transport coefficients of gas-mixture in low-pressure condition [227]

	Mixture properties	Remarks	
Heat capacity of mixture	$C_{p,m}=\sum_i y_i c_{p_i}$	✓ y_i the mole fraction of *i*, ✓ C_{pi} heat capacity of *i* component	
Heat capacity ratio of mixture	$\gamma_m=\frac{1}{1-\frac{R}{C_{p_{,m}}}}$ *or* $\gamma_m=1+\frac{1}{f}$	✓ R the gas constant, ✓ f degree of freedom	
Viscosity of mixture	$\mu_m=\sum_{i=1}^{n}\frac{y_i\mu_i}{\sum_{j=1}^{n}y_j\phi_{ij}}$	$\phi_{ij}=\frac{[1+(\mu_i/\mu_j)^{0.5}(M_j/M_i)^{0.25}]^2}{[8(1+M_i/M_j)]^{0.5}}$ $\phi_{ji}=\frac{\mu_j}{\mu_i}\frac{M_i}{M_j}\phi_{ij}$	✓ μ_i the viscosity of pure i, ✓ M_i the molecular weight ✓ y_i the mole fraction of *i*, ✓ ϕ is the interaction parameter for gas-mixture viscosity
Thermal conductivity of the mixture	$\kappa_m=\sum_{i=1}^{n}\frac{y_i\kappa_i}{\sum_{j=1}^{n}y_jA_{ij}}$	$A_{ij}=\frac{\varepsilon[1+(\kappa_{tr_i}/\kappa_{tr_j})^{0.5}(M_i/M_j)^{0.25}]^2}{[8(1+M_i/M_j)]^{0.5}}$ $\frac{\kappa_{tr_i}}{\kappa_{tr_j}}=\frac{\mu_i}{\mu_j}\frac{M_j}{M_i}$	✓ κ_i thermal conductivity of pure *i*, ✓ A_{ii}=1, ✓ κ_{tr} monatomic value of the thermal conductivity, ✓ ε numerical constant near unity
Bulk viscosity	$\mu_b=\lambda+\frac{2}{3}\mu_m$	✓ second coefficient of viscosity (λ) [105].	

8.6.3 Three-dimensional lid-driven cavity flow

The schematic of the lid-driven cavity and adopted boundary conditions are provided in Fig. 73. All the simulations were conducted by Mach=0.16 and temperature as T=237 k, and the characteristic length is fixed to one. Kn number and Re number were changed based on the initial operating pressure.

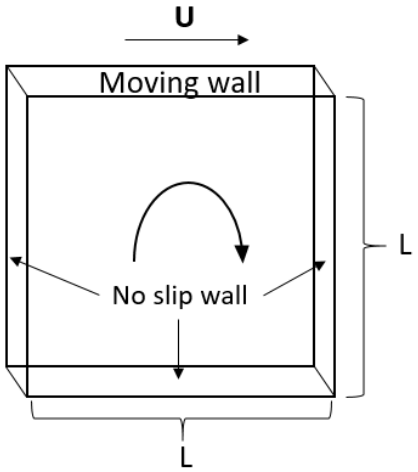

Fig. 73 Schematic of adopted boundary conditions in lid-driven cavity problem

The results were validated by comparing with experimental data provided by [228]and showed good agreement. As it is observed in Fig. 74, by decreasing the Re number (Kn increment) the streamline, as well as v velocity, tend to be symmetry. This phenomenon can be found in the contours of Mach, pressure, and temperature, which are depicted in Fig. 75.

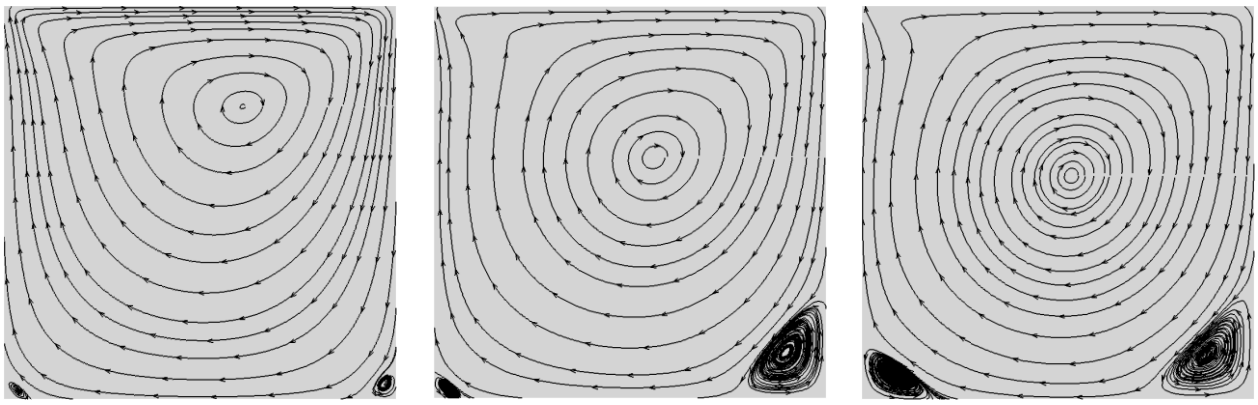

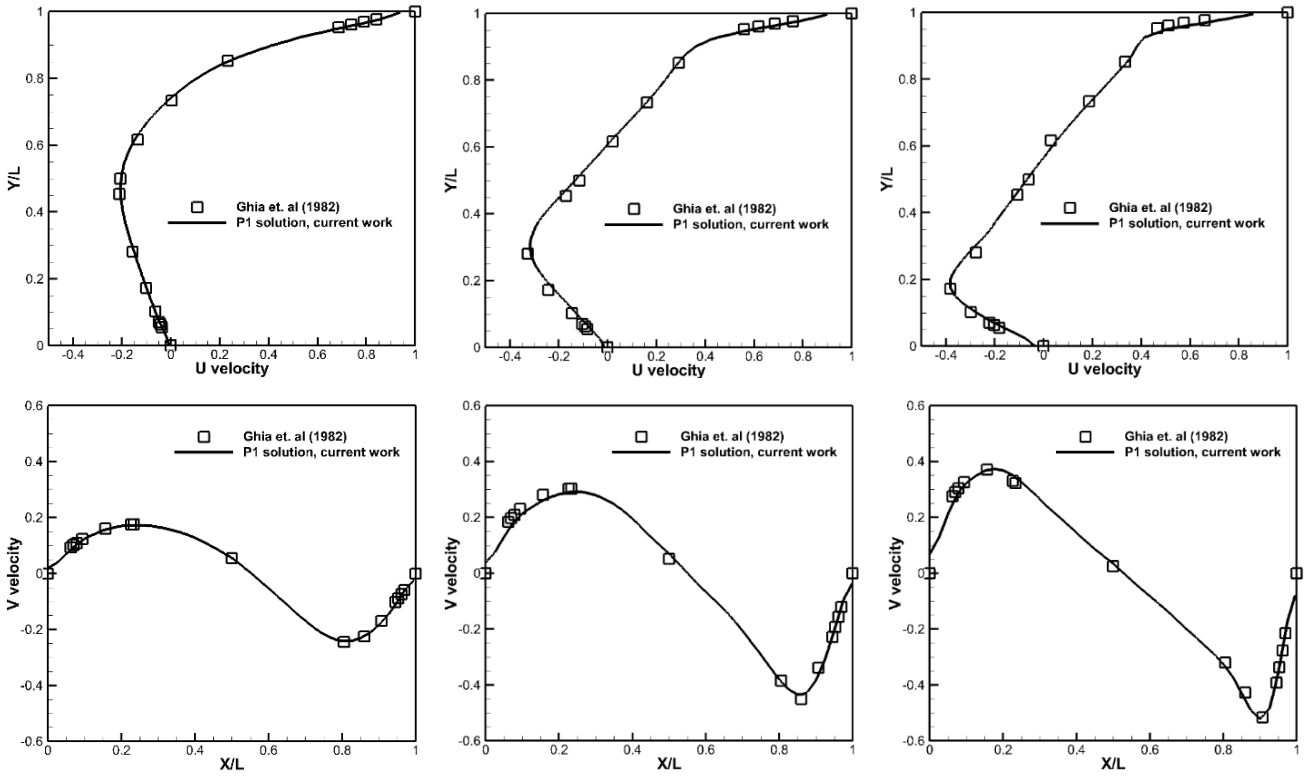

Re=100, *Kn*=2.022E-3 Re=400, Kn=5.054E-4 Re=1000, Kn=2.022E-4

Fig. 74 Streamline, U and V velocity in lid driven cavity for different Reynolds and Knudsen numbers at Mach=0.16

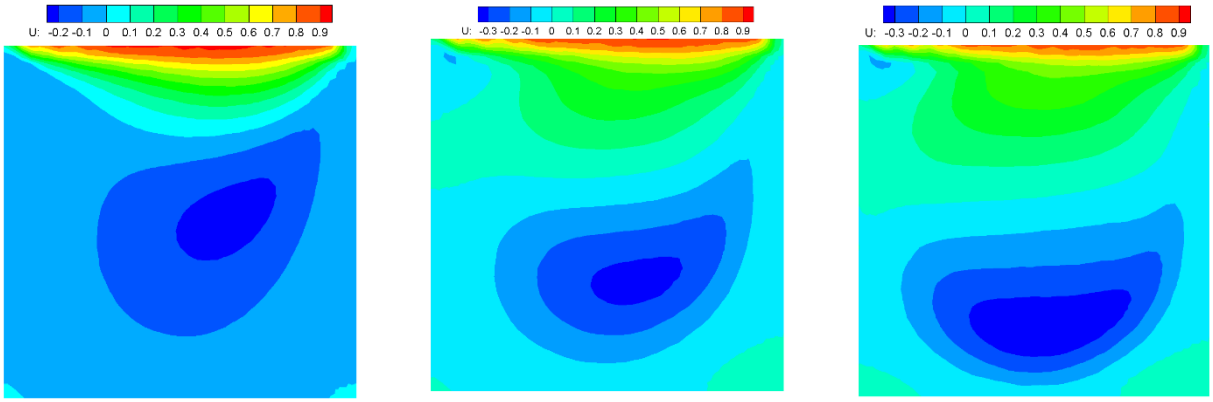

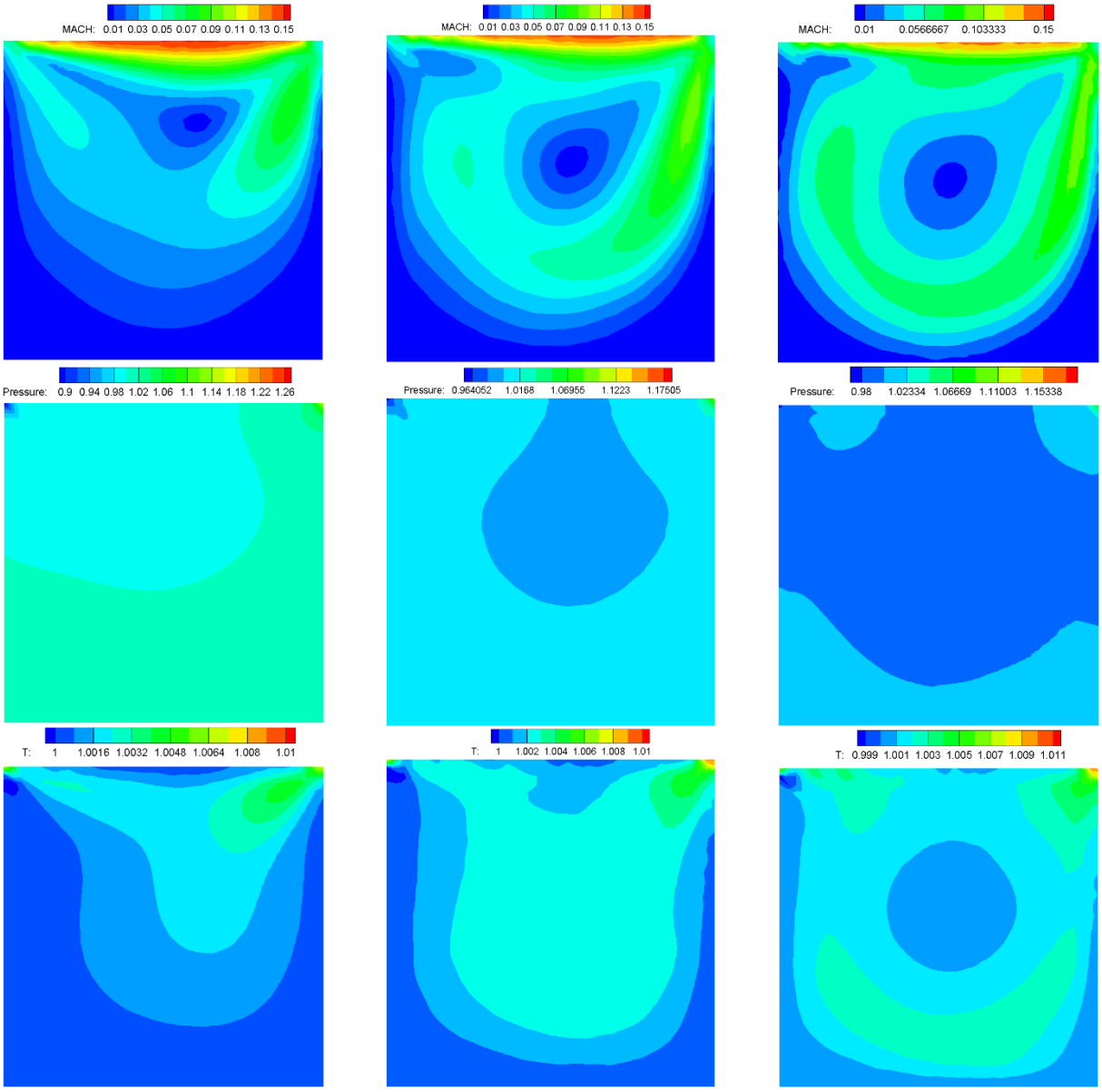

Re=100, *Kn*=2.022E-3 Re=400, Kn=5.054E-4 Re=1000, Kn=2.022E-4

Fig. 75 Contours of U velocity, Mach, pressure, and temperature in lid-driven cavity for different Reynolds and Knudsen numbers at Mach=0.16

8.6.4 Three-dimensional cylindrical Couette flow

We conducted a simulation for cylindrical Couette flow where two concentric cylinders are considered in such a way that the inner is rotating and the outer one is stationary. In this problem, the Kn number is defined by the ratio of the mean free path to a characteristic length where the latter is the distance between two cylinders. It is worth

mentioning that since the Kn is high, there is a need for applying different boundary, including slip wall and temperature jump. To this end, two different slip wall boundary conditions are summarized below. It should be mentioned that in the current study, Maxwell boundary condition is applied to the numerical simulations.

8.6.4.1 **Langmuir condition**

In the Langmuir slip conditions, a gas molecule that gets adsorb is known as "adsorbate," and the surface is called as "adsorbent" [229]. This process of adsorption is described through Langmuir adsorption isotherm [219], where the fraction of adsorbate on the adsorbent is related to the function of gas pressure at a constant temperature.

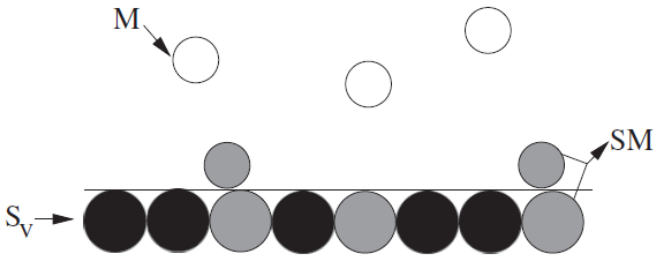

Fig. 76 Langmuir adsorption

The Fig. 76 above shows the sketch of Langmuir adsorption isotherm model, where *M*, *V*, and *MV* are the free gas molecules, vacant surface site (adsorbate) and the occupied surface site (adsorbate). This process can be written through the chemical reaction of gas-surface interaction as:

$$M + V \Rightarrow MV \tag{133}$$

Where the site of occupied surface (*MV*) is proportional to the fraction (α) which is given as,

$$\alpha = \frac{\bar{\beta}}{1+\bar{\beta}}, \qquad \bar{\beta} = \frac{1}{4\omega \mathrm{Kn}},$$
$$\omega = \omega_0(\nu)\left(\frac{T_W}{T_{ref}}\right)^{1+2/(\nu-1)} \exp\left(-\frac{D_e}{k_B T_W}\right),$$
$$\omega_0(\nu) = \frac{8\sqrt{2}}{5\pi} A_2(\nu)\Gamma\left[4-\frac{2}{\nu-1}\right]. \tag{134}$$

Where values of these constants are taken from previous literature [229, 230] based on the gas type, the role of ω is very similar to the slip coefficient (σ) of the Maxwell model.

Using the Langmuir adsorption isotherm, we can re-write the velocity slip and temperature slip conditions as,

$$\mathbf{u}_s = \alpha \mathbf{u}_W + (1-\alpha)\mathbf{u}_g,$$
$$T_s = \alpha T_W + (1-\alpha)T_g. \tag{135}$$

Where the subscripts g and w are the value adjacent to the wall and value at the wall, respectively. In the case of cylindrical Couette flow, we have the modified form of Langmuir conditions of [231],

$$\mathbf{u}_s = \alpha \cdot \boldsymbol{\omega} r + (1-\alpha)\mathbf{u}(\bar{r})\frac{r}{\bar{r}},$$
$$T_s = \alpha T_W + (1-\alpha)T(\bar{r})\frac{r}{\bar{r}},$$
$$r = \sqrt{(x^2+y^2)}, \ \theta = \tan^{-1}\left(y/x\right). \tag{136}$$

Here $\bar{r}$ is the radius of reference position given by,

$$\bar{r}^2 = r_o\left[r_i + (r_o - r_i)\left(1-\frac{r_i}{r_o}\right)\right]. \tag{137}$$

This value of the radius of reference is derived analytically using the equation (136).

8.6.4.2 **Maxwell/Smoluchowski conditions**

According to Maxwell/Smoluchowski conditions, gas molecules are considered to approach or recede the solid surface. Their overall effect can be seen on the viscous drag as it is the difference of the tangential momentum of the approaching stream and that of

the receding stream. Additionally, Maxwell introduced the tangential momentum accommodation coefficient (σ_u) to obtain slip velocity. Using the mean molecular velocity and mean free path λ , we can have the Maxwell velocity slip boundary condition as [9],

$$\mathbf{u}_s = \mathbf{u}_w - \left(\frac{2-\sigma_u}{\sigma_u} \right) \cdot \frac{\lambda}{\mu} \cdot \mathbf{\Pi}_W . \tag{138}$$

Here $\mathbf{\Pi}_W$ refers to the tangential (or wall) shear stress.

Similarly, Smoluchowski presented temperature jump condition. Thus the temperature jump condition is determined by introducing a thermal accommodation coefficient (σ_T). By introducing the internal energy of gas and that of surface and the heat conduction equation, we can have the temperature jump condition as [9]:

$$T_s = T_w + \left(\frac{2-\sigma_T}{\sigma_T} \right) \cdot \frac{2\gamma}{(\gamma+1)} \cdot \frac{\lambda}{\mathrm{Pr}} \cdot \mathbf{Q}_W . \tag{139}$$

Where $\mathbf{Q}_W$ refers to the tangential heat flux.

For this test case, the adopted initial conditions are provided by [232] where Mach=0.99, wall temperature on inner cylinder T_inner=303 k, wall temperature on outer cylinder T_outer=311 k, velocity accommodation coefficient is equal to 0.927 and temperature accommodation coefficient is considered as 0.99. The schematic of two concentric cylinders and the boundary conditions are shown if Fig. 77.

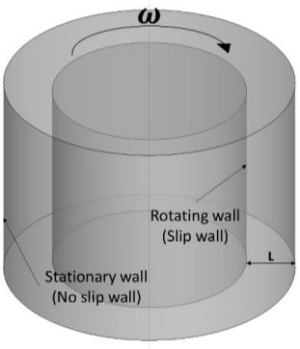

Fig. 77 Schematic of two concentric cylinders and boundary conditions in cylindrical Couette flow problem

As it is depicted in Fig. 78, the results with first order slip are in accordance with experimental data, particularly when Kn=0.0426. However, as Kn increases, which implies that flow falls into the transition regime, the numerical results deviate from experiments. Moreover, a comparison of normalized variables, including velocity, pressure, temperature, density for different Kn number is illustrated in Fig. 79. The results, particularly velocity and temperature profiles, reveal the deviation of no-slip wall from slip wall boundary condition as well as alteration of temperature after implementing temperature jump on the wall condition.

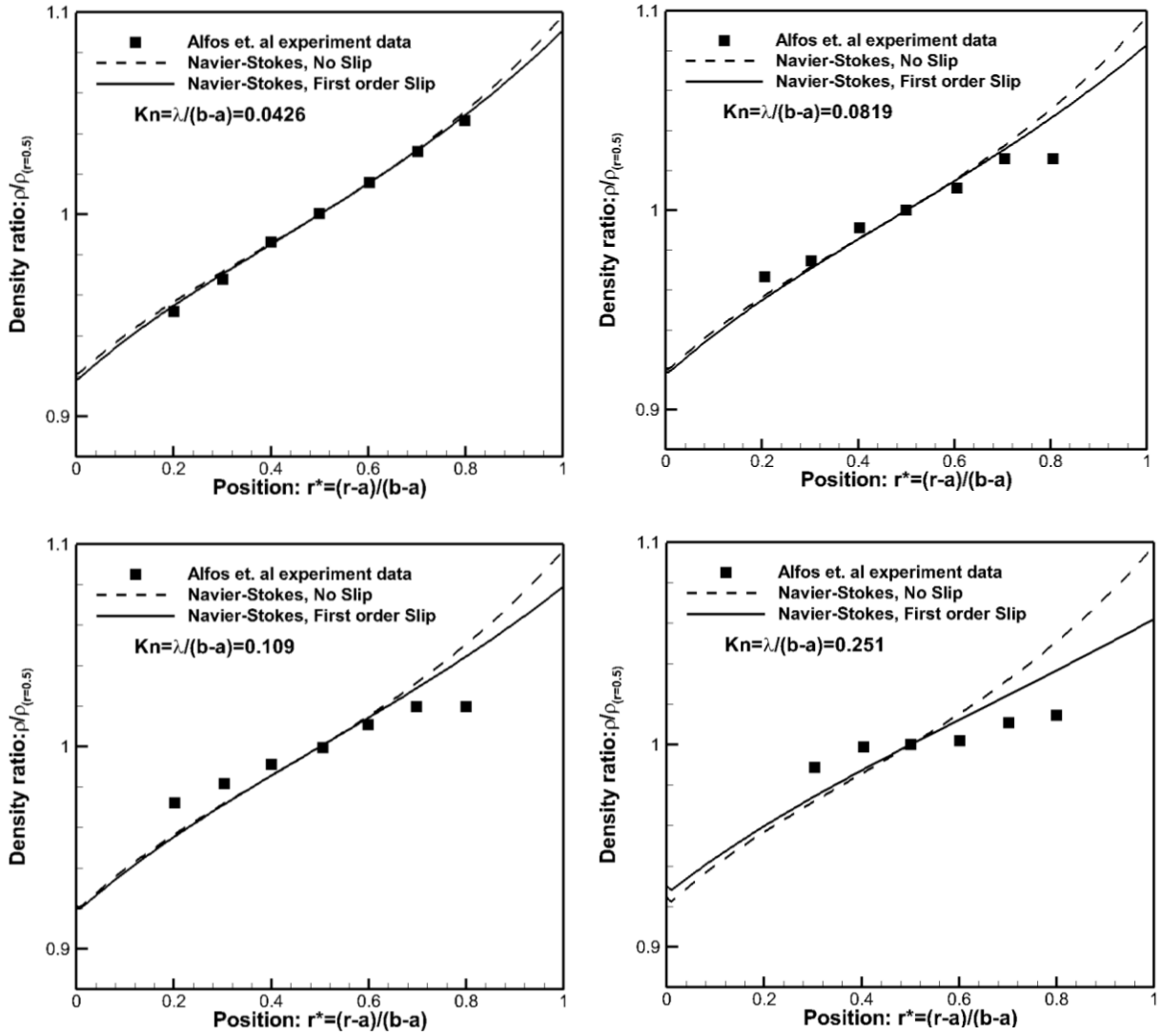

Fig. 78 Density ratio versus position. Comparison between experimental data and numerical results

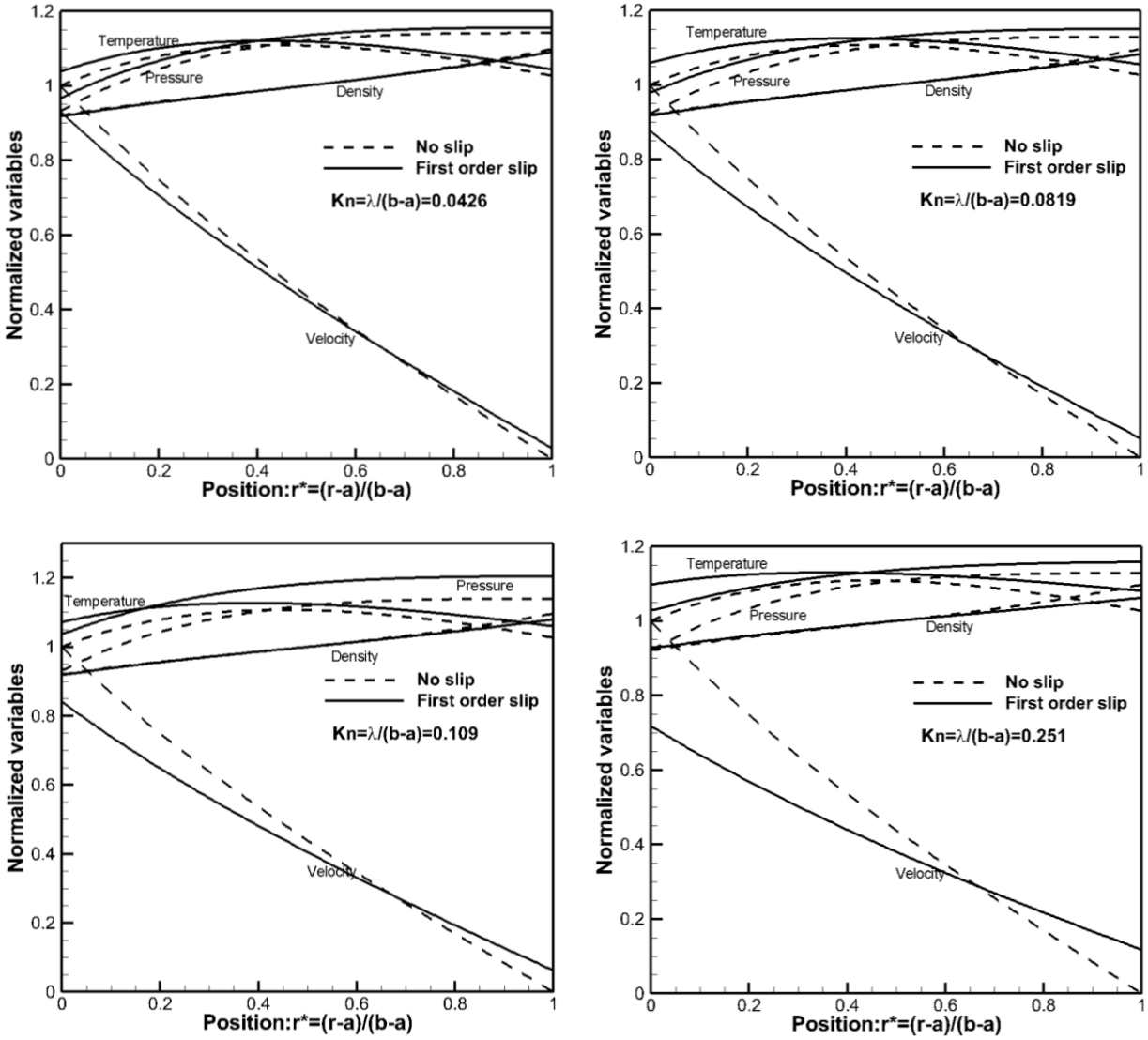

Fig. 79 Normalized variables versus position. Comparison of numerical results between no-slip and slip along with temperature jump

8.6.5 Three-dimensional proposed simplified geometry simulation

In this section, we are focusing on a problem in which the main concern is the distribution of flow on the surface. For this purpose, a simplified geometry is employed, where two concentric cylinders, one as a rotating substrate and the other one is a stationary wall. The substrate is continuously exposed to a flow coming from the inlet

boundary, which is supposed to be a gas mixture carrying organic vapor by precursor gas. The schematic of the initial condition and geometry is illustrated in Fig. 80.

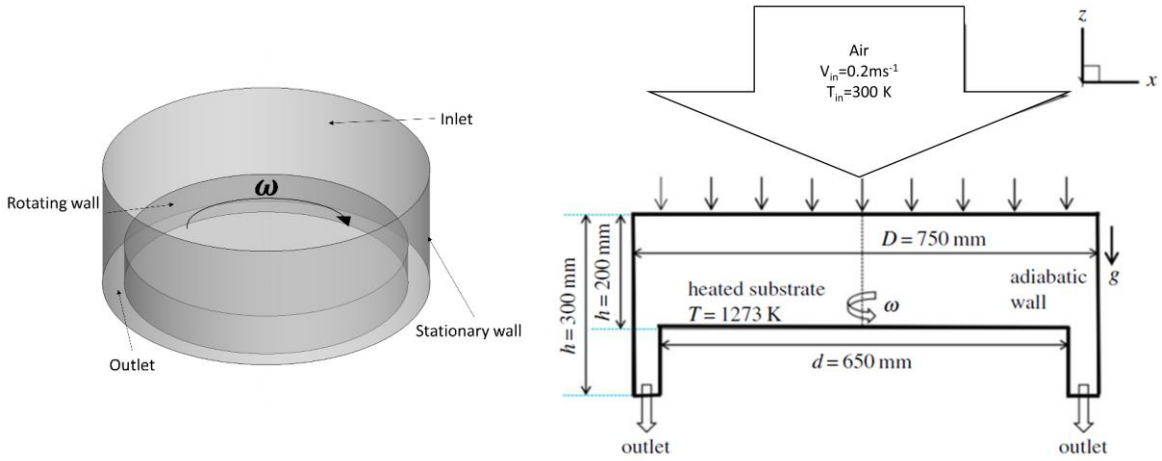

(a) (b)

Fig. 80 Schematic of the initial condition, boundary conditions, and geometry

As it is shown in Fig. 81, the velocity and pressure distributions on the substrate are uniform. It is revealed that as the pressure in the chamber decreases, which leads to the increment of Kn number, the morphology of the surface is enhanced. Another factor that boosts the uniform growth of organic film on the surface is the rotating velocity of the substrate. Indeed, the high rotating velocity of the substrate along with the low velocity of inlet gas mixture has a significant effect on organic material coating onto the substrate.

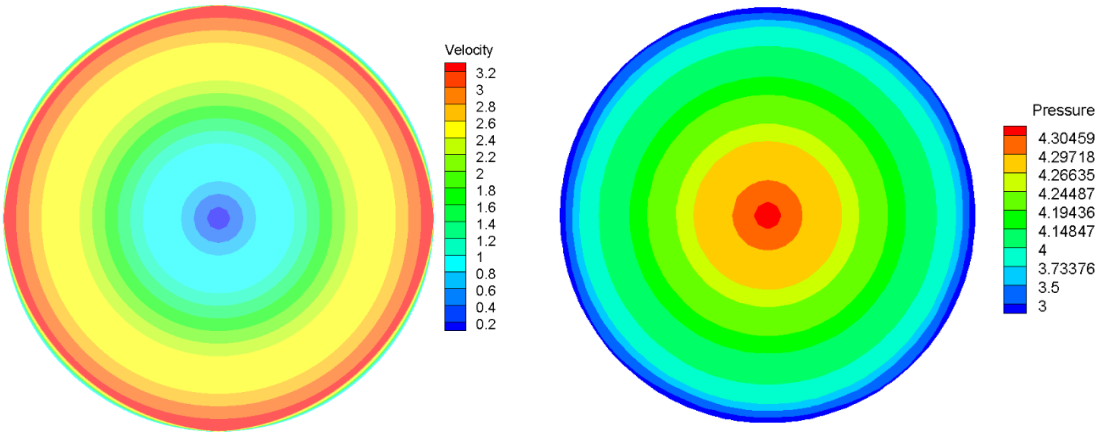

(a) (b)

Fig. 81 Uniform velocity and pressure distribution on the substrate

Chapter 9. Conclusion and future works

9.1 Concluding remarks

In the current dissertation, the Eulerian-Eulerian and Eulerian-Lagrangian approaches were employed to investigate dusty gas flows in a continuum and near-continuum conditions. The research was substantiated by providing a solution to the near-field of plume-surface interaction in the problem of Lunar landing. To grasp more on the physics of multiphase flow, discontinuous Galerkin method was applied to solve the conservation laws in the two-fluid model framework. Application of DG made the treatment of source terms in the two-fluid model equation possible. Various benchmark problems for zeroth-order, first-order models were undertaken with numerical experiments, and these results were discussed in detail.

9.1.1 Conclusions regarding the inviscid flows

In the case of zeroth-order constitutive equations (Euler equations), the complex wave patterns which are rarely investigated in the literature were extensively analyzed. The complex physical phenomena were explained carefully. In particular, it was shown that, when a dust contact discontinuity is present in the dusty gas flow, a pseudo-compound wave, as well as a composite wave, can form. Further, the new DG scheme not only meets the demands of high order accuracy (at least second-order) of simulating dusty gas flows, but it can also handle the tricky source terms of coupling effects between the two phases, without resorting to the complicated operator splitting method commonly employed in the conventional method. In fact, in the study of multiphase flow,

developing a robust DG solver for dusty gas flows has recently been considered a challenging topic which deserves attention.

It turned out that the orthogonality of the basis functions, the backbone of the DG method, again played a critical role in the novel treatment of the high order moments of the polynomial approximations to the source-term. Based on the new DG scheme, various benchmark problems with different physical features in one- and two-dimensional space were studied. In order to elaborate the complex wave patterns in gas-particle flows, the wave propagation mechanisms in the one-dimensional shock tube problem of the dusty gas were first investigated in detail. Several abnormal waves in dusty gas flows—most of them not previously identified—were highlighted and a physical explanation on the origin of such abnormal waves was given.

Also, the new unstructured DG scheme was applied to two different types of problems with and without the presence of boundary effects. The results in both cases were shown to be in accordance with the previous data. The new scheme was then applied to investigate the compression corner problem for both the single and multi-phase applications. Both single and double Mach reflection problems were solved, and the higher order solutions (up to a polynomial order of two) were successfully obtained.

Furthermore, a detailed parametric study on particulate loading and particle diameter size was conducted. Isopycnic surfaces indicated that the particulate loading substantially affects the structure of the double Mach reflection, including the configuration of triple points. The main reason for this change is the amplification of the relaxation region, that is, the main element of the abnormal waves in dusty gas flows. In all cases, it was found that the secondary triple point was much more affected by the dust particles. Moreover, the convex Mach stem formed in the pure gas flow changed into a perpendicular Mach stem in the dusty gas flows. It was found that the particle diameter and mass loading

affect the slope and curvature of the reflected waves as well. While an increase in particle diameter causes the secondary reflected wave to align along the primary wave, the increase in mass loading leads to an increase of the intersection angle of these two waves. It was also found that as the particle diameter and mass loading increases, the structure of the DMR becomes blurrier.

Lastly, The Shardin's problem was considered in order to investigate the effects of the presence of dust particles on the flow in the shock-vortex interaction. It was observed that the fundamental structures observed in the pure gas are also observed in the dusty gas with a time lag. Formation of a dust free region in the core of vortex and a concentrated region on the edge of the vortex was also demonstrated. More detailed parametric studies on solid phase parameters and investigation of transient evolution of the flow may be required for further understanding of these complicated physical phenomena.

9.1.2 Conclusions regarding the viscous flow

Based on axisymmetric formulation, the problem of the particle-laden free under-expanded jet was investigated for the purpose of validating the numerical simulation in capturing multiphase interactions. Even though a slight over-estimation of Mach disk location and jet boundary width was found in the numerical solutions, the important feature of upstream movement of the Mach disk was shown to be in good agreement with experimental results.

The contradictory patterns of location of the Mach disk when solid particles are added into the underexpanded jet predicted in previous works was the main motivation of the current paper. Unlike the previous works which focus only on the diameter of the particles, we proposed that all the parameters which are present in the correlation of the Stokes number can affect the Mach disk location. Among these parameters, the effect of variation of particle diameter and the characteristic length were investigated after the

numerical tool was validated. After demonstrating the counter-intuitive trend of the Mach disk location for different particle diameters, the effect of variation of the Stokes number independently by assigning various characteristic lengths is investigated. It was shown that the Stokes number is the main parameter which controls the mechanism of Mach disk location. For low Stokes, number flows, there is a downstream movement, while for high Stokes number flows, there is an upstream movement. The transition in the trend of Mach disk location takes place around Stokes number of 1 where the response time of the particles is in the same order of the characteristic time of the flow at the nozzle exit plane. It was shown that the effect (either upstream or downstream movement) is amplified when the particulate loading is increased.

Moreover, the deviation of the numerical results from experiments which can be modified by assigning a reduced (equilibrium speed) velocity at the exit plane of the jet was investigated. In a realistic test case (or an experimental setup) the gas and particles interact before exiting into the ambient; Therefore, the exit gas velocity is less than that of the pure gas which can substantially affect the structure of the jet. It was also shown that this consideration would lead to Mach disk locations predictions much more close to the experimental results.

9.1.3 Conclusions regarding the near-filed plume-surface interaction and regolith erosion

The impingement of a rocket plume on the lunar surface can cause significant dust dispersal when the lunar lander approaches a landing site. The present study investigated the near-field plume impingement on the dusty surface of the Moon for a proposed lunar lander configuration, using the physical conservation laws, with first-order NSF constitutive relations in the Eulerian framework for the gas phase, and the particle-based DPM in the Lagrangian framework for the solid phase. The effects of the plume-surface

interaction on the lunar lander components were analyzed to provide a more efficient method of obtaining predictive results for engineering design, compared to the computationally expensive DSMC method. Also, by evaluating a non-equilibrium quantifier and a measure directly related to entropy production in non-equilibrium processes, it was shown that most regions in the near-field interaction of the plume (and in particular, multiple plumes) and the lunar surface at low altitude hover were either in equilibrium or near equilibrium.

Simulations of a complicated lunar lander configuration with five nozzles, four bumpers, four landfall legs, and eight connectors were also conducted. The results revealed regions with high pressure and hot spots on the landfall legs, the connectors as well as the bottom of the module, which may impose further design restrictions.

To simulate the surface erosion phenomena and consequent entrainment of regolith grains, particles were injected from the surface with an erosion rate calculated using the Roberts' model based on excess shear stress. The role of the critical parameter in the Roberts' theory—the fraction of velocity that the particles gain from the carrier phase—was investigated for different particle diameters, hover altitude, Mach number of flow, and number density of particles. The simulation results indicated that the maximum particle velocity decreases with increasing particle diameter, irrespective of hover altitudes, and coupling models.

Interestingly, the maximum inclined angle exhibited different behaviors depending on the Stokes number of the flow. For a bed covered with small particles, the corresponding Stokes number is less than 1, and the inclined angle decreased with increasing particle diameter. However, for larger particle diameters with a Stokes number higher than 1, the inclined angle increased with increasing particle diameter.

To investigate the effect of a small crater from which the particles may be entrained into the flow field with higher inclined angle, a case with the lunar lander hovering above a small crater was simulated. The trajectory of grains revealed that the possibility that eroded particles would strike lander components grew with increasing particle diameter. Hence, extra consideration should be taken to protect module components from particle impact in the presence of a crater with larger size particles.

The present work focused on near-field plume-surface interactions and regolith erosion and dispersal defined by low altitude hover, and the use of a first-order NSF model based on the assumption of not-far-from-equilibrium. However, second-order (or higher) gas kinetic models or DSMC may be necessary to provide a more accurate and far-field description of this multi-physics multi-scale problem. We hope to report the investigation of this challenging problem in future work using second-order Boltzmann-based constitutive relations.

9.2 Future works

There are various directions through which this work can be extended. From a modeling point of view extension of the second-order Boltzmann-based constitutive equation for the dust, the phase is an interesting subject. Also a classification of dusty gas flow regimes based on solid phase Knudsen number or a similar parameter like $N_{\delta,}$ which shows the range of validity of the existing models is not available in the literature. The N_{δ} parameter for the gas itself is not well-defined, and the existing ranges are based on insufficient numerical observations. The refining of the Knudsen regimes based on this parameter can be achieved by applying more comprehensive comparisons of classical models with DSMC or NCCR solutions.

From the numerical point of view, a comparison of the previously developed methods for handling the source terms with the current approach or using the current idea in

combination with other methods, for example, with splitting. In Euler-type problems, the non-strictly hyperbolic equations of dust can be converted to strictly hyperbolic by adding a pressure-like term to both sides of the equations. This simple idea has been applied to shallow water equations in the simulation of atmospheric aircraft icing problems and can be equivalently applied in two-fluid equations of dusty gas. In some of the test cases of this work, it was observed that the convergence of the method improves extensively when source terms are present. This feature combined with the idea explained before (adding a term in both sides of the equation) might be useful as a new acceleration method for a specific class of problems.

There are a variety of problems which were discussed very briefly in this thesis, and more extensive investigation of physical features in those problems can be followed in the future. For example, it was observed that in the one-dimensional problem of dusty gas shock tube, a wave is reflected into the high-pressure side. The type of reflected wave depends on the specific heats of the solid particle and gas as well as the particulate loading of the mixture. Reflection of the shock wave was investigated in this work. However, the reflection of the rarefaction wave was not investigated, which can be a topic of future studies. There are various benchmark problems which can be used in the dusty gas framework to provide more fundamental knowledge on the complex behavior of the dusty gas flows.

A number of unsolved issues in the problem of under-expanded jets which has been extensively investigated either experimentally or numerically still exists. These can be poorly managed Mach disk diameter and curvature, the effect of viscous forces on the transition to turbulence as well as interactions with hydrodynamic instabilities [211]. With the efficient and high-order numerical tool developed in this work, not only those issues can be investigated but also more areas where either rarefaction or presence of dust

play a role can be further investigated. Effect of the addition of particles on under-expanded jets which has applications in volcanic eruptions is one of the other directions which can be followed. Asymmetric under-expanded jet can be investigated within the three-dimensional formulation framework. The effect of rarefaction and dust has never been investigated on the structure of these 3D configuration types of flows.

Investigation of dusty gas microflows, pressure impactors are the other directions which can be followed.

More detailed investigations on the Lunar landing problem including parametric studies and inclusion of more accurate erosion models in another direction. Even though in the current study by applying Lagrangian framework the solid phase was modeled separately for different particle diameter, one can take advantage of Lagrangian modeling by providing a simulation regarding eroded particles via conducting particle size distribution. Comparison of the method with Lagrangian counterpart can also provide more details on the strength and weaknesses of the currently developed tool.

Moreover, multiphase turbulent flows can be called an almost new topic in fluid dynamics. The current tool with the incorporation of turbulence models (or approaches) can be used in this area as well. In this case, one of the most interesting problems at hand is the aircraft atmospheric icing. Here, instead of solid particles, liquid droplets or bubbles need to be modeled, and further necessary modifications to simulate the ice formation after collection of droplets on the surface need to be taken into account.

There are other classes of two-fluid models with interphase tracking, and the developed code can be further extended to be applied to problems in which interphase shape and location is important.

Manufacturing techniques in a vacuum and near-vacuum conditions in the semiconductor industry for the production of OLED panels have become extremely

important in the last few decades. Such industries are required to optimize the geometry of the setup to obtain better deposition on the substrates frequently. Therefore, simulation of the problem above can be conducted either by NSF along with slip and temperature jump boundary conditions or by non-equilibrium simulations employing the second-order Boltzmann-based continuum solver developed by Aerospace Computational Modeling Laboratory.

Appendix A. Derivation of conservation laws from the Boltzmann transport equation

The Boltzmann transport equation (BTE) for monatomic, diatomic and linear polyatomic particles known as Boltzmann-Curtiss equation in the absence of external body forces can be written as [233-235],

$$\left(\frac{\partial}{\partial t}+\mathbf{v}\cdot\nabla+\frac{j}{I}\frac{\partial}{\partial\theta}\right)f\left(\mathbf{v},\mathbf{r},t\right)=C\left[f,f_1\right] \tag{140}$$

In the above equation j, I, and θ are the magnitude of the angular momentum, moment of inertia, and azimuthal angle. We derive the conservation laws for the Boltzmann-Curtis, which is an extended version of the Boltzmann equation. The third term in the above relation (and in the rest of the derivation process accordingly) will vanish for the case of monatomic gases.

Before deriving the conservation equations, statistical mechanics definitions of some macroscopic parameters which are necessary for the derivation process are provided in the table below.

Table 20 Statistical definition of macroscopic parameters

Macroscopic quantity	Statistical definition
Number density	$n=\left\langle f\left(t,\mathbf{r},\mathbf{v}\right)\right\rangle$
Density	$\rho=\left\langle mf\left(t,\mathbf{r},\mathbf{v}\right)\right\rangle$
Momentum	$\rho\mathbf{u}=\left\langle m\mathbf{v}f\left(t,\mathbf{r},\mathbf{v}\right)\right\rangle$
Energy	$\rho E=\left\langle\left(\frac{1}{2}mc^2+H_{rot}\right)f\left(t,\mathbf{r},\mathbf{v}\right)\right\rangle$
Stress tensor	$\mathbf{P}=\left\langle m\mathbf{c}\mathbf{c}f\left(t,\mathbf{r},\mathbf{v}\right)\right\rangle$

Shear stress tensor $\mathbf{\Pi} = \left\langle m\left[\mathbf{cc}\right]^2 f\left(t,\mathbf{r},\mathbf{v}\right)\right\rangle$

Excess normal stress $\Delta = \left\langle \left(\frac{1}{3}\mathrm{Tr}\left(m\mathbf{cc}\right) - \frac{p}{n}\right) f\left(t,\mathbf{r},\mathbf{v}\right)\right\rangle$

Heat flux vector $\mathbf{Q} = \left\langle \left(\frac{1}{2}mc^2 + H_{rot} - m\hat{h}\right)\mathbf{c}f\left(t,\mathbf{r},\mathbf{v}\right)\right\rangle$

Differentiating the above statistical definitions introduced above with time and combining with BTE will give the conservation equations and constitutive relations. It should be noticed that the t, **r,** and **v** are independent variables, whereas peculiar velocity is not independent of space and time. Moreover, molecular, average, and peculiar (random) velocities are related by **v**=**u**+**c**. By defining the material time derivative as $\frac{D}{Dt} = \frac{\partial}{\partial t} + \mathbf{u}.\nabla$, equation (140) can be written as,

$$\frac{Df}{Dt} + \mathbf{c}\frac{\partial f}{\partial \mathbf{x}} + \frac{j}{I}\frac{\partial f}{\partial \theta} = C\left[f, f_1\right]. \tag{141}$$

For the derivation of the mass conservation, the Boltzmann-Curtiss equation is multiplied by *m* and integrated over velocity space to yield

$$\left\langle m\frac{\partial f}{\partial t}\right\rangle + \left\langle m\mathbf{v}\cdot\nabla f\right\rangle + \left\langle m\frac{j}{I}\frac{\partial f}{\partial \theta}\right\rangle = \left\langle mC\left[f, f_1\right]\right\rangle. \tag{142}$$

As mass is a collision invariant of BTE the right-hand-side term will be zero:

$$\left\langle m\frac{\partial f}{\partial t}\right\rangle + \left\langle m\mathbf{v}\cdot\nabla f\right\rangle + \left\langle m\frac{j}{I}\frac{\partial f}{\partial \theta}\right\rangle = 0. \tag{143}$$

The above relation can be further simplified as

$$\frac{\partial}{\partial t}\left\langle mf\right\rangle + \nabla.\left\langle m\mathbf{v}f\right\rangle + \left\langle m\frac{j}{I}\frac{\partial f}{\partial \theta}\right\rangle = 0. \tag{144}$$

Curtiss stated that *f* does not depend on the azimuthal angle and it only depends weakly on the position of gas molecules. With the use of a statistical definition of density and momentum in Table 20, we can get the mass conservation equation:

$$\frac{\partial \rho}{\partial t} + \nabla.\left(\rho \mathbf{u}\right) = 0\,. \tag{145}$$

The above equation is the same as the mass conservation form in continuum theory. With a similar approach, it can be shown that the Boltzmann equation fulfills the requirement of the momentum conservation law. This is achieved by differentiation of statistical definition of momentum and use of Boltzmann-Curtiss equation as follows

$$\left\langle m\mathbf{v}\frac{\partial f}{\partial t}\right\rangle + \left\langle m\mathbf{v}\mathbf{v}\cdot\nabla f\right\rangle + \left\langle m\mathbf{v}\frac{j}{I}\frac{\partial f}{\partial \theta}\right\rangle = \left\langle m\mathbf{v}C\left[f, f_1\right]\right\rangle. \tag{146}$$

The other collision invariant of the BTE is the momentum. Therefore,

$$\left\langle m\mathbf{v}\frac{\partial f}{\partial t}\right\rangle + \left\langle m\mathbf{v}\mathbf{v}\cdot\nabla f\right\rangle + \left\langle m\mathbf{v}\frac{j}{I}\frac{\partial f}{\partial \theta}\right\rangle = 0\,. \tag{147}$$

Curtiss's assumption implies that

$$\left\langle m\mathbf{v}\frac{\partial f}{\partial t}\right\rangle + \left\langle m\mathbf{v}\mathbf{v}\cdot\nabla f\right\rangle = 0\,. \tag{148}$$

By substituting the molecular velocity in terms of thermal and macroscopic velocities in the second term, and use of statistical definitions of viscous stress tensor and excess normal stress we get

$$\begin{aligned}
&\nabla.\left\langle m\mathbf{v}\mathbf{v}f\right\rangle = \nabla.\left\langle m\left(\mathbf{c}+\mathbf{u}\right)\left(\mathbf{c}+\mathbf{u}\right)f\right\rangle \\
&= \nabla.\left\langle m\mathbf{c}\mathbf{c}f\right\rangle + \nabla.\left\langle m\mathbf{c}\mathbf{u}f\right\rangle + \nabla.\left\langle m\mathbf{u}\mathbf{c}f\right\rangle + \nabla.\left\langle m\mathbf{u}\mathbf{u}f\right\rangle \\
&= \nabla.\left\langle m\left(\left[\mathbf{c}\mathbf{c}\right]^2 - \frac{1}{3}Tr\left(\mathbf{c}\mathbf{c}\right)\mathbf{I}\right)f\right\rangle + \nabla.\left\langle mf\right\rangle\mathbf{u}\mathbf{u} \\
&= \nabla.\left\langle m\left[\mathbf{c}\mathbf{c}\right]^2 f\right\rangle - \nabla.\left\langle\frac{1}{3}Tr\left(\mathbf{c}\mathbf{c}\right)f\right\rangle\mathbf{I} + \nabla.\left(\rho\mathbf{u}\mathbf{u}\right) \\
&= \nabla.\boldsymbol{\Pi} - \nabla.\left\langle\frac{1}{3}Tr\left(\mathbf{c}\mathbf{c}\right)f\right\rangle\mathbf{I} + \nabla.\left(\rho\mathbf{u}\mathbf{u}\right) \\
&= \nabla.\boldsymbol{\Pi} - \nabla.\left(\Delta + p\right)\mathbf{I} + \nabla.\left(\rho\mathbf{u}\mathbf{u}\right) \\
&= \nabla.\left(\rho\mathbf{u}\mathbf{u}\right) + \nabla.\left(\left(\Delta + p\right)\mathbf{I} + \boldsymbol{\Pi}\right) \\
&= \nabla.\left(\rho\mathbf{u}\mathbf{u}\right) + \nabla.\mathbf{P}.
\end{aligned} \tag{149}$$

In the above relation, **P** is the stress tensor, which is decomposable into hydrostatic pressure, excess trace part, and traceless part. Finally, the momentum equation can be expressed as,

$$\frac{\partial}{\partial t}\rho\mathbf{u}+\nabla.\left(\rho\mathbf{uu}+p\mathbf{I}\right)+\nabla.\left(\mathbf{\Pi}+\Delta\mathbf{I}\right)=0\,. \tag{150}$$

Accordingly, with the help of the statistical definition of the internal energy density of the fluid and consequent substitution and differentiation as has been done for the derivation of mass and momentum conservation equations, we can derive the energy conservation law or the first law of thermodynamics.

$$\begin{aligned}&\left\langle\left(\frac{1}{2}mc^2+H_{rot}\right)\frac{\partial f}{\partial t}\right\rangle+\left\langle\left(\frac{1}{2}mc^2+H_{rot}\right)\mathbf{v}\cdot\nabla f\right\rangle+\left\langle\left(\frac{1}{2}mc^2+H_{rot}\right)\frac{j}{I}\frac{\partial f}{\partial\theta}\right\rangle\\&=\left\langle\left(\frac{1}{2}mc^2+H_{rot}\right)C\left[f,f_1\right]\right\rangle.\end{aligned} \tag{151}$$

The third collisional invariant of the Boltzmann equation is the energy, therefore,

$$\left\langle\left(\frac{1}{2}mc^2+H_{rot}\right)\frac{\partial f}{\partial t}\right\rangle+\left\langle\left(\frac{1}{2}mc^2+H_{rot}\right)\mathbf{v}\cdot\nabla f\right\rangle+\left\langle\left(\frac{1}{2}mc^2+H_{rot}\right)\frac{j}{I}\frac{\partial f}{\partial\theta}\right\rangle=0 \tag{152}$$

The above equation can be further simplified as follows

$$\begin{aligned}&\frac{\partial}{\partial t}\left\langle\left(\frac{1}{2}mc^2+H_{rot}\right)f\right\rangle+\left\langle\frac{1}{2}mc^2\mathbf{v}\cdot\nabla f\right\rangle+\left\langle H_{rot}\mathbf{v}\cdot\nabla f\right\rangle=0\\&\frac{\partial}{\partial t}\left\langle\left(\frac{1}{2}mc^2+H_{rot}\right)f\right\rangle+\left\langle\frac{1}{2}m\mathbf{v}\left(c^2\cdot\nabla f\right)\right\rangle+\left\langle\mathbf{v}\left(H_{rot}\cdot\nabla f\right)\right\rangle=0\\&\frac{\partial}{\partial t}\left\langle\left(\frac{1}{2}mc^2+H_{rot}\right)f\right\rangle+\left\langle\frac{1}{2}m\mathbf{v}\nabla.\left(c^2f\right)\right\rangle-\left\langle\frac{1}{2}m\mathbf{v}\left(f.\nabla c^2\right)\right\rangle\\&+\nabla.\left\langle\mathbf{v}\left(H_{rot}f\right)\right\rangle-\left\langle\mathbf{v}f\left(\nabla.H_{rot}\right)\right\rangle=0\\&\frac{\partial}{\partial t}\left\langle\left(\frac{1}{2}mc^2+H_{rot}\right)f\right\rangle+\left\langle\frac{1}{2}m\mathbf{v}\nabla.\left(c^2f\right)\right\rangle-\left\langle\frac{1}{2}m\mathbf{v}\left(f.\nabla c^2\right)\right\rangle\\&+\nabla.\left\langle\mathbf{v}\left(H_{rot}f\right)\right\rangle=0.\end{aligned} \tag{153}$$

By substituting the molecular velocity in terms of thermal and macroscopic velocities:

$$\frac{\partial}{\partial t}\left\langle\left(\frac{1}{2}mc^2+H_{rot}\right)f\right\rangle+\nabla.\left\langle\frac{1}{2}m(\mathbf{c}+\mathbf{u})c^2f\right\rangle$$
$$+\left\langle m(\mathbf{c}+\mathbf{u})\mathbf{c}f\right\rangle.(\nabla.\mathbf{u})+\nabla.\left\langle(\mathbf{c}+\mathbf{u})(H_{rot}f)\right\rangle=0$$

$$\frac{\partial}{\partial t}\left\langle\left(\frac{1}{2}mc^2+H_{rot}\right)f\right\rangle+\nabla.\left\langle\frac{1}{2}m\mathbf{c}c^2f\right\rangle+\nabla.\mathbf{u}\left\langle\frac{1}{2}mc^2f\right\rangle$$
$$+\left\langle m\mathbf{c}\mathbf{c}f\right\rangle.(\nabla.\mathbf{u})+\mathbf{u}\left\langle m\mathbf{c}f\right\rangle.\nabla\mathbf{u}+\nabla.\left\langle\mathbf{c}H_{rot}f\right\rangle+\nabla.\left\langle\mathbf{u}H_{rot}f\right\rangle=0 \qquad (154)$$

$$\frac{\partial}{\partial t}\left\langle\left(\frac{1}{2}mc^2+H_{rot}\right)f\right\rangle+\nabla.\left\langle\left(\frac{1}{2}mc^2+H_{rot}\right)cf\right\rangle$$
$$+\nabla.\mathbf{u}\left\langle\left(\frac{1}{2}mc^2+H_{rot}\right)f\right\rangle+\left\langle m\mathbf{c}\mathbf{c}f\right\rangle.(\nabla.\mathbf{u})=0$$

Finally, we can write the energy conservation as

$$\frac{\partial}{\partial t}\rho E+\nabla.\left[(\rho E)\mathbf{u}+\mathbf{Q}\right]+\mathbf{P}:\nabla\mathbf{u}=0 \qquad (155)$$

Alternatively, the above equation can be written as

$$\frac{\partial}{\partial t}\rho E+\nabla.\left[(\rho E+p)\mathbf{u}\right]+\nabla.\left[(\mathbf{\Pi}+\Delta\mathbf{I}).\mathbf{u}+\mathbf{Q}\right]=0 \qquad (156)$$

Appendix B. Derivation of constitutive relations from the Boltzmann transport equation

It was shown in Chapter 3 that the moment equations can be obtained by differentiating the statistical definition of the variable with respect to time and combining it with Boltzmann (Boltzmann-Curtiss for diatomic and linear polyatomic) transport equation which yields the general moment $h^{(n)}$ as follows [234-236],

$$\left(\frac{\partial}{\partial t}+\mathbf{u}.\nabla\right)\left\langle h^{(n)} f\right\rangle+\left\langle h^{(n)} f\right\rangle.\nabla\mathbf{u}+\nabla\cdot\left\langle \mathbf{c}h^{(n)} f\right\rangle$$
$$-\left\langle f\left(\frac{\partial}{\partial t}+\mathbf{u}.\nabla+\mathbf{c}.\nabla+\frac{j}{I}\frac{\partial}{\partial\theta}\right)h^{(n)}\right\rangle=\mathbf{\Lambda}^{(n)} \tag{157}$$

By defining $\mathbf{\Psi}^{(n)}$ as the flux of $\left\langle h^{(n)} f\right\rangle$ (high-order moments), $\mathbf{Z}^{(n)}$ kinematic term due to hydrodynamic streaming effect and $\mathbf{\Lambda}^{(n)}$ the dissipation term to account for energy dissipation in the irreversible process as

$$\mathbf{\Psi}^{(n)}=\left\langle ch^{(n)} f\right\rangle$$
$$\mathbf{Z}^{(n)}=\left\langle f\left(\frac{D}{Dt}+\mathbf{c}.\nabla+\frac{j}{I}\frac{\partial}{\partial\theta}\right)h^{(n)}\right\rangle \tag{158}$$
$$\mathbf{\Lambda}^{(n)}=\left\langle h^{(n)} C[f,f_1]\right\rangle$$

Moreover, after denoting $\left\langle h^{(n)} f\right\rangle/\rho$ as $\hat{h}^{(n)}$ the general evolution can be written as

$$\rho\frac{D}{D}\hat{h}^{(n)}+\nabla.\mathbf{\Psi}^{(n)}-\mathbf{Z}^{(n)}=\mathbf{\Lambda}^{(n)} \tag{159}$$

The constitutive equation for viscous stress tensor $\mathbf{\Pi}=\left\langle m\left[\mathbf{cc}\right]^{(2)} f\right\rangle$ can be derived by taking $h^{(1)}=m\left[\mathbf{cc}\right]^{(2)}$ as follows

$$\rho\frac{D}{D}\left(\frac{\mathbf{\Pi}}{\rho}\right)+\nabla.\mathbf{\Psi}^{(\Pi)}-\mathbf{Z}^{(\Pi)}=\mathbf{\Lambda}^{(\Pi)} \tag{160}$$

The kinematic term can be expanded as follows

$$
\begin{aligned}
\mathbf{Z}^{(\Pi)} &= \left\langle f\left(\frac{D}{Dt}+\mathbf{c}.\nabla+\frac{j}{I}\frac{\partial}{\partial\theta}\right)h^{(1)}\right\rangle \\
&= \left\langle f\,\frac{D}{Dt}h^{(1)}\right\rangle + \left\langle f\mathbf{c}.\nabla h^{(1)}\right\rangle + \left\langle f\,\frac{j}{I}\frac{\partial}{\partial\theta}h^{(1)}\right\rangle \\
&= \left\langle f\,\frac{D}{Dt}m\left[\mathbf{cc}\right]^{(2)}\right\rangle + \left\langle f\mathbf{c}.\nabla h^{(1)}\right\rangle + \left\langle f\,\frac{j}{I}\frac{\partial}{\partial\theta}h^{(1)}\right\rangle \\
&= \left\langle f\,\frac{D}{Dt}m\left[\mathbf{cc}\right]^{(2)}\right\rangle + \left\langle f\,\frac{D}{Dt}m\left[\mathbf{cc}\right]^{(2)}\right\rangle + \left\langle f\mathbf{c}.\nabla h^{(1)}\right\rangle + \left\langle f\,\frac{j}{I}\frac{\partial}{\partial\theta}h^{(1)}\right\rangle \\
&= -2\left[\mathbf{J}\,\frac{D\mathbf{u}}{Dt}\right] - 2\left(p+\mathbf{\Delta}\right)\left[\nabla\mathbf{u}\right]^{(2)} - 2\left[\Pi.\nabla\mathbf{u}\right]^{(2)}
\end{aligned}
\tag{161}
$$

In the above equation $\mathbf{J}=\langle m\mathbf{c}f\rangle$ is the diffusion flux, which can be neglected for single species flows. The final equation of constitutive equation for shear stress then reduces to

$$
\rho\frac{D}{D}\left(\frac{\mathbf{\Pi}}{\rho}\right)+\nabla.\mathbf{\Psi}^{(\Pi)}+2\left(p+\mathbf{\Delta}\right)\left[\nabla\mathbf{u}\right]^{(2)}+2\left[\Pi.\nabla\mathbf{u}\right]^{(2)}=\mathbf{\Lambda}^{(\Pi)} \tag{162}
$$

The excess normal stress $\Delta=\left\langle\left(mC^2/3-p/n\right)f\right\rangle$ balance equation can be achieved by setting $h^{(2)}=mc^2/3-p/n$, with n as number density in the general evolution equation,

$$
\rho\frac{D}{D}\hat{h}^{(2)}+\nabla.\mathbf{\Psi}^{(2)}-\mathbf{Z}^{(2)}=\mathbf{\Lambda}^{(2)} \tag{163}
$$

Equivalently,

$$
\rho\frac{D}{D}\left(\frac{\mathbf{\Delta}}{\rho}\right)+\nabla.\mathbf{\Psi}^{(\Delta)}-\mathbf{Z}^{(\Delta)}=\mathbf{\Lambda}^{(\Delta)} \tag{164}
$$

Again, the kinematic term can be expanded as

$$
\begin{aligned}
\mathbf{Z}^{(\Delta)} &= \left\langle f\left(\frac{D}{Dt}+\mathbf{c}.\nabla+\frac{j}{I}\frac{\partial}{\partial\theta}\right)h^{(2)}\right\rangle \\
&= \left\langle f\frac{D}{Dt}h^{(2)}\right\rangle+\left\langle f\mathbf{c}.\nabla h^{(2)}\right\rangle+\left\langle f\frac{j}{I}\frac{\partial}{\partial\theta}h^{(2)}\right\rangle \\
&= \left\langle f\frac{D}{Dt}\left(\frac{1}{3}mC^2-\frac{p}{n}\right)\right\rangle+\left\langle f\mathbf{c}.\nabla\left(\frac{1}{3}mC^2-\frac{p}{n}\right)\right\rangle+\left\langle f\frac{j}{I}\frac{\partial}{\partial\theta}\left(\frac{1}{3}mC^2-\frac{p}{n}\right)\right\rangle \\
&= -2\gamma'\left(\mathbf{\Pi}+\Delta\mathbf{I}\right):\nabla\mathbf{u}-\frac{2}{3}\gamma' p\nabla.\mathbf{u}
\end{aligned}
\tag{165}
$$

Therefore, the excess normal stress constitutive relation can be written as

$$
\rho\frac{D}{D}\left(\frac{\mathbf{\Delta}}{\rho}\right)+\nabla.\mathbf{\Psi}^{(\Delta)}+2\gamma'\left(\mathbf{\Pi}+\Delta\mathbf{I}\right):\nabla\mathbf{u}+\frac{2}{3}\gamma' p\nabla.\mathbf{u}=\mathbf{\Lambda}^{(\Delta)} \tag{166}
$$

The heat flux $\mathbf{Q}=\left\langle\left(mC^2/2+H_{rot}-m\hat{h}\right)\mathbf{c}f\right\rangle$ balance equation can be achieved by setting $h^{(3)}=\left(mC^2/2+H_{rot}-m\hat{h}\right)\mathbf{c}$, with H_{rot} and $\hat{h}$ as rotational Hamiltonian of the molecule and the enthalpy density per unit mass, in the general evolution equation,

$$
\rho\frac{D}{D}\hat{h}^{(3)}+\nabla.\mathbf{\Psi}^{(3)}-\mathbf{Z}^{(3)}=\mathbf{\Lambda}^{(3)}. \tag{167}
$$

Similar to derivation previous in previous parameters the kinematic term can be expanded as

$$
\rho\frac{D}{D}\left(\frac{\mathbf{Q}}{\rho}\right)+\nabla.\mathbf{\Psi}^{(Q)}-\mathbf{Z}^{(Q)}=\mathbf{\Lambda}^{(Q)}. \tag{168}
$$

Expanding the kinematic term yields

$$
\begin{aligned}
\mathbf{Z}^{(Q)} &= \left\langle f\left(\frac{D}{Dt}+\mathbf{c}.\nabla+\frac{j}{I}\frac{\partial}{\partial\theta}\right)h^{(3)}\right\rangle \\
&= \left\langle f\frac{D}{Dt}h^{(3)}\right\rangle+\left\langle f\mathbf{c}.\nabla h^{(3)}\right\rangle+\left\langle f\frac{j}{I}\frac{\partial}{\partial\theta}h^{(3)}\right\rangle \\
&= \left\langle f\frac{D}{Dt}\left(\frac{1}{2}mC^2+H_{rot}-m\tilde{h}\right)\right\rangle+\left\langle f\mathbf{c}.\nabla\left(\frac{1}{2}mC^2+H_{rot}-mh\right)\right\rangle \\
&+\left\langle f\frac{j}{I}\frac{\partial}{\partial\theta}\left(\frac{1}{2}mC^2+H_{rot}-m\hat{h}\right)\right\rangle \\
&= -\psi^{(P)}:\nabla\mathbf{u}-\frac{d\mathbf{u}}{dt}.\left(\mathbf{\Pi}+\Delta\mathbf{I}\right)-\left(p+\Delta\right)C_p\nabla T-\mathbf{\Pi}.C_p\nabla T-\mathbf{Q}\nabla\mathbf{u}
\end{aligned}
\tag{169}
$$

Finally, the constitutive equation for heat flux can be written as

$$
\begin{aligned}
&\rho\frac{D}{D}\left(\frac{\mathbf{Q}}{\rho}\right)+\nabla.\mathbf{\Psi}^{(Q)}+\psi^{(P)}:\nabla\mathbf{u}+\frac{d\mathbf{u}}{dt}.\left(\mathbf{\Pi}+\Delta\mathbf{I}\right)+\left(p+\Delta\right)C_p\nabla T \\
&+\mathbf{\Pi}.C_p\nabla T+\mathbf{Q}\nabla\mathbf{u}=\mathbf{\Lambda}^{(Q)}
\end{aligned}
\tag{170}
$$

Appendix C. Applied basis functions and integration process of the source term vector for triangular elements

In this appendix, the applied basis functions and the analytical integration, which shows that only the first term of $\mathbf{\Theta}'$ vector has non-zero value is provided.

$$
\mathbf{\Theta}'=\begin{bmatrix}\int_{\Omega_k}\varphi_1(\mathbf{x})\left|J'\right|\mathrm{d}\mathbf{\Omega}_k\\ \int_{\Omega_k}\varphi_2(\mathbf{x})\left|J'\right|\mathrm{d}\mathbf{\Omega}_k\\ \vdots\\ \int_{\Omega_k}\varphi_n(\mathbf{x})\left|J'\right|\mathrm{d}\mathbf{\Omega}_k\end{bmatrix}=\begin{bmatrix}\text{Cell Area}/2\\ 0\\ \vdots\\ 0\end{bmatrix}
\tag{171}
$$

The vector of basis functions, which is used in order to achieve a third order (P^2) solution, is as follows:

$$\begin{bmatrix}\varphi_1(a,b)\\ \varphi_2(a,b)\\ \varphi_3(a,b)\\ \varphi_4(a,b)\\ \varphi_5(a,b)\\ \varphi_6(a,b)\end{bmatrix}=\begin{bmatrix}1\\ \frac{1}{2}(1+3b)\\ -\frac{1}{4}(-1+b)(3+5b)a\\ -\frac{1}{2}(-1+b)a\\ (\frac{-1}{2}+b+\frac{5b^2}{2})\\ -\frac{1}{8}\left(-1+b\right)\left(1+3b\left(6+7b\right)\right)a\end{bmatrix} \tag{172}$$

The transformation Jacobian is (1-*b*)/2; therefore,

$$\begin{aligned}&\int_{\Omega_k}\varphi_1(\mathbf{x})\left|J'\right|\mathrm{d}\mathbf{\Omega}_k=\int_{-1}^{1}\int_{-1}^{1}1.\frac{(1-b)}{2}dadb\\ &=\int_{-1}^{-1}\int_{-1}^{-1}1.\frac{(1-b)}{2}dbda=1/2\int_{-1}^{1}\left(\left(b-\frac{b^2}{2}\right)\Big|_{-1}^{1}\right)da=\frac{1}{2}\int_{-1}^{1}\left(\left(1-\frac{1}{2}\right)-\left(-1-\frac{1}{2}\right)\right)da\\ &=\frac{1}{2}\int_{-1}^{1}(2)da=a\Big|_{-1}^{1}=1-(-1)=2\end{aligned} \tag{173}$$

$$\begin{aligned}&\int_{\Omega_k}\varphi_2(\mathbf{x})\left|J'\right|\mathrm{d}\mathbf{\Omega}_k=\int_{-1}^{1}\int_{-1}^{1}\frac{1}{2}(1+3b)\frac{(1-b)}{2}dadb=\frac{1}{4}\int_{-1}^{1}\int_{-1}^{1}\left(1+2b-3b^2\right)dadb\\ &=\frac{1}{4}\int_{-1}^{-1}\int_{-1}^{-1}\left(b+b^2-b^3\right)dbda=\frac{1}{4}\int_{-1}^{1}\left(b+b^2-b^3\right)\Big|_{-1}^{1})da=\\ &\frac{1}{4}\int_{-1}^{1}\left(\left(1+1-1\right)-\left(-1+1+1\right)\right)da=\frac{1}{4}\int_{-1}^{1}(0)da=0\end{aligned} \tag{174}$$

$$\begin{aligned}&\int_{\Omega_k}\varphi_3(\mathbf{x})\left|J'\right|\mathrm{d}\mathbf{\Omega}_k=\int_{-1}^{1}\int_{-1}^{1}\frac{-1}{2}(-1+b)(3+5b)a\frac{(1-b)}{2}dadb\\ &=\frac{-1}{8}\int_{-1}^{1}(-1+b)(3+5b)(1-b)\int_{-1}^{1}adadb\\ &=\frac{-1}{16}\int_{-1}^{1}(-1+b)(3+5b)(1-b)(a^2\Big|_{-1}^{1})db\\ &=\frac{-1}{16}\int_{-1}^{1}(-1+b)(3+5b)(1-b)(1-1)db=0\end{aligned} \tag{175}$$

$$\int_{\Omega_k} \varphi_4(\mathbf{x})\left|J'\right|\mathrm{d}\mathbf{\Omega}_k = \int_{-1}^{1}\int_{-1}^{1} \frac{-1}{2}(-1+b)a\frac{(1-b)}{2}\,dadb$$
$$= \frac{-1}{4}\int_{-1}^{1}(-1+b)(1-b)\int_{-1}^{1} adadb = \frac{-1}{4}\int_{-1}^{1}(-1+b)(1-b)(a^2\Big|_{-1}^{1})db \qquad (176)$$
$$= \frac{-1}{4}\int_{-1}^{1}(-1+b)(1-b)(1-1)db = 0$$

$$\int_{\Omega_k} \varphi_5(\mathbf{x})\left|J'\right|\mathrm{d}\mathbf{\Omega}_k = \int_{-1}^{1}\int_{-1}^{1} (\frac{-1}{2}+b+\frac{5b^2}{2})\frac{(1-b)}{2}\,dadb$$
$$= \int_{-1}^{1}\int_{-1}^{1}(-\frac{5b^3}{2}+\frac{3b^2}{2}+\frac{3b}{2}-\frac{1}{2})dadb = \frac{1}{2}\int_{-1}^{1}\left(\left(-\frac{5b^4}{8}+\frac{3b^3}{6}+\frac{3b^2}{4}-\frac{b}{2}\right)\Big|_{-1}^{1}\right)da \qquad (177)$$
$$= \frac{-1}{4}\int_{-1}^{1}(0)da = 0$$

$$\int_{\Omega_k} \varphi_6(\mathbf{x})\left|J'\right|\mathrm{d}\mathbf{\Omega}_k = \int_{-1}^{1}\int_{-1}^{1}\left(-\frac{1}{8}(-1+b)\left(1+3b\left(6+7b\right)\right)a\right)\frac{(1-b)}{2}\,dadb$$
$$= \int_{-1}^{1}\int_{-1}^{1}\left(-\frac{1}{8}(-1+b)\left(1+3b\left(6+7b\right)\right)\frac{(1-b)}{2}\right)adadb$$
$$= \int_{-1}^{1}\int_{-1}^{1}\left(-\frac{1}{8}(-1+b)\left(1+3b\left(6+7b\right)\right)\frac{(1-b)}{2}\right)\left(\frac{a^2}{2}\Big|_{-1}^{1}\right)db \qquad (178)$$
$$= \int_{-1}^{1}\int_{-1}^{1}\left(-\frac{1}{8}(-1+b)\left(1+3b\left(6+7b\right)\right)\frac{(1-b)}{2}\right)\left(\frac{1}{2}-\frac{1}{2}\right)db = 0$$

Appendix D. Thermodynamic properties and estimation of essential factors by Lennard-Jones parameters for usually used gases in the CVD process

Table 21 Heat capacity estimation for usually used gases in CVD adopted from reference [224]

Gas	$c_p = a_0 + a_1 T + a_2 T^2$ [J/(kg.K)]		
	a_0	a_1	a_2
Ar	5.20 x 10^2	0.00 x 10^0	0.00 x 10^0
AsH_3	2.45 x 10^2	1.08 x 10^0	4.24 x 10^{-4}
$Ga(CH_3)_3$	3.36 x 10^2	2.54 x 10^0	-9.27 x 10^{-4}
H_2	1.44 x 10^4	-2.61 x 10^{-1}	8.67 x 10^{-4}
HF	1.48 x 10^3	-1.20 x 10^{-1}	1.47 x 10^{-4}
N_2	1.03 x 10^3	4.58 x 10^{-3}	1.34 x 10^{-4}
SiF_4	4.73 x 10^2	9.73 x 10^{-1}	-4.55 x 10^{-4}

SiH_2	9.02×10^2	9.32×10^{-1}	-2.07×10^{-4}
SiH_4	4.74×10^2	3.26×10^0	-1.08×10^{-3}
Si_2H_4	5.83×10^2	2.24×10^0	-9.97×10^{-4}
Si_2H_6	3.44×10^2	3.57×10^0	-1.55×10^{-3}
Si_3H_8	3.71×10^2	3.44×10^0	-1.55×10^{-3}
WF_6	3.25×10^2	4.69×10^{-1}	-2.94×10^{-4}

Table 22 Lennard-Jones parameters for usually used gases in CVD adopted from reference [224]

Gas	Molecular weight (m) [kg/mole]	Collision diameter (σ) [$\dot{A}ng$]	The maximum energy of attraction (ε/k) [K]
Ar	39.944	3.542	93.3
AsH_3	77.95	4.145	259.8
$Ga(CH_3)_3$	114.83	5.68	398
H_2	2.016	2.827	59.7
HF	20.01	3.138	330
N_2	28.02	3.798	71.4
SiF_4	104.09	4.88	171.9
SiH_2	30.10	3.803	133.1
SiH_4	32.12	4.084	207.6
Si_2H_4	60.21	4.601	312.6
Si_2H_6	62.23	4.828	301.3
Si_3H_8	92.33	5.562	331.2

WF_6	297.84	5.21	338

Table 23 Integral function estimation for usually used gases in CVD adopted from reference [224]

T^* interval	$\Omega_\mu = a_0 + a_1 T^* + a_2 (T^*)^2 + a_3 (T^*)^3$			
	a_0	a_1	a_2	a_3
$0.3 \le T^* < 1$	4.0384 x 10^0	-5.2953 x 10^0	4.0846 x 10^0	-1.2414 x 10^0
$1 \le T^* < 3$	2.7015 x 10^0	-1.6152 x 10^0	5.6831 x 10^{-1}	-7.1633 x 10^{-2}
$3 \le T^* < 10$	1.3824 x 10^0	-1.6174 x 10^{-1}	1.7603 x 10^{-2}	-7.1058 x 10^{-4}
$10 \le T^* \le 30$	9.8307 x 10^{-1}	-1.9520 x 10^{-2}	4.4911 x 10^{-4}	-3.8432 x 10^{-6}

Bibliography

1. Lyndon, B., Apollo program summary report. *Johnson Space Center, NASA, TM X*, 1975. **68725**.
2. Klotz, I., New moon. *Aviation Week & Space Technology November 27-December*, 2017. **10**: pp. 60-61.
3. Lee, K.H., Lunar orbiter trade study and conceptual design of onboard propulsion system. *Journal of spacecraft and rockets*, 2011. **48**(2): pp. 346-354.
4. Gaier, J.R., The effects of lunar dust on EVA systems during the Apollo missions. 2007.
5. Apollo 16 Astronaut John Young, July 2004.
6. Tosh, A., Liever, P.A., Arslanbekov, R.R., et al., Numerical analysis of spacecraft rocket plume impingement under lunar environment. *Journal of Spacecraft and Rockets*, 2011. **48**(1): pp. 93.
7. Ejtehadi, O., A second-order Boltzmann-based continuum model for simulation of dusty gas flows in non-equlibrium using a discontinuous Galerkin method, Ph.D. dissertation 2018, Gyeongsang National University.
8. Singh, S., Karchani, A., and Myong, R.S., Non-equilibrium effects of diatomic and polyatomic gases on the shock-vortex interaction based on the second-order

constitutive model of the Boltzmann-Curtiss equation. *Physics of Fluids*, 2018. **30**(1): pp. 016109.

9. Le, N., Xiao, H., and Myong, R. S., A triangular discontinuous Galerkin method for non-Newtonian implicit constitutive models of rarefied and microscale gases. *Journal of Computational Physics*, 2014. **273**: pp. 160-184.
10. Myong, R. S., A generalized hydrodynamic computational model for rarefied and microscale diatomic gas flows. *Journal of Computational Physics*, 2004. **195**(2): pp. 655-676.
11. Myong, R.S., A computational method for Eu's generalized hydrodynamic equations of rarefied and microscale gasdynamics. *Journal of Computational Physics*, 2001. **168**(1): pp. 47-72.
12. Myong, R.S., Thermodynamically consistent hydrodynamic computational models for high-Knudsen-number gas flows. *Physics of Fluids*, 1999. **11**(9): pp. 2788-2802.
13. Roberts, L., The interaction of a rocket exhaust with the lunar surface, *The Fluid Dynamic Aspects of Space Flight, Proceeding of the AGARD-NATO Specialists Meeting*. 1966. pp. 269-290.
14. Roberts, L. and South, J., Comments on exhaust flow field and surface impingement. *AIAA Journal*, 1964. **2**(5): pp. 971-973.
15. Lane, J.E., Metzger, P.T., Immer, C.D., et al., Lagrangian trajectory modeling of lunar dust particles, *Earth & Space 2008: Engineering, Science, Construction, and Operations in Challenging Environments*. 2008: pp. 1-9.
16. Lane, J., Metzger, P., and Carlson, J., Lunar dust particles blown by lander engine exhaust in rarefied and compressible flow, *Earth and Space 2010: Engineering, Science, Construction, and Operations in Challenging Environments*. 2010. pp. 134-142.
17. Li, Y., Ren, D., Bo, Z., et al., Gas-particle two-way coupled method for simulating the interaction between a rocket plume and lunar dust. *Acta Astronautica*, 2019. **157**: pp. 123-133.
18. Ejtehadi, O., Rahimi, A., Karchani, A., Myong, R.S., Complex wave patterns in dilute gas–particle flows based on a novel discontinuous Galerkin scheme. *International Journal of Multiphase Flow*, 2018. **104**: pp. 125-151.
19. Schwarzkopf, J.D., Sommerfeld, M., Crowe, C.T., et al., Multiphase Flows with Droplets and Particles. 2011: CRC Press.

20. Metzger, P.T., Lane, J.E., and Immer, C.D., Modification of Roberts' Theory for Rocket Exhaust Plumes Eroding Lunar Soil, *Earth & Space 2008: Engineering, Science, Construction, and Operations in Challenging Environments*. 2008. pp. 1-8.
21. Lamont, P. and Hunt, B., The impingement of underexpanded, axisymmetric jets on perpendicular and inclined flat plates. *Journal of Fluid Mechanics*, 1980. **100**(3): pp. 471-511.
22. Al-Qutub, A. and Budair, M. Experiments on the flow over a flat surface impinged by a supersonic jet, *31st Joint Propulsion Conference and Exhibit*. 1995.
23. Carling, J. and Hunt, B., The near wall jet of a normally impinging, uniform, axisymmetric, supersonic jet. *Journal of Fluid Mechanics*, 1974. **66**(1): pp. 159-176.
24. Kalghatgi, G. and Hunt, B., The occurrence of stagnation bubbles in supersonic jet impingement flows. *The Aeronautical Quarterly*, 1976. **27**(3): pp. 169-185.
25. Nakai, Y., Fujimatsu, N., and Fujii, K., Experimental study of underexpanded supersonic jet impingement on an inclined flat plate. *AIAA journal*, 2006. **44**(11): pp. 2691-2699.
26. Pamadi, B., On the impingement of supersonic jet on a normal flat surface. *The Aeronautical Quarterly*, 1982. **33**(3): pp. 199-218.
27. Khasawneh, K., Liu, H., and Cai, C., Highly rarefied two-dimensional jet impingement on a flat plate. *Physics of Fluids*, 2010. **22**(11): pp. 117101.
28. Cai, C., Gaskinetic modeling on dilute gaseous plume impingement flows. *Aerospace*, 2016. **3**(4): p. 43.
29. Cai, S., Cai, C., Zhang, K., et al., Rarefication effects on jet impingement loads. *Aerospace*, 2017. **4**(3): p. 48.
30. Lumpkin III, F.E., Marichalar, J., and Stewart, B.D., High fidelity simulations of plume impingement to the international space station. 2012.
31. Lumpkin, F., Marichalar, J., and Piplica, A., Plume Impingement to the Lunar Surface: A Challenging Problem for DSMC. 2007.
32. Gimelshein, S., Alexeenko, A., Wadsworth, D., et al. The influence of particulates on thruster plume/shock layer interaction at high altitudes, *43rd AIAA Aerospace Sciences Meeting and Exhibit*. 2004.

33. Gimeishein, S., Ketsdever, A., and Wadsworth, D., Particle Simulation of Plume-Plume and Plume-Surface Interactions. 2004, California Univ. Los angeles Dept. of Mechanical and Aerospace Engineering.
34. Morïñigo, J.A. and Salvá, J.J., Numerical study of the start-up process in an optimized rocket nozzle. *Aerospace Science and Technology*, 2008. **12**(6): pp. 485-489.
35. Hadjadj, A., Perrot, Y., and Verma, S., Numerical study of shock/boundary layer interaction in supersonic overexpanded nozzles. *Aerospace Science and Technology*, 2015. **42**: pp. 158-168.
36. Hagemann, G. and Frey, M., Shock pattern in the plume of rocket nozzles: needs for design consideration. *Shock Waves*, 2008. **17**(6): pp. 387-395.
37. Wrisdale, I.E., Mikulskis, D.F., and Gilmore, M.R., Navier-Stokes calculations of a twin-nozzle rocket plume. *AIAA Paper*, 1996(96-1881).
38. Ebrahimi, H.B., Levine, J., and Kawasaki, A., Numerical investigation of twin-nozzle rocket plume phenomenology. *Journal of Propulsion and Power*, 2000. **16**(2): pp. 178-186.
39. Ebrahimi, H.B., Numerical Investigation of Multi-Plume Rocket Phenomenology. *Joint Propulsion, AIAA*, 1997: pp. 97-2942.
40. Kiris, C.C., Housman, J.A., Barad, M.F., et al., Computational framework for launch, ascent, and vehicle aerodynamics (LAVA). *Aerospace Science and Technology*, 2016. **55**: pp. 189-219.
41. He, B., He, X., Zhang, M., et al., Plume aerodynamic effects of cushion engine in lunar landing. *Chinese Journal of Aeronautics*, 2013. **26**(2): pp. 269-278.
42. Yim, J.T., Sibé, F., and Ierardo, N., Plume Impingement Analysis for the European Service Module Propulsion System. 2014.
43. A. Sharma, D.K.A., J. C. Pisharady, S. Sunil Kumar, *Plume Flow Field Analysis for Lander Propulsion System of Chandrayaan-2 Mission*, in *68th International Astronautical Congress (IAC)*. 2017: Adelaide, Australia. pp. 11.
44. Zheng, G., Nie, H., Chen, J., et al., Dynamic analysis of lunar lander during soft landing using explicit finite element method. *Acta Astronautica*, 2018. **148**: pp. 69-81.
45. Wei, X., Lin, Q., Nie, H., et al., Investigation on soft-landing dynamics of four-legged lunar lander. *Acta Astronautica*, 2014. **101**: pp. 55-66.

46. Scott, R.F. and Ko, H.-Y., Transient rocket-engine gas flow in soil. *AIAA J*, 1968. **6**(2): pp. 258-264.
47. Roberts, L., The action of a hypersonic jet on a dust layer. 1963.
48. Roberts, L., The interaction of a rocket exhaust with the lunar surface, *The Fluid Dynamoic Aspects of Space Flight, Proceeding of the AGARD-NATO Specialists Meeting*, 1966. pp. 269-290.
49. Metzger, P.T., Immer, C.D., Donahue, C.M., et al., Jet-induced cratering of a granular surface with application to lunar spaceports. *Journal of Aerospace Engineering*, 2009. **22**(1): pp. 24-32.
50. Morris, A., Goldstein, D., Varghese, P., et al. Plume impingement on a dusty lunar surface, in *AIP Conference Proceedings*. 2011. AIP.
51. Morris, A.B., Simulation of rocket plume impingement and dust dispersal on the lunar surface, 2012.
52. Morris, A.B., Goldstein, D.B., Varghese, P.L., et al., Approach for modeling rocket plume impingement and dust dispersal on the moon. *Journal of Spacecraft and Rockets*, 2015. **52**(2): pp. 362-374.
53. Gallis, M., Torczynski, J., and Rader, D., An approach for simulating the transport of spherical particles in a rarefied gas flow via the direct simulation Monte Carlo method. *Physics of Fluids*, 2001. **13**(11): pp. 3482-3492.
54. Burt, J. and Boyd, I. Development of a two-way coupled model for two phase rarefied flows, in *42nd AIAA Aerospace Sciences Meeting and Exhibit*. 2004.
55. Liu, D., Yang, S., Wang, Z., et al. On rocket plume, lunar crater and lunar dust interactions, in *48th AIAA Aerospace Sciences Meeting Including the New Horizons Forum and Aerospace Exposition*. 2013.
56. He, X., He, B., and Cai, G., Simulation of rocket plume and lunar dust using DSMC method. *Acta Astronautica*, 2012. **70**: pp. 100-111.
57. Morris, A., Goldstein, D., Varghese, P., et al., Modeling the interaction between a rocket plume, scoured regolith, and a plume deflection fence, *Earth and Space 2012: Engineering, Science, Construction, and Operations in Challenging Environments*. 2012. pp. 189-198.
58. Wright, M.J., Candler, G.V., and Bose, D., Data-parallel line relaxation method for the Navier-Stokes equations. *AIAA journal*, 1998. **36**(9): pp. 1603-1609.

59. Chinnappan, A.K. and Kumar, R., Modeling of high speed gas-granular flow over a 2D cylinder in the direct simulation Monte-Carlo framework. *Granular Matter*, 2016. **18**(3): pp. 35.
60. Tung, F.-C., Wang, Y.-S., Lai, S.-H., et al., OLED fabrication by using a novel planar evaporation technique. *International Journal of Photoenergy*, 2014. **2014**.
61. Farber, K., Farber, P., Gräbel, J., et al., Development and validation of a coupled Navier–Stokes/DSMC simulation for rarefied gas flow in the production process for OLEDs. *Applied Mathematics and Computation*, 2016. **272**: pp. 648-656.
62. Navarro, F.F., Djurovich, P.I., and Thompson, M.E., Metal deposition for optoelectronic devices using a low vacuum vapor phase deposition (VPD) system. *Organic Electronics*, 2014. **15**(11): pp. 3052-3060.
63. Sapko, M.J., Weiss, E.S., Cashdollar, K.L., et al., Experimental mine and laboratory dust explosion research at NIOSH. *Journal of Loss Prevention in the Process Industries*, 2000. **13**(3): pp. 229-242.
64. Wan, G., Sun, G., Xue, X., et al., Solids concentration simulation of different size particles in a cyclone separator. *Powder Technology*, 2008. **183**(1): pp. 94-104.
65. Metzger, P.T., Smith, J., and Lane, J.E., Phenomenology of soil erosion due to rocket exhaust on the Moon and the Mauna Kea lunar test site. *Journal of Geophysical Research: Planets*, 2011. **116**(E6).
66. Walker, G.P., Generation and dispersal of fine ash and dust by volcanic eruptions. *Journal of Volcanology and Geothermal Research*, 1981. **11**(1): pp. 81-92.
67. Popel, S. and Gisko, A., Charged dust and shock phenomena in the solar system. *Nonlinear Processes in Geophysics*, 2006. **13**(2): pp. 223-229.
68. Kührt, E. and Keller, H., On the importance of dust in cometary nuclei. *Earth, Moon, and Planets*, 1996. **72**(1): pp. 79-89.
69. Marble, F.E., Dynamics of dusty gases. *Annual Review of Fluid Mechanics*, 1970. **2**(1): pp. 397-446.
70. Rudinger, G., Some properties of shock relaxation in gas flows carrying small particles. *Physics of Fluids*, 1964. **7**(5): pp. 658-663.
71. Satofuka, N. and Tokita, K., Finite difference calculation of gas-particle flows in shock tubes. *Mem. Fac. Ind. Arts, Kyoto Techn. Univ*, 1979. **28**: pp. 28-39.
72. Sommerfeld, M., The unsteadiness of shock waves propagating through gas-particle mixtures. *Experiments in Fluids*, 1985. **3**(4): pp. 197-206.

73. Lock, G., Experimental measurements in a dusty-gas shock tube. *International Journal of Multiphase Flow*, 1994. **20**(1): pp. 81-98.
74. Brennen, C.E., Fundamentals of Multiphase Flow. 2005: Cambridge University Press.
75. Miura, H. and Glass, I.I. On a dusty-gas shock tube, *Proceedings of the Royal Society of London A: Mathematical, Physical and Engineering Sciences*. 1982. The Royal Society.
76. Igra, O., Ben-Dor, G., and Rakib, Z., The effect of dust and water droplets on the relaxation zone developed behind strong normal shock waves. *International Journal of Multiphase Flow*, 1985. **11**(2): pp. 121-132.
77. Toumi, I. and Kumbaro, A., An approximate linearized Riemann solver for a two-fluid model. *Journal of Computational Physics*, 1996. **124**(2): pp. 286-300.
78. Tiselj, I. and Petelin, S., Modelling of two-phase flow with second-order accurate scheme. *Journal of Computational Physics*, 1997. **136**(2): pp. 503-521.
79. Sainsaulieu, L., Finite volume approximation of two phase-fluid flows based on an approximate Roe-type Riemann solver. *Journal of Computational Physics*, 1995. **121**(1): pp. 1-28.
80. Saito, T., Numerical analysis of dusty-gas flows. *Journal of Computational Physics*, 2002. **176**(1): pp. 129-144.
81. Saito, T., Marumoto, M., and Takayama, K., Numerical investigations of shock waves in gas-particle mixtures. *Shock Waves*, 2003. **13**(4): pp. 299-322.
82. Igra, O., Elperin, I., and Ben-Dor, G., Dusty gas flow in a converging-diverging nozzle. *Journal of Fluids Engineering*, 1999. **121**(4): pp. 908-913.
83. Igra, O., Hu, G., Falcovitz, J., et al., Shock wave reflection from a wedge in a dusty gas. *International Journal of Multiphase Flow*, 2004. **30**(9): pp. 1139-1169.
84. Volkov, A., Tsirkunov, Y.M., and Oesterle, B., Numerical simulation of a supersonic gas–solid flow over a blunt body: The role of inter-particle collisions and two-way coupling effects. *International Journal of Multiphase Flow*, 2005. **31**(12): pp. 1244-1275.
85. Pelanti, M. and LeVeque, R.J., High-resolution finite volume methods for dusty gas jets and plumes. *SIAM Journal on Scientific Computing*, 2006. **28**(4): pp. 1335-1360.

86. Gurris, M., Kuzmin, D., and Turek, S., Finite element simulation of compressible particle-laden gas flows. *Journal of Computational and Applied Mathematics*, 2010. **233**(12): pp. 3121-3129.
87. Carcano, S., Bonaventura, L., Esposti Ongaro, T., et al., A semi-implicit, second-order-accurate numerical model for multiphase underexpanded volcanic jets. *Geoscientific Model Development*, 2013. **6**(6): pp. 1905-1924.
88. Carcano, S., Ongaro, T.E., Bonaventura, L., et al., Influence of grain-size distribution on the dynamics of underexpanded volcanic jets. *Journal of Volcanology and Geothermal Research*, 2014. **285**: pp. 60-80.
89. Vié, A., Pouransari, H., Zamansky, R., et al., Particle-laden flows forced by the disperse phase: Comparison between Lagrangian and Eulerian simulations. *International Journal of Multiphase Flow*, 2016. **79**: pp. 144-158.
90. Balachandar, S. and Eaton, J.K., Turbulent dispersed multiphase flow. *Annual Review of Fluid Mechanics*, 2010. **42**: pp. 111-133.
91. Crowe, C.T., Multiphase Flow Handbook. Vol. 59. 2005: CRC Press.
92. Dobran, F., Neri, A., and Macedonio, G., Numerical simulation of collapsing volcanic columns. *Journal of Geophysical Research: Solid Earth*, 1993. **98**(B3): pp. 4231-4259.
93. Ongaro, T.E., Cavazzoni, C., Erbacci, G., et al., A parallel multiphase flow code for the 3D simulation of explosive volcanic eruptions. *Parallel Computing*, 2007. **33**(7): pp. 541-560.
94. Zhang, Y. and Reese, J.M., Continuum Modelling of Granular Particle Flow with Inelastic Inter-Particle Collisions. *Chemical Engineering Research and Design*, 2003. **81**(4): pp. 483-488.
95. Mitter, A., Malhotra, J., and Jadeja, H., The two-fluid modelling of gas-particle transport phenomenon in confined systems considering inter particle collision effects. *International Journal of Numerical Methods for Heat & Fluid Flow*, 2004. **14**(5): pp. 579-605.
96. Zhang, Y. and Reese, J.M., Particle–gas turbulence interactions in a kinetic theory approach to granular flows. *International journal of multiphase flow*, 2001. **27**(11): pp. 1945-1964.
97. Gidaspow, D., Multiphase Flow and Fluidization: Continuum and Kinetic Theory Descriptions. 1994: Academic Press.

98. Morsi, S. and Alexander, A., An investigation of particle trajectories in two-phase flow systems. *Journal of Fluid Mechanics*, 1972. **55**(2): pp. 193-208.
99. Durst, F., Miloievic, D., and Schönung, B., Eulerian and Lagrangian predictions of particulate two-phase flows: a numerical study. *Applied Mathematical Modelling*, 1984. **8**(2): pp. 101-115.
100. Soo, S.l., Fluid Dynamics of Multiphase Systems. 1967: Waltham, Mass., Blaisdell Pub. Co.
101. Fuks, N.A., The Mechanics of Aerosols. 1989: Dover Publications.
102. Gilbert, M., Velocity lag of particles in linearly accelerated combustion gases. *Journal of Jet Propulsion*, 1955. **25**(1): pp. 26-30.
103. Clift, R., Grace, J.R., and Weber, M.E., Bubbles, Drops, and Particles. 2005: Courier Corporation.
104. Henderson, C.B., Drag coefficients of spheres in continuum and rarefied flows. *AIAA journal*, 1976. **14**(6): pp. 707-708.
105. White, F.M. and Corfield, I., Viscous Fluid Flow. Vol. 3. 2006: McGraw-Hill New York.
106. Ben-Dor, G., Igra, O., and Wang, L., Shock wave reflections in dust-gas suspensions. *Journal of fluids engineering*, 2001. **123**(1): pp. 145-153.
107. Knudsen, J.G. and Katz, D.L., Fluid Dynamics and Heat Transfer. 1958: New York, McGraw-Hill Book Company.
108. Ranz, W. and Marshall, W.R., Evaporation from drops. *Chem. Eng. Prog*, 1952. **48**(3): pp. 141-146.
109. Gunn, D., Transfer of heat or mass to particles in fixed and fluidised beds. *International Journal of Heat and Mass Transfer*, 1978. **21**(4): pp. 467-476.
110. Feng, Z.-G. and Michaelides, E.E., A numerical study on the transient heat transfer from a sphere at high Reynolds and Peclet numbers. *International Journal of Heat and Mass Transfer*, 2000. **43**(2): pp. 219-229.
111. Van der Hoef, M.A., Ye, M., van Sint Annaland, M., et al., Multiscale Modeling of Gas-Fluidized Beds, *Advances in Chemical Engineering*, G.B. Marin, Editor. 2006, Academic Press. pp. 65-149.
112. Myong, R.S., On the high Mach number shock structure singularity caused by overreach of Maxwellian molecules. *Physics of Fluids*, 2014. **26**(5): 056102.

113. Deschambault, R. and Glass, I., An update on non-stationary oblique shock-wave reflections: Actual isopycnics and numerical experiments. *Journal of Fluid Mechanics*, 1983. **131**: pp. 27-57.
114. Saito, T. and Glass, I.I., Application of random-choice method to problems in gasdynamics. *Progress in Aerospace Sciences*, 1984. **21**(Supplement C): pp. 201-247.
115. Ishii, R., Umeda, Y., and Yuhi, M., Numerical analysis of gas-particle two-phase flows. *Journal of fluid mechanics*, 1989. **203**: pp. 475-515.
116. Kim, S.W. and Chang, K.S., Reflection of shock wave from a compression corner in a particle-laden gas region. *Shock Waves*, 1991. **1**(1): pp. 65-73.
117. Sommerfeld, M., The structure of particle-laden, underexpanded free jets. *Shock waves*, 1994. **3**(4): pp. 299-311.
118. Castellanos, A., Valverde, J.M., Pérez, A.T., et al., Flow regimes in fine cohesive powders. *Physical review letters*, 1999. **82**(6): pp. 1156.
119. Anderson, T.B. and Jackson, R., Fluid mechanical description of fluidized beds. Equations of motion. *Industrial & Engineering Chemistry Fundamentals*, 1967. **6**(4): pp. 527-539.
120. Tsuo, Y.P. and Gidaspow, D., Computation of flow patterns in circulating fluidized beds. *AIChE Journal*, 1990. **36**(6): pp. 885-896.
121. Kuipers, J., Van Duin, K., Van Beckum, F., et al., A numerical model of gas-fluidized beds. *Chemical Engineering Science*, 1992. **47**(8): pp. 1913-1924.
122. Lun, C., Savage, S.B., Jeffrey, D., et al., Kinetic theories for granular flow: inelastic particles in Couette flow and slightly inelastic particles in a general flowfield. *Journal of Fluid Mechanics*, 1984. **140**: pp. 223-256.
123. Reeks, M., On the constitutive relations for dispersed particles in nonuniform flows. I: Dispersion in a simple shear flow. *Physics of Fluids A: Fluid Dynamics*, 1993. **5**(3): pp. 750-761.
124. Gantt, J.A. and Gatzke, E.P., Kinetic theory of granular flow limitations for modeling high-shear mixing. *Industrial & Engineering Chemistry Research*, 2006. **45**(20): pp. 6721-6727.
125. Schneiderbauer, S., Aigner, A., and Pirker, S., A comprehensive frictional-kinetic model for gas–particle flows: Analysis of fluidized and moving bed regimes. *Chemical Engineering Science*, 2012. **80**: pp. 279-292.

126. Syal, M. and Leishman, J.G., Modeling of bombardment ejections in the rotorcraft brownout problem. *AIAA Journal*, 2013. **51**(4): pp. 849-866.
127. Shao, Y., Physics and Modelling of Wind Erosion. Vol. 37. 2008: Springer Science & Business Media.
128. Kundu, P. and Cohen, L., Fluid Mechanics, 638 pp. *Academic, Calif*, 1990.
129. Chepil, W., The use of evenly spaced hemispheres to evaluate aerodynamic forces on a soil surface. *Eos, Transactions American Geophysical Union*, 1958. **39**(3): pp. 397-404.
130. Tritton, D., *Physical fluid dynamics. Clarendon*. 1988, Oxford.
131. White, B.R. and Schulz, J.C., Magnus effect in saltation. *Journal of Fluid Mechanics*, 1977. **81**(3): pp. 497-512.
132. Anderson, R.S. and Hallet, B., Sediment transport by wind: toward a general model. *Geological Society of America Bulletin*, 1986. **97**(5): pp. 523-535.
133. Zheng, X., He, L., and Zhou, Y., Theoretical model of the electric field produced by charged particles in windblown sand flux. *Journal of Geophysical Research: Atmospheres*, 2004. **109**(D15).
134. Bagnold, R.A., The Physics of Blown Sand and Desert Dunes. 2012: Courier Corporation.
135. Metzger, P.T., Latta III, R.C., Schuler, J.M., et al. Craters formed in granular beds by impinging jets of gas, in *AIP Conference Proceedings*. 2009. AIP.
136. Metzger, P., Lane, J.E., Immer, C., et al., Scaling of erosion rate in subsonic jet experiments and Apollo lunar module landings, *Earth and Space 2010: Engineering, Science, Construction, and Operations in Challenging Environments*. 2010. p. 191-207.
137. Wang, Z.J., Spectral (finite) volume method for conservation laws on unstructured grids. Basic formulation: Basic formulation. *Journal of Computational Physics*, 2002. **178**(1): pp. 210-251.
138. Liu, Y., Vinokur, M., and Wang, Z.J., Spectral difference method for unstructured grids I: Basic formulation. *Journal of Computational Physics*, 2006. **216**(2): pp. 780-801.
139. Huynh, H.T. A reconstruction approach to high-order schemnes including discontinuous galerkin for diffusion, *47th AIAA Aerospace Sciences Meeting Including the New Horizons Forum and Aerospace Exposition*. 2009.

140. Wang, Z. and Gao, H. A unifying lifting collocation penalty formulation for the Euler equations on mixed grids, *47th AIAA Aerospace Sciences Meeting including The New Horizons Forum and Aerospace Exposition*. 2009.
141. Ekaterinaris, J.A., High-order accurate, low numerical diffusion methods for aerodynamics. *Progress in Aerospace Sciences*, 2005. **41**(3-4): pp. 192-300.
142. Wang, Z.J., High-order methods for the Euler and Navier–Stokes equations on unstructured grids. *Progress in Aerospace Sciences*, 2007. **43**(1): pp. 1-41.
143. Shu, C.W., Discontinuous Galerkin methods for time-dependent convection dominated problems: Basics, recent developments and comparison with other methods, *Building Bridges: Connections and Challenges in Modern Approaches to Numerical Partial Differential Equations*. 2016, Springer. pp. 371-399.
144. Reed, W.H. and Hill, T.R., Triangular mesh methods for the neutron transport equation, *Technical Report LA-UR-73-479*. 1973, Los Alamos Scientific Lab., N. Mex.(USA).
145. Cockburn, B. and Shu, C.W., The Runge-Kutta local projection P^1-discontinuous-Galerkin finite element method for scalar conservation laws. *Rairo-Modélisation Mathématique et Analyse Numérique*, 1988. **25**(3): pp. 337-361.
146. Cockburn, B. and Shu, C.W., TVB Runge-Kutta local projection discontinuous Galerkin finite element method for conservation laws. II. General framework. *Mathematics of Computation*, 1989. **52**(186): pp. 411-435.
147. Cockburn, B. and Shu, C.W., The Runge–Kutta discontinuous Galerkin method for conservation laws V: multidimensional systems. *Journal of Computational Physics*, 1998. **141**(2): pp. 199-224.
148. Cockburn, B., Karniadakis, G.E., and Shu, C.W., The development of discontinuous Galerkin methods, *Discontinuous Galerkin Methods*. 2000, Springer. pp. 3-50.
149. Sun, S. and Wheeler, M.F., Discontinuous Galerkin methods for coupled flow and reactive transport problems. *Applied Numerical Mathematics*, 2005. **52**(2): pp. 273-298.
150. Klieber, W. and Rivière, B., Adaptive simulations of two-phase flow by discontinuous Galerkin methods. *Computer Methods in Applied Mechanics and Engineering*, 2006. **196**(1–3): pp. 404-419.

151. Franquet, E. and Perrier, V., Runge–Kutta discontinuous Galerkin method for the approximation of Baer and Nunziato type multiphase models. *Journal of Computational Physics*, 2012. **231**(11): pp. 4096-4141.
152. Franquet, E. and Perrier, V., Runge–Kutta discontinuous Galerkin method for reactive multiphase flows. *Computers & Fluids*, 2013. **83**: pp. 157-163.
153. Owkes, M. and Desjardins, O., A discontinuous Galerkin conservative level set scheme for interface capturing in multiphase flows. *Journal of Computational Physics*, 2013. **249**: pp. 275-302.
154. Lu, H., Zhu, J., Wang, D., et al., Runge–Kutta discontinuous Galerkin method with front tracking method for solving the compressible two-medium flow. *Computers & Fluids*, 2016. **126**: pp. 1-11.
155. De Frahan, M.T.H., Varadan, S., and Johnsen, E., A new limiting procedure for discontinuous Galerkin methods applied to compressible multiphase flows with shocks and interfaces. *Journal of Computational Physics*, 2015. **280**: pp. 489-509.
156. Dumbser, M. and Loubère, R., A simple robust and accurate a posteriori sub-cell finite volume limiter for the discontinuous Galerkin method on unstructured meshes. *Journal of Computational Physics*, 2016. **319**: pp. 163-199.
157. Diehl, D., Kremser, J., Kröner, D., et al., Numerical solution of Navier–Stokes–Korteweg systems by Local Discontinuous Galerkin methods in multiple space dimensions. *Applied Mathematics and Computation*, 2016. **272**: pp. 309-335.
158. Barth, T.J. and Jespersen, D.C., The design and application of upwind schemes on unstructured meshes, *27th Aerospace Sciences Meeting*. 1989, American Institute of Aeronautics and Astronautics.
159. Zhang, X. and Shu, C.W., On positivity-preserving high order discontinuous Galerkin schemes for compressible Euler equations on rectangular meshes. *Journal of Computational Physics*, 2010. **229**(23): pp. 8918-8934.
160. Wang, C., Zhang, X., Shu, C.W., et al., Robust high order discontinuous Galerkin schemes for two-dimensional gaseous detonations. *Journal of Computational Physics*, 2012. **231**(2): pp. 653-665.
161. Kontzialis, K. and Ekaterinaris, J.A., High order discontinuous Galerkin discretizations with a new limiting approach and positivity preservation for strong moving shocks. *Computers & Fluids*, 2013. **71**: pp. 98-112.
162. Dubiner, M., Spectral methods on triangles and other domains. *Journal of Scientific Computing*, 1991. **6**(4): pp. 345-390.

163. Karniadakis, G. and Sherwin, S., Spectral/hp Element Methods for Computational Fluid Dynamics. 2013: Oxford University Press.
164. Bassi, F. and Rebay, S., A High-Order Accurate Discontinuous Finite Element Method for the Numerical Solution of the Compressible Navier–Stokes Equations. *Journal of Computational Physics*, 1997. **131**(2): pp. 267-279.
165. Harten, A., Lax, P.D., and Leer, B.v., On upstream differencing and Godunov-type schemes for hyperbolic conservation laws. *SIAM review*, 1983. **25**(1): pp. 35-61.
166. Toro, E.F., Riemann Solvers and Numerical Methods for Fluid Dynamics: a Practical Introduction. 2013: Springer Science & Business Media.
167. Hirsch, C., Numerical Computation of Internal and External Flows. 1990, John Willy & Son.
168. LeVeque, R.J., Conservative Methods for Nonlinear Problems, in Numerical Methods for Conservation Laws. 1990, Springer. pp. 122-135.
169. Thomas, J.W., Numerical Partial Differential Equations: Conservation Laws and Elliptic Equations. Vol. 33. 2013: Springer Science & Business Media.
170. Rusanov, V.V.e., Calculation of Interaction of Non-Steady Shock Waves with Obstacles. 1962: NRC, Division of Mechanical Engineering.
171. Nishikawa, H. and Kitamura, K., Very simple, carbuncle-free, boundary-layer-resolving, rotated-hybrid Riemann solvers. *Journal of Computational Physics*, 2008. **227**(4): pp. 2560-2581.
172. Arnold, D.N., Brezzi, F., Cockburn, B., et al., Discontinuous Galerkin methods for elliptic problems, *Discontinuous Galerkin Methods*. 2000, Springer. pp. 89-101.
173. Arnold, D.N., Brezzi, F., Cockburn, B., et al., Unified analysis of discontinuous Galerkin methods for elliptic problems. *SIAM Journal on Numerical Analysis*, 2002. **39**(5): pp. 1749-1779.
174. Brezzi, F., Manzini, G., Marini, D., et al., Discontinuous finite elements for diffusion problems. *Atti Convegno in onore di F. Brioschi (Milano 1997), Istituto Lombardo, Accademia di Scienze e Lettere*, 1999: pp. 197-217.
175. Cockburn, B. and Shu, C.-W., The local discontinuous Galerkin method for time-dependent convection-diffusion systems. *SIAM Journal on Numerical Analysis*, 1998. **35**(6): pp. 2440-2463.

176. Douglas, J. and Dupont, T., Interior penalty procedures for elliptic and parabolic Galerkin methods, *Computing methods in applied sciences*. 1976, Springer. pp. 207-216.
177. Bassi, F., Rebay, S., Mariotti, G., et al. A high-order accurate discontinuous finite element method for inviscid and viscous turbomachinery flows, *Proceedings of the 2nd European Conference on Turbomachinery Fluid Dynamics and Thermodynamics*. 1997. Antwerpen, Belgium.
178. Zhang, X. and Shu, C.W., Positivity-preserving high order discontinuous Galerkin schemes for compressible Euler equations with source terms. *Journal of Computational Physics*, 2011. **230**(4): pp. 1238-1248.
179. Zhang, X. and Shu, C.W., On maximum-principle-satisfying high order schemes for scalar conservation laws. *Journal of Computational Physics*, 2010. **229**(9): pp. 3091-3120.
180. Saurel, R., Daniel, E., and Loraud, J.C., Two-phase flows: Second-order schemes and boundary conditions. *AIAA Journal*, 1994. **32**(6): pp. 1214-1221.
181. Béreux, F., Zero-relaxation limit versus operator splitting for two-phase fluid flow computations. *Computer Methods in Applied Mechanics and Engineering*, 1996. **133**(1): pp. 93-124.
182. LeVeque, R.J. and Yee, H.C., A study of numerical methods for hyperbolic conservation laws with stiff source terms. *Journal of Computational Physics*, 1990. **86**(1): pp. 187-210.
183. Lucier, B.J., Error bounds for the methods of Glimm, Godunov and LeVeque. *Siam Journal on Numerical Analysis*, 1985. **22**(6): pp. 1074-1081.
184. Karchani, A., Discontinuous Galerkin Methods for the Second-Order Boltzmann-Based Hydrodynamic Models, Ph.D. dissertation 2017, Gyeongsang National University.
185. Singh, S., Development of a 3D Discontinuous Galerkin Method for the Second-Order Boltzmann-Curtiss Based Hydrodynamic Models of Diatomic and Polyatomic Gases, Ph.D. dissertation 2018, Gyeongsang National University
186. LeVeque, R.J., Finite Volume Methods for Hyperbolic Problems. Vol. 31. 2002: Cambridge University Press.
187. ANSYS FLUENT Theory Guide. *Knowl. Creat. Diffus. Util*, 2011. **15317**: pp. 724-746.
188. ANSYS FLUENT, *Release 14.5," ANSYS FLUENT UDF Manual," ANSYS*. Inc.

189. Qiu, J., Khoo, B.C., and Shu, C.W., A numerical study for the performance of the Runge–Kutta discontinuous Galerkin method based on different numerical fluxes. *Journal of Computational Physics*, 2006. **212**(2): pp. 540-565.
190. Perot, J.B., An analysis of the fractional step method. *Journal of Computational Physics*, 1993. **108**(1): pp. 51-58.
191. Myong, R.S. and Roe, P.L., Shock waves and rarefaction waves in magnetohydrodynamics. Part 2. The MHD system. *Journal of Plasma Physics*, 1997. **58**(3): pp. 521-552.
192. Woodward, P. and Colella, P., The numerical simulation of two-dimensional fluid flow with strong shocks. *Journal of Computational Physics*, 1984. **54**(1): pp. 115-173.
193. Li, H. and Ben-Dor, G., Analysis of double-Mach-reflection wave configurations with convexly curved Mach stems. *Shock Waves*, 1999. **9**(5): pp. 319-326.
194. Pao, S. and Seiner, J., Shock-associated noise in supersonic jets. *AIAA Journal*, 1983. **21**(5): pp. 687-693.
195. Ribner, H.S., Cylindrical sound wave generated by shock-vortex interaction. *AIAA Journal*, 1985. **23**(11): pp. 1708-1715.
196. Lu, P. and Wu, K., On the shock enhancement of confined supersonic mixing flows. *Physics of Fluids A: Fluid Dynamics*, 1991. **3**(12): pp. 3046-3062.
197. Guichard, L., Vervisch, L., and Domingo, P., Two-dimensional weak shock-vortex interaction in a mixing zone. *AIAA Journal*, 1995. **33**(10): pp. 1797-1802.
198. Smart, M., Kalkhoran, I., and Popovic, S., Some aspects of streamwise vortex behavior during oblique shock wave/vortex interaction. *Shock Waves*, 1998. **8**(4): pp. 243-255.
199. Ejtehadi, O., Rahimi, A., and Myong, R.S., Numerical investigation of the counter-intuitive behavior of mach disk movement in underexpanded gas-particle jets. *Journal of Computational Fluid Engineering*, 2019. **24**(1): pp. 19-28.
200. Chang, S.-M. and Chang, K.S., On the shock–vortex interaction in Schardin's problem. *Shock Waves*, 2000. **10**(5): pp. 333-343.
201. Carlson, D. and Lewis, C., Normal shock location in underexpanded gas and gas-particle jets. *AIAA Journal*, 1964. **2**(4): pp. 776-777.
202. Crist, S., Glass, D., and Sherman, P., Study of the highly underexpanded sonic jet. *AIAA Journal*, 1966. **4**(1): pp. 68-71.

203. Avduevskii, V.S., Ivanov, A., Karpman, I.M., et al., Flow in supersonic viscous under expanded jet. *Fluid Dynamics*, 1970. **5**(3): pp. 409-414.
204. Driftmyer, R.T., A correlation of freejet data. *AIAA Journal*, 1972. **10**(8): pp. 1093-1095.
205. Antsupov, A., Properties of underexpanded and overexpanded supersonic gas jets. *Soviet Physics Technical Physics*, 1974. **19**: pp. 234.
206. Addy, A., Effects of axisymmetric sonic nozzle geometry on Mach disk characteristics. *AIAA Journal*, 1981. **19**(1): pp. 121-122.
207. Matsuda, T., Umeda, Y., Ishii, R., et al. Numerical and experimental studies on choked underexpanded jets, in *19th AIAA, Fluid Dynamics, Plasma Dynamics, and Lasers Conference*. 1987.
208. Prudhomme, S. and Haj-Hariri, H., Investigation of supersonic underexpanded jets using adaptive unstructured finite elements. *Finite Elements in Analysis and Design*, 1994. **17**(1): pp. 21-40.
209. Gribben, B.J., Badcock, K.J., and Richards, B.E., Numerical study of shock-reflection hysteresis in an underexpanded jet. *AIAA Journal*, 2000. **38**(2): pp. 275-283.
210. Otobe, Y., Kashimura, H., Matsuo, S., et al., Influence of nozzle geometry on the near-field structure of a highly underexpanded sonic jet. *Journal of Fluids and Structures*, 2008. **24**(2): pp. 281-293.
211. Franquet, E., Perrier, V., Gibout, S., et al., Free underexpanded jets in a quiescent medium: A review. *Progress in Aerospace Sciences*, 2015. **77**: pp. 25-53.
212. Sommerfeld, M., Expansion of a gas/particle mixture in supersonic free jet flow. *Zeitschrift fur Flugwissenschaften und Weltraumforschung*, 1987. **11**: pp. 87-96.
213. Sommerfeld, M., Numerical simulation of supersonic two-phase gas-particle flows. *Shock tubes and waves*, 1988: pp. 235-241.
214. Hayashi, A.K., Fujiwara, T., Arashi, K., et al. Numerical simulation of gas-solid two-phase nozzle and jet flows, *AIAA, Thermophysics, Plasmadynamics and Lasers Conference*. 1988.
215. Draper, J. and Jarvinen, P., Underexpanded gas-particle jets. *AIAA Journal*, 1967. **5**(4): pp. 824-825.
216. Lewis, C. and Carlson, D., Normal shock location in underexpanded gas and gas-particle jets. *AIAA Journal*, 1964. **2**(4): pp. 776-777.

217. Morris, A.B., Simulation of rocket plume impingement and dust dispersal on the lunar surface, Ph.D. dissertation 2012, University of Texas at Austin.
218. Tsien, H.-S., Superaerodynamics, mechanics of rarefied gases. *Journal of the Aeronautical Sciences*, 1946. **13**(12): pp. 653-664.
219. Myong, R.S., Gaseous slip models based on the Langmuir adsorption isotherm. *Physics of Fluids*, 2004. **16**(1): pp. 104-117.
220. Anderson, J.D., Modern Compressible Flow: with Historical Perspective. Vol. 12. 1990: McGraw-Hill New York.
221. Roberts, L., The action of a hypersonic jet on a dust layer, *IAS Paper No. 65-50*. 1963: Institute of the Aerospace Sciences 31st Annual Meeting. pp. 21-23.
222. Marble, F.E., Dynamics of a gas containing small solid particles. 1963.
223. Land, N.S. and Clark, L.V., Experimental Investigation of Jet Impingement on Surfaces of Fine Particles in a Vacuum Environment. Vol. 2633. 1965: National Aeronautics and Space Administration.
224. Kleijn, C.R., Transport phenomena in chemical vapour deposition reactors. 1993.
225. Wilke, C., A viscosity equation for gas mixtures. *The Journal of Chemical Physics*, 1950. **18**(4): pp. 517-519.
226. Wassiljewa, A., Heat conduction in gas mixtures. *Physikalische Zeitschrift*, 1904. **5**(22): pp. 737-742.
227. Reid, R.C., Prausnitz, J.M., and Poling, B.E., The properties of gases and liquids. 1987.
228. Ghia, U., Ghia, K.N., and Shin, C., High-Re solutions for incompressible flow using the Navier-Stokes equations and a multigrid method. *Journal of Computational Physics*, 1982. **48**(3): pp. 387-411.
229. Le, N.T., White, C., Reese, J.M., Myong, R.S., Langmuir–Maxwell and Langmuir–Smoluchowski boundary conditions for thermal gas flow simulations in hypersonic aerodynamics. *International Journal of Heat and Mass Transfer*, 2012. **55**(19-20): pp. 5032-5043.
230. Myong, R.S., Lockerby, D.A., and Reese, J.M., The effect of gaseous slip on microscale heat transfer: An extended Graetz problem. *International Journal of Heat and Mass Transfer*, 2006. **49**(15-16): pp. 2502-2513.
231. Myong, R.S., Reese, J.M., Barber, R.W., Emerson, D.R., Velocity slip in microscale cylindrical Couette flow: the Langmuir model. *Physics of Fluids*, 2005. **17**(8): pp. 087105.

232. Alofs, D.J. and Springer, G.S., Cylindrical Couette flow experiments in the transition regime. *The Physics of Fluids*, 1971. **14**(2): pp. 298-305.
233. Eu, B.C., Kinetic Theory and Irreversible Thermodynamics. 1992: John Wiley and Sons, Inc.
234. Eu, B.C. and Ohr, Y.G., Generalized hydrodynamics, bulk viscosity, and sound wave absorption and dispersion in dilute rigid molecular gases. *Physics of Fluids*, 2001. **13**(3): pp. 744-753.
235. Myong, R.S., A generalized hydrodynamic computational model for rarefied and microscale diatomic gas flows. *Journal of Computational Physics*, 2004. **195**(2): pp. 655-676.
236. Al-Ghoul, M. and Eu, B.C., Generalized hydrodynamic theory of shock waves in rigid diatomic gases. *Physical Review E*, 2001. **64**(4): pp. 046303.